Stratospheric Aerosol: Budgets, Chemistry and radiative Transfer based on a complex Chemistry Climate Model and Satellite and Field Campaign Data

Dissertation

zur Erlangung des Grades
„Doktor der Naturwissenschaften“
(Dr. rer. nat.)

Institut für Physik der Atmosphäre
am Fachbereich Physik, Mathematik und Informatik
der Johannes Gutenberg-Universität in Mainz

angefertigt am
Max-Planck-Institut für Chemie in Mainz

Jennifer Schallock
geboren in Mainz

Mainz, im Dezember 2020

Tag der mündlichen Prüfung: 23.04.2021

Abstract

In the stratosphere aerosol particles consisting of sulfuric acid (H_2SO_4) are formed and accumulate in the Junge-aerosol layer. There they reflect the incoming solar radiation and absorb the solar as well as the outgoing terrestrial radiation. This influences the radiation budget of the earth's atmosphere. The sulfur concentrations in the stratosphere are dominated by strong irregular variations due to volcanic emissions. These variations cannot be predicted in the climate development and therefore require constant observation.

The last major volcanic eruption was the Pinatubo in the Philippines in 1991. Since then there have only been small to medium sized eruptions. Observations from satellites and the herein performed model simulations show, however, that these small eruptions are also relevant for the Earth's radiation budget due to their frequency. For this reason, a Volcanic Sulfur Emissions Inventory is created on the basis of various satellite data sets that includes almost 500 volcanic eruptions. During the implementation of emissions into the model, each volcanic eruption has to be treated individually. The implemented sulfur dioxide (SO_2) emissions are then automatically converted into aerosol particles by the model and their influence on the earth's radiative forcing is calculated. The resulting Aerosol Optical Depth (AOD) and the global negative radiative forcing coincide relatively well with the observations of the various satellites in the new model simulations. Only in the case of large volcanic eruptions, such as the Pinatubo in 1991, will saturation effects of the satellite instruments or overestimated removal processes of aerosol particles in the model lead to slight deviations between observations and model simulations.

Even during periods of low volcanic activity background concentrations of sulfur aerosols remain in the stratosphere. This is based on the conversion of various sulfur precursors gases into SO_2. Here carbonyl sulfide (OCS) plays an important role in the sulfur budget of the stratosphere due to its long atmospheric lifetime.

To identify missing sources of OCS, sensitivity studies are carried out. For this reason emissions of carbon disulfide (CS_2) and dimethyl disulfide (DMDS) have been added to the model and a comprehensive New Sulfur Chemistry Mechanism has been implemented. The newly implemented chemical reactions convert CS_2 and dimethyl sulfide (DMS) into OCS. This increases the mixing ratio of OCS in the UTLS region, especially in tropical regions from approx. $500\,\mathrm{ppt}_v$ to $550\,\mathrm{ppt}_v$. In return, DMS is broken down and the production of methyl sulfonic acid (MSA) is reduced.

The model results are then evaluated by comparing them with aircraft measurements from the StratoClim campaign during the Asian Summer Monsoon in 2017. An improvement in the model is achieved through the newly added comprehensive Sulfur Chemistry Mechanism, which results in increases of the OCS mixing ratio. The latter was previously substantially underestimated in the region of performed measurements. In addition, the observations suggest unusually high particle number concentrations in the UTLS region. These can be verified by comparing them with the model simulations and satellite data as well as traced back to the increased SO_2 emissions of the Sinabung volcano. Thus, this work shows the successful combination of model simulations, satellite observations and airborne in-situ measurements.

Zusammenfassung

In der Stratosphäre werden Aerosolpartikel aus Schwefelsäure (H_2SO_4) gebildet, die sich in der Junge-Aerosolschicht ansammeln. Dort reflektieren sie die einfallende solare Strahlung und absorbieren die solare, sowie die ausgehende terrestrische Strahlung. Dies nimmt Einfluss auf die Strahlungsbilanz der Erdatmosphäre. Die Schwefelkonzentrationen in der Stratosphäre werden durch starke, unregelmäßige Schwankungen aufgrund von Vulkanemissionen dominiert. Diese Schwankungen lassen sich in der Klimaentwicklung nicht vorhersagen und bedürfen daher ständiger Beobachtung.

Der letzte größere Vulkanausbruch war 1991 der Pinatubo auf den Philippinen. Seitdem gab es nur noch kleine bis mittlere Eruptionen. Beobachtungen von Satelliten und die hier durchgeführten Modellsimulationen zeigen aber, dass auch diese kleinen Eruptionen aufgrund ihrer häufigen Anzahl relevant für den Strahlungshaushalt der Erde sind. Daher wurde auf Basis verschiedener Satellitendatensätze ein Inventar der vulkanischen Schwefelemissionen erstellt. Dieses umfasst fast 500 Vulkanausbrüche. Bei der Implementierung der Emissionen im Modell ist jeder Vulkanausbruch einzeln und individuell zu behandeln. Die implementierten Schwefeldioxid (SO_2) Emissionen werden anschließend vom Modell automatisch in Aerosolpartikel umgewandelt und ihr Einfluss auf die Strahlungsbilanz der Erde berechnet. Die daraus resultierende Aerosol Optische Dicke (AOD) und der globale negative Strahlungsantrieb stimmen bei den neu durchgeführten Modellsimulationen relativ gut mit den Beobachtungen der verschiedenen Satelliten überein. Lediglich bei großen Eruptionen, wie beim Pinatubo 1991, kommt es durch Sättigungseffekte der Messinstrumente oder überschätzte Entfernungsprozesse der Aerosolpartikel im Modell zu geringen Abweichungen zwischen den Beobachtungen und den Modellsimulationen.

Auch in Perioden mit geringer vulkanischer Aktivität bleibt eine Hintergrundkonzentration von Schwefelaerosolen in der Stratosphäre erhalten. Diese beruht auf der Umwandlung verschiedener Schwefelvorläufersubstanzen in SO_2. Dabei spielt Carbonylsulfid (OCS) aufgrund seiner langen atmosphärischen Lebensdauer eine entscheidende Rolle im Schwefelhaushalt der Stratosphäre.

Auf der Suche nach einer fehlenden Quelle für OCS werden Sensitivitätsstudien durchgeführt. Zum Einen werden Emissionen wie Kohlenstoffdisulfid (CS_2) und Dimethyldisulfid (DMDS) neu in das Model eingefügt, zum Anderem wird ein neuer komplexer Schwefelchemiemechanismus entwickelt. Durch die neu eingebauten Reaktionen werden CS_2 und Dimethylsulfid (DMS) in OCS umgewandelt. Hierdurch steigt das Mischungsverhältnis von OCS in der UTLS Region an, besonders in den Tropen von ca. $500\,\mathrm{ppt}_v$ auf $550\,\mathrm{ppt}_v$. Im Gegenzug wird DMS abgebaut und die Produktion von Methansulfonsäure (MSA) reduziert.

Anschließend werden die Modellergebnisse durch Vergleiche mit Flugzeugmessungen der StratoClim Kampagne während des Asiatischen Sommermonsuns in 2017 überprüft. Hierbei zeigt sich eine Verbesserung des Modells durch den neu hinzugefügten komplexen Schwefelchemiemechanismus, die zu einer Erhöhung des OCS-Mischungsverhältnisses führt. Letzteres wurde bisher im Bereich der durchgeführten Messungen deutlich unterschätzt. Außerdem weisen die Messergebnisse ungewöhnlich hohe Partikelanzahlkonzentrationen in der UTLS Region auf. Diese können durch den Vergleich mit den Modellsimulationen und Satellitendaten verifiziert und auf die erhöhten SO_2 Emissionen des Vulkans Sinabung zurückgeführt werden. Somit zeigt sich in dieser Arbeit das erfolgreiche Zusammenwirken von Modellsimulationen, Satellitenbeobachtungen und flugzeuggetragenen in-situ Messungen.

Contents

Chapter 1

Introduction

This chapter gives a short introduction into the scientific field and an overview of the structure of this thesis.

1.1 Motivation

The stratospheric aerosol layer, which is called Junge-aerosol layer (Junge et al., 1961), at an altitude of 15 km to 27 km, has an important effect on the solar radiation balance of earth's atmosphere. The aerosol particles reflect the incoming solar radiation and absorb the incoming solar radiation as well as outgoing terrestrial radiation. They can have a net cooling effect on surface temperatures as well as a local heating effect in the stratosphere. A major current issue is to understand the relative impact of volcanic eruptions, of anthropogenic sulfur emissions and other aerosol sources on the evolution of the stratospheric aerosol burden. Uncertainties still exist since the optical depth of this aerosol layer depends on optical properties influenced by the size distribution, composition and concentration of aerosol particles. There can be big differences between climate models and observations. The emphasis of this study lies on the implementation of stratospheric aerosol, including the sulfur budgets, the sulfur chemistry and the radiative transfer in a complex Chemistry Climate Model (CCM). This serves the goal of better understanding of the complex processes in the stratosphere and the interaction with the global climate system.

To improve the sulfur budget of the stratosphere in the CCM model, sources and sinks of sulfur as well as its precursor gases components have to be identified. There are strong temporal and spatial variations in the concentration of stratospheric aerosol. One important precursor gas of stratospheric aerosol is sulfur dioxide (SO_2), which can be injected into the stratosphere by big, explosive volcanic eruptions, where it is converted into sulfate particles (Vernier et al., 2011b). These explosive volcanic eruptions dominate the sulfate burden in the stratosphere during volcanically active periods. For this reason there is made a distinction between background concentrations and volcanically active periods. This influences the changes of the radiative forcing at tropopause altitudes and can even have a large impact on the global climate for some years after the eruptions (IPCC, 2013). This can be seen by the influence of big volcanic eruptions on parts of the global circulation, such as the El Niño-Southern Oscillation (ENSO) system in the Pacific Ocean (Predybaylo et al., 2017).

Previous studies show that model simulations often cannot completely reproduce the aerosol optical depth of satellite observations or the global forcing of the stratospheric aerosol layer (Solomon et al., 2011) because the number of volcanic eruptions reaching the stratosphere is underestimated in most of the current analysis (Mills et al., 2016; Brühl et al., 2015). Sometimes the intensity of single eruptions is overestimated because of incorrect vertical distribution for the injection patterns. Smaller volcanic eruptions have often been underestimated in former studies (Brühl et al., 2015), even though they caused a radiative forcing of –0.11 (–0.15 to –0.08) $\mathrm{W m^{-2}}$ for the years 2008 to 2011, which is approximately twice as strong as during volcanically quiescent periods (1999 to 2002) (IPCC, 2013). Therefore the SO_2 injections into the stratosphere of formerly underestimated and unknown volcanic eruptions have to be recalculated based on recent satellite data sets, in particularly applying to limb sounding instruments.

Explosive volcanic eruptions are not the only sulfur source, even in volcanically quiescent periods there is still a background concentration of stratospheric aerosol. Sources are the oxidation of carbonyl sulfide (OCS) (Crutzen, 1976; Brühl et al., 2012, 2015), tropospheric transport of biogenic and anthropogenic aerosol particles, anthropogenic SO_2 pollution and outgassing volcanoes reaching the stratosphere. Because of its low solubility in water and slow photochemistry OCS is not removed from the troposphere and has a long lifetime to reach the stratosphere (Brühl et al., 2012). Another source for the stratospheric aerosol layer is the oxidation of dimethyl sulfide (DMS), which is emitted by the oceans (Lennartz et al., 2015). Other chemical reactions of various tropospheric precursor gases, like carbon disulfide (CS_2) which is mostly oxidized to OCS or hydrogen sulfide (H_2S), may also play a role for the sulfur budget and have to be investigated.

The availability of in-situ aircraft measurements in the UTLS (upper troposphere/lower stratosphere) region, by M55-Geophysica from the StratoClim (Stratospheric and upper tropospheric processes for better climate predictions) project providing information on sulfate and silicate fraction as well as size distribution appears to be very important for comparing values with the model output and to improve the optimal model configuration further.

1.2 Structure of the Thesis

Figure 1.1 illustrates different relevant processes of the stratospheric aerosol life cycle, which are structured in this thesis as follows: After this short introduction the necessary background knowledge is given in chapter 2. In chapter 3 the setup for the used climate model simulations and the instruments of the airborne and satellite measurements of aerosols and SO_2 are described. Chapter 4 contains a volcanic sulfur emission inventory with all detected relevant eruptions between 1990 and 2017, which are included into the model simulations. Some selected case studies of volcanic eruptions are discussed in section 4.2. The influence of these volcanic eruptions on the stratosphere is analyzed in chapter 5. Furthermore, a newly developed Sulfur Chemistry Mechanism is implemented into the model in chapter 6 and the model simulations are compared with in-situ measurements in chapter 7. In the end, the results are put into a larger context, including the final conclusion (chapter 8) and an outlook (chapter 9) for further research needs. Appendix A shows the reaction tables for the implemented Sulfur Chemistry Mechanism in the submodel CAABA/MECCA (Chemistry As A Boxmodel Application/Module Efficiently Calculating the Chemistry of the Atmosphere). Acronyms, chemical species and variables used in the formulas and their units are listed in Appendix B.

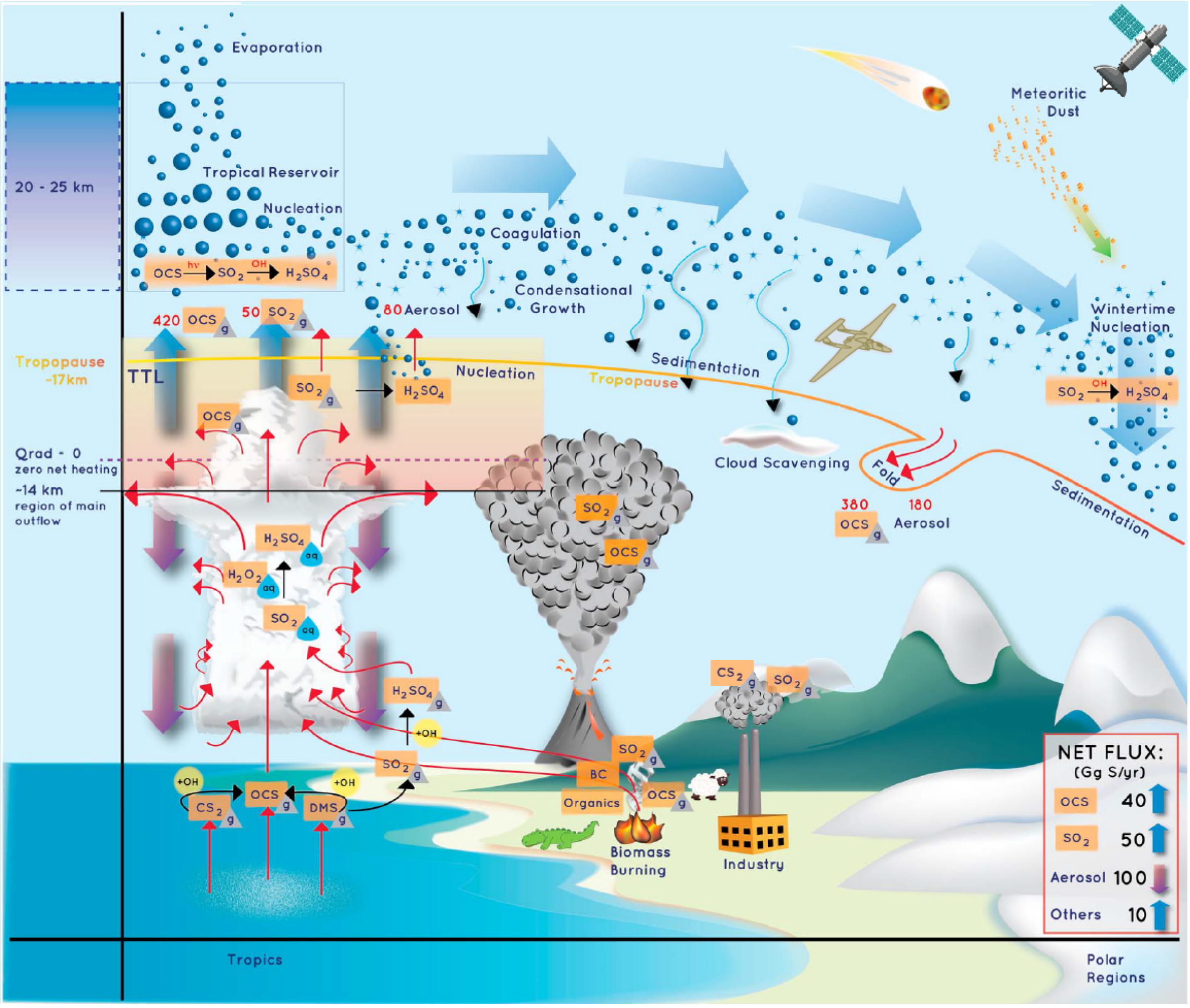

Figure 1.1: Schematic of the stratospheric aerosol life cycle modified from Kremser et al. (2016), illustrating an overview of different relevant processes in the atmosphere: The thick, blue arrows show the large scale circulation of aerosol particles in the Brewer-Dobson Circulation (subsection 2.1.1). Transport processes and air mass exchange through the tropopause are indicated by red arrows (subsection 2.1.2), with the net fluxes (red numbers) of sulfur precursor gases (subsection 2.3.1) such as OCS, DMS or CS_2. Volcanic emissions of SO_2 (section 2.4) and chemical reactions (black arrows) forming sulfuric acid (H_2SO_4) (chapter 6) are relevant for the stratospheric aerosol burden. Meteoric dust (subsection 2.3.4) has a role in the processes of particle formation as well. The growth of particles due to condensation and coagulation, as well as removal by scavenging, sedimentation (wavy blue arrows) and evaporation are included in the model simulations (section 3.1). The influence on radiative forcing in the model simulations is shown in chapter 5. SO_2 emission files for the model simulations are taken from different satellite data sets (chapter 4). In chapter 7 the model results are compared with in-situ measurements of aircraft campaigns.

Chapter 2

Theory

In this chapter the scientific background information from the interdisciplinary fields combined in this thesis is presented.

2.1 The Stratosphere

The stratosphere is the second layer in the atmosphere (above the troposphere). Although the stratosphere with a thickness of 30 km has a much larger volume than the troposphere, it only consists of 10% - 20% of the total mass of the atmosphere. This is due to the decrease in air pressure from 100 hPa to 1 hPa with increasing altitude. The lower boundary of the stratosphere is the tropopause, at an altitude of 8 km to 18 km, depending on the geographical latitude. Due to tropopause folding and lifting processes there is an additional strong variability of the tropopause height in location and time. The upper boundary of the stratosphere is the stratopause in 50 km to 55 km altitude, also depending on latitude (Holton, 1992).

One important feature of the stratosphere is the ozone layer, with maximum concentration of ozone (O_3) in an altitude between 15 km to 35 km. The ozone layer absorbs the incoming Ultra Violet (UV) radiation and produces a positive temperature gradient with temperatures ranging from about -60 °C to 0 °C (273 K). For that reasons the stratosphere is very stable without convection and has almost no clouds (except of Polar Stratospheric Clouds (PSCs)).

The water vapor content of the stratosphere of 3 - 5 parts per million by volume (10^{-6}) (ppm_v) is reduced by freezing when passing the tropopause (about -80 °C) and is much lower than in the troposphere, where it is in the range of 100 ppm_v to 4 %. When an air parcel crosses the tropical tropopause the water vapor content is fixed like on a “tape recorder” and can be detected up to an altitude of 10 hPa for about 18 months (Mote et al., 1996). As the water vapor content is coupled to the temperature at the tropopause, there is a seasonal cycle in the stratospheric water vapor mixing ratios. The water vapor content increases slightly by oxidation of methane (CH_4) molecules in the upper stratosphere. Without precipitation the transport and sedimentation processes are the main sink for stratospheric aerosol particles and their lifetime is much longer than in the troposphere.

2.1.1 Transport Processes in the Stratosphere

On the basis of measurements of long-lived trace gases such as methane (CH_4) and water vapor (H_2O) or the O_3 distribution, the meridional stratospheric transport pathways can be investigated. The resulting characteristic mean meridional circulation of the stratosphere was originally postulated by Dobson and Brewer (Brewer, 1949) and named after them. This Brewer-Dobson circulation can be divided into three sections, as illustrated in Figure 2.1. At the equator, the air is transported upward from the troposphere up to the stratosphere by radiation heating, illustrated by the short, wide arrows in Figure 2.1. When passing the tropopause, the temperature drops down to 193 K. As a result, almost all water vapor condenses and precipitates through freezing and the stratosphere is very dry.

In the second section of the Brewer-Dobson circulation, the air in the stratosphere is transported on average in the direction of mid latitudes. This transport process is seasonal and significantly stronger in the winter hemisphere. The averaged global scale diabatic circulation in the middle atmosphere transports tropical stratospheric air to the extra tropical troposphere. This "downward control" of extra tropical diabatic circulations depends on wave- and eddy-induced mean zonal forces (Haynes et al., 1991). This downward transport can be an important removal process for stratospheric species like O_3 or aerosol particles.

In the last section, the downward transport takes place at the poles by radiation cooling. Due to the different land-ocean distribution and orography, the Brewer-Dobson circulation differs in the northern and southern hemisphere. In the winter, a strong polar vortex forms over the Antarctic and acts as a transport barrier (left green vertical bar in Figure 2.1). This prevents on the one hand the influx of warmer, ozone-rich air from low latitudes while on the other hand the present air in the vortex cools down in the absence of short-wave radiation. The interaction of these factors makes the polar vortex self-stabilizing. This results in very low temperatures, sometimes below 180 K, and promotes the formation of PSCs in 12 km to 25 km altitude at a temperature threshold below 195 K (-78 °C). This supports chemical reactions for the ozone destruction (Solomon, 1999) and the formation of the ozone hole in the Antarctic spring (Seinfeld and Pandis, 1998, Chapter 5).

2.1.2 Air Mass Exchange between Troposphere and Stratosphere

The stratosphere is not completely isolated from the troposphere, there are still some ways for transport of air masses and chemical substances through the tropopause in both directions (see Figure 2.1). This exchange is a significant loss process for aerosol particles in the stratosphere and can take place in a variety of ways, as shown in the overview for different processes of transport through the tropopause. The mean time for exchange between stratosphere and troposphere is 15 - 18 months up to 2 years, which correlates well with the lifetime of stratospheric aerosols.

- During summer high incoming solar radiation, especially in the Southeast Asian monsoon (see section 2.2), causes deep convection with transport into the stratosphere. The large-scale wave forcing causes the tropical upwelling (white thick arrows). The tropospheric air is transported by large-scale wave dynamics in the stratosphere whereas radiative cooling regionally can cause downwelling (Lelieveld et al., 2007).
- Since the tropopause is higher in the tropics than in the high latitudes, horizontal transport of air masses is possible in both directions. This occurs along isentropes, levels with a constant

potential temperature about 380 K near the 100 hPa pressure level (wavy orange arrows), connecting the upper troposphere in the tropics and the lower stratosphere in the extra tropics (Holton et al., 1995).

- Jetstreams occur on both hemispheres in the latitudes of 30° - 35° (Subtropic Jet) and 50° - 60° (Polar Jet). In these areas, the formation of tropopause folds can take place in synoptic weather systems (e.g. stratospheric intrusion after a cold front or warm conveyor belts). As a result stratospheric air flows into the troposphere along the isentropes. The stratospheric air in the troposphere sometimes forms so-called filaments, typically in an order of magnitude up to a thickness of 1 km and a length of 100 km. Thinner filaments can occur, reaching a greater length.
- In the middle and high latitudes, the altitude of the tropopause varies with the seasons. As the tropopause altitude increases, stratospheric air remains at a level that now belongs to the troposphere. If the tropopause decreases again, the stratosphere penetrates into areas that previously belonged to the troposphere. This exchange covers approximately 25% of the mass of the lower stratosphere, which corresponds to 10% of the mass of the entire stratosphere (Roedel and Wagner, 2011).

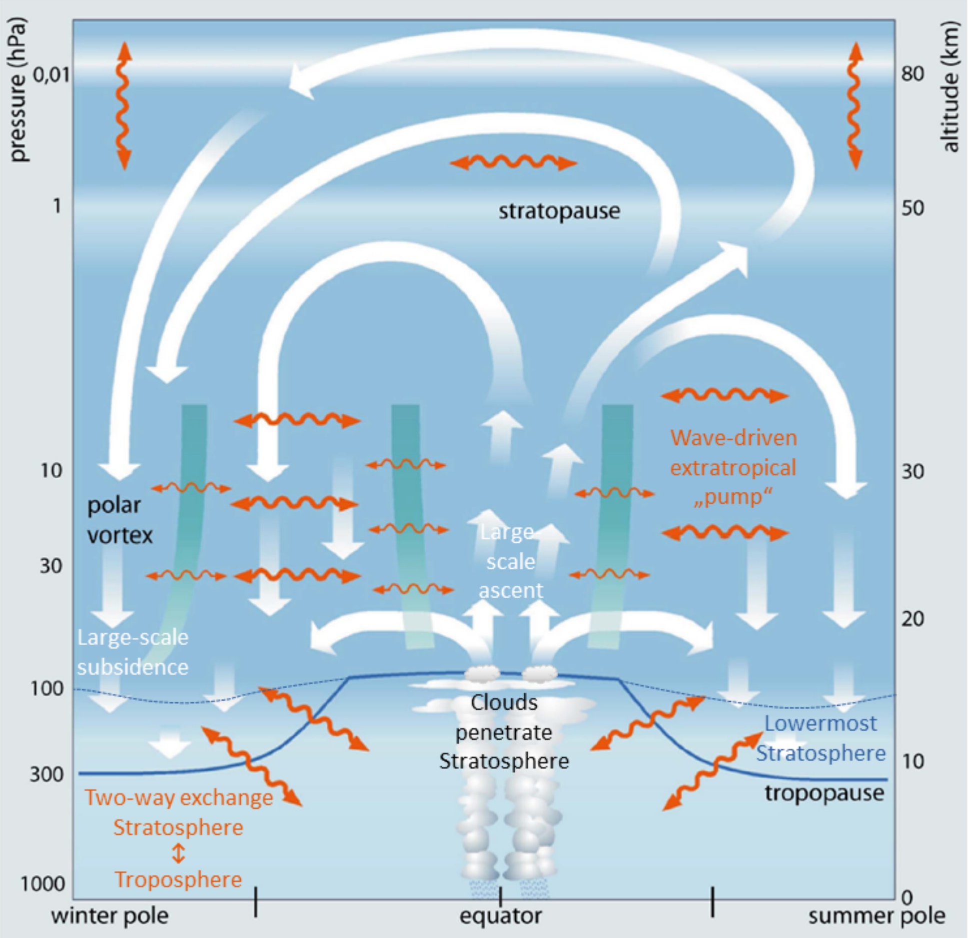

Figure 2.1: Schematic vertical profile of the Brewer-Dobson Circulation adapted from Bönisch et al. (2011, Figure 1), with the thick white arrows as representation of the mass transport by the overall stratospheric residual circulation. The wavy orange arrows are indicating two-way mixing processes. The dark blue line indicates the tropopause and the thin dotted blue line the region of the lowermost stratosphere. Transport and mixing barriers in the stratosphere are represented by thick green vertical bulks.

2.2 The Asian Summer Monsoon

The Asian Summer Monsoon is a seasonal phenomenon that has a strong impact on the climate of the Indian subcontinent. Water vapor is transported from the ocean to the continent and causes strong rainfalls in the summer, starting in June/July and ending in September/October.

Figure 2.2 shows the different layers of the Asian Summer Monsoon circulation. Due to strong convection natural emissions and anthropogenic pollutions are transported to the upper troposphere and partly even to the lower stratosphere (see also subsection 2.1.2). Furthermore the South Asian pollution emissions dominate the anticyclone composition of carbon monoxide (CO), nitrogen oxide (NO_x), SO_2 and other species in the whole monsoon region (Lelieveld et al., 2018). Therefore the Asian Tropopause Aerosol Layer (ATAL) is building up at an altitude of 13 km to 18 km in the Asian monsoon season (Vernier et al., 2011a). This can change the chemical composition and reactions in the UTLS region and can even influence the ozone budget (Solomon et al., 2016).

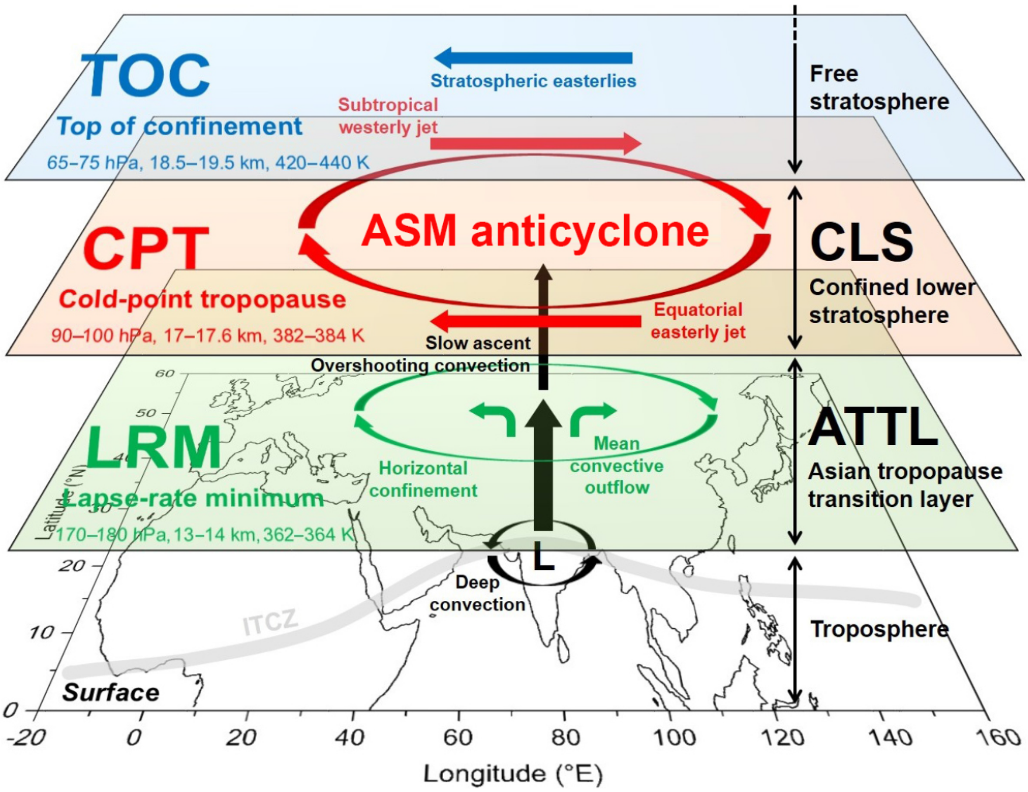

Figure 2.2: The scheme of the vertical structure of the Asian Summer Monsoon by Brunamonti et al. (2018) is showing the different layers at the upper troposphere Asian Tropopause Transition Layer (ATTL) and the Confined Lower Stratosphere (CLS) for the Stratospheric and upper tropospheric processes for better climate predictions (StratoClim) campaign (subsection 3.3.1) in summer 2017.

Studies of Bourassa et al. (2012b) have shown, that the Asian Summer Monsoon can also transport large volcanic aerosol load (section 2.4) into the stratosphere, like the eruption of Nabro in June 2011 (chapter 4) and influence the radiative forcing (section 2.5). To get a better scientific understanding of the involved processes and the impact of the Asian Summer Monsoon on the climate, research aircraft campaigns (section 3.3) were carried out to collect data from in-situ measurements.

2.3 Atmospheric Aerosol

Atmospheric aerosols consists of a suspension of aerosol particles and the surrounding air molecules. They can influence the climate by reflecting incoming solar radiation and by absorbing solar and terrestrial radiation, this is called the primary aerosol effect (section 2.5). Aerosol particles are also essential for the formation of cloud droplets by condensation of water molecules on the particle surface. Hence aerosols can influence the formation, precipitation and evaporation of clouds, which have an important influence on the earth climate, this is called the secondary aerosol effect. There are many different kinds of aerosol particles which differ in properties of the surface, size and shape for condensation of droplets, reflecting and absorbing radiation. The amount and properties of these aerosol particles are rapidly varying in time and space. They are classified by their particle size distribution, production processes or chemical consistence into different modes:

- To a certain extent, aerosol particles can be distinguished by their size, the order of magnitude of aerosols is between a few nanometers and ≈100 µm. The particle size distribution n_N ($\mu\mathrm{m}^{-1}\mathrm{cm}^{-3}$) can be represented over all orders of magnitude with a logarithmic function of the particle diameter D_p (Seinfeld and Pandis, 1998, Chapter 7):

  $$n_N(\log(D_p)) = \frac{dn}{d\log(D_p)} = \frac{n}{\sqrt{2\pi}\log(\sigma)} \cdot \exp\left[-\frac{1}{2}\frac{(\log(D_p) - \log(\overline{D}_p))^2}{\log^2(\sigma)}\right] . \tag{2.1}$$

  σ represents the standard deviation of the particle size distribution around the mean diameter $\overline{D_p}$ of the particle number distribution and n is the number concentration (number of particles per cm^{-3}). From here multimodal distributions consist of several of these log normal distributions.

  Based on the particle size distribution, calculated for the equivalent spherical diameter, there can be distinguished typically four modes for the atmospheric Aerosol: The nucleation mode (3 nm to 10 nm) for ultra fine particles, the Aitken mode (10 nm to 100 nm) and the accumulation mode (100 nm to 2.5 µm) for fine particles, and the coarse mode > 2.5 µm for coarse particles (see Seinfeld and Pandis, 1998, p. 100). Previous measurements of Thomason and Peter (2006) have shown that there is a bimodal particle distribution up to a height of 25 km. They measured small particles within the Aitken mode and larger particles within the accumulation mode.

- Aerosols can also be distinguished by the production process of primary and secondary particles. Primary particles are directly released into the atmosphere, mechanically generated by wind erosion, waves, or volcanic eruptions (usually accumulation and coarse mode). Tropospheric aerosol formation is dominated by combustion processes and the whirling up of dust and other small particles. Secondary particles are general newly formed by nucleation from gas-to-particle-conversion (GPC). The nucleation of new particles from the gas phase can be differentiated between homogeneous and heterogeneous nucleation. Their size (nucleation and Aitken mode) is smaller than primary particles, but they can grow by particle condensation and coagulation (accumulation mode). Secondary particles can also be produced by ion-induced nucleation.

- The chemical composition of the aerosols influences the hygroscopic properties (absorption capacity of water) and thus on droplet formation. The composition of atmospheric aerosol can consists of a huge variety of components such as:
  - Sea salt or sea spray aerosol are primary particles emitted from breaking waves.
  - Mineral dust are primary particles often emitted in deserts or from agriculture land use.
  - Black carbon (soot) is emitted from biomass burning, traffic and industries.
  - Organic compounds often emitted as pollen, bacteria and fungi (primary particles).
  - Secondary Organic Aerosol produced from natural and anthropogenic sources by reactions of volatile organic compounds with airborne chemicals and sunlight.
  - Sulfate aerosols are secondary particles, formed in the atmosphere by nucleation from gas-to-particle conversion.

2.3.1 Fluxes of Sulfate Precursor Gases

Stratospheric aerosol particles mostly consist of a mixture of sulfuric acid (H_2SO_4) and water (H_2O) liquid droplets, which are condensed from the gas phase by secondary particle formation. The Study of Finlayson-Pitts and Pitts (1986) shows sulfur emissions from soils, water and vegetation in form of DMS, OCS, CS_2, hydrogen sulfide (H_2S) and small amounts of DMDS, methyl mercaptan (CH_3SH) and other sulfur components, illustrated above in Figure 1.1. The global atmospheric sources and budgets of sulfur and its components are estimated in Table 2.1 - 2.3 to get the total amount of sulfur burden in the atmosphere. On the one hand the ocean can be a main sulfur source for natural emissions, on the other hand anthropogenic emissions with local hot spots in the monsoon area seem to have an influence on the sulfur budget. Subsequently further research is needed as there are still large uncertainties for the sulfur fluxes and no balance between global sulfur sources and sinks.

Source	Annual flux [Tg S/a]	Reference
Ocean	22.99±6.23	Watts (2000)
Biogenic	5.49±2.66	Watts (2000)
Volcanism	1.15±0.98	Watts (2000)
Chemistry	0.67±0.23	Watts (2000)
Anthropogenic	3.89±0.60	Watts (2000)

Table 2.1: Global sulfur sources for annual fluxes of DMS, OCS, CS_2 and H_2S [Tg S/a] without SO_2 emissions.

Stratospheric H_2SO_4 is produced from different sulfur precursor gases like DMS, OCS, CS_2, H_2S and SO_2 in various chemical reactions (see Figure 6.3). Some of these precursor gases, for instance DMS and OCS, are not sufficiently soluble and are not scavenged effectively in the troposphere. Accordingly they can be transported to the upper troposphere and from there also reach the stratosphere. Some others like CS_2 and H_2S have a short lifetime in the troposphere and are transformed fast to OCS and SO_2. An overview from literature of the global annual sources and sinks for these sulfur components is given in Table 2.2 and compared with the total annual net fluxes into the atmosphere. Missing values are marked with N/A. Table 2.2 illustrates the lack of data and shows gaps in the global sulfur cycle.

Sulfur species	Annual sources [Tg S/a]	Annual sinks [Tg S/a]	Reference	Annual fluxes [Tg S/a] (Kettle et al., 2002)
OCS	1.23(0.83 - 1.71)	0.79(0.30 - 1.52)	Chin and Davis (1993)	0.105 ± 0.186
	1.21	1.19	Glatthor et al. (2015)	
	1.31 ± 0.25	1.66 ± 0.79	Watts (2000)	
H_2S	7.72 ± 1.25	8.50 ± 2.80	Watts (2000)	N/A
DMS	28.10 ± 6.30	N/A	Lana et al. (2011)	0.154 ± 0.037
	24.45 ± 5.30	N/A	Watts (2000)	
DMDS	0.119	N/A	Meinardi et al. (2003)	N/A
CS_2	0.57(0.34 - 0.82)	0.57(0.34 - 0.82)	Chin and Davis (1993)	0.200 ± 0.112
	0.66 ± 0.19	1.01 ± 0.45	Watts (2000)	
Anthropogenic fraction	0.34 ± 0.17	N/A	Watts (2000)	0.116 ± 0.058

Table 2.2: List of the global annual sources and sinks [Tg S/a] of OCS, H_2S, DMS, DMDS and CS_2 compared with the total annual net fluxes from Kettle et al. (2002) into the atmosphere.

The Source Gas Carbonyl sulfide (OCS)

OCS is a relatively long-lived one-carbon sulfur compound in the atmosphere. As OCS has a low chemical reactivity and is relatively insoluble it has a lifetime of 2.1 ± 1.3 years in the global troposphere and 47 ± 16 years in the stratosphere (Karu, 2019). The mean concentration of OCS in the troposphere is between 419 ± 0.8 parts per trillion by volume (10^{-12}) (ppt$_v$) and 510 ± 8.3 ppt$_v$ from the tropical Atlantic to the North Atlantic (Johnson et al., 1993). The flux of OCS from the troposphere to the stratosphere is estimated by 118 ± 39 Gg S/a with a stratospheric sink of 44 - 90 Gg S/a (Karu, 2019). Sources are mostly natural by soil emissions and out-gassing from the oceans following a seasonal cycle with a minimum in winter and a maximum in summer/autumn (Watts, 2000). Regardless, there is still a missing source for OCS, which is estimated to be the chemical oxidation of DMS and CS_2 (Lennartz et al., 2017). Sinks of OCS are the uptake by soils and vegetation, which are overestimated in older studies (Lennartz et al., 2017) and the chemical oxidation by hydroxyl radical (OH) (Kettle and Andreae, 2000). In the stratosphere OCS is photodissociated into SO_2 and is the main gaseous precursor for the stratospheric background aerosol layer during periods with low volcanic activity (e.g. Boucher, 2015) and has a direct effect on the global climate (Glatthor et al., 2015).

The Source Gas Hydrogen sulfide (H_2S)

H_2S is emitted by volcanoes and decomposition of organic matter in soils and in stagnating water (Pruppacher and Klett, 2010). The rate of H_2S release by coastal marine sediments strongly depends on the light intensity. During the daytime no or extremely little H_2S is emitted, while it reaches the maximum at midnight (Hartmann Hansen et al., 1978). The surface mixing ratio is only estimated at 30 ppt$_v$ (Weisenstein, 1997). H_2S is slightly soluble in water and its lifetime is estimated to be about 5 days (Finlayson-Pitts and Pitts, 1986). A known sink in the atmosphere is the oxidation to SO_2, fraught with very little data, and very large uncertainties (Watts, 2000).

The Source Gas Dimethyl sulfide (DMS)

DMS (CH_3SCH_3) is a relative short living organic tracer gas with a lifetime of less than 1 day in the troposphere (Johnson and Bates, 1993). The main source for DMS is the ocean (sea to air flux) from phytoplankton and bacterial decomposition, with an average mixing ratio of 80 ppt_v to 110 ppt_v in the marine boundary layer (Seinfeld and Pandis, 1998). A sink for DMS is the oxidation with the OH to dimethyl sulfoxide (DMSO) (CH_3SOCH_3) and other sulfur products (discussed in more detail in chapter 6). Due to strong convection DMS can be transported upward to the upper troposphere/lower stratosphere (UTLS) region, where it is converted to OCS and SO_2 to become a part of the stratospheric aerosol cycle. Moreover it is converted during daylight hours to MSA which undergoes dry deposition and may be able to participate in nucleation (Hodshire et al., 2019). Nevertheless, there are still remaining large uncertainties for these processes that require further research (Lennartz et al., 2017).

The Source Gas Dimethyl disulfide (DMDS)

Dimethyl disulfide (DMDS) is a reduced organic sulfur-containing gas with a similar molecular structure (CH_3SSCH_3) to DMS. It is emitted from biomass burning with estimated annual emissions of up to 175 Gg DMDS/a (119 Gg S/a) (Meinardi et al., 2003). DMDS has an even shorter lifetime than DMS with only 0.3 - 3 hours. The main removal process is by fast reactions with OH, and it will be converted into SO_2 or MSA (see Figure 6.3) while a minor fractions is photolyzed.

The Source Gas Carbon disulfide (CS_2)

The main sources of the organosulfur species CS_2 are decaying organic matter in oceans, soils and marshes. It has an additional source from volcanic and anthropogenic emissions. The mixing ratio of CS_2 has a maximum on the order of 100 ppt_v in industrialized areas, whereas normal background mixing ratios at the surface are on a level of 30 ppt_v (Wine et al., 1981). Local concentrations are dominated by anthropogenic sources of CS_2 with major industrial sources including carbon black production, rayon manufacture (textile production), CS_2 use and production. The largest contributing regions are located in China (43%), India (30%), and Japan (18%) (Blake et al., 2004). Similar to OCS CS_2 is relatively insoluble but it has an relative short tropospheric lifetime of approximately 6 days (Johnson and Bates, 1993) and is quickly oxidized with OH to OCS and SO_2 in the atmosphere (Watts, 2000). Another tropospheric sink for CS_2 is by photooxidation to OCS (Wine et al., 1981).

The Source Gas Sulfur dioxide (SO_2)

SO_2 emissions are the biggest source of sulfur in the troposphere and are mainly emitted by anthropogenic sources like fossil fuel burning from transport or industries. It is also formed in the atmosphere by chemical reactions of other sulfur species such as OCS or CS_2. The lifetime of SO_2 is limited to few days (2.5 days Sheng et al. (2015)) in the troposphere because it hydrolyzes and reacts in the aqueous phase of rain-, fog- and cloud-droplets as well as in moist aerosol particles (Kremser et al., 2016), so that only a small fraction can reach the stratosphere. A smaller natural source are non eruptive permanent degassing volcanoes which are treated separately from active explosive volcanic eruptions which can transport huge amounts of SO_2 very fast or inject it directly into the stratosphere (chapter 4).

Source	Annual flux [Tg S/a]	Reference
Biogenic	1.90	Sheng et al. (2015)
	1.34	Lee et al. (2011)
Volcanism (non explosiv)	12.60	Sheng et al. (2015)
	6.55	Lee et al. (2011)
	18.00±3.00	Halmer et al. (2002)
Anthropogenic	51.30	Sheng et al. (2015)
	56.34	Lee et al. (2011)

Table 2.3: Global annual emissions of SO_2 background sources [Tg S/a].

Gaseous Sulfuric acid (H_2SO_4)

The lifetime of gaseous sulfuric acid (H_2SO_4) in the troposphere is limited to the order of minutes mostly by removal through wet deposition (Thomason and Peter, 2006). Accordingly the most important source for gaseous H_2SO_4 in the stratosphere is the end product of oxidized sulfur species. It is mostly formed by the oxidation of gaseous SO_2 with OH (Pruppacher and Klett, 2010, S. 227).

$$\mathrm{SO_2 + OH + M \longrightarrow HOSO_2 + M} \tag{2.2}$$

$$\mathrm{HOSO_2 + O_2 \longrightarrow SO_3 + HO_2} \tag{2.3}$$

$$\mathrm{SO_3 + H_2O \longrightarrow H_2SO_4} \tag{2.4}$$

Gaseous H_2SO_4 is very hygroscopic and forms strong hydrogen bonds with water (H_2O) molecules as well as with other H_2SO_4 molecules.

2.3.2 Stratospheric Sulfate Aerosol

The focus of this thesis is on stratospheric sulfur aerosol particles. When new particles nucleate, stable clusters arise directly from the gas phase, with no pre-existing particles involved. Sulfate aerosols are secondary particles formed in the atmosphere by homogeneously heteromolecular nucleation of several chemical substances, such as sulfuric acid (H_2SO_4) and water molecules (binary nucleation) and sometimes also ammonia (ternary nucleation) (Curtius, 2006).

$$\mathrm{H_2SO_{4(\mathit{vap})} + H_2O \longrightarrow gas-to-particle-conversion(GPC) \longrightarrow sulfate\ aerosol} \tag{2.5}$$

The sulfuric acid molecules in the stratosphere are supersaturated with respect to H_2O and therefore new particles are created due to nucleation directly from the gas phase (so called “GPC“). Homogeneous homomolecular nucleation of only one chemical substance generally does not occur under normal atmospheric conditions, because this process requires a very high nucleation energy and supersaturation compared to the saturation vapor pressure (Roedel and Wagner, 2011). These processes are solved by parametrizations (e.g from Vehkamäki et al. (2002)) in computer models like the Modular Earth Submodel System (MESSy) (section 3.1.3).

Stable clusters continue to grow in the stratosphere through the condensation of water and sulfuric acid. Other chemical substances, especially nitric acid, can diffuse into the aerosol phase and contribute to growth. Aerosol particles and droplets can also grow through coagulation, where small particles collide and form a new, correspondingly larger particle. A prerequisite for effective aerosol growth through coagulation is a sufficiently high particle concentration so that the relative distances between the particles are small and collision rates are high. The typical number median diameter of these aerosol particles is between 200 nm for the background aerosol and 600 nm for Pinatubo conditions (Brühl et al., 2015).

As there are no clouds and precipitation or turbulent vertical mixing processes in the stratosphere the lifetime of aerosol particles is very long and can exceed more than one year. One loss process of stratospheric aerosol is gravitational sedimentation into the troposphere, where as larger particles are removed faster than smaller ones. The sedimentation velocities for particles with a diameter of 200 nm is about 100 m/month (Thomason and Peter, 2006). Since these stratospheric aerosol particles sediment very slowly out of the stratosphere, they are mainly removed by the exchange processes between stratosphere and troposphere (Benduhn and Lawrence, 2013). Accordingly to their high life expectancy, the stratospheric aerosol particles can be distributed globally through the Brewer - Dobson circulation (subsection 2.1.1) and cannot generally be assigned to a specific source location. However, the stratospheric aerosol shows a tendency to accumulate in the lower stratospheric aerosol layer between 15 km to 25 km altitude (Junge et al., 1961).

Increasing temperatures and decreasing air pressure in the upper stratosphere above an altitude of ≈ 30 km to 35 km results in too high partial vapor pressure of sulfuric acid over the droplet surface. The ambient vapor pressure of H_2SO_4 is too low and the liquid sulfate particles starts to evaporate back to the gas phase. This effect leads to the evaporation of about 9 kilotons of aerosol mass per year (Weisenstein, 1997).

2.3.3 Mineral Dust

Mineral Dust is a primary aerosol type and enters the lower troposphere by wind friction of soil particles. This mechanism is called saltation bombardment and depends on the particle size, the soil texture and humidity, as well as the meteorological conditions, especially the wind speed near the surface (Astitha et al., 2012). Mineral dust particles are emitted from natural sources as well as from anthropogenic activities (Seinfeld and Pandis, 1998), which are present worldwide, primarily in deserts for instance the Sahara or Taklamakan Desert in northwest China (Klingmüller et al., 2014). The global annual emission flux of dust particles is estimated to 1000 – 3000 Tg per year (Boucher, 2015).

Only the smallest particles (< 60 µm) are lifted high up enough to be transported by the wind, whereas larger particles (> 60 µm to 2000 µm) are too big and fall down before they reach a height of more than 1 m (Boucher, 2015). These small dust particles can be transported over long distances of thousands of kilometers, especially from the Sahara desert in Africa over the Atlantic Ocean to the Amazon rain forest, where they can have a significant impact as fertilizer on global ecosystems and influence the air quality, before they are removed by deposition or scavenging. Otherwise they can reach the upper troposphere and lower stratosphere where they influence the atmospheric radiation transfer and cloud properties.

2.3.4 Meteoric Dust

Due to the decreasing saturation vapor pressure, the liquid sulfuric acid aerosols begin to evaporate above a height of about 30 km to 35 km (Weisenstein, 1997). Regardless, observations show an additional source of aerosol particles in higher altitudes (Schneider et al., 2020). Every day 40 ± 20 kt meteoric material (Love and Brownlee, 1993) with a diameter between 10 µm to 500 µm (Hervig et al., 2009) enters the Earths atmosphere. The cosmic material mostly consists of olivine ($FeMgSiO_4$) and metals like magnesium (Mg), silicon (Si), iron (Fe), aluminum (Al), calcium (Ca), potassium (K), sodium (Na) and nickel (Ni) (Plane, 2012; Plane et al., 2015). The melting point of meteoroids is at approximately 1800 K and ablation takes place at an altitude of 85 km to 95 km in Earths atmosphere (Figure 2.3).

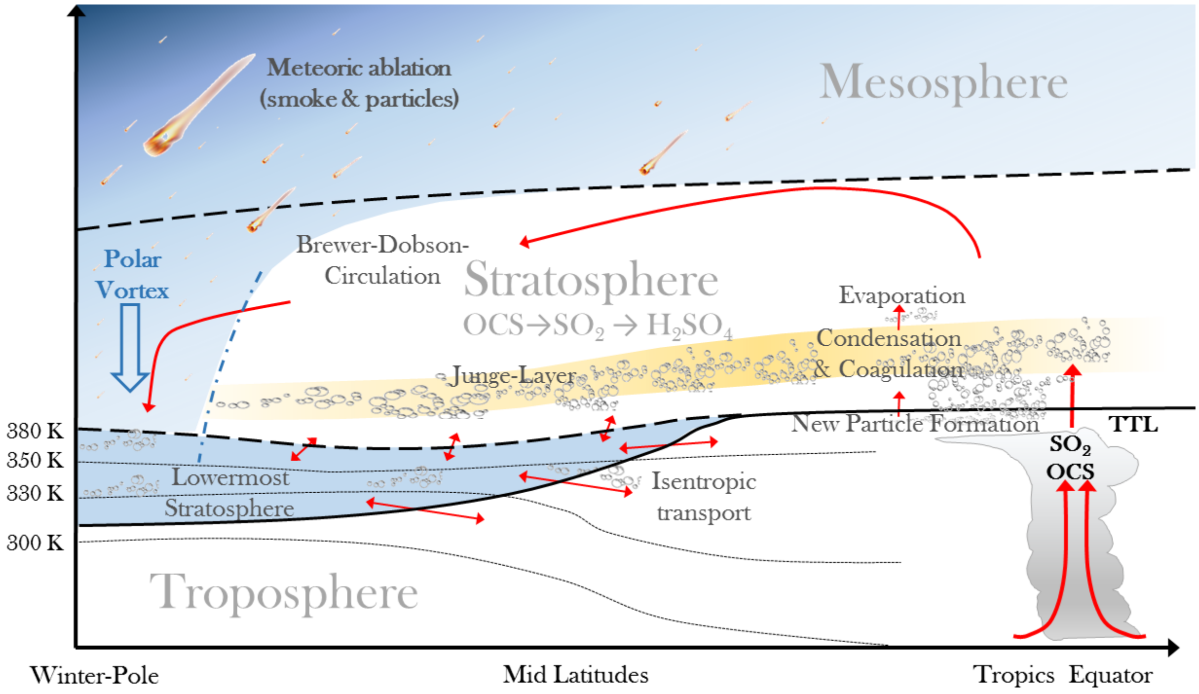

Figure 2.3: Meteors are melting by entering the upper atmosphere to meteoric dust particles and become a part of the stratospheric aerosol layer. Plotted with MS Power Point, inspired by presentation of Weigel, 2018.

These meteoric dust particles are transported downward by the Brewer-Dobson circulation (subsection 2.1.1) at high latitudes and act as nucleation nuclei for sulfate aerosols. The new meteoric material could influence the properties of the refractive index, the aerosol extinction and size distribution of the stratospheric aerosol particles and act as sink for gaseous H_2SO_4. A study of Neely et al. (2011) shows, that meteoric smoke becomes the dominant source of aerosol extinction in the upper stratosphere and mesosphere above 40 km in the tropics and above 35 km polewards of 30 degrees in latitude. Thus the aerosol extinction for the upper stratosphere and mesosphere could be underestimated in model simulations without implementation of meteoric material.

2.4 Volcanoes

Volcanism occurs when a heat source from the earth core melts material from the earth crust and transports gas, liquids and solid emissions to the surface. This is mainly driven by plate tectonics, which often occur along convecting plates called subduction zones (blue triangles in Figure 2.4). When the oceanic lithosphere dives under continental lithosphere the subcontinental mantel melts, and the rising magma is the reason for strong volcanic activity (red dots in Figure 2.4). The most active volcanic region on Earth is the "pacific ring of fire" along the border of the pacific plate.

Other regions of volcanic activity are along mid-ocean ridges, where new oceanic crust is built up at divergent plates (red lines in Figure 2.4) and volcanoes are rising under water (Mid-Atlantic Ridge). Sometimes there can also be interplate volcanoes over a hot spot on oceanic plates, in particular the Hawaii volcanoes, or even on continental plates especially the Yellowstone volcano or the East African Rift System.

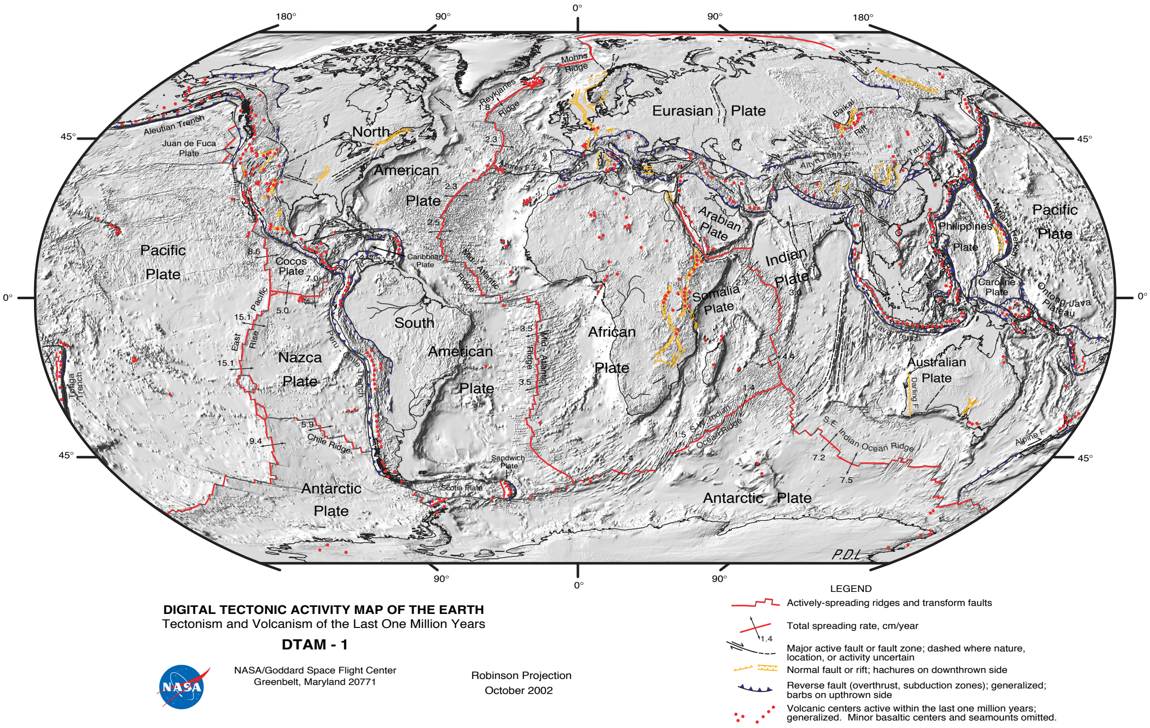

Figure 2.4: Tectonic activity map of the earth including active volcanoes from National Aeronautics and Space Administration (NASA): https://visibleearth.nasa.gov/view.php?id=88415 (18 December 2020).

Volcanic eruptions are a purely natural phenomenon and inject sporadically large amounts of gases and ash into the atmosphere. After water vapor and carbon dioxide (CO_2), sulfur dioxide is the third most common gas in volcanic emissions (von Glasow et al., 2009). In the atmosphere SO_2 is further oxidized to H_2SO_4, which nucleates to sulfate aerosol particles. Other chemical species can also be lifted up from the free troposphere to higher altitudes by entrainment into the eruption column. The impact of volcanic eruptions on earth climate depends on the strength of the eruption called Volcanic Explosivity Index (VEI) (see Table 2.4), the injection height into the atmosphere, the geographical location, the chemical composition (sulfate load) and weather influences (seasons, wind direction, scavenging by rain). They change the radiative forcing at tropopause altitudes and can even have a large impact on the global climate for some years after the eruptions (IPCC, 2013). For example big volcanic eruptions can influence parts of the global circulation as the ENSO system in the Pacific Ocean (Predybaylo et al., 2017). Big volcanic ash plumes can disturb the SO_2 signal in satellite measurements, and satellites could be "blind" during the first few days after an eruption (Höpfner et al., 2015). However volcanic ash particles are too big and sediment after some hours or days, so they have only little climatic significance (Boucher, 2015) and are not discussed in detail.

The VEI is a logarithmic scale defined by the ejected volume of pyroclastic material from the volcano (Newhall and Self, 1982). Most large volcanic eruptions (VEI ≥ 4) are documented well. Whereas the signal of smaller eruptions (VEI ≤ 3) is often too weak, so only 50% of VEI 3, 13% of VEI 2, 4% of VEI 1 and 5% of VEI 0 eruptions are detected (Carn et al., 2016) and for pre-satellite times even worse. The database of the "Global Volcanism Program, Smithsonian Institution", an inventory of all detected volcanic eruptions is available online `https://volcano.si.edu/` (18 December 2020).

VEI	Volume km^3	altitude km	frequency	eruptions in 1500 - 1979	eruptions in 1979 - 2014
0	0.000001	<0.1	persistent	682	222
1	0.00001	0.1-1	daily	1245	507
2	0.001	1-5	weekly	5146	479
3	0.01	3-15	monthly	656	162
4	0.1	10-25	yearly	106	26
5	1	>25	10 years	14	5
6	10	>25	100 years	3	1
7	100	>40	1000 years	1	0
8	1000	>40	10000 years	0	0

Table 2.4: Definition of the Volcanic Explosivity Index (VEI) and the classification of detected volcanic eruptions from 1500-1979 (Newhall and Self, 1982) and 1979-2014 (Carn et al., 2016).

It is even complicated to define the ongoing trend for stratospheric optical depth and forcing, due to the uncertainty in the variation of the magnitude in volcanic emissions. Table 2.5 (Carn et al., 2016) shows the variety of explosive and total annual SO_2 emissions from volcanic eruptions in 1979 to 2014. Here you can see periods with very low volcanic activity with less than 100 kt SO_2 emissions per year, as well as years including big eruption events, e.g. 1991, with more than 26000 kt SO_2 emissions per year. In addition, the percentage amount of explosive SO_2 emissions varies between a few and 100 percent of the total annual SO_2 emissions. When comparing the SO_2 emissions of this thesis with Carn et al. (2016) you have to keep in mind, that Carn et al. (2016) is using total SO_2 emissions, including fast removed tropospheric SO_2, while this study is implementing only the long living, climate relevant stratospheric fraction of the emitted SO_2. On both sides missing or underestimated eruptions are possible due to low data coverage or data gaps. Especially before the year 2002 the data coverage is low, e.g. in 1990 Carn et al. (2016) is underestimating the SO_2 emissions of Kelut and other eruptions, in Table 4.1 detected by the Stratospheric Aerosol and Gas Experiment (SAGE) II. Until today the influence of volcanic eruptions is not included in climate predicting simulation studies of the Intergovernmental Panel on Climate Change (IPCC) (IPCC, 2013), due to the unpredictability of volcanic eruptions.

Year	Total SO_2 (kt)	Explosive SO_2 (kt)	in %	Stratospheric SO_2 (kt) in this study
1979	2945	63	2.1	-
1980	2882	1228	43	-
1981	5562	1430	26	-
1982	11033	9950	90	-
1983	348	260	75	-
1984	3957	252	6.4	-
1985	1241	852	69	-
1986	2086	872	42	-
1987	38	10	26	-
1988	580	300	52	-
1989	2329	177	7.6	-
1990	186	186	100	744
1991	26082	24214	93	18424
1992	810	810	100	794
1993	450	450	100	426
1994	1874	360	19	337
1995	TOMS data gap			156
1996	987	100	10	436
1997	41	41	100	254
1998	3265	38	1.2	255
1999	130	85	65	398
2000	653	336	51	185
2001	1783	122	6.8	400
2002	2626	271	10	368
2003	679	679	100	207
2004	2997	410	14	256
2005	4634	2501	54	445
2006	1347	661	49	611
2007	712	122	17	450
2008	2625	2318	88	688
2009	1934	1379	71	839
2010	1470	867	59	424
2011	6030	4310	71	689
2012	763	563	74	355
2013	185	180	97	448
2014	5296	608	11	716
2015	-	-	-	993
2016	-	-	-	748
2017	-	-	-	499
Total	100647	57092	57	31545
Mean	2873	1629		1127

Table 2.5: Variety of the explosive and total annual amount of global volcanic sulfur dioxide (SO_2) emissions and the percentage of explosive emissions, calculated from satellite observations in 1979 to 2014 (Carn et al., 2016), and the explosive volcanic sulfur dioxide (SO_2) emissions reaching the stratosphere from the Volcanic Sulfur Emission Inventory (Table 4.1) in this study, ending in August 2017.

2.5 Aerosol Radiative Forcing

The total anthropogenic impact on the global radiative forcing is estimated to 2.29 (1.13 - 3.33) Wm^{-2} for the year 2011 relative to 1750 (IPCC, 2013). Whereby aerosols contribute to the largest uncertainty of the total radiative forcing estimate, as they have a direct and an indirect effect on the radiation budget of the earth.

Stratospheric aerosol has a negative radiative forcing on the troposphere as a result of reduced solar radiation reaching the surface and the lower atmosphere by enhanced scattering of the particles. The influence of stratospheric volcanic aerosols is investigated in chapter 5. They interact with the solar (shortwave) as well as with the terrestrial (longwave) radiation which is called the **direct aerosol effect**.

The radiation properties of the aerosol particles change over the course of their lifetime with their chemical composition and size. The reflectivity of individual particles is highly dependent on size, as well as on the wavelength of the reflected light. Rasch et al. (2008) showed, that small particles primarily scatter solar shortwave radiation, and play no role in the long wave spectrum, with most effective particle diameter in the order of 100 nm (Benduhn et al., 2016).

While the reflection of the shortwave incoming radiation reduces the surface temperature and counteracts the global warming, the absorption of the incoming solar as well as the outgoing terrestrial radiation leads to a local heating within the stratospheric aerosol layer, shown in section 5.4. The absorptivity depends in particular on the material properties. The emission of long-wave radiation by the aerosol particles is preceded by the absorption of radiation energy and increases by size, resulting in a net surface heating at diameters greater than 4 µm (Grainger et al., 1995).

The Beer's Law applies to long and short wave radiation and describes the process of extinction, the decrease in the intensity of the radiation along its path through the atmosphere reduced by scattering and absorption processes. The variation dI of the radiation intensity I depends on the Aerosol Optical Depth (AOD) τ:

$$dI = -I\tau. \tag{2.6}$$

The light intensity I is given by the integration of dI, with $I(0)$=I_0:

$$I = I_0 \cdot \exp(-\tau). \tag{2.7}$$

With the term from the exponent, the optical depth τ can be determined, which is a measure of the transmissivity of the atmosphere and describes the decrease of the radiation as it penetrates the atmosphere. The optical depth τ is the integral of the extinction coefficient σ_{ext} in function of the distance (Twomey, 1977):

$$\tau = \int_{surface}^{top\,of\,atmosphere} \sigma_{ext}(z)\, dz, \tag{2.8}$$

with dz the infinitesimal path. This is used for the calculation of the stratospheric Aerosol Optical Depth (AOD) with the tropopause as lower boundary.

The extinction coefficient σ_{ext} is the sum of the scattering σ_{sca} and absorption σ_{abs} coefficients: $\sigma_{ext} = \sigma_{sca} + \sigma_{abs}$ (Boucher, 2015). An extinction coefficient of 1 km^{-1} is defined as the weakening of the radiation intensity I over a distance of 1 km to $\mathrm{e}^{-1} \approx 0.37$ of the initial value. In the spectrum of the Mie theory (particle diameters are approximately equal to the wavelength of the light) this is wavelength dependent. It also depends on the number concentration n_i and the extinction efficiency Q of the aerosol particles in function of the particle radius r:

$$\sigma_i = \int_0^\infty \pi r^2 Q_i(r)\; n(r)\; dr. \tag{2.9}$$

The extinction describes the reduction of radiation Q_{ext} by the sum of the effects of reflection Q_{sca} and absorption Q_{abs} (Boucher, 2015).

$$Q_{ext} = Q_{sca} + Q_{abs}. \tag{2.10}$$

In the next step the altitude coordinates dz are transformed into pressure coordinates Δp by means of the hydrostatic equation, with the gravitational acceleration $g = 9.81\,\mathrm{ms}^{-2}$ and the density of air ρ_a:

$$dz = -\frac{dp}{g\rho_a}, \tag{2.11}$$

Splitting of the number concentration n into the Avogadro constant N_A, the molar mass of air M_A and the number mixing ratio χ of the particles and the air molecules leads to:

$$I = I_0 \cdot \exp\left(\pi r^2 Q\, \chi \frac{N_A}{M_A}\, \frac{\Delta p}{g}\right). \tag{2.12}$$

This can be used for the calculation of the mixing ratios based on the extinction coefficients from satellite measurements.

An other effect is the interaction between aerosol particles, clouds and their radiation effects in the troposphere, which is called the **indirect aerosol effect**. Aerosol particles are essential as condensation nuclei in cloud formation, creating a complex relationship between the number of particles and the cloud droplet density. Simplified, the influence of the aerosol particles on the radiation properties of the clouds can be divided into two processes. On the one hand, the reflectivity of the clouds tends to increase with the number of condensation nuclei, which is called the first indirect effect (Rosenfeld, 2007). Smaller cloud droplets have a stronger reflexion coefficient and the clouds are brighter (Twomey effect) than clouds with bigger droplets (Twomey, 1977). On the other hand, a correlation between the number of particles and the lifetime of the clouds may be suspected and is called the second indirect effect. The changes in cloud microphysics have an impact on the formation of precipitation and can influence the hydrological cycle of the atmosphere. Subsequently clouds cause the biggest uncertainty for climate predictions. Nevertheless, there is high confidence that aerosols and their interactions with clouds have offset a significant portion of global mean forcing from well-mixed greenhouse gases (IPCC, 2013).

The total aerosol effect results in a negative radiative forcing of -0.9 (-1.9 to -0.1) Wm^{-2} in the atmosphere (IPCC, 2013). This includes the indirect aerosol effect with cloud adjustments due to aerosols as well as direct aerosol effects. Most aerosols results in a negative forcing except of a positive contribution from black carbon absorption of solar radiation. They still continue to contribute the largest uncertainty to the total radiative forcing estimate (IPCC, 2013).

Chapter 3

Models and Instrumentation

To study the stratospheric aerosol cycle, with emission sources, transport processes, climate impact and removal processes, complex model simulations are as important as measurements. This chapter has three parts to describe the single components for the setups of the following studies. At first the three dimensional atmospheric Chemistry Climate Model (CCM) EMAC (ECHAM5/MESSy Atmospheric Chemistry) is described for the preformed model simulations. The second part is about the input data from satellite measurements of the Michelson Interferometer for Passive Atmospheric Sounding (MIPAS), Global Ozone Monitoring by Occultation of Stars (GOMOS), Optical Spectrograph and InfraRed Imaging System (OSIRIS) and SAGE instruments. The last part provides an overview of field campaign data from the StratoClim campaign, which are compared to the model output and helpful to improve the setup for further simulations.

3.1 Model description of the ECHAM5/MESSy Atmospheric Chemistry (EMAC) Model

The computations for this thesis have been performed on the mistral supercomputer at Deutsches Klimarechenzentrum (DKRZ), Hamburg, Germany. For this purpose ECHAM5/MESSy Atmospheric Chemistry (EMAC) (Jöckel et al., 2006, 2010), a coupled atmospheric circulation model consisting of the 5^{th} generation of European Centre Hamburg general circulation model (ECHAM5) (Roeckner et al., 2003, 2006) and Modular Earth Submodel System (MESSy) models was used. This was developed for both weather and climate modeling. The model simulations are performed in the period of 2002 to 2012 and extended to 2012 to 2017 and 1990 to 2002 by the global atmospheric chemistry climate model EMAC. At first the base model ECHAM5, which is a comprehensive general circulation model of the atmosphere with self-consistent quasi-biennial oscillation (QBO) in the chosen resolution, is described. It is coupled with MESSy version 2.52, which consists of several submodels that can be switched on or off individually. An overview of this is given in subsection 3.1.2 and the single submodels are described in more detail in the subsection 3.1.3.

3.1.1 The General Circulation Model ECHAM5

ECHAM5 (5^{th} generation of European Centre Hamburg general circulation model) is an atmospheric general circulation model and was developed at the Max-Planck-Institute for Meteorology in Hamburg. It performs the meteorology data by calculation of the primitive equations of atmospheric dynamics and thermodynamics with the basic prognostic variables of temperature (T), the natural logarithm of the surface pressure ($\ln p_s$), divergence (D), vorticity (ξ) and mixing ratios (q_i) of different water species (water vapour, cloud liquid water, cloud ice) as base model for MESSy (Roeckner et al., 2003). To represent realistic synoptic conditions, the model dynamics and temperatures above the boundary layer up to about 100 hPa are nudged to the meteorological ERA-Interim reanalysis data of the European Centre for Medium-Range Weather Forecasts (ECMWF).

There are various vertical and horizontal resolutions for the three dimensional global model available, listed in Table 3.1. The standard vertical resolutions for tropospheric studies consists of 19 or 31 vertical layers up to 10 hPa (~30 km). As this study focuses on the stratosphere the middle atmosphere version with a high vertical resolution of 90 layers, covering a depth of the atmosphere from the surface up to the stratosphere and mesosphere in 0.01 hPa (~80 km) is needed. The vertical coordinates are given in hybrid pressure levels, with constant pressure levels in the stratosphere and terrain following profiles near to the surface (Giorgetta et al., 2006). Near the tropopause the vertical resolution is finer, with about 500 m (Jöckel et al., 2006), to reproduce the exchange processes between the troposphere and stratosphere.

Horizontal resolution	Number of boxes longitude × latitude	Grid	max. box width	Time step Δt (troposphere)	used Δt (stratosphere)
T21	64 × 32	5.62°	625 km	2400 s	
T31	96 × 48	3.75°	417 km	1800 s	900 s
T42	128 × 64	2.81°	313 km	1200 s	720 s
T63	192 × 96	1.87°	208 km	720 s	600 s
T85	256 × 128	1.41°	156 km	480 s	
T106	320 × 160	1.12°	125 km	360 s	300 s
T159	480 × 240	0.75°	83 km	240 s	

Table 3.1: ECHAM5 horizontal resolutions and corresponding time steps for tropospheric conditions from Roeckner et al. (2006, table 1) and for stratospheric conditions used in this thesis.

For these model simulations the resolution T63L90 was chosen, this results in a horizontal grid of 1.87° × 1.87° in latitude and longitude (triangular truncation at wave number 63 for spherical harmonics).

The time steps Δt depend on the vertical and horizontal resolution and are defined in Roeckner et al. (2006) for standard tropospheric conditions up to 10 hPa, but for simulations with the finer horizontal resolution (L90) including stratospheric and mesospheric altitudes up to 0.01 hPa, the model needs smaller time steps. When high wind speeds occur in the middle atmosphere near the poles and in the polar vortex, some fine tuning of the time resolution is needed to avoid instabilities due to Courant–Friedrichs–Lewy condition.

3.1.2 The Modular Earth Submodel System (MESSy)

MESSy (Modular Earth Submodel System) is an earth system model including and coupling many physical, chemical and biological processes on the soil surface, in the oceans and the atmosphere. Thus, the effects and feedback between certain processes can be investigated, including the link between stratosphere and troposphere, chemical-climate interactions or multicomponent aerosol processes. This is possible because MESSy works as a modular system in which individual components and data transfer can be switched on or off in form of submodels. The entire MESSy program code is structured in following four layers (see Figure 3.1).

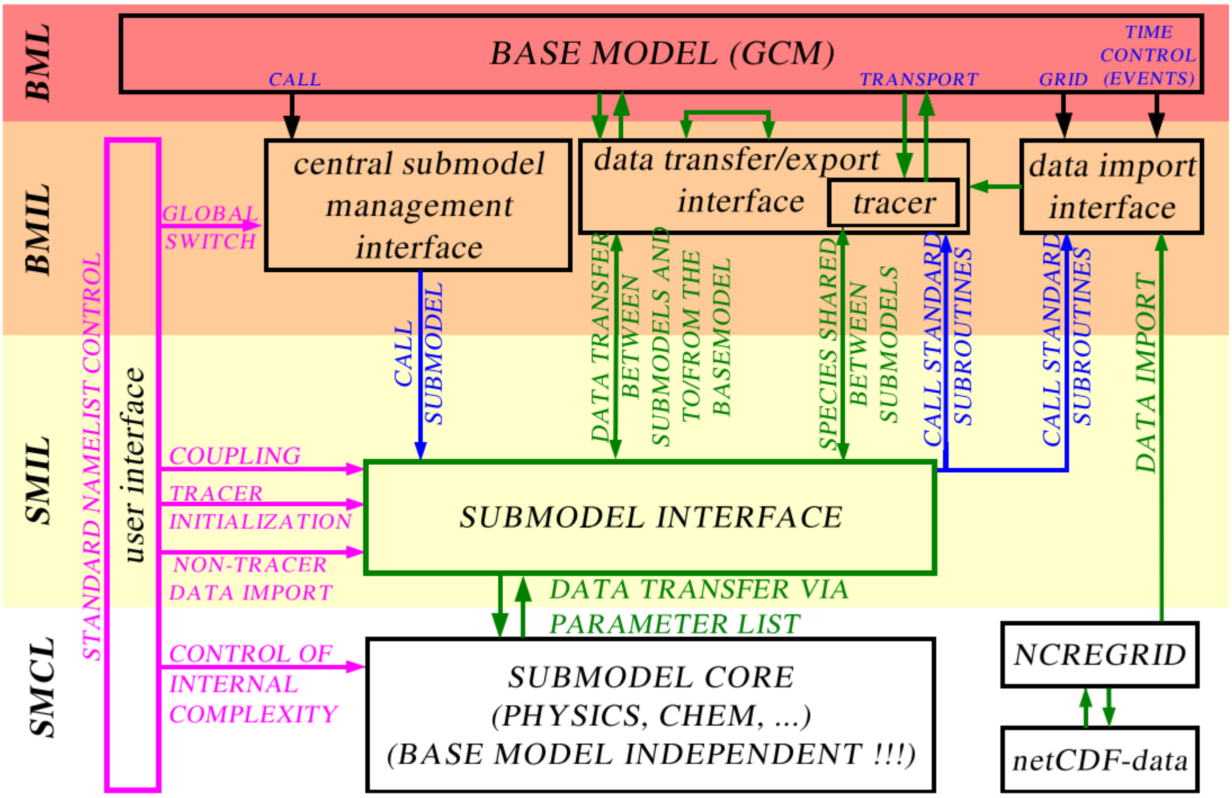

Figure 3.1: The communication structure of the MESSy interface scheme adapted from Jöckel et al. (2005), showing the different levels of the system and coupling between the submodels.

The Base Model Layer (BML) in the base model ECHAM5 takes over the central runtime control for all parts of the model. The base model ECHAM5 manages and controls the individual submodels via the Base Model Interface Layer (BMIL), as well as the data exchange between the base model and the submodels. External initial value conditions and limit value conditions are also imported here. The MESSy user interface is based on a FORTRAN95 namelist concept, whereby each submodel is controlled by two namelists in the SubModel Core Layer (SMCL) and SubModel Interface Layer (SMIL) (Jöckel et al., 2005, 2006, 2010). The SMCL contains the individual programs of the submodels, whereby each model runs independently and has its own parameterizations and calculations, so that it is independent of the base model. Each submodel can be switched on or off individually as required. The SMIL forms the submodel interface between the BMIL and the SMCL, it controls the data exchange between these two layers. All data from the BMIL are collected here and sent to the individual submodels in the SMCL through the parameters in the namelists. Conversely, the results from the submodels are transferred back to the BMIL. This enables the calculation of feedback effects between the different sub-models. An overview of the used submodels in this thesis is given in Table 3.2 and subsection 3.1.3.

Submodel	Function	Reference
AEROPT	Aerosol optical depth	Dietmüller et al. (2016)
AIRSEA	Air-sea exchange of trace gases	Pozzer et al. (2006)
CAABA/MECCA	Atmospheric chemistry	Sander et al. (2011)
CLOUD	Cloud processes and cover	Jöckel et al. (2006)
CLOUDOPT	Cloud optical properties	Dietmüller et al. (2016)
CONVECT	Convection processes	Tost et al. (2006b)
CVTRANS	Convection transport of tracers	Tost et al. (2010)
DDEP	Dry deposition	Kerkweg et al. (2006a)
GMXe	Global Modal Aerosol eXtension	Pringle et al. (2010a,b)
GWAVE	Gravity waves	Manzini et al. (1997)
H2O	Correction of H_2O + feedback	Jöckel et al. (2006)
IMPORT	Import of external data files	Jöckel et al. (2006)
JVAL	Photolysis rate coefficients	Jöckel et al. (2006)
LNOX	NOx lighting production	Tost et al. (2007)
MSBM	Multiphase Stratospheric Box Model	Jöckel et al. (2010)
OFFEMIS	Off-line emissions	Kerkweg et al. (2006b)
ONEMIS	On-line emissions	Kerkweg et al. (2006b)
ORBIT	Orbital parameters	Dietmüller et al. (2016)
QBO	QBO nudging	Giorgetta et al. (2002)
RAD	RADiation	Dietmüller et al. (2016)
S4D	Sampling in 4 Dimensions	Jöckel et al. (2010)
SCAV	Scavenging (wet removal)	Tost et al. (2006a)
SEDI	Aerosol sedimentation	Kerkweg et al. (2006a)
SURFACE	Surface processes	Jöckel et al. (2016)
TNUDGE	Tracer nudging	Kerkweg et al. (2006b)
TROPOP	Tropopause calculation	Jöckel et al. (2006)

Table 3.2: List of used MESSy submodels. Reference and short description referring to http://www.messy-interface.org (18 December 2020).

The atmospheric chemistry is calculated interactive with the submodel Chemistry As A Boxmodel Application/Module Efficiently Calculating the Chemistry of the Atmosphere (CAABA/MECCA) (Sander et al., 2011). The chemical generated SO_2 is calculated from fluxes of sulfate precursor gases DMS, OCS, CS_2 and H_2S. Oceanic DMS and OCS is transformed by sulfur chemistry reactions in CAABA/MECCA to SO_2 and further to H_2SO_4. The Global Modal-aerosol eXtension (GMXe) aerosol module is used for the aerosol physics with 4 soluble (nucleation, Aitken, accumulation and coarse mode) and 3 insoluble (Aitken, accumulation and coarse mode) aerosol modes and is suitable for tropospheric and stratospheric conditions (Pringle et al., 2010b). In the upper stratosphere the liquid sulfate aerosol particles are evaporated due to high temperatures and low pressure and further photolyzed to SO_2 by UV radiation. The aerosol radiative forcing is calculated diagnostically online by the submodel RADiation (RAD). These routines had to be modified for stratospheric aerosol conditions and transferred to features of MESSy version 2.52 from version 1.97, which was used in former studies (Brühl et al., 2015).

3.1.3 MESSy Submodels used in this Thesis

This section gives an overview of the MESSy submodels and namelist settings used in this thesis. A short description of each submodel for MESSy version 2.52 is given in alphabetical order. The program code of MESSy is not free for public and in a continuous developing process by many modelers from several institutions, subsequently some submodels might be changed, renamed or replaced in future versions. For more details see the references in the text and the official MESSy web page `https://www.messy-interface.org/` (18 December 2020).

AEROPT

The AEROPT submodel is for the online calculations of the AERosol OPTical properties in the model (Dietmüller et al., 2016). It is coupled to the GMXe submodel and gets input from precalculated 3 dimensional lookup tables, chosen for stratospheric conditions. The lookup tables provide optical properties for the aerosol modes, such as the extinction coefficient, the single scattering albedo and the asymmetry factor (Pozzer et al., 2012). These Mie size parameters are wavelength dependent and estimated for 32 predefined bands of the ECHAM5 model, 16 in the longwave and 4 in the shortwave spectrum, each divided into 4 subbands. The output is given at wavelengths of 350, 550 and 750 nm for comparison with GOMOS and optionally more wavelengths for other satellite instruments like Infrared Atmospheric Sounding Interferometer (IASI) or Along Track Scanning Radiometer (ATSR). Included aerosol species are aerosol water, sea salt, mineral dust, black carbon, organic carbon and water soluble inorganic ions like sulfate. The parameters from AEROPT are used in the radiation scheme as input for the radiative transfer calculations and to calculate the AOD.

AIRSEA

AIRSEA is a submodel for the transport of trace gases between the ocean and the atmosphere in both directions. It is important for the simulation of the tracer distributions in the troposphere as there are big differences in the mixing ratios of some species in the atmospheric surface layer over the oceans (Pozzer et al., 2006). The exchange between the air-sea interface is simulated in a two-layer model by molecular diffusion with well mixed concentrations. The flux depends on the ratio of the aqueous-phase concentration to the partial pressure in the gas phase of the tracer and the solubility of the species in salt water. For the simulations in this thesis the submodel is applied only for DMS.

CAABA/MECCA

CAABA (Chemistry As A Boxmodel Application) is a box model included in the atmospheric chemistry submodel MECCA (Module Efficiently Calculating the Chemistry of the Atmosphere) (Sander et al., 2011). It calculates gas- and aqueous-phase chemistry for the troposphere and stratosphere, coupled to JVAL for photolysis reactions and to MSBM for heterogeneous reactions on aerosols and PSCs. The Kinetic PreProcessor (KPP) generates the code for the performed chemical integration. The set of chemical reactions is expanded by a replacement file, to include a comprehensive Sulfur Chemistry Mechanism for this thesis in chapter 6. MECCA automatically generates a reaction table (see Appendix A), it consists of 109 species in 224 gas phase reactions, 45 photolysis reactions and 11 heterogeneous reactions.

CLOUD

The submodel CLOUD consists of the original routines from ECHAM5 described in Roeckner et al. (2003), which were adapted to a modularized, MESSy-conform structure. It calculates the cloud cover (using the parametrization of Tompkins (2002)), the cloud distribution, and cloud processes such as the cloud precipitation and the cloud microphysics of water droplet formation from the contents of cloud-vapor, liquid and ice phase (Jöckel et al., 2006). The microphysics also contain phase changes of melting, freezing and sublimation of snow and ice, as well as the evaporation of rain.

CLOUDOPT

The submodel CLOUDOPT for calculation of the cloud optical properties is developed from the ECHAM5 code. The input variables like the cloud cover, cloud liquid and cloud ice water and cloud nuclei concentration are imported from the CLOUD submodel (Dietmüller et al., 2016). These are necessary for the calculation of the shortwave and longwave optical depth, the asymmetry factor and the single scattering albedo of cloud particles. As these parameters are wavelength dependent the calculations are based on Mie theory on solar spectral bands, with 4 bands in the shortwave spectrum and 16 bands in the longwave spectrum.

CONVECT

CONVECT is a submodel for the calculation of the convection and convective precipitation adapted from the ECHAM5 base model. The sub-grid convection processes are parametrized in the large-scale by different convection schemes, compared by Tost et al. (2006b). In this thesis the scheme from Tiedtke (1989) with the Nordeng (1994) closure is chosen via namelist. The parametrization is based on the calculation of the updraft mass-flux, with entrainment and detrainment from the environment and also includes downdrafts, changes of temperature, humidity and tracer concentrations. The convection parametrization is also sensitive to the model resolution, which results in differences in the vertical transport of tracers, like dust and water vapor or ozone (Brühl et al., 2018).

CVTRANS

The ConVective tracer TRANSport (CVTRANS) submodel is developed for the comparison of the tracer transport in different convection schemes from the CONVECT submodel. To guarantee the model consistency CVTRANS adjusts the updraft and downdraft of the convective air mass fluxes and the belonging entrainment and detrainment rates of the convection parametrization (Tost et al., 2010).

DDEP

The Dry DEPosition of gas molecules and aerosol particles from the atmosphere to the surface is calculated by the submodel DDEP. The used dry deposition algorithm is based on the big leaf approach (Ganzeveld and Lelieveld, 1995), assuming that the ecosystem behaves like a single, homogenous "big-leaf". The dry deposition velocities are calculated online in absence of precipitation or clouds and depend on the biological, chemical and physical processes on the surface cover and the near-surface turbulence's (Kerkweg et al., 2006a). The resistance time variates with surface types, which are bare soil, vegetation, snow, wet skin reservoir on surfaces, open ocean and the sea ice.

GMXe

The Global Modal-aerosol eXtension (GMXe) submodel is developed from the former submodel M7 (Kerkweg, 2005; Stier et al., 2005; Vignati et al., 2004) for the parametrization of aerosol microphysical processes and the gas aerosol partitioning.

Aerosol species are divided into interacting lognormal aerosol modes; 4 soluble and 3 insoluble modes. The original mode boundaries of the aerosol size distribution from Pringle et al. (2010b) for the nucleation mode, the Aitken mode, the accumulation mode and the coarse mode are adapted for this setup to volcanic aerosols conditions in the stratosphere in Table 3.3.

Mode boundaries	Pringle et al. (2010b)	σ	Brühl et al. (2018)	σ
Nucleation mode	<10 nm	1.69	1 nm - 12 nm	1.59
Aitken mode	10 nm - 100 nm	1.69	12 nm - 140 nm	1.59
Accumulation mode	100 nm - 1 µm	1.69	140 nm - 3.2 µm	1.49
Coarse mode	>1 µm	2.2	>3.2 µm	1.7

Table 3.3: Diameters of aerosol mode boundaries in GMXe for tropospheric (Pringle et al., 2010b) and volcanic stratosphere conditions (Brühl et al., 2018), including the corresponding mode distribution width (σ).

The nucleation of new particles consists only of completely soluble sulfate aerosols and is calculated by the parametrization of Vehkamäki et al. (2002), which is valid over a temperature range of 190 K to 305.15 K and relative humidities of 0.01% to 100%. The growing of particles is represented by coagulation of two particles, from the same mode and also from different modes. Further the evaporation of liquid sulfate particles back to the gas phase in the middle stratosphere is activated.

The loss of gas phase species by gas/aerosol partitioning to the aerosol through heterogeneous reactions by condensation of gas phase molecules on existing particles is parametrized in 3rd EQuilibrium Simplified Aerosol Model (EQSAM3) (Metzger and Lelieveld, 2007). The uptake of gases on wet and or acid aerosol particles is switched on. A user manual with more detailed description for the setup and instructions for coupling to other submodels CAABA/MECCA, SCAV, DDEP and SEDI is given by Pringle et al. (2010a).

GWAVE

The submodel for Gravity WAVEs controls the strength of the momentum and energy deposition in the stratosphere and mesosphere (Jöckel et al., 2016). It calculates the cutoff wavenumber where the wave breakdown begins for each model level (Manzini et al., 1997), which has influence on the disturbance of the polar vortex. For these simulations the parametrization of non-orographic gravity waves by Hines (1997) from the ECHAM5 code is chosen in the namelist. Gravity waves can also be generated when overcoming orographic obstacles and require their own explicit parametrization of the vertical propagation and the breaking conditions (Eichinger et al., 2020).

H2O

In this submodel H_2O is defined as tracer in the stratosphere and mesosphere. The initialization is from satellite data and the feedback with the humidity of the base-model is controlled (Jöckel et al., 2006). By coupling with the CAABA/MECCA submodel, also the oxidation of methane (CH_4) to H_2O is included, which is important for high altitudes in the stratosphere.

IMPORT

The submodel IMPORT is used for the implementation of external data files, climatologies, tracer boundary conditions, parameters etc. Instead of direct import of datafiles into other submodels, like JVAL, RAD, QBO, AIRSEA, MSBM, GMXe, DDEP, TNUDGE, ONEMIS and OFFEMIS, they should be coupled to the IMPORT submodel.

JVAL

The chemistry of the CAABA/MECCA submodel is containing some photolysis reactions, which need photolysis rate coefficients (J-values) for more than 50 tropospheric and stratospheric species computed by the JVAL submodel. For the new photolysis reactions of CS_2 and H_2S in CAABA/MECCA the recommended absorption cross sections are implemented from Burkholder et al. (2015) into the JVAL PreProcessor (JVPP) (Sander et al., 2014) (see Appendix A). J-values are wavelength dependent and calculated as described in Landgraf and Crutzen (1998) for 8 spectral intervals in the UV and visible spectrum in the range from 178.6 nm to 752.5 nm. For the online calculations of the J-values also the cloud water and ice content, cloudiness and climatological aerosol is used (Jöckel et al., 2006). These are needed for the inclusion of multiple scattering by clouds.

LNOX

The NO_x (=$NO+NO_2+NO_3$) lightning production is calculated by the LNOX submodel, based on the flash frequency. An example for a namelist setup with the different available parametrizations is given in (Jöckel et al., 2010). Here the parametrization of Grewe et al. (2001), estimating the flash frequency on the relation between the updraft velocity within the convective clouds, is used (Tost et al., 2007). The model also can distinguish the ratio of NO_x production between intra-cloud and cloud-to-ground flashes. The resulting annual emissions produced by lightning are estimated to 2 - 10 Tg N per year (Tost, 2006).

MSBM

The Multiphase Stratospheric Box Model (MSBM) combines the program code of the former submodels HETCHEM and PSC from the MESSy1 version (Jöckel et al., 2010). MSBM calculates the stratospheric heterogeneous reaction rate coefficients on stratospheric background aerosol surfaces, this includes also the reactions on sulfate aerosols. It also simulates micro-physical processes that lead to the formation of Polar Stratospheric Clouds (PSCs) in the polar stratosphere (Jöckel et al., 2006). The influence on the hydrological cycle in the stratosphere is given by the re-partitioning of H_2O into the gas- liquid- and ice-phase (Jöckel et al., 2010).

OFFEMIS

OFFEMIS is the submodel for providing the OFF-line EMISsions and tracer tendencies for every single species. The emissions are implicated in form of surface emission fluxes (2-D) and multi-layer emission fluxes at different altitudes (Nx2-D) in molecules $m^{-2}s^{-1}$ or as volume emission fluxes (3-D) in molecules $m^{-3}s^{-1}$ (Kerkweg et al., 2006b). The plumes of outgasing volcanic SO_2 emissions (Diehl et al., 2012) are also imported via OFFEMIS as 3-D field volume emission fluxes. The data are prescribed from files in netCDF format and scaled by the NCREGRID tool (Jöckel, 2006) from the resolution of the input file data to the grid size of the model resolution.

ONEMIS

The submodel for ONline EMIssions calculates 2 dimensional surface emission fluxes for gas-phase and aerosol tracers and also calculates tracer tendencies, re-calculated at each time step during the simulations (Jöckel et al., 2006). There are different emissions of primary aerosol tracers, like sea salt emission fluxes used by Abdelkader et al. (2015) and mineral dust emissions, calculated online using the emission scheme of Astitha et al. (2012) or of gas phase tracers DMS and NO_x. Isoprene and mono-terpene are also available, but not used here. The consideration of changing parameters depend on wind speed, precipitation, radiation and different soil properties, soil temperature and soil wetness. The gas-phase emissions from ONEMIS can be added together directly with emissions from OFFEMIS to the same tracer, while the aerosol emissions must additionally be preformed by the aerosol submodel (Kerkweg et al., 2006b).

ORBIT

ORBIT is developed from the general circulation model ECHAM5 and integrated as submodel into the EMAC structure with coupling to the RAD submodel. It calculates the Earth orbit parameters, which depends on the time and the date in a year: distance between sun and earth, the cosines of the zenith angle of the sun, and the relative day length (Dietmüller et al., 2016).

QBO

The QBO submodel can be used for simulations with a self-consistent free running quasi-biennial oscillation (QBO). Or, as in this study, for nudging of the assimilation of the QBO zonal wind observations (data from Freie Universität Berlin) to the model. For the simulations with QBO the L90 version with a fine vertical resolution is essential to represent the vertical structure (Giorgetta et al., 2002).

RAD

RAD simulates the radiative transfer calculations with coupling to the atmospheric dynamics and chemistry. The influence of stratospheric aerosol on radiative forcing and heating is calculated online via multiple calls of the RAD submodel. The radiative temperature tendency of the first radiation call provides the temperature feedback to the base model. 18 input variables, including radiatively active tracers CO_2, CH_4, O_3, nitrous oxide (N_2O), CF_2Cl_2, and $CFCl_3$, cloud cover, water vapour, and water and ice content in clouds are provided from the other submodels ORBIT, IMPORT, CAABA/MECCA, AEROPT and CLOUDOPT.

It is also including sub-submodels for different shortwave radiation schemes and longwave radiation. One sub-submodel is the shortwave radiation scheme RAD_SHORT_v2, which is available for high aerosol loadings after volcanic eruptions (Thomas, 2008). It is including the interactions between aerosol scattering and gaseous absorption and multiple reflection, which is a dominant effect for particle scattering (Dietmüller et al., 2016). The sub-submodel RAD_FUBRAD is used in a higher spectral resolution to calculate the shortwave heating rates from the absorption of UV by oxygen (O_2) and O_3 in the upper stratosphere and mesosphere. The lower border is shifted from above 70 hPa in the original version of Dietmüller et al. (2016) to 30 hPa - 14 hPa to allow for scattering by the aerosol in the simulations with volcanic emissions.

S4D

The submodel Sampling in 4 Dimensions (S4D) was developed for the model evaluation of data from moving platforms like ships, trains or aircrafts (Jöckel et al., 2010). It is also used for direct comparisons of the in-situ measurements of the StratoClim campaign with the results of the model simulations in this thesis. The model data are interpolated online during the model simulation along the track of the flying aircraft. For that the aircraft coordinates in geographic longitude (in degrees east), geographic latitude (in degrees north) and pressure altitude (in hPa) and time in year, month, day, hour, minute, second (UTC) are provided as input files. An example for the namelist setup of the submodel S4D is also given in (Jöckel et al., 2010).

SCAV

The SCAVenging submodel calculates the removal of atmospheric tracers and aerosols by wet deposition, as well as the liquid phase chemistry in clouds and precipitation (Tost et al., 2006a). The gas phase and aerosol species are parametrized for scavenging in large-scale as well as in convective precipitation events and clouds, and coupled to the global scale in MESSy. The SCAV submodel gets the input from an external source, so the rainwater, including its chemical composition, enters a grid box from above and affects the layers below in the vertical column. For the parametrization of cloud droplets a monodisperse droplet spectrum is used, while a size distribution is assumed for liquid rain droplets (Tost et al., 2006a). Dissolving by micro physical processes of tracers and aerosols during the formation of cloud droplets is called nucleation scavenging and can result in precipitation. The impaction scavenging describes the uptake of gas molecules and aerosols by collision with falling rain droplets in the precipitation flux (Tost, 2006). SCAV also calculates the aqueous phase chemistry in cloud droplets via the KPP preprocessor. The uptake and oxidation of tracers is considered for liquid and mixed phase clouds, also including the aqueous sulfur oxidation of SO_2 to SO_4^{2-}.

SEDI

Aerosol SEDImentation describes the settling process due to gravity for particles and is negligible for gases (Kerkweg et al., 2006a). The flux of particles leaving one box and entering the box below is calculated with the terminal sedimentation velocity v_t:

$$v_t = v_S \cdot f_{Csf} \cdot f_{Slinn} \ , \tag{3.1}$$

consisting of the Stokes velocity v_S:

$$v_S = \frac{2gr^2\left(\rho_p - \rho_a\right)}{9\eta_a} \ , \tag{3.2}$$

the Cunningham-slip-flow correction f_{Csf} for the aerodynamics of non-spherical particles:

$$f_{Csf} = 1 + 1.257\frac{\lambda_a}{r} + 0.4\frac{\lambda_a}{r}\exp\left(\frac{-1.1r}{\lambda_a}\right) \ , \tag{3.3}$$

and the Slinn factor f_{Slinn} for the standard deviation of the aerosol radius distribution σ:

$$f_{Slinn} = \sigma^{2\ln\sigma} \ . \tag{3.4}$$

Here is r the aerosol particle radius, g the gravitational acceleration, ρ_p the aerosol density and ρ_a the air density; η_a denotes the dynamic viscosity of air and λ_a the mean free path of air molecules.

In the used version a sedimentation scheme of Benduhn and Lawrence (2013) with a modified Walcek scheme (Walcek, 2000) is chosen via namelist. The number of aerosol particles ΔN, which is sedimenting to the lower grid box per time interval Δt is:

$$\Delta N = \int_{\Delta t} n v_t \, dt \ , \tag{3.5}$$

with n the number of particles per unit volume.

SURFACE

The surface processes of the ECHAM5 base model have been transformed to the MESSy conform submodel SURFACE (Jöckel et al., 2016). These surface processes are important for the balance of the radiative heating and include: soil heat flux; albedos for different surface types; surface temperatures over land, ice, oceans, lakes, and within the soil; water budgets for lakes, soil and rain water; as well as the water equivalent of snow and ice for thickness and concentration of sea-ice and lake-ice, snow depth and cover of the surface, and the interception of snow by the canopy (Roeckner et al., 2003).

TNUDGE

TNUDGE is a submodel for Tracer NUDGing of prescribed tracer mixing ratios. When an emission flux into the atmosphere of a long living tracer is uncertain or cannot be calculated, observed mixing ratios can be used as boundary conditions. In these model simulations it is used for CO_2, CH_4, N_2O, halocarbons and OCS. TNUDGE simulates pseudo emissions of an artificial tracer flux, with positive flux values as source and negative values as sink of the tracer. Tracer tendencies are calculated for every model time step from the difference between the prescribed mixing ratios and the model simulated tracer mixing ratios and force them to follow the prescribed distributions (Kerkweg et al., 2006b).

TROPOP

The TROPOP submodel calculates the tropopause height (Jöckel et al., 2006), based on the World Meteorological Organization (WMO) temperature lapse rate in tropical regions from 30°S - 30°N and for latitudes above 30°S or 30°N with a potential vorticity iso-surface. Additionally TROPOP calculates the height of the planetary boundary layer.

3.2 Satellite Observations

For running model simulations with volcanic emissions, satellite data are essential for the input emission files. In this study satellite data sets of two instruments on the European Environmental Satellite (ENVISAT), launched on 1 March 2002 and lost signal on 8 April 2012 are analyzed, namely MIPAS and GOMOS. Further the OSIRIS instrument on the Odin satellite is used for continuing the timeline to 2017. For the time period before 2002 the SAGE II instrument is available. These satellite instruments are presented in chronological order. For consistency reasons and for filling data gaps, marked as white areas in all satellite images, (especially MIPAS in 2004) additional SO_2 *column data from Ozone Monitoring Instrument (OMI), Total Ozone Mapping Spectrometer (TOMS) and other satellites are checked.*

3.2.1 Stratospheric Aerosol and Gas Experiment II (SAGE II)

The SAGE II aerosol extinction measurements started in October 1984 and ended in August 2005 on board the Earth Radiation Budget Satellite (ERBS). Hence this data set is important for the model setup before the ENVISAT period starting in 2002. The aerosol extinction gridded on 60° longitude and 10° latitude is derived from the V7.00 L2 profiles provided by the Earth Observing System Data and Information System of NASA (EOSDIS) database with advises by A. Thomason (see Figure 3.2).

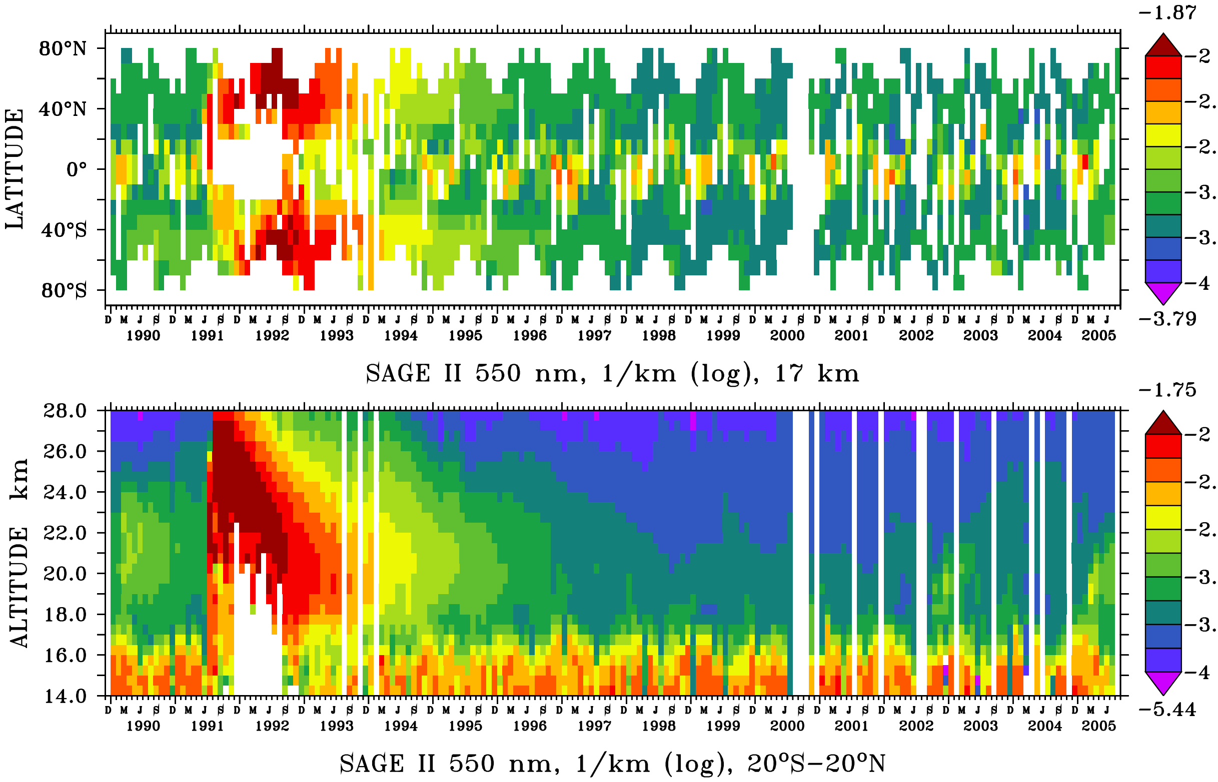

Figure 3.2: The logarithm of the extinction coefficient (1/km) of the SAGE II instrument from Thomason et al. (2008). January 1990 - August 2005: Horizontal distribution at 17 km altitude (top) and vertical distribution for tropical regions 20°S - 20°N (bottom). Maximum and minimum values are written on top (dark red) and bottom (violet) of the color keys. White: no data.

SAGE II was a solar occultation instrument measuring during sunrise and sunset. It covers a range of 80°N to 80°S and 180°E to 180°W with a horizontal grid resolution of 60° in longitude, 10° in latitude and a vertical resolution of 0.5 km between 13 km and 30 km altitude. Since this instrument is measuring in occultation, its measuring principle is similar to GOMOS. Two main differences with GOMOS are that SAGE II used the sun as light source, what results in a much better signal-to-noise ratio. At the opposite, the measurement rate is much lower than in the case of GOMOS since only two measurements (one sunrise and one sunset) are possible per orbit, so that a near-global coverage is achieved in about one month.

Data are provided at seven wavelengths between 386 nm and 1020 nm. The vertical profiles of O_3, nitrogen dioxide (NO_2), water vapor and aerosol extinction coefficients are measured at four wavelengths (386, 452, 525 and 1020 nm) from the middle troposphere to the stratosphere. An estimate of the aerosol surface area density is derived from the extinction coefficient. Aerosol effects for additional wavelengths at 448 nm, 600 nm and 945 nm are estimated by interpolation from the other channels (Thomason et al., 2008).

The uncertainty of the operational product during background periods is depending on several parameters, like the lack of sensitivity to particles with radii smaller than 100 nm, the aerosol extinction kernels for different wavelength channels or the temperature profile used in the data processing and has at least a factor of 2 (Thomason et al., 2008). The uncertainty depends on the altitude with $<35\%$ between 12 km and 18 km, $<25\%$ between 18 km and 30 km and 50% above 30 km (Bingen et al., 2003). After the large eruption of the Pinatubo in 1991 "saturation" effects in lower altitudes of the profiles can be observed for more than 1 year, as indicated by the white areas in Figure 3.2. You can also see the contamination by clouds, increasing the optical depth in the UTLS region on the lower panel of Figure 3.2. The data gaps in 2000 were caused by an instrument error when SAGE II was off for several months.

3.2.2 Global Ozone Monitoring by Occultation of Stars (GOMOS)

Global Ozone Monitoring by Occultation of Stars (GOMOS) is an instrument based on the principle of stellar occultation. GOMOS provides data of stratospheric aerosol extinction as well as O_3, H_2O, NO_2, nitrogen trioxide (NO_3), O_2 and air density. It is installed on board of the European Environmental Satellite (ENVISAT), which was in operation from 15 April 2002 to 8 April 2012 (Bertaux et al., 2010).

In the stellar occultation configuration, the instrument points to the light sources and scans the whole atmosphere while the star is rising or setting. The first measurement is taken above of the atmosphere, providing the spectrum of a star as a reference. The other measurements follow, each after a few seconds, reflecting the way light is absorbed or scattered by the different compounds of the atmosphere. The ratio of each of these spectra with the first reference spectrum gives the transmission of the atmosphere. This results in an altitude- and wavelength-dependent function that decreases with the altitude, reflecting the impact of the increasing air thickness through which the light propagates while the stars becomes closer to the horizon.

Using reference absorption spectra of the main absorbing species (such as the ones provided by the MPI-Mainz UV/VIS Spectral Atlas of Gaseous Molecules of Atmospheric Interest (`http://satellite.mpic.de/spectral_atlas` 18 December 2020) and cross-section values representative for aerosols, it is possible to retrieve the slant column density of gaseous species and the slant aerosol optical depth along the optical path, a process called spectral inversion. In a second step, vertical density profiles of the target gas species and vertical profiles of the aerosol extinction coefficient are obtained from the slant quantities, a process called spatial inversion. (Bertaux et al., 2010).

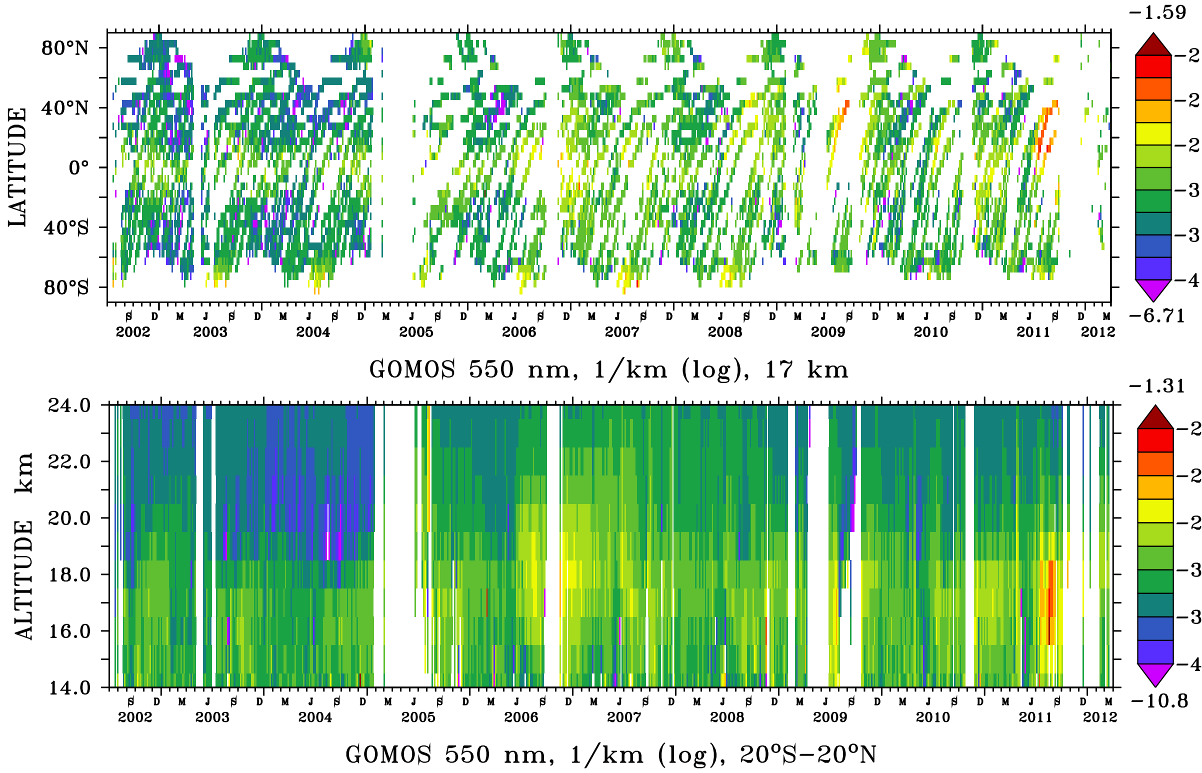

Figure 3.3: The decadal logarithm (log) of the aerosol extinction coefficient (1/km) is derived from the GOMOS instrument data v.3.00 at **550 nm wavelength** from Bingen et al. (2017). 15 April 2002 - 8 April 2012: Horizontal distribution at 17 km altitude (top) and vertical distribution for tropical regions 20°S - 20°N (bottom). Maximum and minimum values are written on top (dark red) and bottom (violet) of the color keys. White: no data.

GOMOS is using four spectrometers to provide measurements for starlight at wavelengths from UV-visible to Near-Infra Red (IR) range in four spectral regions: 248 nm - 371 nm, 387 nm - 693 nm, 750 nm - 776 nm and 915 nm - 956 nm (Robert et al., 2016).

In practice the latest one (915 nm - 956 nm) which was aimed at measuring water vapor, presents some issues (Kyrölä et al., 2010) and is not used for the retrieval of aerosol extinction. In the original inversion algorithm (the operational algorithm IPF), the methodology used was poorly effective to retrieval the aerosol extinction, and only one extinction channel was obtained, at the reference wavelength 550 nm (Vanhellemont et al., 2010). For this reason, a new retrieval algorithm called AerGOM was designed specifically to optimize aerosol retrieval (Vanhellemont et al., 2016; Robert et al., 2016). AerGOM provides the spectral dependence of the aerosol extinction coefficient between about 350 nm and 750 nm. From this algorithm, climate data records (the Climate Change Initiative (CCI) datasets, after the name of the European Space Agency (ESA) Climate Change Initiative) were developed at a wavelength of 550 nm, with a typical extinction uncertainty in the range between 5% to 70%. A main factor influencing the uncertainty is the weakness of the star signal alleviated by the high measurement rate made possible by the abundance of stars. The great variability of star magnitude and temperature of the occultated star also influences significantly the measurement uncertainty, and makes the retrieval challenging. (Bingen et al., 2017).

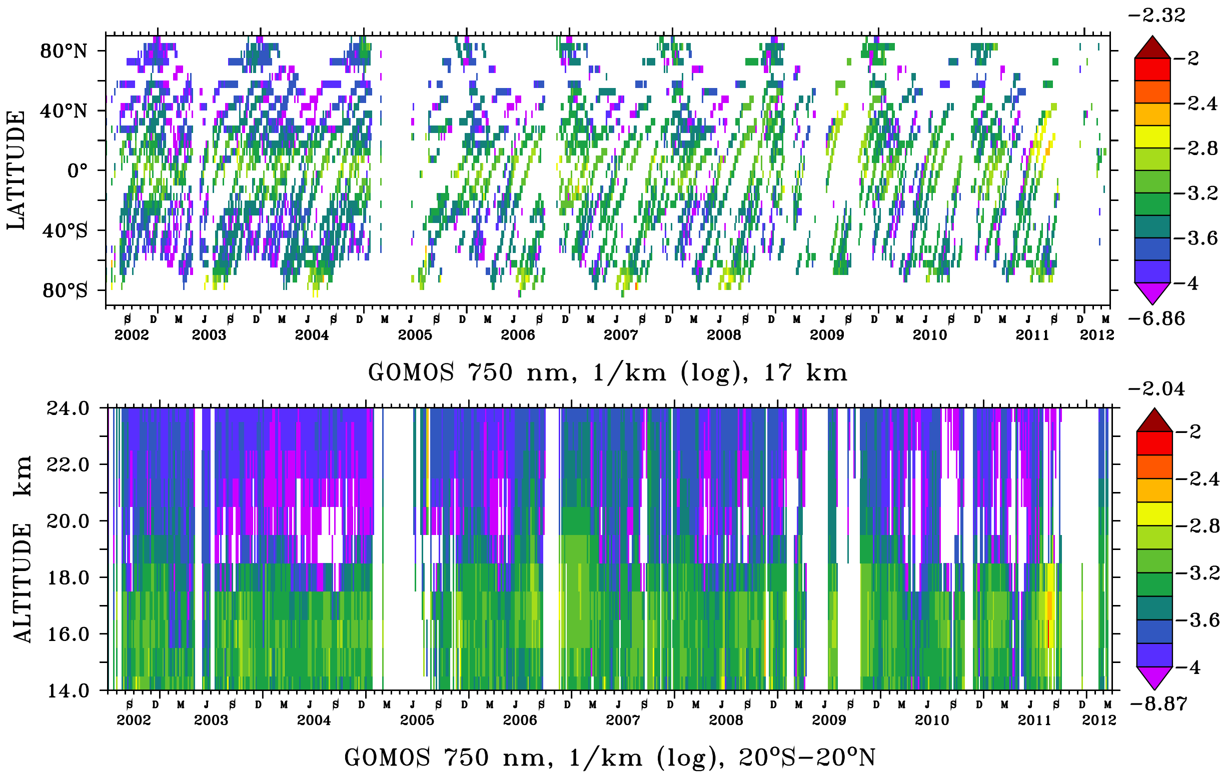

Figure 3.4: The decadal logarithm (log) of the aerosol extinction coefficient (1/km) is derived from the GOMOS instrument data v.3.00 at **750 nm wavelength** from Bingen et al. (2017). 15 April 2002 - 8 April 2012: Horizontal distribution at 17 km altitude (top) and vertical distribution for tropical regions 20°S - 20°N (bottom). Maximum and minimum values are written on top (dark red) and bottom (violet) of the color keys. White: no data.

The illustration of the CCI data set in the version 3.00, described in Bingen et al. (2017), shows the aerosol extinction from the GOMOS instrument at a wavelength of 550 nm (Figure 3.3) and a wavelength of 750 nm (Figure 3.4) on a logarithmic scale. The grid resolution was optimized to a grid of 5° latitude by 60° longitude and a time resolution of 5 days. This choice is made possible by the high measurement rate, and is more suitable to describe the zonal aerosol distribution than zonal monthly means, because it allows detecting of the signature of aerosol patterns with a lifetime down to about a week (e.g. medium volcanic eruptions). The CCI-GOMOS dataset is very important to fill data gaps of other instruments on the ENVISAT satellite (Robert et al., 2016). For instance to compensate lack of data from the MIPAS instrument (subsection 3.2.3), where several important eruptions in 2004 and 2006 couldn't be identified (Bingen et al., 2017).

3.2.3 Michelson Interferometer for Passive Atmospheric Sounding (MIPAS)

MIPAS is a mid-infrared emission spectrometer on board of the ENVISAT satellite. MIPAS is scanning across the horizon and detects the infrared radiation emitted by the Earth's atmosphere. The atmospheric spectra ranging from 4.15 µm to 14.6 µm are inverted to vertical profiles of temperature, cloud distributions and volume mixing ratios of 25 different trace species like SO_2, H_2O, O_3, CH_4, N_2O, NO_2, nitric acid (HNO_3) (Fischer et al., 2008) and OCS (Glatthor et al., 2015). In addition, a data set of observations of PSCs is provided by Spang et al. (2018).

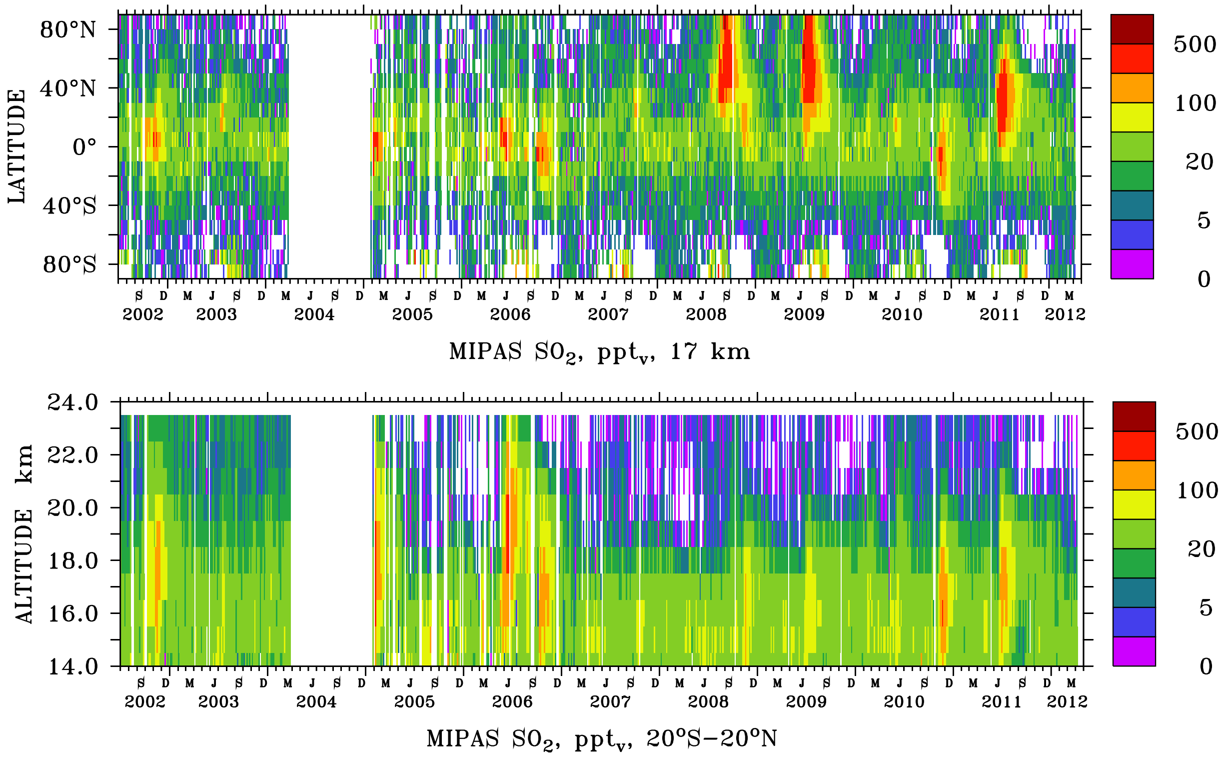

Figure 3.5: The volume mixing ratios of SO_2 in ppt_v is derived from the MIPAS instrument by data from Höpfner et al. (2015). 1 July 2002 - 8 April 2012: Horizontal distribution at 17 km altitude (top) and vertical distribution for tropical regions 20°S - 20°N (bottom). White: no data.

Vertical SO_2 profiles (Figure 3.5) of the data from the MIPAS retrieval version in Höpfner et al. (2015) are used to identify plumes of volcanic eruptions. The gridded dataset has a 3 dimensional resolution of 60° longitude, 10° latitude, 1 km altitude with a vertical coverage of 10 km to 23 km and a temporal resolution of 5 days. The lower altitude limit varies with the top of clouds in the troposphere, especially in tropical regions. This 5-day resolution looks safer, because monthly data are not sufficient for attribution of eruptions. The typical error for a single measurement of a volume mixing ratio profile is estimated to a value of $70 - 100\,ppt_v$. The averaged systematic errors of $10 - 75\,ppt_v$ (10–180%) are estimated for background concentrations and $10 - 110\,ppt_v$ (10–75%) with volcanic influence (Höpfner et al., 2015). After strong volcanic eruptions the detected mass of SO_2 could be underestimated, because the spectral instrument is saturated around a volume mixing ratio of more than $13\,ppb_v$ (Höpfner et al., 2015). Secondly the cloud clearing algorithm excludes ash plumes after a big eruption and other spectra with a cloud-index smaller than 4.5, which is equal to a particle volume density of about 1–2 $\mu m^3 cm^{-3}$ (Höpfner et al., 2013).

3.2.4 Optical Spectrograph and InfraRed Imaging System (OSIRIS)

The data from Optical Spectrograph and InfraRed Imaging System (OSIRIS) is important to continue the timeline series after losing the signal of the ENVISAT satellite in 2012. OSIRIS is a limb scatter instrument still in operation on board of the Odin satellite, launched on 20 February 2001. It preforms limb scans of atmospheric radiance spectra at wavelengths from the ultra-violet to the near infra-red (274 nm - 810 nm) (Bourassa et al., 2012a). To get the vertical profiles of aerosol extinction in 10 km to 35 km altitude (Rieger et al., 2015), the aerosol scattering properties are calculated with a refractive index of $1.427+ i7.167\times10^{-8}$ using Mie theory at 750 nm wavelength and a sulfate concentration of 75% H_2SO_4 and 25% H_2O (Rieger et al., 2018).

For this thesis the OSIRIS version 5.10 aerosol retrieval was used (see for details Bourassa et al. (2012a)). OSIRIS provides a surface coverage from 82°S - 82°N, except in polar winter when there is no sunlight (see Figure 3.6). The grid resolution is 2 km in altitude, 5° latitude and 30° longitude with daily averaged time intervals.

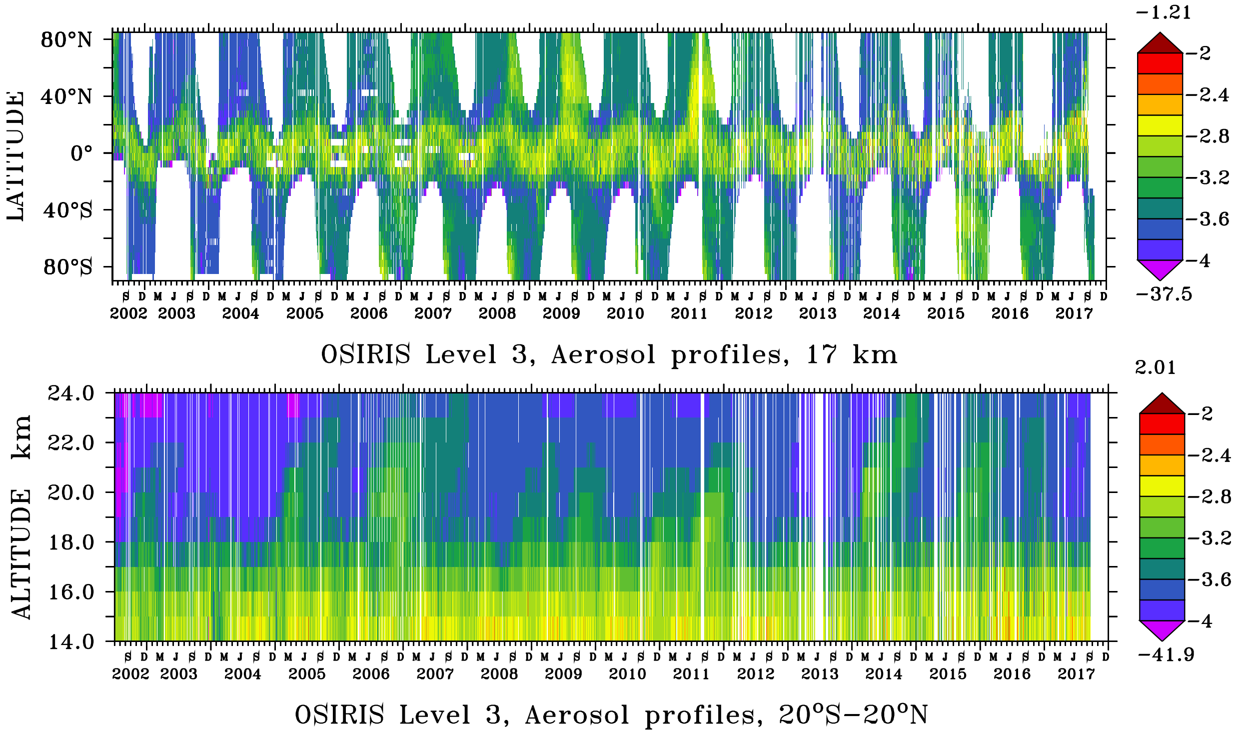

Figure 3.6: The logarithm log(1/km) of the aerosol extinction is derived from the OSIRIS instrument at **750 nm wavelength** by Bourassa et al. (2012a). 1 July 2002 - September 2017: Horizontal distribution at 17 km altitude (top) and vertical distribution for tropical regions 20°S - 20°N (bottom). Maximum and minimum values are written on top (dark red) and bottom (violet) of the color keys. White: no data.

The total error is approximated to 10 - 15% in the aerosol layer between 15 - 30 km, where the sensitivity of the measurements is decreasing with increasing optical depth. Due to measurement noise the error becomes dominant to the signal above 30 km and below 15 km (Rieger et al., 2015). In lower altitudes near the tropopause, the OSIRIS instrument is more sensitive to cloud perturbation than MIPAS and GOMOS, as can be seen in Figure 3.6 (bottom), and the uncertainty is higher.

3.3 Aircraft Field Campaign

As the resolution of satellite data is often too insufficient in time, location and altitude and often contains big data gaps, the use of data sets from in-situ measurements of aircraft campaigns is essential. The comparison of data from aircraft campaigns with the model output helps to improve the understanding of atmospheric processes and to get a validation for a good configuration of global chemistry climate models like EMAC. Improved climate models are important to find more robust and accurate predictions for climate simulations.

3.3.1 The StratoClim Project

StratoClim (Stratospheric and upper tropospheric processes for better climate predictions) (`http://www.stratoclim.org/` 18 December 2020) is a project funded by the European Union under Project No. 603557 within the 7th Research Framework Program. The StratoClim project started in December 2013 and combines the research activities of different scientific experimental and theoretical working groups of 28 partner institutes from 11 countries. This thesis is part of "Workpackage 5", the global climate modelling group.

Due to political and logistical constrains most phases of the project, including the main tropical aircraft campaign in the Asian Summer Monsoon region have been postponed multiple times. Finally the aircraft campaign took place with the M55-Geophysica in Kathmandu, Nepal during the Asian Summer Monsoon from 27 July to 10 August 2017. An overview of the 8 scientific flights over Nepal, India and Bangladesh is given in Figure 3.7.

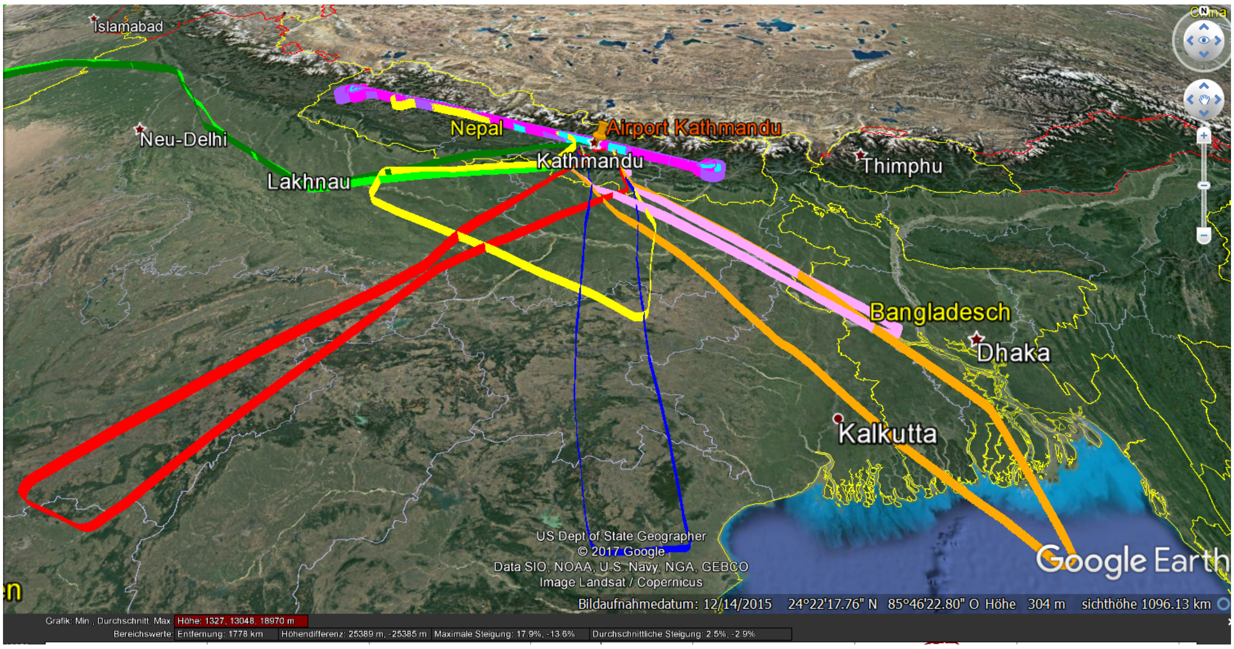

Figure 3.7: Flightpath of the Geophysica during the StratoClim campaign over Nepal, India and Bangladesh in summer 2017 (Plotted with Google Earth).
Flight number: 1: 27 July (rose), **2: 29 July (violet)**, **3: 31 July (red)**, **4: 2 August (magenta)**, 5: 4 August (cyan), 6: 6 August (orange), **7: 8 August (blue)**, 8: 10 August (yellow), **transfer (green)**.

The goal of the project is to improve the understanding of microphysical, chemical and dynamical processes in the upper troposphere/lower stratosphere region. A special focus lies on the impact of the Asian Summer Monsoon (section 2.2) on the climate in form of stratospheric air composition and on radiation forcing (section 2.5).

3.3.2 Instrumentation on board the M55-Geophysica

The Russian high-flying research aircraft M55-Geophysica (Figure 3.8) is flying in the sub-tropical upper troposphere/lower stratosphere (UTLS) region with altitudes up to 21 km (ca. 60 hPa) (Stefanutti et al., 1999) and temperatures down to -90 °C. The typical flight velocity of the aircraft is between 700 – 750 km/h (Höpfner et al., 2019). On the StratoClim Payload List are 26 different atmospheric measurement instruments with in-situ as well as remote-sensing technologies. StratoClim provides measurements of H_2O, O_3, OCS, SO_2, H_2SO_4, CO, CO_2, hydrogen cyanide (HCN), long-lived tracers, nitrogen oxides, active halogen species, as well as the particle size distribution, optical properties and chemical composition of droplets, aerosol and ice particles in the Asian Summer Monsoon at high altitudes. A short description of each instrument used for the model evaluation in this thesis (chapter 7) is given in alphabetical order.

Figure 3.8: Russian high altitude research aircraft M-55 Geophysica.
Image adapted from `http://www.stratoclim.org/` (18 December 2020).

The Airborne Mid-Infrared CAvity enhanced spectrometer (AMICA)

The AMICA instrument measures trace gases OCS, CO and CO_2 on board of the M55-Geophysica aircraft during the StratoClim campaign. The construction of this instrument is presented in Kloss (2017). AMICA is based on the technologies of the Integrated Cavity Output Spectroscopy (ICOS), which was first implemented in the Mid-Infrared Cavity enhanced Absorption spectrometer (MICA). The instrument consists of a laser, a cavity and a detector. Different gases are absorbing light at discrete wavelengths corresponding to distinct energy levels. The OCS molecule has a strong absorption line in the Mid-Infrared region of the spectrum at 2050.396634 cm^{-1}, which is chosen for the absorption spectroscopy. The instrument has to be robust against vibrations of the aircraft and has to work under low temperature (-80 °C) and low pressure (50 hPa) conditions.

The COndensation PArticle counting System (COPAS)

COPAS is an ultra-fine aerosol condensation particle counter on board of the M55-Geophysica aircraft, measuring the number concentration of aerosol particles with a diameter from 6 nm up to 1 µm (Weigel et al., 2009) during the StratoClim campaign.

COPAS has an aerosol inlet and two separate dual-channel (in total 4 channels) continuous flow Condensation Particle Counters (CPCs). The CPC channels characterize different particle sizes by using different temperature settings, typical diameters are set to $d_{p50} \geq 6$ nm (COPAS-II-2), $d_{p50} \geq 11$ nm (COPAS-I-2) and $d_{p50} \geq 15$ nm (COPAS-II-1) (Weigel et al., 2009). As a result, in addition to measuring the total particle number concentration, the number concentration of ultra-fine, freshly nucleated particles can be derived. To quantify the nonvolatile fraction of the aerosol particles, the fourth CPC channel is including an aerosol heating line (250 °C) to evaporate the aerosol particles with a diameter between 11 nm and 200 nm.

The sampling is done with a frequency of 1 Hz and provides measurements as 15 s averages (Weigel et al., 2011), with an estimated uncertainty of less than 30% (Höpfner et al., 2019). The instrument is adapted to airborne operations at high altitudes of 21 km with low pressure (50 hPa) and temperature (-80 °C) conditions (Weigel et al., 2009) to perform measurements in the UTLS.

The ERc Instrument for Chemical composition of Aerosols (ERICA)

With the ERICA instrument the quantitative chemical composition of single aerosol particles can be analyzed (Höpfner et al., 2019). The description of this newly developed instrument is given by Hünig (2020). The construction combines two measurement techniques of the ERICA-Laser Ablation Mass Spectrometer (LAMS) and the ERICA-Aerosol Mass Spectrometer (AMS) coupled in series in one instrument to get a compact design and save space and weight in the aircraft. The uncertainty for the ERICA-AMS mass concentration measurements from the StratoClim campaign is estimated to be ±30% (Höpfner et al., 2019). To prevent contamination of the measurements by the material of the instrument through collisions with particles, the surface of the inlet system is plated with gold.

In the first part of the instrument the ERICA-LAMS detects and analysis single particles with a geometric diameter from 80 nm up to 5 µm. The ERICA-LAMS consists of two parallel units, each containing a detection laser and an ellipsoidal reflector, which focuses the light scattered by the particle on a photomultiplier tube. Then the aerodynamic diameter is calculated from the particle flight time. In the ablation region an UV laser pulse evaporates and ionizes the particle. Here the positive and negative ions are measured by a bipolar time-of-flight mass spectrometer simultaneously to analyze the chemical composition of the particle. All particles passing the ERICA-LAMS without ablation enter the second part of the instrument.

In the ERICA-AMS all remaining aerosol particles are vaporized at 600 °C followed by an electron impact ionization of the vapor. Only the chemical composition of the particle ensembles is analyzed by positive ions and consists of non-refractory sulfate, nitrate, ammonium, chloride and organic compounds. The measured size range is between 60 nm up to 5 µm geometric diameter (Hünig, 2020).

The Fast OZone ANalizer (FOZAN)

The FOZAN instrument detects the ozone concentration. To prevent the influence of varying air temperature the incoming airflow is thermostated with a heater on 60 °C and splitted into two parallel channels (Ravegnani et al., 1999). During the flight the instrument can change between measurements or calibration mode. The calibration is done with an ozone generator at constant ozone concentration. The luminescence intensity of the chemioluminescent heterophase reaction between ozone in the airflow and a solid state sensor is detected. The ozone concentration is proportional to luminescence intensity registered by the photomultiplier. The range is 10 - 500 µg/m^3 with an uncertainty of <10%. The operating pressure (altitude) range is between 1100 hPa and 30 hPa (0 - 25 km) (Ulanovsky et al., 2001).

The Ultra High Sensitivity Aerosol Spectrometer (UHSAS)

UHSAS is an optical particle counter and covers particle size diameters in the range from 65 nm up to 1 µm. It classifies particles with a high sensitivity resolution of 1 nm/bin in 99 size channels. The classification of the size channels of the instrument differ from the aerosol mode boundaries in the model setup, which could cause discrepancy in the direct comparison of the aerosol size distributions in chapter 7. The instrument is operating with an optical-scattering laser-based aerosol spectrometer at 1.054 µm wavelength (Cai et al., 2008). The laser illuminates the aerosol particles, which scatter the light signals to 4 optical detectors (Uin, 2016). For the StratoClim campaign UHSAS was modified to operate under stratospheric conditions. The estimated uncertainty of the UHSAS Airborne in-situ aerosol observation data are below 30% (Höpfner et al., 2019).

Chapter 4

Observations of Volcanic Eruptions

A previous inventory of volcanic eruptions, based on SO_2 vertical profiles from MIPAS, was used to estimate the aerosol radiative forcing from 2002 to 2011 by simulating the evolution of SO_2 emissions in the atmosphere by Brühl et al. (2015) and improved by Bingen et al. (2017). The results of these simulations showed that significant discrepancies remained with respect to radiative forcing estimated from measurements (Brühl et al., 2018). In this chapter an improved Volcanic Sulfur Emission Inventory is evolved from analyzing additional satellite data sets, including all identified relevant eruptions between 1990 and 2017. Geological information is received from the "Global Volcanism Program, Smithsonian Institution" (`https://volcano.si.edu/` 18 December 2020).

4.1 Creation of a Volcanic Sulfur Emission Inventory

The process starts with searching for higher values in the SO_2 signal of the MIPAS instrument (subsection 3.2.3) and higher optical depth in GOMOS data (subsection 3.2.2), checking with other satellites and the entries in the Smithsonian database. For comparing the different data sets you have to consider a time shift of about 2 weeks between the measurements of SO_2 emissions from MIPAS instrument and the aerosol extinction from GOMOS instrument, as a result of the particle formation from the gas phase. Before the launch of the ENVISAT satellite starting in 2002, only level 2 data of profiles of aerosol extinction measurements from SAGE II (subsection 3.2.1) are available, the same after 2012 for the level 3 data of OSIRIS instrument (subsection 3.2.4). Table 4.1 is containing the name of the volcano or the region of the eruption if the name of the volcano is unknown, the injection time into the model, the coordinates and the amount of emitted SO_2. The amount of sulfur for every single eruption is calculated by integration of SO_2 vertical profiles from MIPAS observations (Höpfner et al., 2015), excluding tropospheric emissions below 12 km in high latitudes, 13 km in mid latitudes and 14 km in low latitudes. The listed altitudes and coordinates indicate the maxima of the volcanic plumes in the satellite data sets. The date of the volcanic eruption can differ some days from the date of injection in the model simulation, because the time resolution of the data sets is at least about 5 days (some weeks in the SAGE period). Sometimes there is more than one eruption in the same time step within an interval of 5 days, thus several eruptions are listed in the same line. The integration time has to be extended for data gaps, which increases the uncertainty and makes it difficult to identify the right volcano, marked with a "?". In some of these cases the SO_2 emissions of two volcanoes can not be separated and are marked with a "+" in the same line. This happens often in the Republic of Vanuatu, an island country located in one of the most volcanic active regions in the South Pacific, indicated with "Vanuatu" in Table 4.1.

Volcano or region	Time	Latitude (°)	Longitude (°)	Altitude (km)	SO_2 (kt)	Instrument
Kelut	11 Feb 1990	-8	112	16, 22	410	S
Gamalama	25 Apr 1990	0	127	16	96	S
Raung (?)	25 Jul 1990	-8	115	16	63	S
Pacaya +	16 Sep 1990	15	-90	16	100	S
Sabancaya	6 Oct 1990	-16	-72	17	75	S
Papua +	12 Jan 1991	-4	145	17	88	S
Fernandina	20 Apr 1991	0	-92	16	118	S
Pinatubo	16 Jun 1991	15	120	23	16942	S
Hudson	10 Aug 1991	-46	-73	18	1276	S
Cerro Negro	10 Apr 1992	12	-87	22	18	S
Spurr	28 Jun 1992	61	-152	17	291	S
Spurr	19 Aug 1992	61	-152	16, 18	298	S
Spurr	18 Sep 1992	61	-152	17	187	S
Lascar	18 Apr 1993	-23	-68	22	376	S
Langila, Galeras (?)	30 Oct 1993	-5, 1	145, -70	17	50	S
Yasur?	17 Mar 1994	-16	165	16	80	S
Rinjani, Nyamuragira, Central America	6 Jul 1994	-8, -1, 12	117, 30, -90	16	63	S
Rabaul	20 Sep 1994	-4	150	18-22	89	S
Merapi, Ecuador	23 Nov 1994	-7, 1	110, -70	17, 17	48, 57	S
Peru, Africa, Vanuatu	15 Feb 1995	-15, -1, -15	-78, 30, 168	17, 16, 16	7, 43, 25	S
Mexico + Soufriere Hills	10 Aug 1995	16	-98, -62	16	81	S
Peru + Colombia, Rabaul	10 Feb 1996	-15, 5, -4	-80, -80, 150	17, 16, 16	65, 96	S
Soufriere Hills	26 May 1996	16	-62	16	53	S
Soufriere Hills+Mexico, Rabaul	18 Sep 1996	16, -4	-62, -98, 150	16	59, 28	S
Nyamuragira, Manam	3 Dec 1996	-1, -5	30, 145	17	45, 90	S
Manam + Langila	11 Feb 1997	-5	145	17	107	S
Popocatepetl	1 Jul 1997	19	-98	16	32	S
Soufriere Hills, Philippines	20 Oct 1997	16	-62	15, 16	36, 20	S
Soufriere Hills, Papua	26 Dec 1997	16	-62, 150	16	37, 22	S
Tungurahua (?), Vanuatu	2 Feb 1998	-1, -16	-78, 168	17, 16	98, 15	S
Soufriere Hills	4 Jul 1998	16	-62	16	56	S
Manam, Cerro Azul, Nyamuragira	7 Oct 1998	-5, 0, -1	144, -90, 30	17, 17, 16	28, 39, 19	S
Guagua Pinch + Tungurahua, Vanuatu	23 Jan 1999	-1, -16	-78, 165	17, 16	75, 49	S
Cameroon	31 Mar 1999	4	10	16	63	S
Mayon, Colombia	22 Jun 1999	13, 2	124, -80	17, 16	41, 46	S
Soufriere Hills +	24 Jul 1999	16	-62	17	42	S
Ulawun, Tungurahua + Guagua Pichincha	16 Nov 1999	-5, -1	150, -78	17	31, 51	S
Vanuatu, Nyamuragira, Tungurahua	4 Feb 2000	-16, -1, 0	165, 30, -78	17, 16, 16	33, 41, 12	S

Volcano or region	Time	Latitude (°)	Longitude (°)	Altitude (km)	SO_2 (kt)	Instrument
Mayon +Vanuatu,Tungurahua	29 Feb 2000	13, -16, -1	124, 168, -78	16, 16, 16	25, 32	S
Ulawun (+ Miyakejima)	26 Sep 2000	-5	150	17	42	S
Nyamuragira, Mayon(?)	13 Feb 2001	-1, 13	30, 124	16, 18	47, 88	S
Ulawun	29 Apr 2001	-5	150	16	41	S
Mayon, Lopevi	23 Jun 2001	13, -16	124, 168	16, 16	49, 22	S
Tungurahua, Soufriere Hills	7 Aug 2001	0, 16	-78, -62	16, 16	29, 46	S
Africa, Tungurahua +	25 Sep 2001	-1, 0	30, -78	16	31, 47	S
Tungurahua (+ Manam), Nyiragongo	14 Jan 2002	-5, -1	-78(144), 30	17, 15	83, 19	S
Tungurahua (+ Africa)	20 Mar 2002	-1	-78 (30)	17	77	S
Nyamuragira	23 Jul 2002	-1	30	15	23	M
Witori	2 Aug 2002	-6	150	14	18	M
Ruang	26 Sep 2002	2	125	18	71	M, G
El Reventador	5 Nov 2002	0	-78	17	77	M, G
Nyiragongo, Lokon	9 Jan 2003	-1, 1	30, 125	15, 16	12, 10	M, G
Nyiargongo, Lokon (Rabaul?)	5 Mar 2003	-5, 1	30, 125	17, 15	12, 13	M, G
Anatahan, Nyiaragongo, Ulawun	14 May 2003	16, -1, -5	143, 30, 150	16, 16, 17	9, 15, 6	M
Lewotobi, Kanlaon	13 Jun 2003	-8, 10	123, 123	15, 15	9, 15	M, G
Soufriere Hills	13 Jul 2003	16	-62	17	41	M, G
Gamalama, Japan, M	17 Aug 2003	1, 33	128, 131	16, 16	8, 7	M, G
Bezymianny or Klyuchevskoy	6 Sep 2003	56	160	14	8	G
Lokon, Soufriere Hills+Masaya	26 Sep 2003	2, 15	125, -62	16, 16	7, 5	M, G
Rabaul	10 Nov 2003	-5	150	16	17	M, G
Rabaul	5 Dec 2003	-5	150	16	13	M, G
Rabaul, Nyiaragongo?	9 Jan 2004	-5, -1	150, 30	17, 15	11, 9	M, G
Langila, Nyiaragongo?	3 Feb 2004	-5, -1	150, 30	17, 17	11, 3	M, G
Soufriere Hills	4 Mar 2004	10	-62	17	22	M, G
Nyamuragira, Awu + Tengger	12 Jun 2004	-1, 4, -8	30, 125, 112	17, 15	20, 18	G
Pacaya, Galeras	17 Jul 2004	15, 1	-91, -77	17, 17	11, 11	G
Galeras	11 Aug 2004	1	-77	16	15	G
Vanuatu, Rinjani + Kerinci	30 Sep 2004	-16, -8, -2	168, 116, 101	15, 15, 17	7, 15	G
Manam, Soputan	30 Oct 2004	-4, 1	144, 125	16, 16	8, 11	G
Manam, Nyiragongo	24 Nov 2004	-4, -1	144, 30	17, 15	18, 11	G
Nyiaragongo, Reventador	4 Dec 2004	0, 0	30, -77	16, 16	19, 5	G
Vanuatu, Soputan	24 Dec 2004	-16, 1	168, 125	17, 15	15, 16	G
Manam	28 Jan 2005	-4	144	18	130	M, G
Anatahan, (+)	3 Apr 2005	16	143	15	15	M
Anatahan, Soufriere Hills	23 Apr 2005	16, 16	143, -62	16, 16	21, 21	M
Anatahan, Fernadina, Vanuatu	18 May 2005	16, 0, -16	143, -91, 168	15, 15, 15	8, 11, 6	M
Anatahan, Santa Ana	12 Jun 2005	16, 14	143, -90	15, 15	12, 9	M
Anatahan, Soufriere Hills	12 Jul 2005	16, 16	143, -62	15, 15	14, 10	M
Anatahan, Raung	6 Aug 2005	16, -8	143, 113	15, 15	13, 20	M
Anatahan, Raung	16 Aug 2005	16, -8	143, 113	15, 15	14, 17	M, G
Santa Ana	5 Oct 2005	14	-90	17	32	M
Sierra Negra, Dabbahu	25 Oct 2005	-1, -13	-91, 40	15, 15	16, 22	G

Volcano or region	Time	Latitude (°)	Longitude (°)	Altitude (km)	SO_2 (kt)	Instrument
Karthala, Galeras	24 Nov 2005	-10, -2	43, -80	16, 16	13, 11	M, G
Soputan, Lopevi	24 Dec 2005	1, -16	125, 168	16, 16	23, 13	M, G
Rabaul +	23 Jan 2006	-5	152	16	25	G
Manam, Chile	4 Mar 2006	-5, -40	144, -70	17, 16	58, 6	G, T
Cleveland	14 Mar 2006	53	-170	13	8	G
Ecuador, Tinakula, Lascar	18 Apr 2006	-5, -10, -23	-78, 166, -68	17, 17, 17	13, 17, 3	M
Soufriere Hills	23 May 2006	16	-62	19	125	M, G, T
Kanlaon	2 Jul 2006	10	123	20	42	M
Tungurahua, Rabaul	16 Aug 2006	-2, -4	-78, 150	19, 17	40, 20	M, G, T
Rabaul	10 Oct 2006	-4	150	17	131	M, T
Ubinas, Vanuatu	25 Oct 2006	-20, -20	-70, 168	17, 15	8, 25	M
Ambrym	9 Nov 2006	-10	160	17	27	M, T
Nyamuragira, Mexico	29 Nov 2006	5, 5	30, -90	17, 15	28, 21	M, G, T
Bulusan, Soputan, Vanuatu	24 Dec 2006	13, 1, -16	125, 125, 168	18, 16, 15	8, 8, 14	M, G
Karthala, Bulusan, Lascar, Shiveluch, Vanuatu	23 Jan 2007	-10,13, -23, 57, -16	43, 125, -68, 160, 168	17, 17, 15, 15, 15	5, 5, 6, 7, 5	M, G, T
Nevado del Huila, Karthala, Vanuatu	22 Feb 2007	0, -10, -16	-70, 43, 168	16, 15, 16	8, 10, 8	M, G, T
Etna, Reventador, Ambrym	24 Mar 2007	38, 0, -16	15, -78, 160	15, 16, 17	8, 17, 14	M, G, T
Piton de la Fournaise, Reventador +	8 Apr 2007	-20, 0	57, -80	16, 16	22, 11	M, G, T
Ulawun, Vanuatu, Nevado del Huila	3 May 2007	-5, -25, 3	150, 160, -70	15, 15, 15	11, 5, 6	M, G, T
Papua, Kamchatka, Nyamuragira, Ubinas + Lascar	13 May 2007	-10, 50, 0, -20	150, 150, 30, -75	16, 16, 16, 16	6, 1, 10, 6	M, G
Llaima, Vanuatu, Bulusan	23 May 2007	-30, -15, 13	-70, 160, 125	18, 15, 17	10, 6, 7	M, G
Soputan, Bezymianny, Telica	12 Jun 2007	1, 56, 13	125, 160, -87	16, 14, 15	13, 7, 9	M, G
Lengai, Mexico, M	2 Jul 2007	2, 20	29, -90	16, 15	14, 9	M
Raung, Japan, M (+)	27 Jul 2007	-5, 35	110, 130	15, 15	10, 10	M
Manda Hararo, Java, M	11 Aug 2007	12, -5	40, 115	17, 15	13, 14	M, T
Vanuatu, Mexico, M	20 Sep 2007	-5, 20	180, -90	16, 16	8, 13	M
Jebel al Tair, Galeras	5 Oct 2007	16, 1	42, -80	16, 16	41, 8	M, T
Galeras, Jebel al Tair, Soputan	4 Nov 2007	-2, 15, -5	-80, 42, 110	16, 16, 16	7, 5, 8	M, G
Soputan or Krakatau, Galeras, Chikurachki	14 Nov 2007	-5, -1, 50	110, -75, 155	16, 16, 15	9, 8, 10	M
Talang, Galeras	9 Dec 2007	0, 0	100, -75	16, 16	10, 12	M
Ulawun?	19 Dec 2007	1	150	17	17	M, G
Nevado del Huila, Llaima	3 Jan 2008	1, -35	-75, -71	17, 15	26, 4	M
Galeras, Anatahan	23 Jan 2008	-3, 15	-80, 145	16, 16	14, 7	M
Tungurahua, Papua	12 Feb 2008	-5, -5	-80, 155	16, 17	13, 10	M
Batu Tara (+)	13 Mar 2008	-5	125	16	26	M, G
Lengai, Andes, Kerinic	28 Mar 2008	-5, 5, -2	36, -80, 101	16, 16, 16	6, 4, 7	M
Egon, Nevado del Huila	12 Apr 2008	-5, 5	122, -76	15, 17	14, 9	M
Mexico, Ibu, Chaiten	27 Apr 2008	15, -35	-90, 125, -70	16, 16, 16	9, 11, 3	M
Mexico, Barren Island, Chaiten	12 May 2008	10, 10, -35	-90, 90, -70	14, 16, 14	10, 14, 5	M
Soputan, Nicaragua/Costa Rica	16 Jun 2008	1, 1	125, -85	16, 16	26, 8	M

Volcano or region	Time	Latitude (°)	Longitude (°)	Altitude (km)	SO_2 (kt)	Instrument
Okmok, Soputan	21 Jul 2008	53, 1	-168, 125	16, 16	51, 27	M
Kasatochi	15 Aug 2008	52	-175	17	273	M, G
Dallafilla, Nevado del Huila, Reventador	13 Nov 2008	14, 3	40, -78	17, 17	39, 28	M
Karangetang, Galeras, Japan	18 Dec 2008	3, 0, 30	125, -80, 130	17, 17, 15	15, 10, 9	M, G
Barren Island, Galeras	2 Jan 2009	10, 3	90, -80	17, 15	10, 10	M
Indonesia?, Galeras	27 Jan 2009	-5, 0	100, -80	16, 16	12, 10	M
Galeras, Villarrica, Karangetang, Vanuatu	16 Feb 2009	- 2, - 35, 3, -16	-78, -75, 100, 168	16, 15, 16, 17	11, 6, 6, 7	M
Redoubt, Galeras	28 Mar 2009	60, 0	-155, -75	13, 15	61, 43	M
Fernandina, Nyamuragira	12 Apr 2009	0, 0	-90, 30	16, 16	12, 16	M
Galeras + Reventador	7 May 2009	0	-75	15	25	M
Rinjani,Vanuatu, Reventador	22 May 2009	-5, -15, 3	116, 165, -80	16, 16, 16	4, 4, 13	M
Sarychev, Manda Hararo	21 Jun 2009	48, 12	153, 40	16, 16	446, 82	M, G
Vanuatu, Mayon, Galeras	4 Oct 2009	-15, 13, 2	165, 120, -80	17, 17, 17	4, 6, 10	M
Tungurahua, Hawaii,Vanuatu	19 Oct 2009	5, 20, - 16	-76, -155,165	16, 16, 16	7, 5, 5	M, G
Galeras, Karkar, Vanuatu	3 Dec 2009	0, -5, - 16	-78, 146, 165	17, 17, 17	12, 10, 4	M
Mayon, Nyamuragira,Vanuatu	2 Jan 2010	13, 0, -15	120, 30, 168	16, 16, 16	8, 8, 9	M
Turrialba, Vanuatu	17 Jan 2010	5, -15	-82, 168	16, 16	9, 9	M
Soufriere Hills	16 Feb 2010	16	-62	17	36	M
Arenal, Indonesia, Vanuatu	2 Apr 2010	9, 0, -16	-84, 120, 168	15, 15, 15	14, 12, 5	M
Tungurahua, Dukono,Vanuatu	2 May 2010	-5, 2, -16	-78, 128, 168	16, 16, 16	14, 10, 7	M
Pacaya, Ulawun, Sarigan	6 Jun 2010	15, -5, 16	-91, 150, 145	17, 16, 15	27, 6, 4	M
Ulawun, Costa Rica, Miyakejima, M	16 Jul 2010	-5, 15, 35	150, -87, 140	16, 16, 16	8, 13, 6	M, G
Karangetang, Nicaragua, Vanuatu	15 Aug 2010	3, 15, -16	125, -85, 168	16, 16, 16	12, 12, 6	M
Galeras, Sinabung M	30 Aug 2010	5, 5	-77, 100	16, 16	10, 12	M
Karangetang, Barren Island	4 Oct 2010	3, 12	125, 94	16, 16	20, 13	M
Merapi	8 Nov 2010	-7	110	17	97	M
Tengger, Tungurahua, Chile	23 Dec 2010	-8, -3, - 40	110, -78, -75	17, 17, 17	16, 13, 8	M
Tengger	7 Jan 2011	-8	110	16	24	M
Lokon, Planchon, Bulusan	26 Feb 2011	1, -35, 13	125, -75, 125	16, 15, 16	13, 4, 12	M
Karangrtang, Sangay, Planchon	23 Mar 2011	2, -2, -35	125, -78, -75	15, 15, 15	10, 10, 5	M
Galeras?, Karangetang	12 Apr 2011	5, 5	-77, 128	16, 16	10, 9	M
Tungurahua, Dukono,Vanuatu	2 May 2011	2, 2, -16	-78, 128, 160	16, 16, 15	13, 9, 5	M
Grimsvötn, Lokon	27 May 2011	65, 1	-20, 125	14, 16	18, 27	M
Puyehue	11 Jun 2011	-41	-71	13	23	G
Nabro	21 Jun 2011	13	41	18	406	M, G
Soputan, Marapi	20 Aug 2011	1, 0	125, 100	18, 16	9, 3	M, G
Manam, Tungurahua	19 Oct 2011	-4, -3	144, -78	16, 16	8, 8	M
Nyamuragira	18 Nov 2011	-2	29	16	31	M
Gamalama, Nyamuragira	18 Dec 2011	1, -1	128, 29	16, 15	19, 13	M
Vanuatu, Nyamuragira	12 Jan 2012	-16, -1	168, 29	16, 14	14, 12	M
Vanuatu, Nyamuragira	11 Feb 2012	-16, -1	168, 29	17, 17	16, 15	M
Nevado del Ruiz, Marapi	12 Mar 2012	-3, 0	-76, 100	16, 17	12, 15	M

Volcano or region	Time	Latitude (°)	Longitude (°)	Altitude (km)	SO_2 (kt)	Instrument
Nyamuragira, Mexico	7 Jun 2012	-1, 20	29, -95	16, 15	30, 4	O
Soputan, Nevado del Ruiz, Mexico	27 Aug 2012	1, 5, 20	124,-76,-95	16, 16, 15	30, 15, 5	O
Nyamuragira, Mexico, Peru	14 Oct 2012	-1, 20, -20	29, -95, -70	16, 16, 15	40, 15, 10	O
Nyamuragira, Paluweh, Nevado del Ruizz	7 Nov 2012	-1, -8, 5	29, 122, -76	15, 16, 17	20, 30, 17	O
Copahue, Lokon +	22 Dec 2012	-38, 1	-71, 125	15, 17	10, 45	O
Paluweh, Karkar	3 Feb 2013	-8, -5	122, 145	16, 17	25, 22	O
Karkar, Vanuatu (+?)	10 Mar 2013	-5, -16	145, 168	17, 16	24, 20	O
Rabaul, Nevado del Ruiz, Nyamuragira	18 Apr 2013	-3, 5, -1	150,-76, 29	17, 17, 16	40, 9, 20	O
Mayon, Turrialba, Pavlof	8 May 2013	13, 10, 55	124, -84,-162	17, 16, 14	35, 24, 6	O
Rabaul, Mexico	10 Jul 2013	-3, 20	150, -95	16, 15	30, 15	O
Pacaya	15 Aug 2013	15	-91	16	43	O
Sinabung, Ubinas	15 Sep 2013	3, -16	98, -71	17, 15	35, 8	O
Merapi, Nyamuragira, Pacaya	18 Nov 2013	-7, -1, 15	110, 29, -91	17, 17, 15	30, 13, 8	O
Sinabung, Nyamuragira	9 Dec 2013	3, -1	98, 29	17, 16	26, 15	O
Sinabung +	11 Jan 2014	3	98	16	29	O
Kelut	15 Feb 2014	-8	112	20	170	O
Merapi, Tungurahua	27 Mar 2014	-7, -1	110, -78	16, 16	31, 33	O
Santa Maria, Semeru	9 May 2014	15, -8	-91, 113	16	25, 39	O
Sangeaang-Api	31 May 2014	-8	119	17	60	O
Nyamuragira, Pavlof, Fuego, Dukono (Tungurahua)	9 Jul 2014	-1, 55, 14, 2	29,-162,-91, 128	16, 15, 15, 16	20, 10, 12, 20	O
Rabaul, Fuego	29 Aug 2014	-3, 14	150, -91	16, 16	36, 20	O
Nyamuragira	11 Sep 2014	-1	29	15	30	O
Ontakesan	27 Sep 2014	36	137	17	34	O
Sinabung, Turrialba	23 Oct 2014	3, 10	98, -84	17, 16	34, 17	O
Fogo, Semeru, Ubinas	24 Nov 2014	15, -8, -16	-24, 113, -71	17, 17, 16	11, 33, 11	O
Nevado del Ruiz, Nyamuragira, Vanuatu	16 Dec 2014	5, -1, -16	-76, 29, 168	15, 17, 16	8, 12, 21	O
Nyamuragira, Vanuatu, Honga Tonga	14 Jan 2015	-1, -16, -21	29, 168, -175	16, 16, 15	21, 17, 13	O
Vanuatu, Nyamuragira, Soputan	16 Feb 2015	-16, -1, 1	168, 29, 124	17, 16, 16	13, 13, 13	O
Soputan, Nevado del Ruiz, Santa Maria, Villarrica	8 Mar 2015	1, 5, 15, -39	125, -76, -91, -72	17, 16, 15, 15	14, 14, 8, 5	O
Tungurahua?, Batu Tara?	5 Apr 2015	-1, -8	-78, 124	17, 17	17, 22	O
Calbuco	25 Apr 2015	-41	-73	18	292	O
Manam, Tungurahua?	8 May 2015	-4, -1	144, -78	17, 17	24, 25	O
Wolf, Aira+Kuchinoerabujima	26 May 2015	0, 32, 30	-91, 131, 130	16, 15	63, 20	O
Raung	4 Jul 2015	-5	110	17	27	O
Cotopaxi, Raung, Suwanosjima, Manam	14 Aug 2015	0, -5, 30, -4	-80, 110, 130, 144	16, 16, 16, 20	24, 18, 10, 16	O
Nevado del Ruiz + Reventador, Fuego, Sum	21 Sep 2015	5, 14, 3	-76, -91, 98	16, 17, 16	13, 8, 19	O

Volcano or region	Time	Latitude (°)	Longitude (°)	Altitude (km)	SO_2 (kt)	Instrument
Sinabung, Fuego, Cotopaxi, Copahue	15 Oct 2015	3, 14, 0, -38	98, -91, -80, -71	16, 17, 15, 15	30, 15, 6, 13	O
Lascar, Sinabung, Nyamuragira, Fuego	30 Oct 2015	-23, 3, -1, 14	-70, 98, 29, -91	17, 17, 16, 16	13, 17, 12, 17	O
Vanuatu, Tungurahua, Telica, Rinjani	17 Nov 2015	-16, -1, 13, -5	168, -78, -87, 116	18, 17, 17, 16	18, 20, 10, 18	O
Vanuatu, Reventador, Tengger	5 Dec 2015	-16, 0, 2	168, -78, 120	17, 16, 16	16, 15, 12	O
Reventador, Sinabung	18 Dec 2015	0, 3	-78, 100	17, 16	16, 16	O
Soputan +, Reventador, Fuego	8 Jan 2016	1, 0, 14	125, -78, -91	16, 17, 14	25, 19, 5	O
Semeru, Fuego	10 Feb 2016	-8, 14	113, -91	17, 16	34, 25	O
Vanuatu +, Tungurahua	27 Feb 2016	-16, -1	168, -78	16, 16	24, 16	O
Tungurahua, Sinabung +, Pavlof	15 Mar 2016	-1, 3, 55	-78, 98, -162	16, 17, 15	23, 26, 7	O
Reventador, Sinabung +, Fuego, Aira	13 Apr 2016	0, 3, 14, 32	-78, 98, -91, 131	17, 16, 15, 15	18, 30, 17, 6	O
Fuego, Nyamuragira + Ecuador, Langila, Sinabung	7 May 2016	14, -1, -5, 3	-91, 29, 150, 98	16, 17, 16, 17	16, 18, 16, 26	O
Bulusan, Sinabung, Semeru, Mexico	10 Jun 2016	13, 3, 8, 15	125, 98, 113, -100	17, 16, 17, 16	16, 14, 16, 10	O
Rinjani, Sinabung, Santa Maria	1 Aug 2016	-5, 3, 15	116, 98, -91	16, 16, 16	10, 30, 24	O
Sinabung + Vanuatu, Fuego	28 Aug 2016	-16, 14	168, -91	16, 16	42, 23	O
Ubinas, Sinabung	3 Oct 2016	-16, 3	-71, 98	15, 16	16, 26	O
Sabancaya, Sinabung+Bulusan	5 Nov 2016	-16, 3	-72, 98	16, 16	38, 46	O
Dukono, Vanuatu, Sabancaya	12 Dec 2016	2, -16, -16	128, 168, -72	17, 18, 15	30, 28, 28	O
Sabancaya, Reventador, Sinabung + Vanuatu	10 Jan 2017	-16, 0, 3	-72, -78, 98	16, 17, 17	20, 30, 23	O
Sabancaya, Colima, Sinabung	4 Feb 2017	-16, 19, 3	-72, -104, 98	15, 16, 16	17, 15, 25	O
Sabancaya, Dukono, Fuego, Manam + Vanuatu, Bogoslof, Nevados de Chillán	5 Mar 2017	-16, 2, 14, -16, 53, -37	-72, 128, -91, 168, -170, -71	16, 17, 17, 17, 15, 15	10, 18, 8, 28, 4, 5	O
Sabancaya, Nevado del Ruiz, Sinabung, Vanuatu, Klyuchevskoy	10 Apr 2017	-16, 5, 3, -16, 56	-72, -75, 98, 168, 160	16, 16, 16, 16, 15	8, 15, 19, 17, 2	O
Sinabung, Manam, Fuego	5 May 2017	3, -4, 14	98, 145, -91	16, 17, 17	26, 10, 19	O
Sheveluch + Bogoslof	19 May 2017	57	161	15	20	O
Santa Maria, Sheveluch +, Manam	16 Jun 2017	15, 57, -4	-91, 161, 145	16, 16, 15	11, 33, 6	O
Fuego, Sinabung+, Sheveluch+	5 Jul 2017	14, 3, 57	-91, 98, 161	15, 16, 15	22, 21, 4	O
Sinabung, Cristobal + Fuego, Sheveluch + Bogoslof	8 Aug 2017	3, 13, 54	98, -87, -168	16, 17, 16 (26?)	31, 27, 5	O

Table 4.1: Inventory of volcanic SO_2 emissions into the stratosphere integrated above 14 km in low latitudes, 13 km in mid latitudes and 12 km in high latitudes. Derived from satellite data (2002-2012), by MIPAS **(M)** and updated on the basis of GOMOS **(G)** and TOMS/OMI **(T)**. Based on former studies from Brühl et al. (2018) with scaling factors for T63 and already published in an earlier version in Bingen et al. (2017). Extended with satellite data from SAGEII(V7.00) **(S)** back to 1990-2002, and from 2012-2017 by OSIRIS **(O)**.

4.2 Case Studies of Volcanic Eruptions

As each volcanic eruption is individual this section illustrates the variety of different kinds of volcanic eruptions, varying in strength, height and chemical composition. For this purpose some case studies, chosen from Table 4.1 and using multiple satellite data sets, are provided.

4.2.1 Pinatubo the Strongest Eruption of the last Century

The eruption on 15 June 1991 of Mount Pinatubo at the Philippines (15.1°N, 120.4°E) with a VEI of 6 was the strongest volcanic eruption of the last one hundred years (Figure 4.1). The mass of about 17 Tg to 20 Tg SO_2 was injected directly into the stratosphere (Guo et al., 2004; Bluth et al., 1992), with a maximum SO_2 mixing ratio of more than 100 parts per billion by volume (10^{-9}) (ppb$_v$) around 24 km to 26 km altitude (see Figure 4.6). The plume reached an estimated maximum altitude of about 39 km (Guo et al., 2004). The volcanic SO_2 cloud moved westwards from Southeast Asia over the Indian Ocean to Africa and surrounded the globe within a few weeks (see the SO_2 cloud images in Guo et al. (2004)).

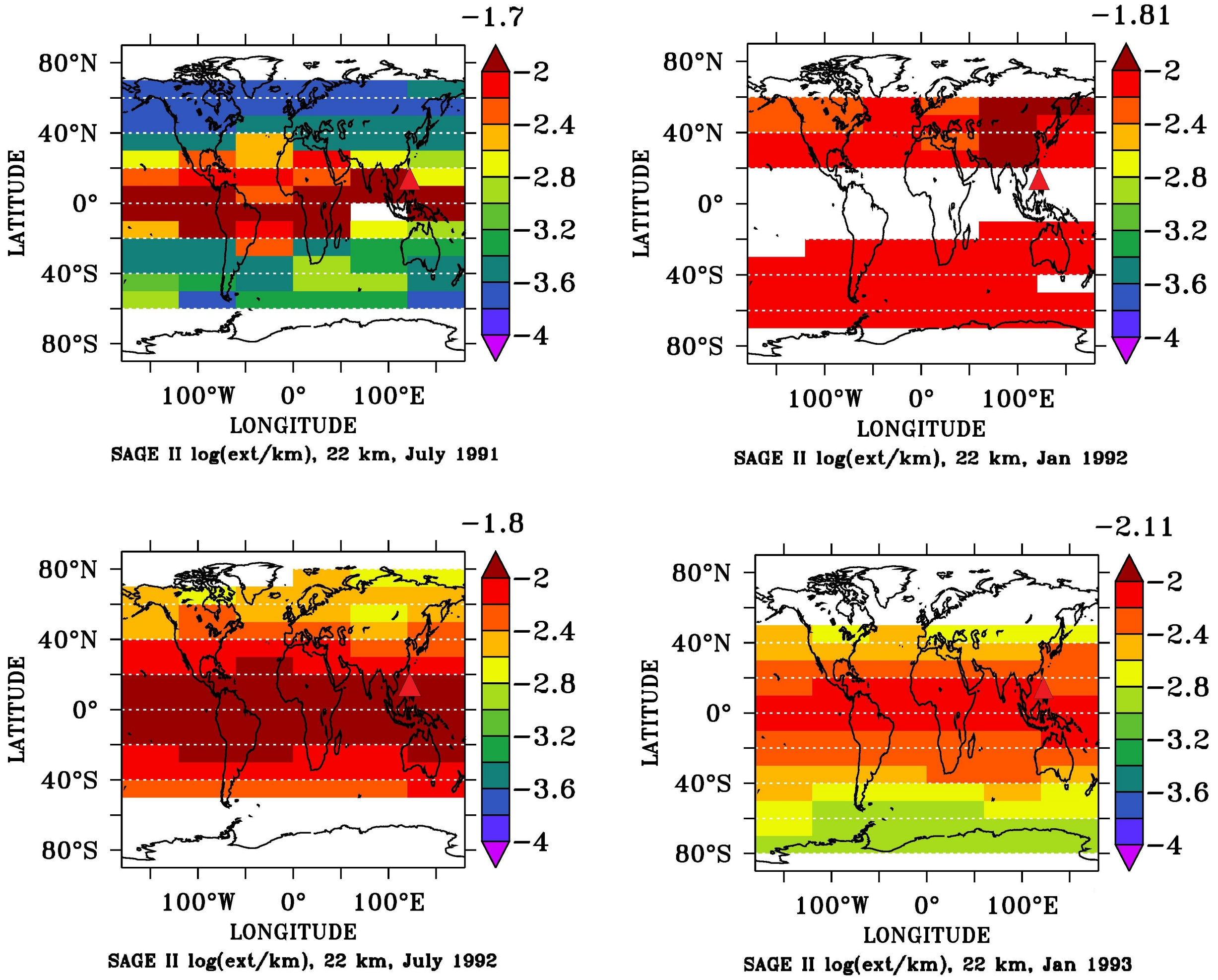

Figure 4.1: Logarithm of the aerosol extinction from satellite data of the SAGE II instrument at 22 km altitude, in July 1991, January 1992, July 1992 and January 1993. White: no data.

Further the SO_2 is oxidized into H_2SO_4 and transformed to sulfate aerosol (see chapter 6) and dominated the stratospheric aerosol burden for several years. As Figure 4.1 shows, the Pinatubo eruption globally covers all other events, even more than one and a half year after the eruption.

Vertical profiles of the aerosol extinction were measured by the SAGE II instrument (see subsection 3.2.1) (McCormick and Veiga, 1992). As the Pinatubo eruption is some orders of magnitude larger than all other volcanic events in the period under consideration, a logarithmic scale has to be chosen for analysis of e.g. the aerosol extinction (Figure 5.1). These high concentrations cause “saturation” effects in the SAGE II aerosol extinction profiles until June 1992 as seen in Figure 4.1 and Figure 3.2, which increases the uncertainty of measurements.

As the eruption took place in the tropics, the volcanic aerosol could spread above both hemispheres via the Brewer-Dobson Circulation (subsection 2.1.1). The volcanic aerosol caused an averaged cooling of about 0.2 °C to 0.3 °C in the troposphere (Gao et al., 2008). A plenty of detailed studies have been carried out (e.g. Timmreck et al., 1999; Brühl et al., 2015; Predybaylo et al., 2017) to analyze the effects on relevant chemical species like O_3, the radiative heating and large scale circulation changes on ENSO due to the enhanced radiative heating after such a large eruption.

4.2.2 Medium Eruptions direct into the Stratosphere

The SO_2 emissions of the eruption of Reventador in Ecuador on 3 November 2002 (VEI 4) are visible on MIPAS satellite images some days after the eruption. Entries in the Bulletin Reports of the Smithsonian Institution (`https://volcano.si.edu/` 18 December 2020) documented a column rose up to 16 - 17 km above the intracaldera cone. So the plume was injected directly into the stratosphere and was transported very fast by westerly winds from Ecuador to Africa and Indonesia. The Reventador is an example for an equatorial eruption with the typical distribution of the volcanic emissions in the tropical stratosphere. This plume is also visible on satellite images from GOMOS, SAGE II, OSIRIS, TOMS, and Atmospheric Infrared Sounder (AIRS). For the model simulations MIPAS-data of 5-day intervals centered on 10 and 15 November are used (Figure 4.2).

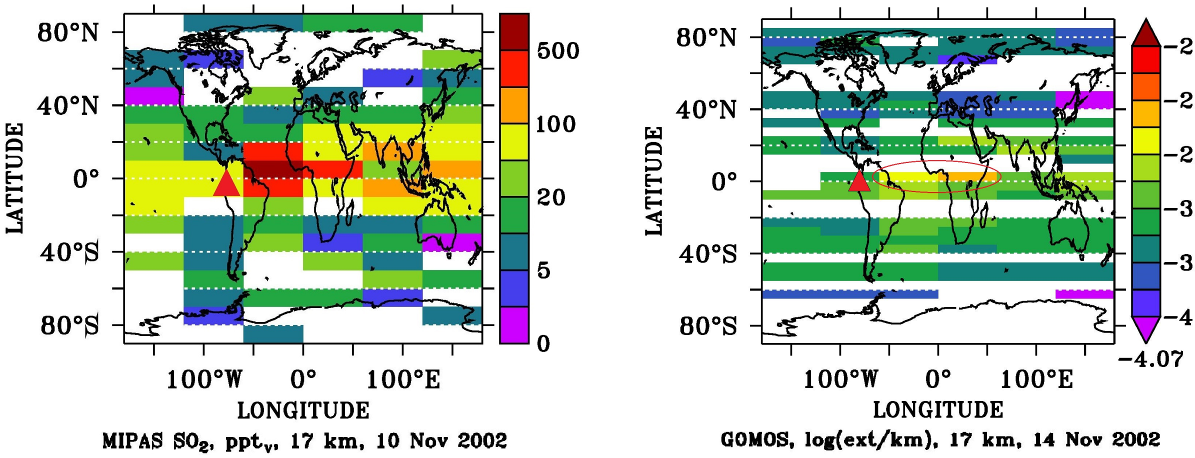

Figure 4.2: Satellite data of the eruption of Reventador in November 2002: (left) SO_2 ppt$_v$ from MIPAS instrument (Höpfner et al., 2015) at 17 km altitude and (right) the logarithm of the aerosol extinction from GOMOS v.3.00 instrument (Bingen et al., 2017) at 17 km altitude. White: no data.

4.2.3 Volcanic Eruptions in the Asian Summer Monsoon Circulation

One of the biggest eruptions in the last years (VEI4) was of the Nabro volcano in Eritrea near to the border with Ethiopia (Höpfner et al., 2015), which started in June 2011 (Figure 4.3 left). The total mass of SO_2 emissions is estimated to 3650 kt, with a injection of more than 400 kt SO_2 direct to the stratosphere with a maximum altitude of 18 km. Within two weeks the plume is drawn into the Asian summer monsoon circulation (Figure 4.3 right) (Fairlie et al., 2014). Due to this fast long range transport the stratospheric aerosol layer in the entire northern hemisphere was influenced for several months. This was also measured by Civil Aircraft for the Regular Investigation of the atmosphere Based on an Instrument Container (CARIBIC) (Martinsson et al., 2017) in the flight with the number LH365, flying from Frankfurt to Chennai crossing the monsoon area on 15 November 2011.

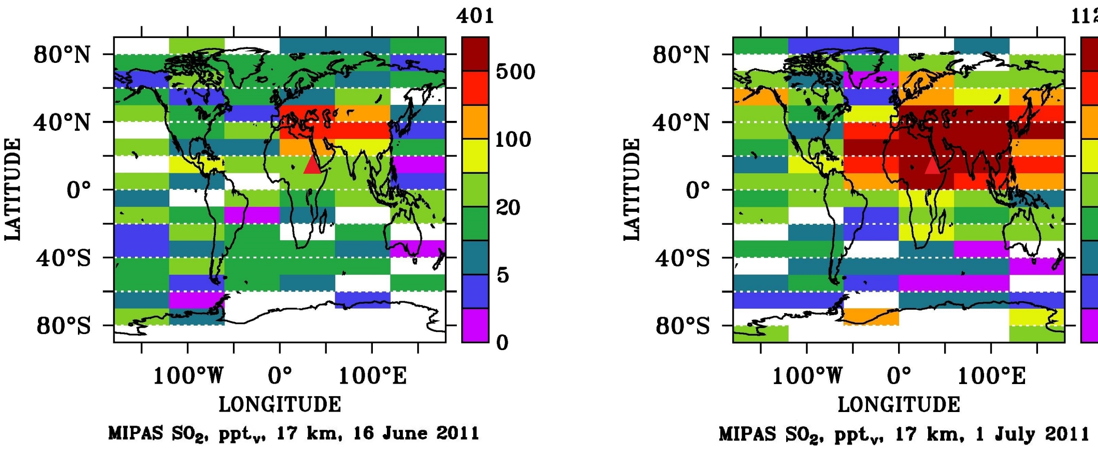

Figure 4.3: SO_2 mixing ratios (ppt_v) from satellite data of the MIPAS instrument (Höpfner et al., 2015) at 17 km altitude at the eruption of Nabro on 16 June 2011 (left) and 1 July 2011 (right). White: no data.

A second example is the Sinabung volcano on the island Sumatra. Its ongoing active period started in 2010 with observed eruptions with a maximum VEI of 4 including pyroclastic flows and ash plumes received from the Smithsonian volcanic data base (`https://volcano.si.edu/` 18 December 2020).

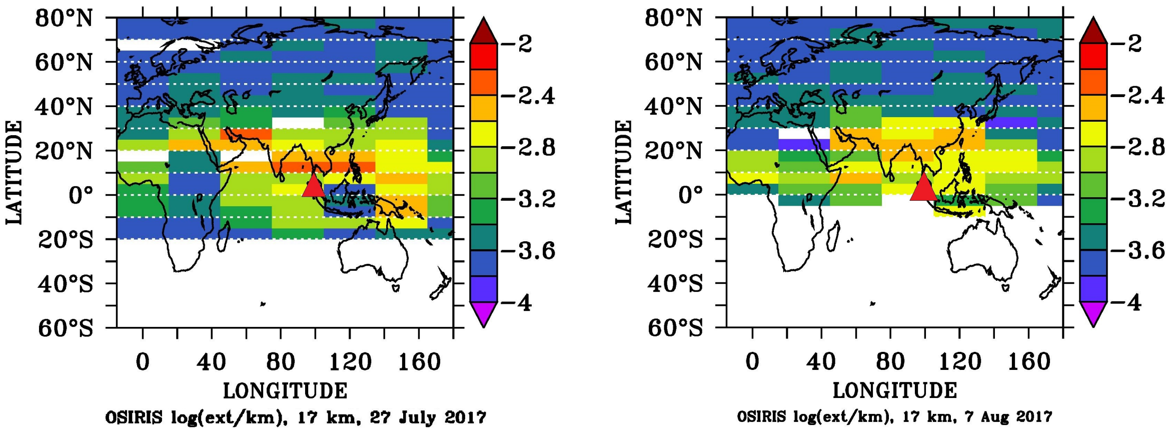

Figure 4.4: Aerosol extinction at 17 km altitude from the OSIRIS instrument of the eruption of Sinabung in July (left) and August 2017 (right). White: no data.

There was also an eruption series during the time of the StratoClim campaign in July and August 2017, which can be seen on the OSIRIS satellite data in Figure 4.4. Several plumes with total emission of 31 kt SO_2 reached the stratosphere (Table 4.1) by the strong convection of the Asian monsoon system and were spread over the whole south east Asia area by the monsoon circulation. This is also observed by the aircraft measurements of the StratoClim campaign (chapter 7).

4.2.4 Small Eruptions up to the Tropopause

The aim of this section is to present some illustration on how the use of the CCI-GOMOS data record could improve the detection of moderate volcanic eruptions in MIPAS data gaps, and the quantification of their sulfur emissions. The eruption of Piton de la Fournaise starting on 6 April 2007 was not visible in the MIPAS data on the date of the eruption, because of a data gap in this 5-day time interval. The next accessible data is the time interval on 13 April with a signal above Australia (Figure 4.5 left). Due to comparison with GOMOS data on 22 April (Figure 4.5 right), it is possible to identify the eruption of Piton de la Fournaise on a small island east of Madagascar, several thousand kilometers away from the MIPAS signal above Australia. This is confirmed by other satellite data of OMI and Global Ozone Monitoring Experiment–2 (GOME-2). Entries in the Bulletin Reports of the Smithsonian Institution documented a caldera collapse on 6 April and ongoing volcanic activity for one month. For the calculation an integral on three-time intervals 3, 13 and 18 April derived from the 3 dimensional MIPAS data sets is used.

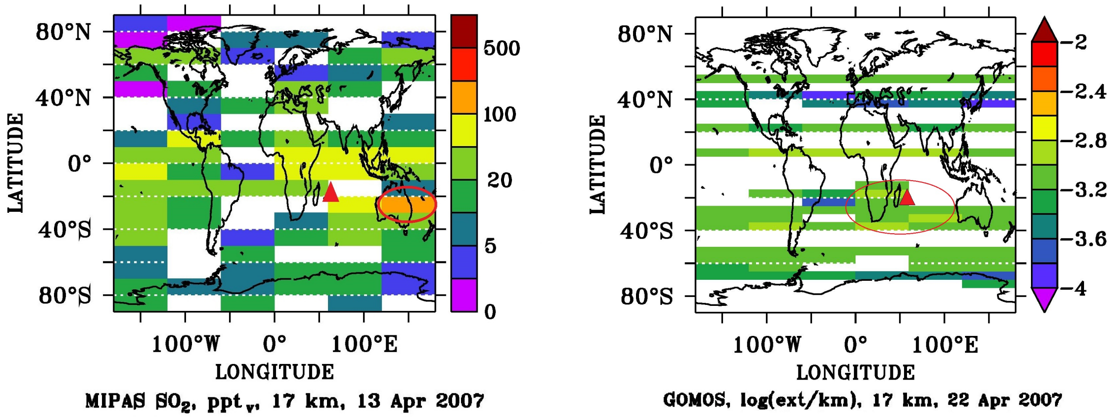

MIPAS SO_2, ppt$_v$, 17 km, 13 Apr 2007

GOMOS, log(ext/km), 17 km, 22 Apr 2007

Figure 4.5: Satellite data of the eruption of Piton de la Fournaise on 6 April 2007: (left) SO_2 in ppt$_v$ from MIPAS instrument (Höpfner et al., 2015) at 17 km altitude and (right) aerosol extinction from GOMOS v.3.00 instrument (Bingen et al., 2017) at 17 km altitude.

4.2.5 Strong Eruptions, without big Influence on the Stratosphere

Volcanic eruptions of Kilauea (Hawaii 19.42°N, 155.29°W) in April/May 2008 and Eyjafjallajökull (Island 63.63°N, 19.62°W) in March-May 2010 are not visible in satellite signals of MIPAS and GOMOS above an altitude of 12 km and don't have a significant influence on radiative forcing. The eruptions had small climatic effects as only a small fraction of the plume reached the stratosphere. CARIBIC measurements of Andersson et al. (2013) show that the proportion of SO_2 in the chemical composition of the Eyjafjallajökull emissions was very low, while big amounts of volcanic ash were emitted to the troposphere around 8 km altitude, which disturbed the air traffic over Europe.

4.3 Implementation of SO_2 from the Volcanic Sulfur Emission Inventory into the EMAC Model

After combining all these satellite data sets the SO_2 amount of each single volcanic eruption is calculated by integrating the vertical SO_2 profiles. Then the SO_2 plumes are implemented into the model simulations by adding the satellite derived 3-dimensional perturbations of SO_2 mixing ratios to the simulated SO_2 at the time of the eruptions. Every single volcanic eruption, even from the same volcano, is individual and can not be checked into the model automatically. Point sources are not used for implementing the SO_2 mixing ratios, to reduce additional errors caused by the low time resolution of the satellite data and to get the correct altitude distribution.

In addition effusive eruptions and quiescent degassing volcanoes from the monthly climatology of Diehl et al. (2012) are added to the tropospheric SO_2 background emissions of the model simulations and truncated at an altitude of 200 hPa to avoid double counting in the stratosphere and uppermost troposphere (Brühl et al., 2018).

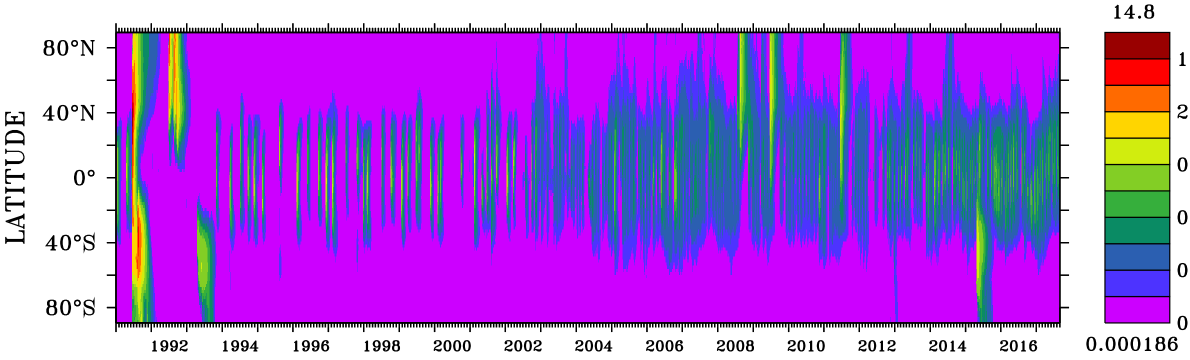

EMAC Simulations of SO_2 in ppb_v at 17 km 1991–2017

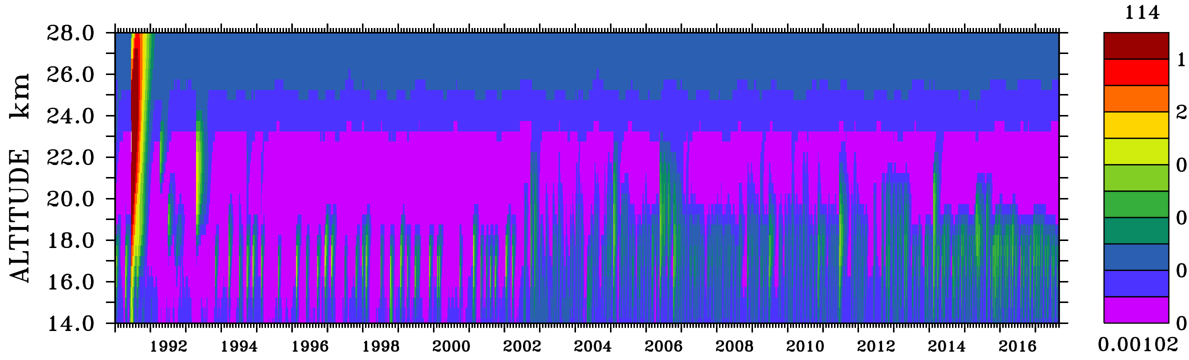

EMAC Simulations of SO_2 in ppb_v at 20°S–20°N 1991–2017

Figure 4.6: EMAC simulation of the stratospheric SO_2 mixing ratio (ppb_v) (January 1991 - August 2017) from the Volcanic Sulfur Emission Inventory (Table 4.1): in horizontal distribution T63 at 17 km altitude (top) and in vertical distribution for tropical regions 20°S - 20°N (bottom). Maximum and minimum values are written on top (dark red) and bottom (violet) of the color keys.

The SO_2 emissions of the Volcanic Sulfur Emission Inventory are implemented into the EMAC model simulations and shown in Figure 4.6, with mixing ratios between back ground conditions with a minimum of 0.001 ppb_v in volcanic quiet periods and a maximum of 114 ppb_v (indicated on the color key) after the Pinatubo eruption. In the Junge-aerosol layer typical mixing ratios of SO_2 are about 0.03 ppb_v. The volcanic eruptions in 1990 are implemented during the spin-up phase of the model simulations and are not shown here, whereby the emissions of the first entry in Table 4.1 are set to the upper limit. The low number of volcanic eruptions in 1991 and the following years is caused by a low coverage of satellite data and saturation effects of the satellite instrument. The signals of medium and small volcanic eruptions are too weak to be seen in front of the high concentrations in the first years after the Pinatubo eruption. After 2002 the frequency of small volcanic eruptions is increasing in the Volcanic Sulfur Emission Inventory. This effect is rather caused by improved data coverage of more satellite instruments, than by a higher volcanic activity.

Thomason and Peter (2006) show that the transport barrier of the “leaky tropical pipe” leads to build-up of a tropical reservoir of the sulfate aerosol mass after a volcanic eruption. Most times the stratospheric SO_2 mixing ratio is highest at tropical latitudes, for this reason tropical regions from 20°S - 20°N are chosen for the vertical distribution in the bottom illustration of Figure 4.6 and following figures. Exceptions to this are single strong volcanic eruptions in high latitudes like Kasatochi (2008) and Sarychev (2009) in the northern hemisphere or Calbuco (2015) in the southern hemisphere. Another special case is the Nabro (2011) eruption (subsection 4.2.2), where the volcanic emissions were transported from the tropics to northern latitudes by the Asian Monsoon Circulation.

Small- and medium-strength volcano eruptions derived from MIPAS and the Smithsonian database typically inject SO_2 in the order of 10 kt to 50 kt (Table 4.1) directly to the UTLS region or transport it indirectly via convection or advection. MIPAS typically observes background SO_2 mixing ratios in the lowermost tropical stratosphere at 16 km to 17 km around 0.02 ppb_v to 0.05 ppb_v (Figure 3.5), which can be simulated only if many more volcanoes are considered than listed in the NASA SO_2 database (Brühl et al., 2015). There can also be identified some time periods between 2000 to 2004 with low volcanic activity resulting in stratospheric background conditions. To reach realistic SO_2 mixing ratios in the lower tropical stratosphere during these time periods, the oxidation of DMS and other sulfur species is needed in the New Sulfur Chemistry Mechanism in chapter 6. The lower panel of Figure 4.6 shows increasing SO_2 with altitude in the upper stratosphere by photolysis of gaseous H_2SO_4 and a secondary maximum above 26 km due to additional OCS photolysis. These are also included in the New Sulfur Chemistry Mechanism and confirm to the simulations and observations in Brühl et al. (2015).

The comparison of the simulated and observed SO_2 shows, that the Volcanic SO_2 emissions from the Volcanic Sulfur Emission Inventory in Table 4.1 are correlating well with the peaks of the mixing ratios in Figure 4.6, as they dominate the stratospheric sulfur burden.

In the stratosphere the SO_2 is converted to sulfate aerosol (chapter 6) and explains most of the interannual variability of stratospheric aerosol burden with its influence on the stratospheric radiation (as shown in chapter 5). Normally the conversion from SO_2 to sulfate aerosol particles takes about two weeks in the UTLS, and about two months in middle and lower stratosphere, enhanced SO_2 stays in mesosphere for years (Brühl et al., 2015). This has to be considered when comparing the MIPAS data with other satellite instruments like GOMOS based on the aerosol extinction. Even after big eruptions like Pinatubo with large amounts of SO_2, most of it is converted to aerosol particles within a few months.

4.4 Discussion of the Implementation of Volcanic Emissions

The result of this study is an improved Volcanic Sulfur Emission Inventory as part in the framework of the Aerosol_CCI project (an older version is already published in Bingen et al. (2017)). The new version is listing almost 500 explosive volcanic eruptions with about 80 eruptions in the first time period between 1990 - 2002 by the SAGE instrument, 240 eruptions in 2002 - 2012 with multiple instruments and 170 eruptions in the last time period between 2012 - 2017 by OSIRIS. Older versions of the Volcanic Sulfur Emission Inventory were not sufficient to assess the real volcanic contribution to the radiative forcing of the atmosphere due to lack of data and span only a period from 2002 - 2012.

Additional actualized 3 dimensional data sets with a better time resolution than monthly of the MIPAS and GOMOS instruments are available. So the time resolution is now 5 days for both instruments and it is possible to identify a number of multiple volcanic eruptions in a short time period now. With the 3 dimensional data sets the differences between the single levels in altitude can be distinguished and the sulfur amount reaching the stratosphere can be calculated much better than by estimation of a total column. To exclude tropospheric emissions and signals from high altitude clouds the integration is set above an altitude of 12 km in high latitudes, 13 km in mid latitudes and 14 km in low latitudes.

Strong volcanic eruptions can inject several teragrams of SO_2 direct into the stratosphere. For this reason the maxima of the global stratospheric SO_2 concentrations are correlating very well with the eruption events of the Volcanic Sulfur Emission Inventory in Table 4.1.

The SO_2 emissions of smaller volcanic eruptions can reach the lower stratosphere by convective transport through the tropopause which results in accumulation of sulfate aerosol in the lower stratosphere. This turned out as essential in volcanic quiescent periods.

The SO_2 values in Table 4.1 are optimized for the model parametrizations in the model resolution T63L90 with a horizontal grid of $1.87° \times 1.87°$ and have to be modified, if using a different model resolution of Table 3.1. Since the convection parametrization of the model was developed for the higher resolution T63L90, the agreement with the satellite observations (section 3.2) is now much better than with the lower resolution T42L90 (Brühl et al., 2018), especially at midlatitudes and in the subtropics.

This study shows how important it is to use multi-instrument satellite data sets to fill data gaps and to detect as many volcanic eruptions as possible, which was best in the time period from 2002 to 2012 with the MIPAS, GOMOS and OSIRIS instruments. The uncertainty is larger in the time period before 2002, as there is only one instrument, SAGE in operation with much more data gaps, as you can see in Figure 4.6. The same after 2012 with the OSIRIS instrument. In any case there are still remaining data gaps and noise in some satellite data sets. Especially over South America and the South Atlantic disturbances are correlated to the South Atlantic Anomaly of the earth's magnetic field (Vernier et al., 2011a). Subsequently, satellite signals have larger uncertainties and some volcanic emissions from the Andes in South America might not be detected in this region.

Brühl et al. (2015) shows, that the observed SO_2 distribution at 40 km altitude can only be reproduced when account for a sulfur sink on meteoric dust (subsection 2.3.4), which is still not implemented in the EMAC model so far and leads to a strong overestimate of SO_2 during high latitude winter.

Chapter 5

Climate Impact of Stratospheric Aerosol in EMAC Model Simulations

In this chapter the global influence of sulfate emissions on different atmospheric optical parameters are compared. With the new data set of the OSIRIS instrument the time line of simulations is extended from 2012 to 2017. So the simulations are 26 years long, including the data from the Volcanic Sulfur Emission Inventory in Table 4.1. The following model simulations for the stratospheric aerosol are performed with the global Chemistry Climate Model EMAC at T63L90 resolution, which corresponds to a grid of approximately 1.87° × 1.87°, *in latitude and longitude and 90 vertical hybrid pressure levels up to 0,01 hPa (about 80 km), as described in section 3.1. The* SO_2 *mixing ratios of the Volcanic Sulfur Emission Inventory are oxidized to* H_2SO_4 *by several chemical reactions in the chemistry submodel CAABA/MECCA (see chapter 6). Further it is transformed to sulfate aerosol particles by the parametrizations of the aerosol microphysics in the GMXe submodel. Based on Mie-theory-lookup tables different optical properties like optical depths, single scattering albedos and asymmetry factors, which are used in radiative transfer calculations, are calculated online for the aerosol types sulfate, dust, organic carbon and black carbon, sea salt, and aerosol water. Via multiple calls of the radiation module RAD the influence of stratospheric aerosol on instantaneous radiative forcing and heating is computed online, also the feedback to atmospheric dynamics is included.*

5.1 EMAC Model Simulations of the Stratospheric Aerosol Extinction

The extinction describes the reduction of radiation by the effects of reflection and absorption through stratospheric aerosol particles and is wavelength dependent (see section 2.5). It is calculated by the submodel AEROPT, depending on the optical properties and the number of aerosol particles. Figure 5.1 and Figure 5.2 show the timeline from 1991 to 2017 of this global stratospheric aerosol extinction (in decadal logarithm) at 550 nm and 750 nm wavelength of the EMAC model simulations at 17 km altitude and in vertical distribution for tropical regions for 20°S - 20°N. For medium eruptions the maximum of the aerosol extinction is at an altitude between 16 km to 18 km. For this reason an altitude of 17 km is chosen in the following analyses.

The EMAC model simulations of the aerosol extinction at 550 nm wavelength (Figure 5.1) agree well with the satellite measurements of GOMOS (Figure 3.3) and SAGE II (Figure 3.2) for the aerosol layer in 16 – 22 km altitude where measured extinction values exceed ≈2×10^{-4} km^{-1}. The strongest event in these model simulations is the Pinatubo (Table 4.1) eruption in 1991. It dominates the stratospheric aerosol extinction for more than 1 year after the eruption with a global distribution from the equator to the poles in both hemispheres and a maximum altitude of more than 26 km. All other eruptions are significantly smaller, for this reason a logarithmic scale is chosen.

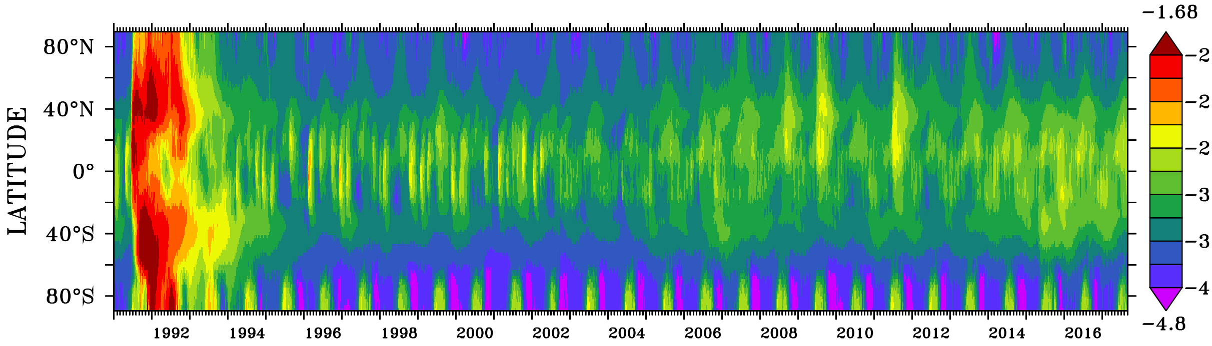

EMAC Simulations of aerosol extinction at 550 nm, 17 km

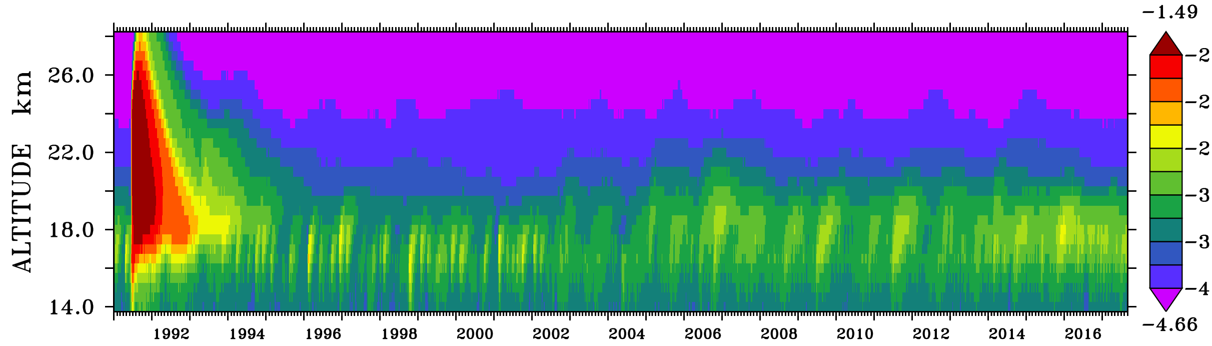

EMAC Simulations of aerosol extinction at 550 nm, 20°S−20°N

Figure 5.1: EMAC simulation of the stratospheric aerosol extinction in logarithmic scale log(1/km) for 550 nm wavelength from January 1991 - August 2017 based on the Volcanic Sulfur Emission Inventory (Table 4.1): in horizontal T63 distribution of zonal mean at 17 km altitude (top) and in vertical distribution for tropical regions 20°S - 20°N (bottom). Maximum and minimum values are written on top (dark red) and bottom (violet) of the color keys.

The model simulations of the aerosol extinction at 750 nm wavelength are required for the comparison to GOMOS (Figure 3.4) and OSIRIS (Figure 3.6). Both figures show a similar distribution of the aerosol extinction at 550 nm and 750 nm wavelength. Due to the wavelength dependency the aerosol extinction is generally higher at 550 nm wavelength.

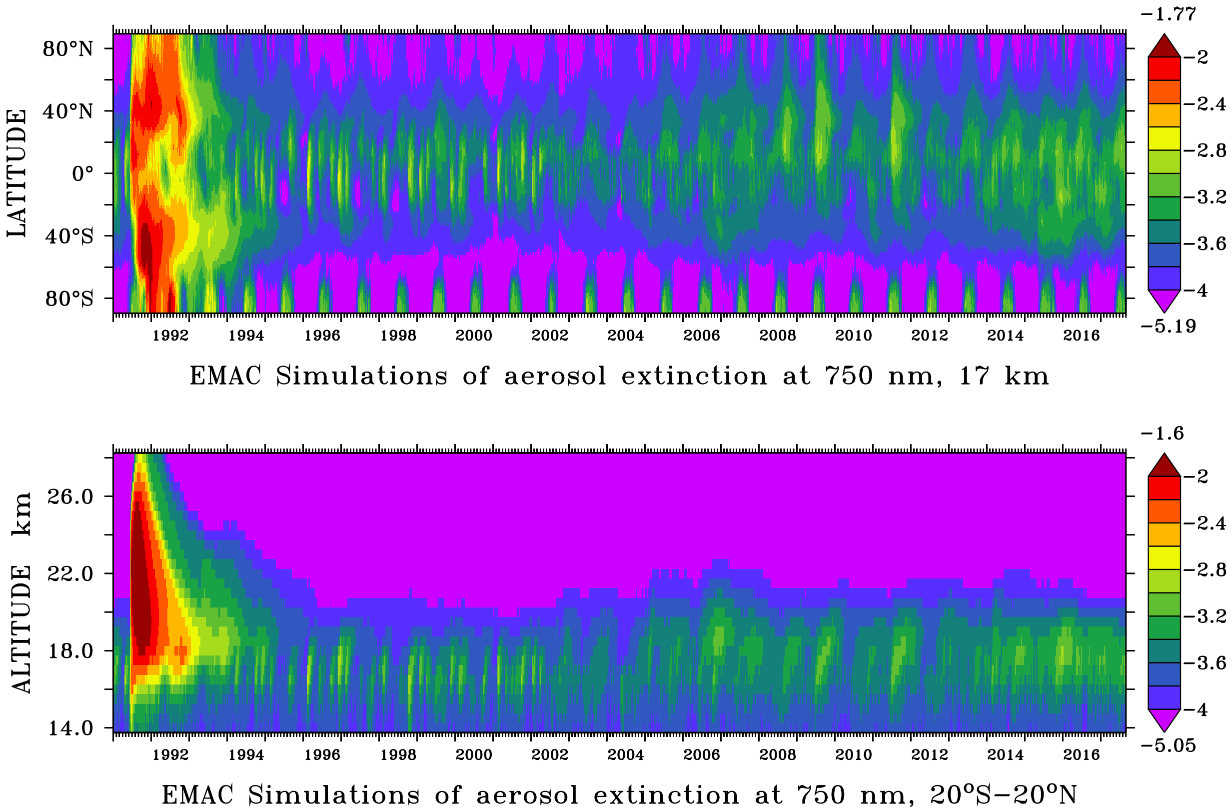

EMAC Simulations of aerosol extinction at 750 nm, 17 km

EMAC Simulations of aerosol extinction at 750 nm, 20°S−20°N

Figure 5.2: EMAC simulation of the stratospheric aerosol extinction in logarithmic scale log(1/km) for 750 nm wavelength from January 1991 - August 2017 based on the Volcanic Sulfur Emission Inventory (Table 4.1): in horizontal T63 distribution of zonal mean at 17 km altitude (top) and in vertical distribution for tropical regions 20°S - 20°N (bottom). Maximum and minimum values are written on top (dark red) and bottom (violet) of the color keys.

The seasonal changes between higher values and minimum values in antarctic regions are not caused by volcanic activity (e. g. Mount Erebus) in Antarctica. The model can also calculate the formation of PSCs in the winter hemisphere and reproduces an increased aerosol extinction in the stratosphere. This effect is stronger in the southern hemisphere than in the northern hemisphere, where the temperature has to drop below -78 °C (195 K).

The gradients between the individual eruptions are less sharp than with direct SO_2 emissions in Figure 4.6, since the conversion to sulfate aerosol takes about two weeks and the subsequent lifetime of the sulfate aerosol particles can take several months to a few years. In addition, there is a permanent background concentration of the stratospheric Junge-aerosol layer, which also consists partly of desert dust and organic carbon aerosols (Brühl et al., 2018).

From a height of 30 km to 35 km, the liquid sulfur aerosol particles evaporate and form a source for the secondary SO_2 maximum at this height in section 4.3. In the model, the aerosol extinction at a height of 35 km to 40 km is too low, since meteoric dust is not implemented in the model, which would otherwise act as a condensation nuclei for aerosol particles (see subsection 2.3.4).

5.2 EMAC Model Simulations comparing the Aerosol Optical Depth (AOD)

The total stratospheric Aerosol Optical Depth (AOD) is determined by the vertical integral of the aerosol extinction above an altitude of about 16 km (for midlatitudes above about 14 km). The stratospheric AOD is shown on a logarithmic scale in Figure 5.3 - Figure 5.4 with the new model simulations (red and pink lines) compared to satellite observations (lightblue, green, and blue lines). In contrast to most other studies, the stratospheric AOD is compared at the original wavelengths derived from different optical channels of the satellite instruments measurements. This avoids additional errors by conversion factors between the different wavelengths.

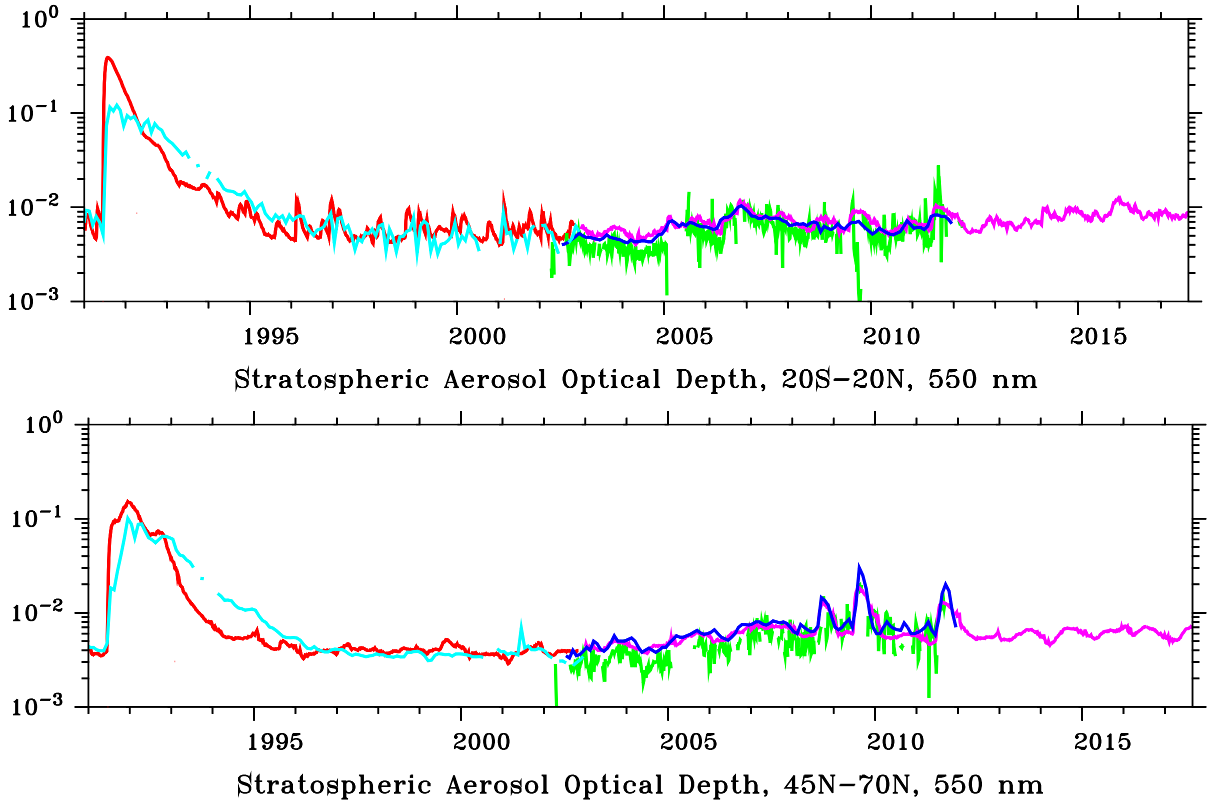

Figure 5.3: The stratospheric Aerosol Optical Depth (AOD) at 550 nm wavelength above 185 hPa for tropical regions 20°S - 20°N is shown on the top and for the northern hemisphere 45°N - 70°N at the bottom. Satellite observations from SAGE II (Thomason et al., 2008) are indicated by the lightblue line, GOMOS (Robert et al., 2016) by the green line, and values derived from SAGE+CALIPSO (upper figure) (Santer et al., 2014) and SAGE+OSIRIS (lower figure) (Glantz et al., 2014) by the blue line. The red and pink lines show the EMAC model simulations using the SO_2 injections of Table 4.1.

From 1991 to 2012 SAGE II (lightblue line), GOMOS (green line) and SAGE+CALIPSO and SAGE+OSIRIS (blue line) provide satellite data at a wavelength of 550 nm (OSIRIS data are converted from 750 nm) (Figure 5.3). The maximum is reached after the Pinatubo eruption with 0.4 stratospheric AOD, which is a magnitude stronger, than the following medium eruption with a stratospheric AOD of about 0.01. The differences after the large Pinatubo eruption in 1991 between the model simulations and the SAGE II observations are caused by “saturation” effects of the satellite instrument and can be observed for more than 1 year, which is also shown above in

Figure 3.2. Between 1993 and 1996 the reduction of the stratospheric AOD in the model simulations is faster than in the satellite observations. This indicates on the one hand that the removal process of the stratospheric aerosol is still too fast in the model and on the other hand the missing of smaller volcanic eruptions, as seen in chapter 4 by the low number of identified events in the years after the Pinatubo eruption.

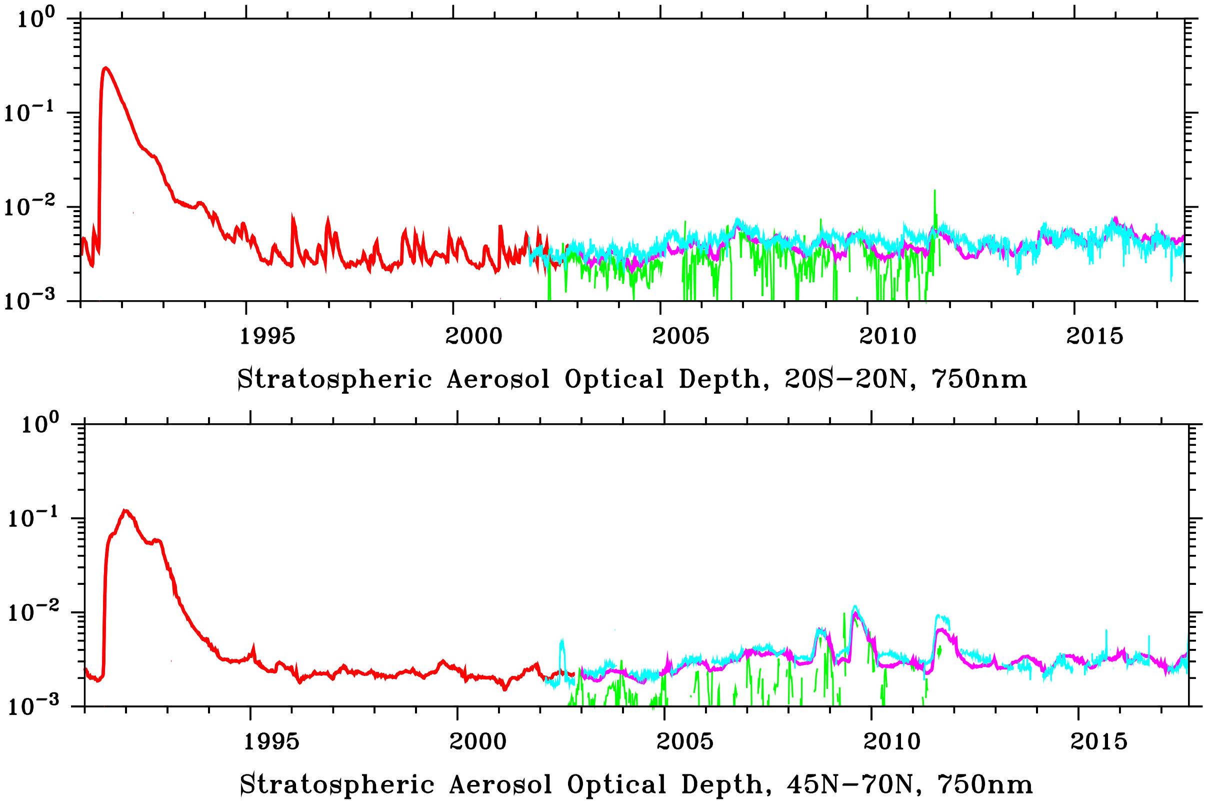

Figure 5.4: The stratospheric Aerosol Optical Depth (AOD) at 750 nm wavelength above 185 hPa for tropical regions 20°S - 20°N is shown on the top and for the northern hemisphere 45°N - 70°N at the bottom. Satellite observations from OSIRIS (Bourassa et al., 2018) are indicated by the lightblue line and GOMOS (Robert et al., 2016) by the green line. The red and pink lines show the EMAC model simulations using the SO_2 injections of Table 4.1.

In Figure 5.4 the coverage of GOMOS (green line) is often too low at a wavelength of 750 nm for the years from 2002 to 2012, so the inclusion of OSIRIS data (lightblue line) is important (Brühl et al., 2018). For the years after 2012 only the data from OSIRIS at 750 nm wavelength are remaining to continue the timeline.

The different distribution of the peaks in the upper and the lower figures depends on the latitude of the volcanic eruptions. If there is a strong eruption in the tropics the emissions reaching the stratosphere are distributed by the Brewer-Dobson circulation over the northern and southern hemisphere even to high latitudes like Soufriere Hills and Rabaul in 2006. But if an eruption takes place in high latitudes (Redoubt 2009) or mid latitudes like Kasatochi (2008) or Sarychev (2009) most of the emissions stay in the northern hemisphere and the signal in the tropics is weaker. One exception is the Nabro (2011) eruption at 13°N where most of the emissions were transported to higher northern latitudes due to influence of the Asian monsoon circulation.

5.3 EMAC Model Simulations comparing the Radiative Forcing at the Tropopause

The AOD has a direct influence on the radiative forcing of the stratospheric aerosol, which is calculated by multiple calls of the RAD submodel. The simulated global negative radiative forcing in Wm^{-2} of stratospheric aerosol at the tropopause is illustrated in Figure 5.5.

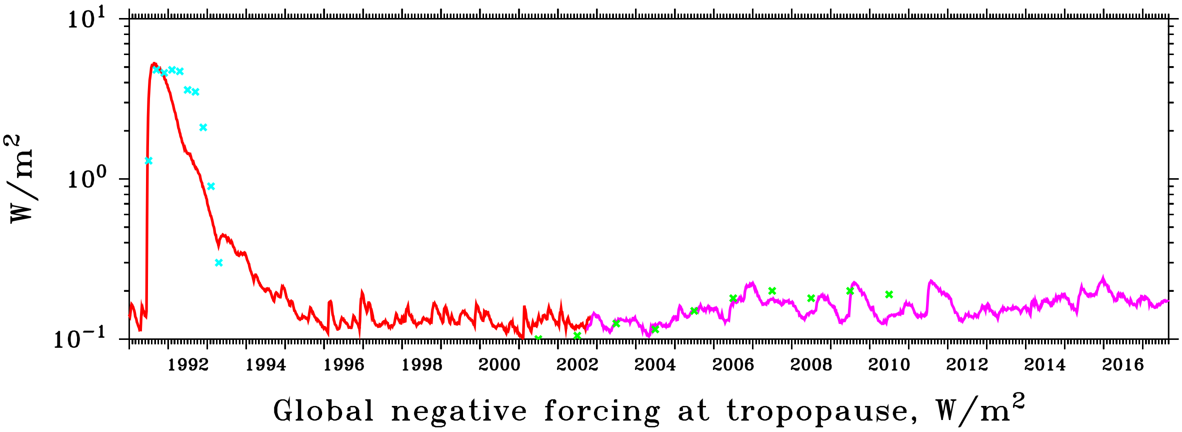

Figure 5.5: Global negative radiative forcing at the tropopause (185 hPa, solar + IR) by stratospheric aerosol. Estimated averages from satellite observations of the Earth Radiation Budget Experiment (ERBE) (Wong et al., 2006) are indicated by lightblue crosses and annual averages from observations by Solomon et al. (2011) as green crosses. The EMAC model simulations with volcanic SO_2 are represented by the red and pink lines.

As the Pinatubo eruption causes a negative radiative forcing of more than a magnitude stronger than the rest of the time line, the y-axis is plotted in inverted logarithmic scale, for instance 10^0 is equal to -1.0 Wm^{-2}. The new model simulations with the additional volcanic eruptions (red and pink lines) are closer to the calculated estimates from satellite extinction measurements of SAGE, GOMOS and Cloud-Aerosol Lidar with Orthogonal Polarization (CALIOP) by Solomon et al. (2011) (green crosses) then in older studies like Brühl et al. (2015). This shows that even medium and small volcanic eruptions can reach the stratosphere and have a relevant influence on the global radiative forcing at the tropopause. Concerning global negative radiative forcing, the volcanoes are the dominating effect with up to 0.13 Wm^{-2} for Rabaul and Nabro compared to the volcanically quiet period in 2002. Nevertheless there are remaining small differences between the model simulation and the observations like in 2010, which still indicate some missing volcanic eruptions. The strongest negative global radiative forcing in the model simulations is caused by the Pinatubo eruption with a maximum of about -5 Wm^{-2}, this is in good agreement with the results of Minnis et al. (1993). However the same effect can be seen in Figure 5.5 as in Figure 5.3, that the maximum of the global negative radiative forcing drops again too quickly after the Pinatubo eruption. On the one hand the sedimentation by large particles, caused by a too large fraction in the coarse mode, has been overestimated for the Pinatubo case, even though the boundary between the accumulation and coarse modes in the aerosol module GMXe was already shifted from a diameter of 2.0 µm to 3.2 µm (Brühl et al., 2015). On the other hand there are missing volcanic eruptions in the Volcanic Sulfur Emission Inventory as the signal of smaller eruptions is still covered up by the Pinatubo signal and the satellite coverage is low before 2002.

5.4 EMAC Model Simulations of the Stratospheric Aerosol Radiative Heating

The absorption of solar and infrared radiation by aerosol particles leads to local heating effects in the stratospheric aerosol layer. The simulated aerosol radiative heating in the model is derived from multiple radiation calls with and without aerosol in the radiation submodel RAD. This requires an adjustment of the model setting for volcanic eruptions as described in section 3.1.3. The aerosol formation is calculated by the GMXe submodel while the aerosol optical properties are calculated by the AEROPT submodel.

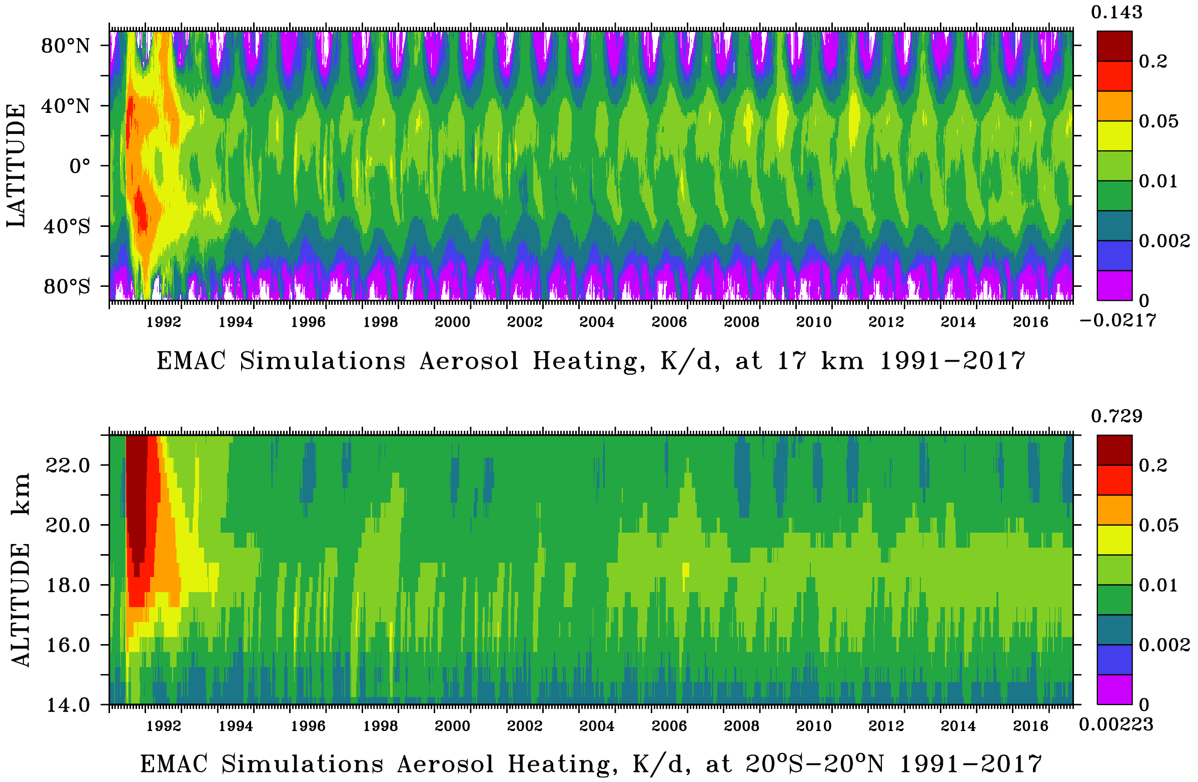
EMAC Simulations Aerosol Heating, K/d, at 17 km 1991–2017

EMAC Simulations Aerosol Heating, K/d, at 20°S–20°N 1991–2017

Figure 5.6: EMAC simulation of the aerosol radiative heating in K/day for solar and infrared radiation from January 1991 - August 2017 based on the Volcanic Sulfur Emission Inventory (Table 4.1): in horizontal distribution at 17 km altitude (top) and in vertical distribution for tropical regions 20°S - 20°N (bottom).

Figure 5.6 shows the local heating effects in the stratospheric aerosol layer. Small and medium volcanic eruptions have the largest effects in 17 km to 18 km altitude and generate a heating of up to 0.02 K/day. Whereas the Pinatubo eruption has significantly stronger effects in 20 km to 25 km altitude and causes a heating of more than 0.7 K/day, which is 35 times lager than all other eruptions in the model simulations. After such a strong volcanic eruption the enhanced radiative heating gives a dynamic response on the circulation, influences the global spread of the volcanic cloud and leads to an upward transport of the aerosol itself as well as of other chemical tracers (Timmreck et al., 1999). Further a seasonal signal contributes significantly to the radiative heating in the northern subtropics. This is caused by transport of desert dust to the UTLS mostly via the Asian summer monsoon convection, and generate additional heating at the time of the Asian summer monsoon (also in Brühl et al. (2018)).

5.5 Discussion of the Model Simulations of Stratospheric Aerosol

This section confirms how important the improvement of the Volcanic Sulfur Emissions Inventory is for the modeling of the radiative effects by stratospheric aerosols and contributes to the framework of the Aerosol_CCI project. The new model simulations demonstrate that volcanic emissions have a dominating impact on the stratospheric aerosol burden and explain most of the interannual variability of the stratospheric aerosol extinction. They have a large impact on the stratospheric aerosol forcing and heating, which influence the climate and the global circulation for a few years after big volcanic eruptions.

Compared to former studies by Brühl et al. (2015, 2018) and Bingen et al. (2017) the horizontal resolution in these new model simulations is improved from T42L90 to T63L90 with a horizontal grid of 1.87° × 1.87°. As the convection parametrization of the model has been developed for this higher T63 resolution also the stratospheric aerosol, especially at midlatitudes and in the subtropics, agree better with the satellite observations than before. Subsequently of the newly available satellite data, the time series could be extended in both directions to 26 years and now covers the years 1991 to 2017. The biggest differences between the new model simulations in this thesis and former studies by Brühl et al. (2015) are in the years 2002 to 2004 and in 2006/2007. This is in the time period of the data gaps in the old MIPAS data set. With the newly available data from the GOMOS and MIPAS instruments these data gaps can be compensated by including every single SO_2 emission file from the Volcanic Sulfur Emission Inventory in Table 4.1. The results of these new simulations close the gaps of missing and underestimated volcanic eruptions, which caused the significant discrepancies in the radiative forcing in former studies of Brühl et al. (2015) and Bingen et al. (2017) compared to the estimates from observations by Solomon et al. (2011).

Comparing the model results with OSIRIS data in the northern tropics Figure 5.4 indicates that some volcanic events are still underestimated or missing in the Volcanic Sulfur Emission Inventory in the year 2010. This would also explain the differences between the model simulations and satellite observations, indicated by green crosses in Figure 5.5 of the radiative forcing in this year.

Moreover it can be seen that the model setup has still to be improved to slow down the removal processes of stratospheric aerosol after big volcanic eruptions. Even so this has already been attempted by adapting the borders of the aerosol accumulation mode for volcanic conditions.

In any case the results from the IPCC (2013) report are confirmed, that a frequency of volcanic eruptions with moderate and small intensity, injecting sulfur gases to the upper troposphere and lower stratosphere, contribute significantly to the stratosphere aerosol layer by accumulation and causes an negative radiative forcing of 0.11 (0.15 to 0.08) Wm^{-2} at the surface. In particular this shows, that also medium volcanic eruptions can contribute to a slowdown of global warming.

The model also includes mineral dust and organics from the troposphere transported up to the UTLS layer. The aged dust aerosol in the UTLS region of the Asian monsoon causes a seasonal signal in the stratospheric AOD confirmed by satellite data (Klingmüller et al., 2018). Simulations of volcanic ash are not included in the model. For these additional satellite data of Cloud-Aerosol Lidar and Infrared Pathfinder Satellite Observations (CALIPSO) are required to distinguish aspherical ash particles from spherical sulfate particles (Vernier et al., 2016) as well as modifications in GMXe and AEROPT. For the background concentrations without volcanic activity, the formation of aerosol from different sulfur species is considered in the next chapter 6.

Chapter 6

Sulfur Chemistry

Even during volcanically quiescent periods there is an aerosol layer in the lower stratosphere present. These aerosol particle droplets mostly consist of a binary H_2SO_4/H_2O *solution and develop by microphysical processes from sulfur-containing gases. For analyzing these processes a comprehensive New Sulfur Chemistry Mechanism is developed and implemented into CAABA/MECCA the chemistry module of the EMAC model. The aerosol particles and their optical properties in these model simulations are calculated from precursor gases and emissions, instead of using prescribed climatologies. As there is still a missing source for OCS in literature (see section 2.3.1), the aim of this sensitivity study is to proof the postulate by Lennartz et al. (2017), if the production of OCS by chemical oxidation from DMS and* CS_2 *is significant.*

As these processes are very complex and non-linear, this chapter evaluates the sulfur chemistry in several steps. At first in section 6.1 additional sulfur emissions are added to the model, followed by a newly developed comprehensive Sulfur Chemistry Mechanism (section 6.2), including short lived intermediate radicals which are implemented into the CAABA/MECCA submodel. The differences between the Sulfur Chemistry Mechanisms are analyzed in section 6.3 for DMS, OCS, MSA, and SO_2*. The simulations are carried out at the time of the StratoClim campaign in 2017 to evaluate the different model setups with the campaign data in chapter 7. A preliminary version of the comprehensive New Sulfur Chemistry Mechanism has already been included in the MESSy version 2.54. The final Sulfur Chemistry Mechanism will be available for all EMAC members in a future version of MESSy.*

6.1 Implementation of Sulfur Emissions

Many databases have been used for the implementation of the sulfur containing emissions into the EMAC model. Background concentrations of SO_2 are added via OFFEMIS (section 3.1.3) to the troposphere from the monthly climatology of Diehl et al. (2012) to include the emissions of degassing volcanoes. These are truncated above an altitude of 200 hPa to avoid double counting in the stratosphere with the input from the Volcanic Sulfur Emission Inventory in chapter 4.

The sulfur source gas OCS is imported by the submodel TNUDGE from observed monthly zonal average surface volume mixing ratios (update of the data by Montzka et al. (2007)). Marine DMS is inserted into the model emissions as a natural sulfur source with the AIRSEA module by Pozzer et al. (2006) based on the exchange fluxes between seawater and atmosphere from the Lana et al. (2011) climatology. With the implemented New Sulfur Chemistry Mechanism DMS is also oxidized into OCS.

New global emissions for DMDS are included by coupling with biomass burning, based on the emission inventories ACCMIP-MACCity from the Chemistry Climate Model Initiative (CCMI) (Jöckel et al., 2016). The emission ratios for DMDS are calculated relative to CO emitted during biomass burning (Meinardi et al., 2003) with an average emission ratio of 0.016 ± 0.001 $\mathrm{ppb}_v/\mathrm{ppm}_v$ (Figure 6.1 left).

Anthropogenic sulfur emissions are included from the DLR-MACCity emission inventory including faster growth of SO_2 over India from Lelieveld et al. (2018), which also includes CO, NO_x, organic and black carbon.

To analyze the effect from textile production and other industries in the Asian monsoon area, one third of the anthropogenic fraction of CS_2 emissions (0.11 Tg S/a) from Watts (2000) is emitted over India (Figure 6.1 right). As CS_2 has a short lifetime and is fast oxidized to OCS, it doesn't disperse over a wide area.

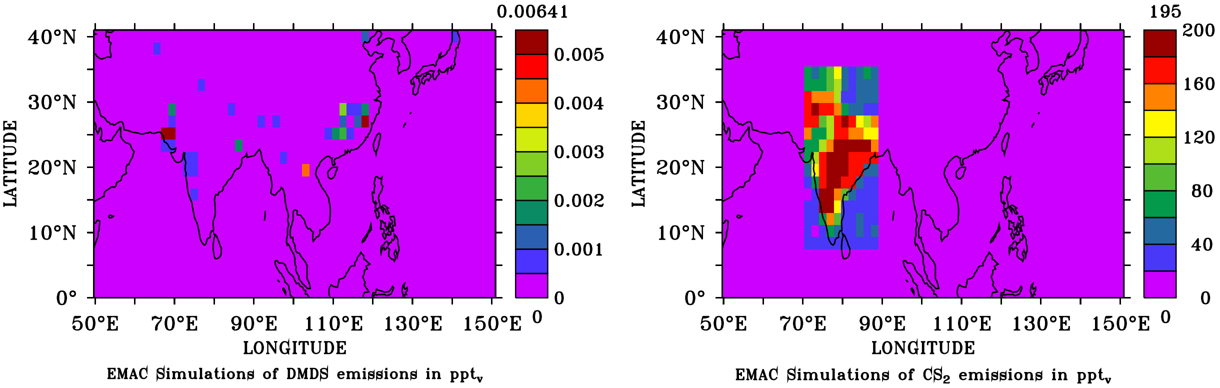

Figure 6.1: Snapshot of resulting mixing ratios of the EMAC simulations including the New Sulfur Chemistry Mechanism with emissions of DMDS in ppt_v coupled to biomass burning (left side) and anthropogenic emissions of CS_2 in ppt_v above the surface layer over India (right side).

The model also includes non-sulfate aerosols, like sea salt and mineral dust emissions or other gas phase tracers as NO_x like described in ONEMIS section 3.1.3.

6.2 Implementation of the comprehensive New Sulfur Chemistry Mechanism

A specific knowledge of atmospheric processes and kinetics are essential to accomplish the sulfur budget and understand the sulfur cycle in the atmosphere. There are many different organic and inorganic sulfur species in the atmosphere, as sulfur can exist with oxidation states from S(-2) to S(+6) in the atmosphere (Kremser et al., 2016). As a part of the global sulfur cycle these sulfur compounds are transformed in chemical reactions, normally from a lower to a higher oxidation state (Figure 6.2), and forming stratospheric aerosol particles through microphysical processes. This New Sulfur Chemistry Mechanism is implemented into the chemistry submodel CAABA/MECCA which describes the transformation of chemical species like DMS and OCS to SO_2 and further to H_2SO_4. The model simulations in this chapter are performed with the same setup of the MESSy simulations as in chapter 4. The New Sulfur Chemistry Mechanism in Figure 6.3 is replacing the standard sulfur chemistry reactions of the CAABA/MECCA submodel (Appendix A). This also includes some photolysis reactions (see Appendix A), which are added to the EMAC model. The year 2017 is chosen for the calculations with the New Sulfur Chemistry Mechanism, as the different model setups can be evaluated directly with the in-situ measurements from the StratoClim campaign in the same year (see chapter 7).

To get an easier overview, Figure 6.2 shows a simplified summary of the comprehensive New Sulfur Chemistry Mechanism in Figure 6.3. The focus lies on the main involved reaction pathways, summarizing multistep reactions without showing intermediate products.

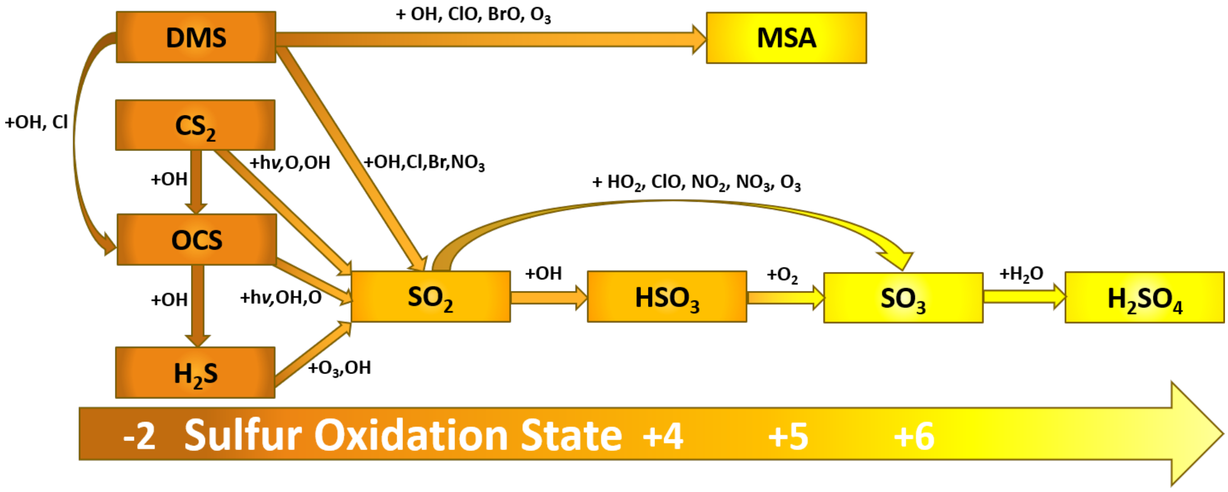

Figure 6.2: Simplified illustration of the New Sulfur Chemistry Mechanism in Figure 6.3. Arrows are showing the main reaction pathways, without intermediate products. The yellow color shade indicates the Sulfur Oxidation States of single sulfur species from S(-2) to S(+6). Plotted with MS Power Point.

Using the chemistry databases of Jet Propulsion Laboratory (JPL) by NASA (Burkholder et al., 2015), International Union of Pure and Applied Chemistry (IUPAC) (Atkinson et al., 2007) and National Institute of Standards and Technology (NIST) this New Sulfur Chemistry Mechanism consists of various chemical reactions and rate constants to describe the cycle of the sulfate budget in the atmosphere.

There are two main reaction pathways for transformation of DMS (CH_3SCH_3) to SO_2. The first pathway is a line of several reactions involving OCS (Barnes et al., 1994, 2006) which is further oxidized to SO_2.

$$CH_3SCH_3 + OH \longrightarrow CH_3SCH_2 + H_2O \tag{6.1}$$

$$CH_3SCH_2 + O_2 + M \longrightarrow CH_3SCH_2OO + M \tag{6.2}$$

$$CH_3SCH_2OO + NO \longrightarrow CH_3SCH_2O + NO_2 \tag{6.3}$$

$$CH_3SCH_2O + O_2 \longrightarrow CH_3SCHO + HO_2 \tag{6.4}$$

$$CH_3SCHO + OH \longrightarrow OCS + CH_3 + H_2O \tag{6.5}$$

The second pathway to get SO_2 is through the oxidation of DMSO (CH_3SOCH_3). Concurrently a significant fraction of DMSO is transformed into methyl sulfonic acid (MSA) (CH_3SO_3H) with sulfur oxidation state S(+5) which does not easily transform further to SO_2, as it has a lower oxidation state S(+4). Hence MSA acts as a reservoir species for sulfur in the atmosphere until it is absorbed and accommodated into the atmospheric aqueous-phase aerosol.

$$CH_3SCH_3 + OH + O_2 \longrightarrow CH_3SOCH_3 + HO_2 \tag{6.6}$$

$$\begin{aligned} CH_3SOCH_3 + OH + M &\longrightarrow 60\,\%(SO_2 + CH_3O_2 + HCHO + M) \\ CH_3SOCH_3 + OH &\longrightarrow 40\,\%(CH_3SO_3H + HO_2 + HCHO) \end{aligned} \tag{6.7}$$

Similar to DMS, dimethyl disulfide (DMDS) (CH_3SSCH_3) is gradually oxidized into MSA or OCS. CS_2, OCS and H_2S with oxidation states of S(-2) are transformed to SO_2 with S(+4) in several reaction steps. The newly implemented CS_2 can be converted to OCS in three different pathways.

$$CS_2 + OH \longrightarrow OCS + SH \tag{6.8}$$

$$\begin{aligned} CS_2 + OH &\longrightarrow CS_2OH \\ CS_2OH + O_2 &\longrightarrow OCS + HOSO \end{aligned} \tag{6.9}$$

$$\begin{aligned} CS_2 + O &\longrightarrow CS + SO \\ CS + O_3 &\longrightarrow OCS + O_2 \end{aligned} \tag{6.10}$$

SO_2 plays a key role in the chemical mechanism, as the most abundant sulfur containing gas emitted in the lower troposphere, not being efficiently removed by surface sinks and dry/wet deposition, are eventually converted into SO_2. However a considerable exception to this is the formation of MSA from DMS. SO_2 is further oxidized to sulfur trioxide (SO_3) and converted to H_2SO_4 (see section 2.3.1), which is highly sensitive to the temperature and the water vapor concentration (Sander et al., 2011).

Figure 6.3 is generated by the model output from the EMAC submodel CAABA/MECCA and shows an overview of the implemented New Sulfur Chemistry Mechanism. The yellow ovals indicate the individual sulfur species. The black arrows in between represent the single chemical reactions with the reaction number of the model above the arrows. Detailed information about the single reactions sorted by the reaction number, including reaction products and rate coefficients, are listed in Appendix A.

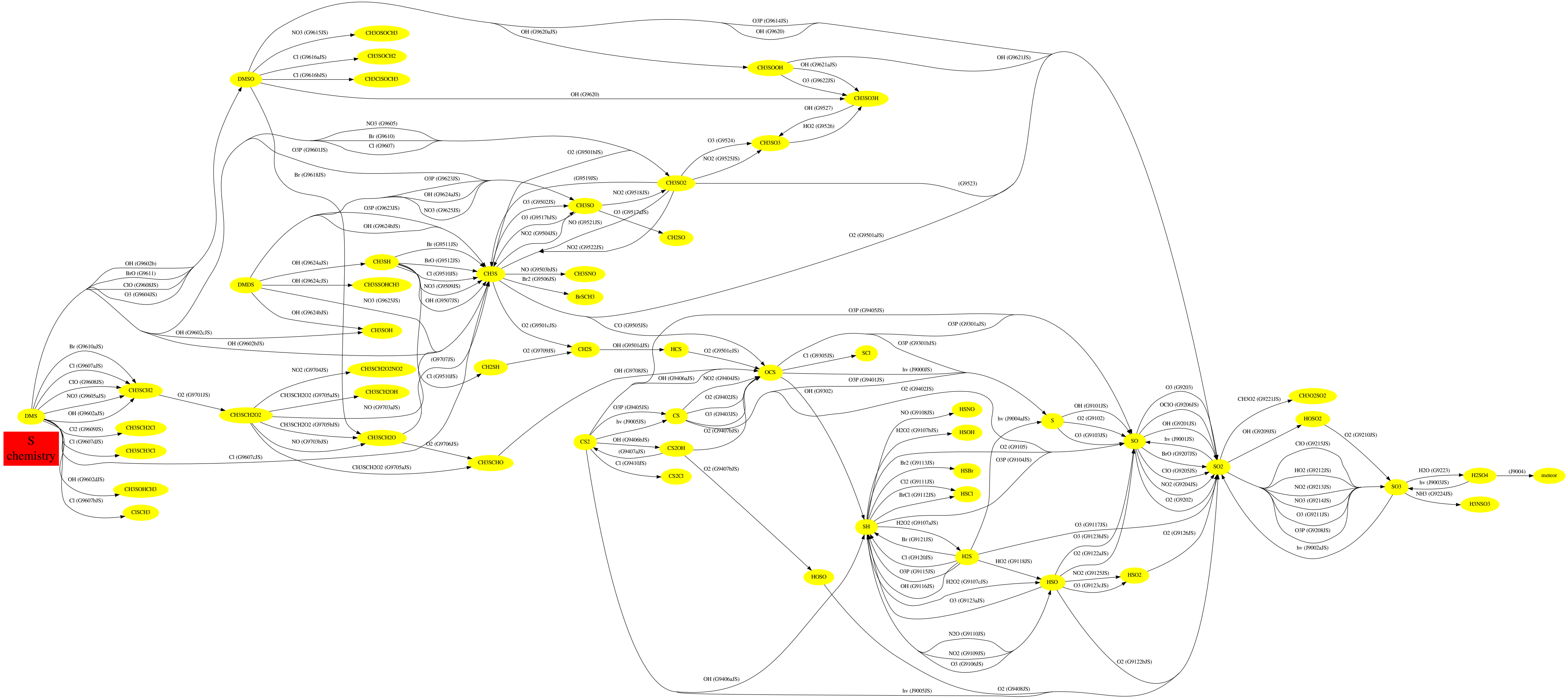

Figure 6.3: New Sulfur Chemistry Mechanism included in the EMAC submodel CAABA/MECCA.

6.3 Comparison of the different Model Setups

The main precursors of stratospheric background aerosols DMS, OCS and SO_2 as well as MSA are compared between the model simulations with the New Sulfur Chemistry Mechanism (upper right figures) and the standard Old Sulfur Chemistry Mechanism (upper left figures) without CS_2, DMDS, H_2S and with simplified sulfur chemistry in Brühl et al. (2018) and older studies. Since CS_2 and DMDS are only newly implemented in the model, a comparison with older model simulations is not available. The effects on the resulting aerosol extinction at 750 nm wavelength are also considered.

6.3.1 Comparison of DMS Simulations

Figure 6.4 shows the DMS mixing ratios in comparison of the different model setups. The highest mixing ratios occur over the tropical oceans, which are also the most important source regions. The newly implemented chemical reactions (see Figure 6.3) generate an increased DMS oxidation by OH, NO_3 and halogen oxide radicals, especially in these tropical oceanic regions, which leads to a reduction in DMS concentrations (upper right figure) compared to the old chemistry setup (upper left figure).

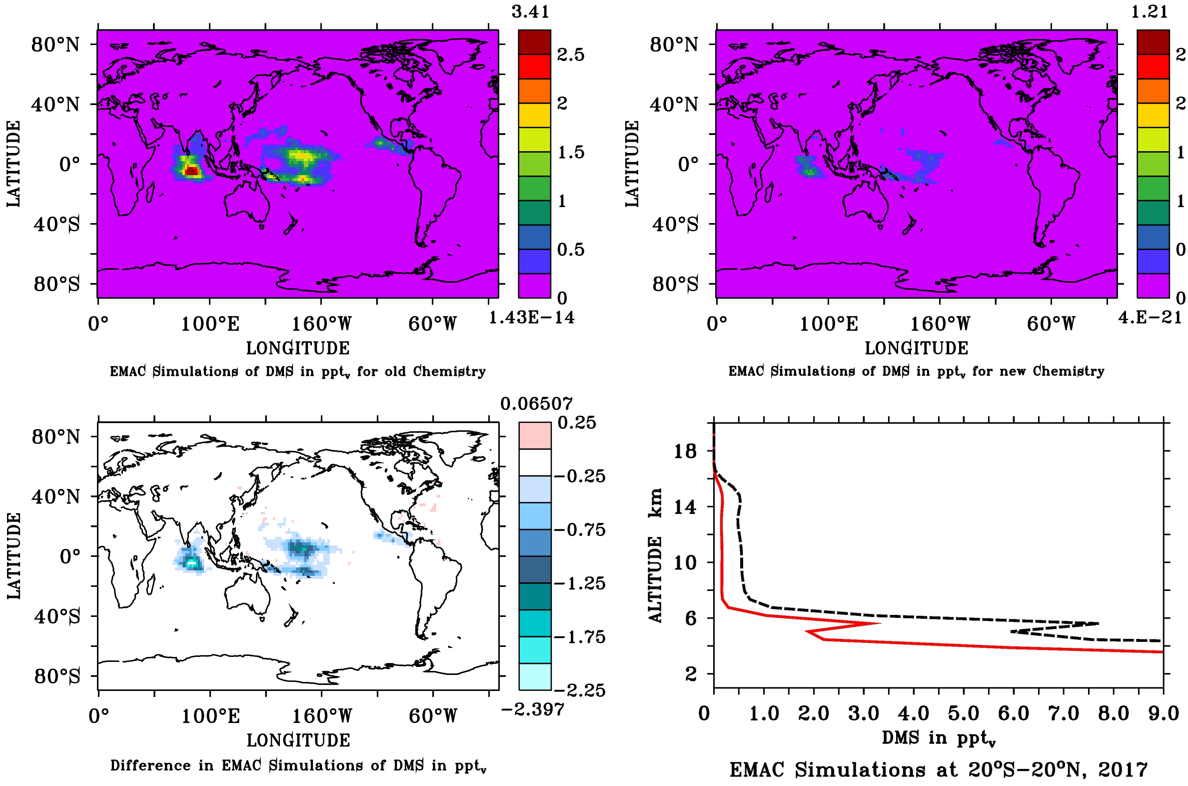

Figure 6.4: Comparison of the DMS mixing ratios in ppt$_v$ between the model setups without (upper left figure) and including the New Sulfur Chemistry Mechanism (upper right figure), averaged for June - August 2017 around an altitude of 17 km. The differences of the DMS mixing ratios in ppt$_v$ between the model setups are shown in the lower left figure. Vertical profiles comparing the New Sulfur Chemistry Mechanism (red line) and the Old Chemistry Setup (*black dashed line*) of zonal means for tropical regions 20°S - 20°N (lower right figure).

The vertical profiles of DMS mixing ratios for tropical regions 20°S - 20°N are calculated with the New Sulfur Chemistry Mechanism, represented by the red line and the Old Sulfur Chemistry Mechanism setup represented by the *black dashed line.* The vertical profiles show, that DMS has the highest concentrations above the surface and a second maximum around 6 km altitude. DMS is quickly oxidized in the troposphere, so that only a small proportion reaches into the stratosphere directly. As a result of the newly implemented chemical reactions in the new chemistry simulation, DMS is significantly more reduced in the troposphere than before. This is additionally causing lower DMS values in the UTLS region.

6.3.2 Comparison of OCS Simulations

In comparison to the Old Sulfur Chemistry Mechanism (upper left figure) Figure 6.5 shows an increase of the global OCS mixing ratios, for the implemented New Sulfur Chemistry Mechanism (upper right figure) due to more chemical reactions producing OCS. The newly implemented chemical oxidation of DMS to OCS results especially in tropical and subtropical regions in increased OCS mixing ratios.

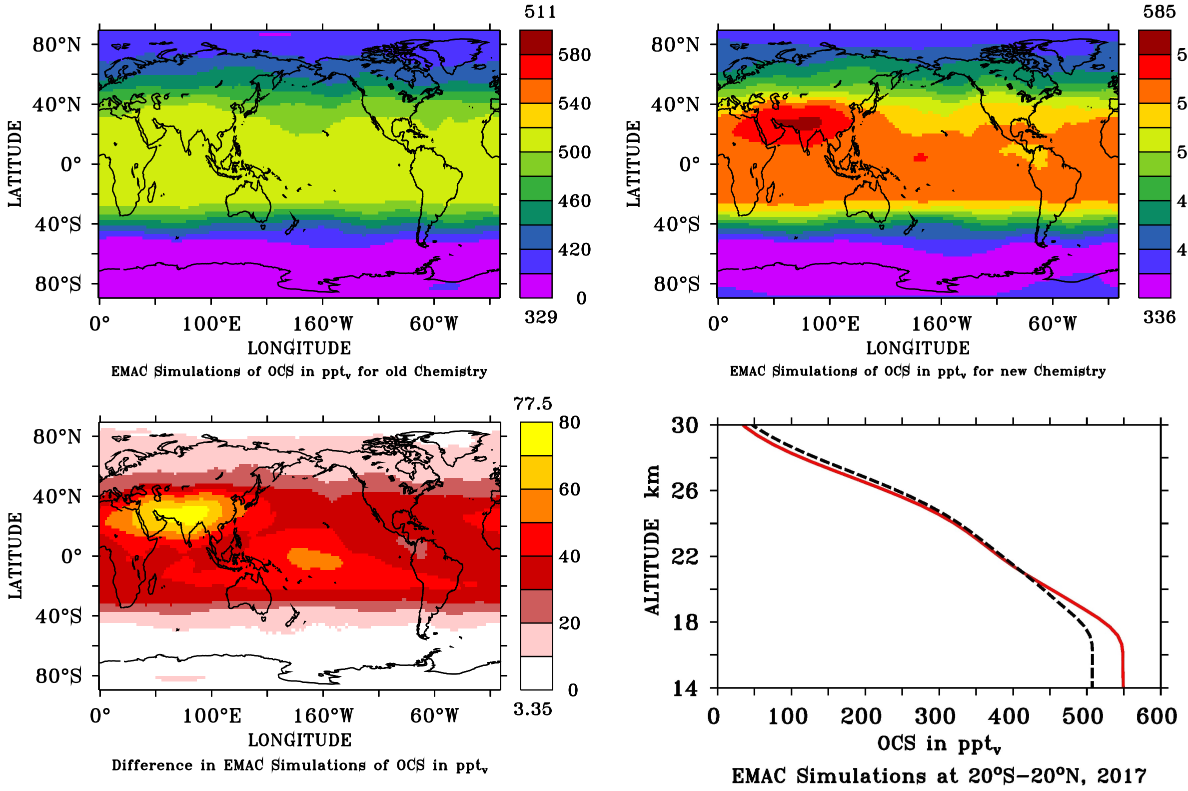

Figure 6.5: Comparison of the OCS mixing ratios in ppt$_v$ between the model setups without (upper left figure) and including the New Sulfur Chemistry Mechanism (upper right figure), averaged for June - August 2017 around an altitude of 17 km. The differences of the OCS mixing ratios in ppt$_v$ between the model setups are shown in the lower left figure. Vertical profiles comparing the New Sulfur Chemistry Mechanism (red line) and the Old Sulfur Chemistry Mechanism (*black dashed line*) of zonal means for tropical regions 20°S - 20°N (lower right figure).

A significant maximum in OCS differences (lower left figure) is located in the Asian monsoon area over India, connected to the newly implemented source of CS_2 (Figure 6.1). As OCS has a longer lifetime than CS_2, the newly formed OCS is not limited to the local emission area of the anthropogenic CS_2 emissions in the surface layer from textile industry and is transported over the whole monsoon area, rising up to the UTLS region.

The vertical profiles of OCS mixing ratios (lower right figure) for tropical regions 20°S - 20°N calculated with the New Sulfur Chemistry Mechanism in red line and the Old Sulfur Chemistry Mechanism in *black dashed line* have the same shape. The model simulations show almost constant OCS mixing ratios in the range of 500 ppt_v (*black dashed line*) in the troposphere, where OCS is only oxidated to hydrosulfide (SH) by slow reactions with OH radicals, with an increase of 50 ppt_v below 18 km altitude for the new simulations (red line). As a consequence of photodissociation and chemical reactions with elemental oxygen (O) and OH radicals, OCS decreases rapidly in the stratosphere as in Brühl et al. (2012). Those results are furthermore in good agreement with the simulations of the 1990s by Sheng et al. (2015) for prescribed surface mixing ratios of 500 ppt_v on the ground. A validation with in-situ measurements from the StratoClim campaign is shown in subsection 7.1.3.

6.3.3 Comparison of MSA Simulations

Another reaction product from the oxidation of DMS is MSA, illustrated in Figure 6.6.

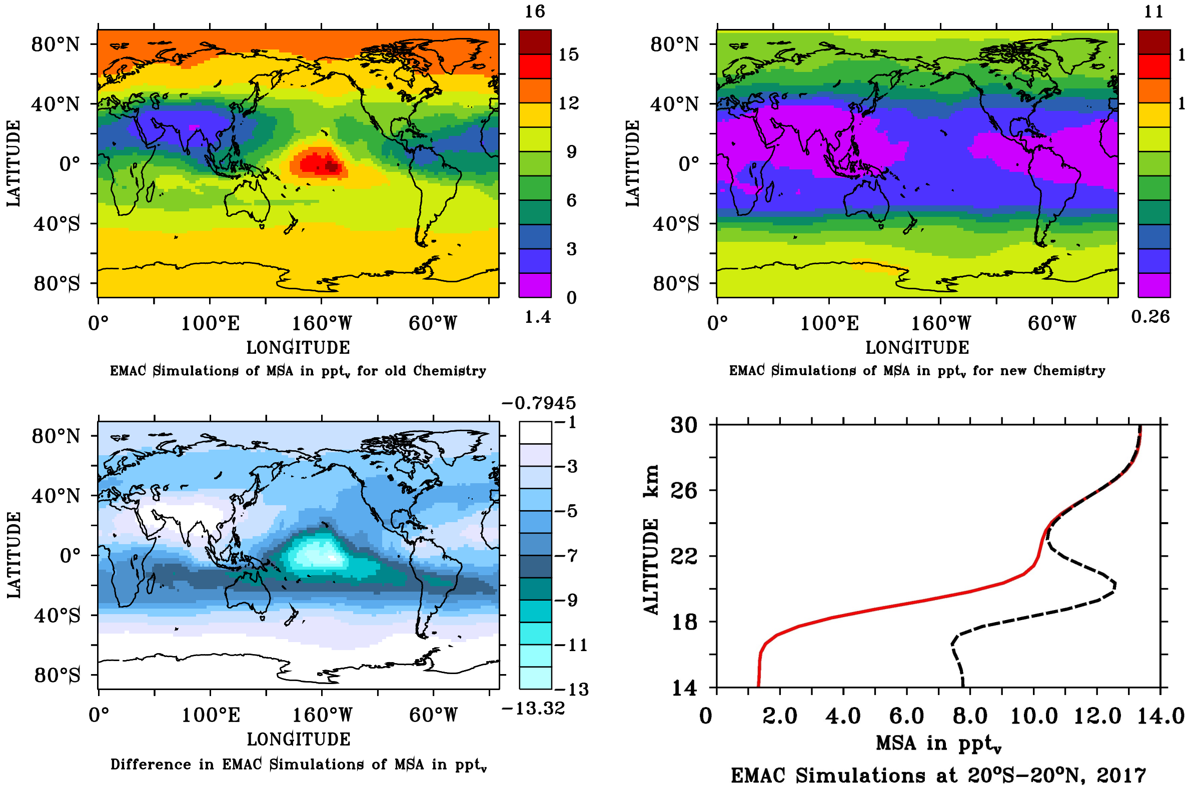

Figure 6.6: Comparison of the MSA mixing ratios in ppt_v between the model setups without (upper left figure) and including the New Sulfur Chemistry Mechanism (upper right figure), averaged for June - August 2017 around an altitude of 17 km. The differences of the MSA mixing ratios in ppt_v between the model setups are shown in the lower left figure. Vertical profiles comparing the New Sulfur Chemistry Mechanism (red line) and the Old Sulfur Chemistry Mechanism (*black dashed line*) of zonal means for tropical regions 20°S - 20°N (lower right figure).

In the Old Sulfur Chemistry Mechanism (upper left figure) the MSA maximum is correlating to the maximum of DMS in Figure 6.4 over the tropical Pacific Ocean. The minimum of MSA mixing ratios is located in the Asian monsoon region. A strong global decrease of MSA mixing ratios is shown in the upper right figure for the New Sulfur Chemistry Mechanism. The greatest difference between the simulations (lower left figure) is located above the tropical Pacific Ocean, caused by the newly implemented chemical reactions transforming DMS to OCS (see Figure 6.3), which is resulting in less production of MSA.

The vertical profiles of MSA (lower right figure) show rising mixing ratios by altitude. In this connection the concentrations below 24 km altitude are significant lower for the new sulfur chemistry simulations (red line) than for the standard chemistry setup (*black dashed line*). In the upper stratosphere the MSA mixing ratios are converging again.

6.3.4 Comparison of SO_2 Simulations

Figure 6.7 shows the EMAC simulations of SO_2 mixing ratios for the Old Sulfur Chemistry Mechanism (upper left figure) and the New Sulfur Chemistry Mechanism (upper right figure) around 17 km altitude.

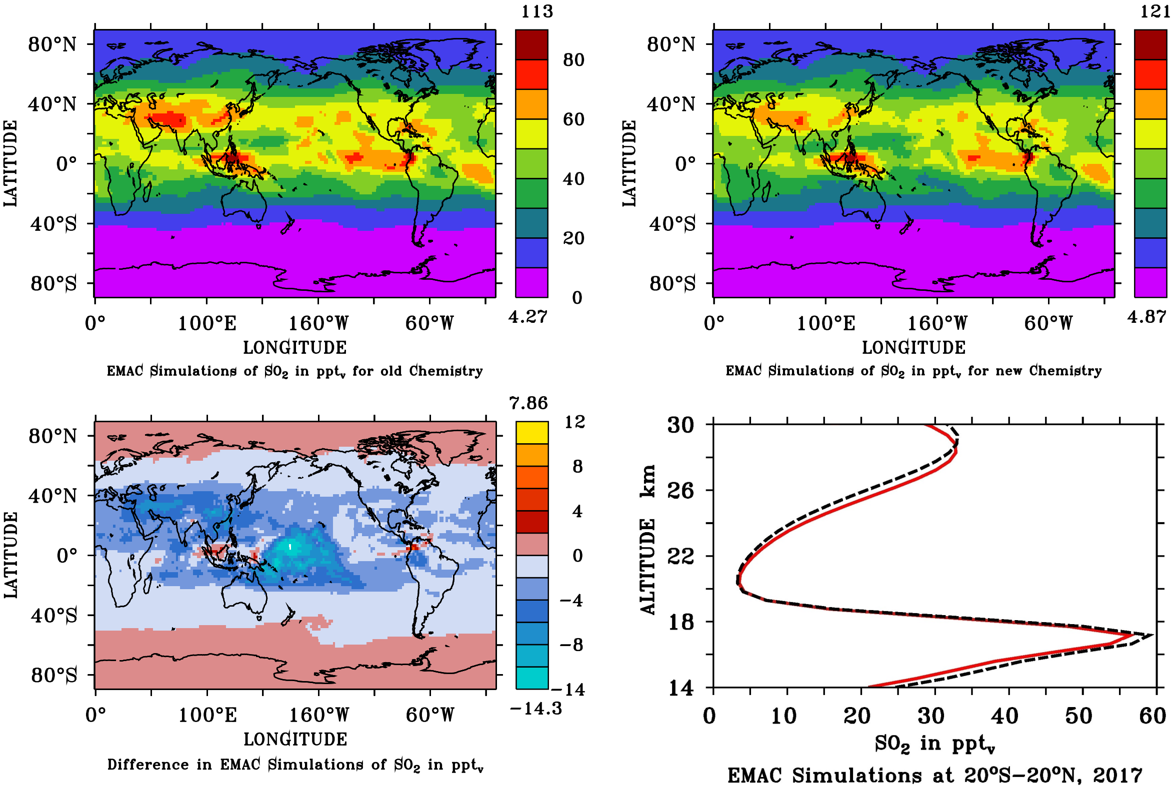

Figure 6.7: Comparison of the SO_2 mixing ratios in ppt_v between the model setups without (upper left figure) and including the New Sulfur Chemistry Mechanism (upper right figure), averaged for June - August 2017 around an altitude of 17 km. The differences of the SO_2 mixing ratios in ppt_v between the model setups are shown in the lower left figure. Vertical profiles comparing the New Sulfur Chemistry Mechanism (red line) and the Old Sulfur Chemistry Mechanism (*black dashed line*) of zonal means for tropical regions 20°S - 20°N (lower right figure).

Both simulations show strong volcanic SO_2 emissions in the time period between June and August 2017 (Table 4.1), in Central America of San Cristobal and Fuego, in Southeast Asia from the volcano Manam and a plume of Sinabung mixing with the emissions in the Asian monsoon area. The differences between both simulations (lower left figure) show a slight increase of SO_2 in the polar regions at 17 km altitude as well as a slight decrease in the tropics and subtropics. The maximum difference are decreasing mixing ratios in the region of the tropical Pacific Ocean, similar to MSA above in Figure 6.6.

The vertical profiles of SO_2 mixing ratios for tropical regions 20°S - 20°N in the lower right figure are calculated with New Sulfur Chemistry Mechanism in red line and Old Sulfur Chemistry Mechanism in *black dashed line*. The first maximum shows the Asian Tropopause Aerosol Layer (ATAL) around 17 km altitude. Here the differences between both simulations are quite small, with slightly reduced SO_2 mixing ratios for the New Sulfur Chemistry Mechanism in tropical latitudes. Compared to the other sulfur precursor gases above, the newly implemented chemical reactions have only little direct impact on the SO_2 mixing ratios, which are dominated by the volcanic events. The second maximum represents the Junge-aerosol layer with about 30 ppt_v. Here is a slight increase by the New Sulfur Chemistry Mechanism from the oxidation of additional OCS.

6.3.5 Comparison of Aerosol Extinction Simulations

Figure 6.8 compares the resulting differences in the aerosol extinction coefficients at 750 nm wavelength between the model simulations without (upper left figure) and including the New Sulfur Chemistry Mechanism (upper right figure) with the satellite retrieval data from OSIRIS (lower left figure). The aerosol extinction coefficients in the new model simulations are improved but still underestimated in comparison to the OSIRIS satellite data at 750 nm wavelength (lower left figure).

The vertical profiles (lower right figure) show a slight increase in aerosol extinction coefficients in the ATAL between 17 km and 18 km and in the Junge-aerosol layer at 22 km to 26 km for the New Sulfur Chemistry Mechanism (red line) compared to the standard Old Sulfur Chemistry Mechanism (*black dashed line*).

The aerosol extinction in the lower stratosphere is primarily determined by volcanoes (here Sinabung) and aerosol water. At these altitudes, the uncertainties are determined by the satellite resolution and by cloud contamination in the satellite data. Furthermore there are height uncertainties of the volcanic emission estimates, regridder, convection effects and simplifying assumptions in the model.

OCS only plays a minor role for the extinction profiles, it is only important for the background at about 22 km to 24 km altitude, where the model matches well with the satellite data. In the middle and upper stratosphere missing meteoric dust, which is acting as condensation nuclei for aerosol particles, leads to large differences between both model setups with the OSIRIS satellite data.

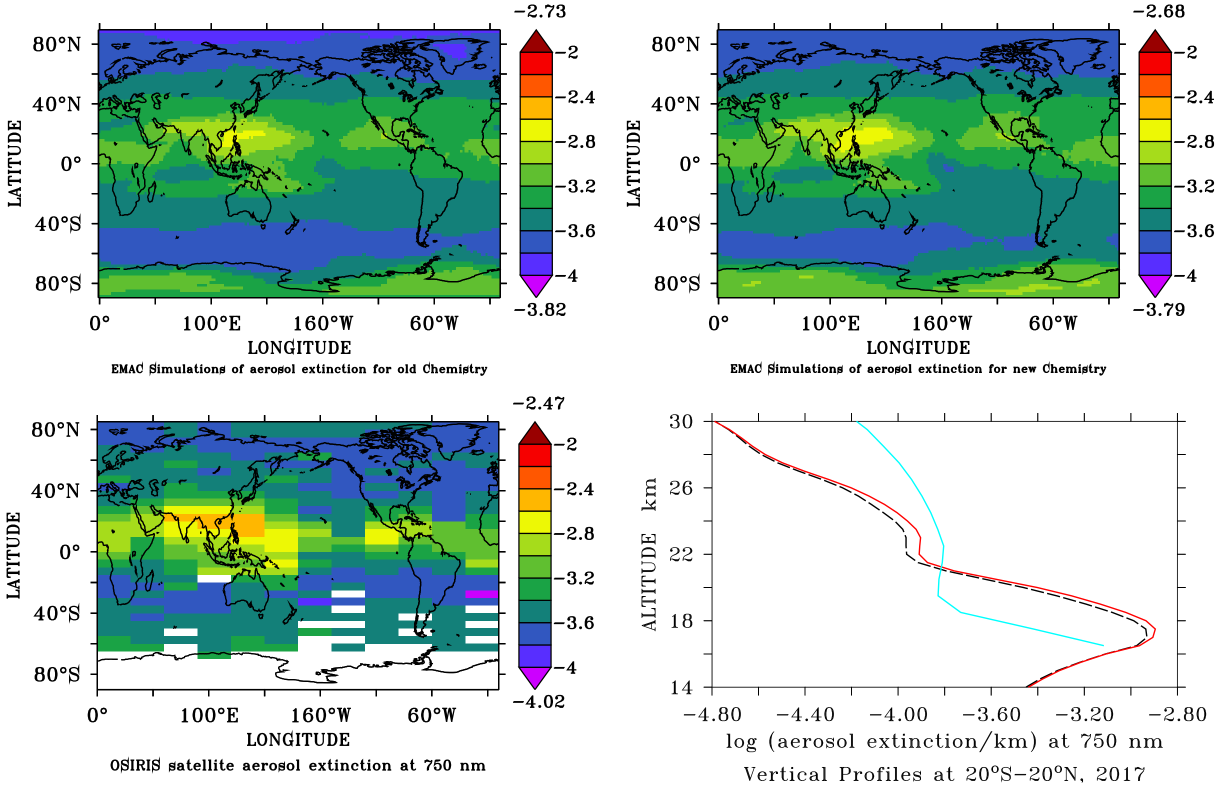

Figure 6.8: Comparison of the aerosol extinction in logarithmic scale at 750 nm wavelength between the OSIRIS satellite data (lower left figure) and the model setups without (upper left figure) and including the New Sulfur Chemistry Mechanism (upper right figure), averaged for June - August 2017 around an altitude of 17 km. Vertical profiles comparing the satellite data from OSIRIS instrument (lightblue line) with the New Sulfur Chemistry Mechanism (red line) and the Old Sulfur Chemistry Mechanism (*black dashed line*) of zonal means for tropical regions 20°S - 20°N (lower right figure).

6.4 Discussion of the Sulfur Chemistry Mechanism

In chapter 4 it was shown, that moderate and even small sized volcanic eruptions could have a strong influence on the stratospheric aerosol loading and dominate other natural and anthropogenic SO_2 emissions at the time of volcanically active periods. Under non-volcanic conditions the model simulations show that the Sulfur Chemistry Mechanism is important for the background sulfate budget and can also have strong impact on the local and regional scale like in the Asian monsoon area.

In this chapter a New Sulfur Chemistry Mechanism is developed and successfully implemented into the model. This New Sulfur Chemistry Mechanism is including new sulfur sources of CS_2 and DMDS, additional chemical species and extended chemical reactions as well as the photolysis of CS_2 and H_2S. Reduced sulfur compounds with an oxidation state of S(-2) from various sources are oxidized to compounds such as SO_2 or H_2SO_4, which otherwise would not be present in the atmosphere in substantial amounts that are observed, and little sulfur would reach into the stratosphere, except during the large volcanic eruptions (Kremser et al., 2016).

Newly added emissions of DMDS are correlated to CO emissions from biomass burning markers (Meinardi et al., 2003). Since the implemented DMDS mixing ratios are very low ($< 0.01\,\mathrm{ppt}_v$), there are also minor direct effects on the total sulfur budget.

The newly implemented local anthropogenic CS_2 emissions from textile industry over India and Bangladesh area are quickly transformed into OCS in the troposphere by the added sulfur chemistry reactions. Subsequently this is resulting in rising OCS mixing ratios in the Asian monsoon area. These increased values also fit better with measurements by Mallik et al. (2016) over Ahmedabad, India, where the local annual mean OCS mixing ratio is found to be $830 \pm 430\,\mathrm{ppt}_v$.

The decrease of DMS and MSA mixing ratios is caused by the newly implemented reactions producing OCS from DMS. This supports the thesis of Lennartz et al. (2017) that the oxidation of DMS and CS_2 are significant for OCS formation. In this connection the biggest effects for DMS, MSA and OCS mixing ratios are located in the troposphere.

The slight decrease in SO_2 mixing ratios below 18 km altitude could be caused by a shorter lifetime, due to a faster conversion to sulfate aerosol by the newly implemented reactions, resulting in a slight increase in the aerosol extinction. Another reason could be, that the rising OCS mixing ratios bind the sulfur in the lower layers, whereby SO_2 decreases. Beyond 22 km altitude SO_2 mixing ratios starts to increase by the transformation from the additionally available OCS.

The differences in SO_3 and H_2SO_4 between the simulations are very small, below 0.1 parts per quadrillion by volume (10^{-15}) (ppq_v) respectively $0.1\,\mathrm{ppt}_v$, and are therefore not shown in more detail here. The resulting aerosol extinction slightly increases by the rising OCS and decreasing MSA mixing ratios, and fits the model results better to the OSIRIS satellite data.

Simulations of the year 2017 are chosen for analyzing the influence of the different setups of Sulfur Chemistry Mechanisms for validation with in-situ measurements from StratoClim campaign in the next chapter 7.

There are still missing sources for sulfur containing emissions such as H_2S, e.g. from wetlands (see section 2.3.1), assumptions of emission climatologies and interpolations for missing data due to lack of observations, which would be essential, since all subsequent calculations could be flawed by uncertain initial values. Kremser et al. (2016) shows, that additional biochemical processes in living organisms play an important role in the global biogeochemical sulfur cycle and has to be considered in the model. Simultaneously, the sulfur uptake of plants must be taken into account, which plays an important role in boreal forests in particular, as was observed by Karu (2019) during field campaigns in Finland. At the same location CS_2 mixing ratios of $1.53 \pm 0.86\,\mathrm{ppt}_v$ were measured, which have the consequence that CS_2 emissions should be extended globally in the model.

Furthermore there are remaining uncertainties, even for reactions that have already been implemented, as there are no available values from laboratory measurement studies of many sulfur containing species for reaction products and rate coefficients.

Chapter 7

Validation of EMAC with Aircraft Measurements in the Asian Summer Monsoon

The simulations of the EMAC model are validated by using the S4D submodel (section 3.1.3) for comparisons with data from in-situ measurements. For this purpose the data of the Geophysica aircraft from the StratoClim campaign (section 3.3) in the lowermost stratosphere during the Asian Summer Monsoon (ASM) in 2017 are used. The data of the StratoClim campaign will be available within the HALO database at `https://halo-db.pa.op.dlr.de/mission/101` (18 December 2020) at Deutsches Zentrum für Luft- und Raumfahrt (DLR).

7.1 Evaluation of Flights from the StratoClim Campaign

The flight number 3 on 31 July 2017 (left side in red) and flight number 7 on 8 August 2017 (right side in blue) of the StratoClim campaign are chosen for the analysis. The flight tracks are illustrated on the map in Figure 7.1, with the profiles of the flight altitudes on the lower part of the figures.

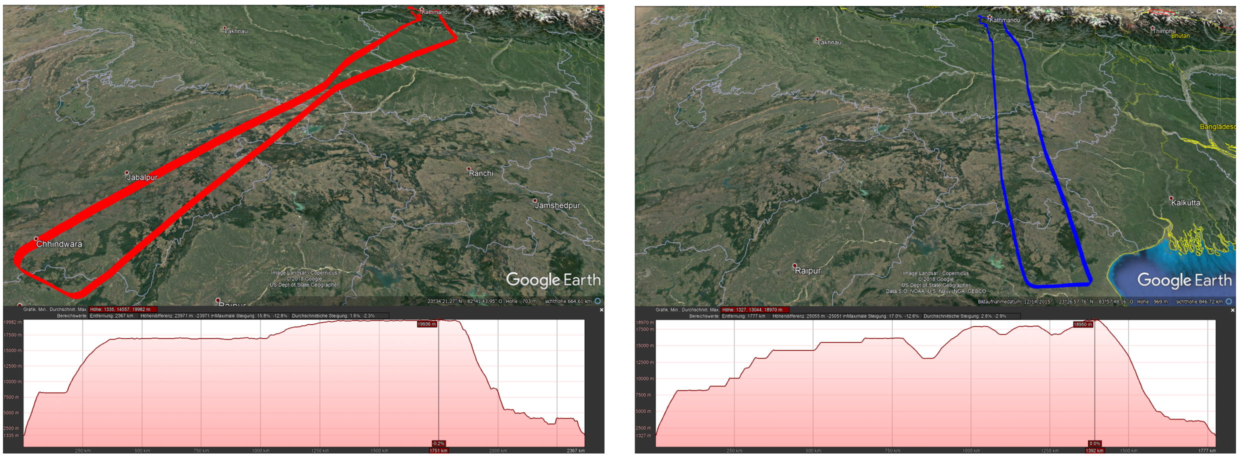

Figure 7.1: Map of the flight paths of the StratoClim campaign of Flight 3 on the 31 July 2017 (left) and Flight 7 on the 8 August 2017 (right). Plotted with Google Earth.

The Geophysica aircraft has its takeoff and landing airport in Kathmandu, Nepal and is flying clockwise from north to south over northern India and back to Nepal at altitudes of the UTLS region. In flight number 3 on 31 July 2017 (left side in red) the Geophysica aircraft is flying in southwestern direction to the Indian city Nagpur before it turns back to Nepal and reaches a maximum altitude of almost 20 km (vertical profile of the flight below the map in Figure 7.1). During flight number 7 on 8 August 2017 (right side in blue) to the north eastern border of India, passing the city Patna and staying western of Kalkutta and the Bay of Bengal the Geophysica aircraft reaches a maximum altitude of 19 km. This covers a region with a high population density and high air pollutant emissions.

7.1.1 Comparison of Ozone Measurements

The y-axis of all plots Figure 7.2 - Figure 7.9 shows the altitude in logarithmic pressure coordinates, so 2.00 is equal to an altitude of 100 hPa. The colored ribbons in the plots are the values from the in-situ measurements along the flight tracks, plotted over the EMAC model simulations, by using the S4D submodel to get the same coordinates and time in the same color bar. The x-axis gives the time in Universal Time Coordinated (UTC), which has a time shift of +5:45 hours to Nepal local time. That means measurements starting at 3:00 UTC corresponds to 8:45 Nepal local time.

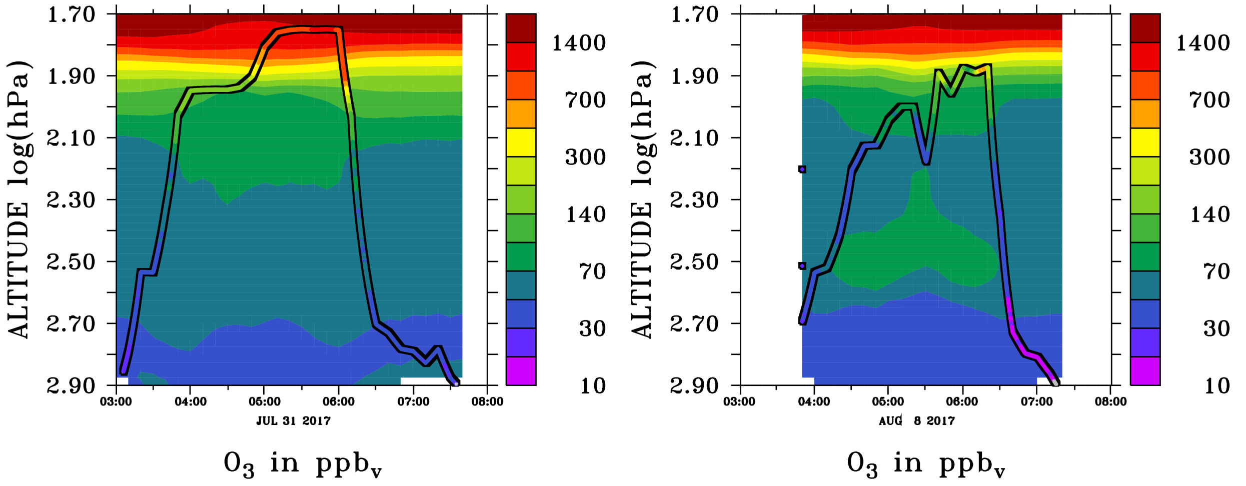

Figure 7.2: Comparison of the O_3 mixing ratios in ppb_v from the in-situ measurements of the FOZAN instrument on the StratoClim campaign (colored ribbons) with the EMAC model simulations (same color bar) on the 31 July 2017 (left) and 8 August 2017 (right). Grey: no data.

O_3 measurements from the FOZAN instrument (section 3.3.2) are compared to the EMAC model simulations in Figure 7.2. High O_3 concentrations are a good indicator for the airplane entering into the stratospheric air masses. Figure 7.2 shows, that the measurements fit well with the stratospheric setup of the model simulations in the UTLS layer. This indicates that the vertical distribution and the calculation of the tropopause in the model is correct, which is essential for all following analyzes. Nevertheless there can be local variations in tropopause height and tropopause foldings are not considered, because of the model resolution.

On the 31 July 2017 (left) the Geophysica enters the lower Stratosphere, as indicated by the high O_3 concentrations, while it stays in lower altitudes on 8 August 2017 (right).

7.1.2 Comparison of CO Measurements

CO has a long lifetime and is well suited as trace gas for long distance transport of pollution. South Asian emissions of 122 Tg CO dominate the monsoon anticyclone composition and leads to increased CO values inside the monsoon circulation compared to lower values outside (Lelieveld et al., 2018). For this reason CO mixing ratios can be used for identifying entering of the aircraft into monsoon influenced air masses. The CO mixing ratios have their maximum at ground levels and values are decreasing by altitude with a strong gradient at the tropopause.

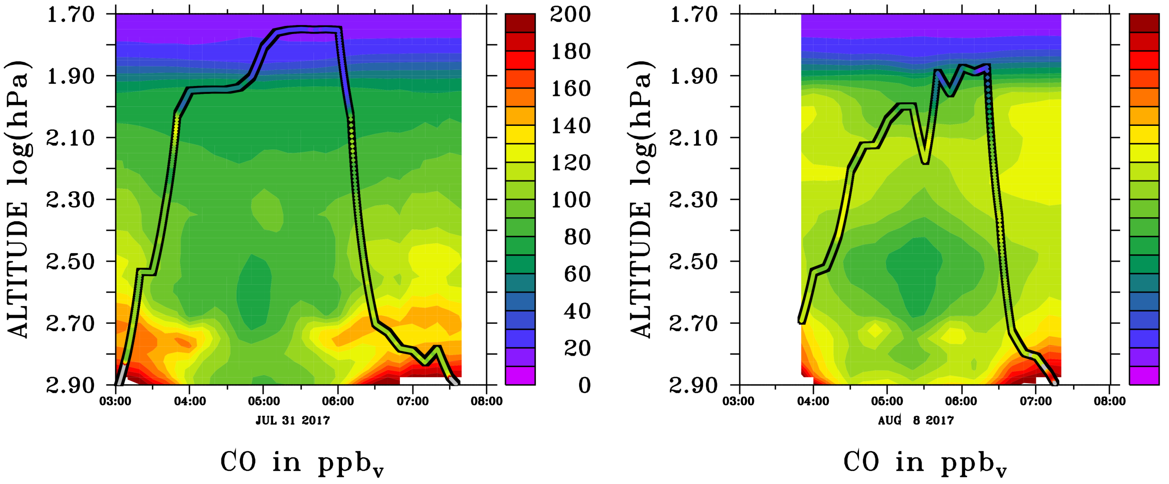

Figure 7.3: Comparison of the CO mixing ratios in ppb$_v$ from the in-situ measurements of the AMICA instrument on the StratoClim campaign (colored ribbons) with the EMAC model simulations (same color bar) on the 31 July 2017 (left) and 8 August 2017 (right). Grey: no data.

The AMICA instrument (section 3.3.2) can take simultaneous measurement of OCS, CO and CO_2. Figure 7.3 compares the in-situ data of the AMICA CO measurements with the EMAC S4D simulations. Figure 7.3 shows enhanced CO in the UTLS, which indicates being inside the monsoon anti-cyclone. The mixing ratios of EMAC show a similar vertical distribution for CO as the in-situ data. Furthermore, the simulated mixture ratios have the same order of magnitude as the measured data.

Regardless, there are some small divergences remaining between simulations and measurements. The CO values are elevated in the lower troposphere in the northern part of the flight track, which can be related to local differences in the model emissions. On the 31 July 2017 (Figure 7.3 left side) is a thin layer with increased values in the aircraft measurements below 100 hPa, which cannot be resolved by the model resolution. Furthermore this effect is visible too in the CO data of the Carbon Oxide Laser Detector (COLD), a second instrument measuring CO during the StratoClim campaign. An error in the measurements and the calibration is therefore unlikely. Nonetheless, it can be said that, the model agrees relatively well with the measurements on the 8 August 2017.

7.1.3 Comparison of OCS Measurements

In this section the OCS mixing ratios in the Indian monsoon region are compared between the different model setups and evaluated with the aircraft measurements of the AMICA instrument on the StratoClim campaign. Which is helpful for the quantification of the sulfur input to the stratosphere via OCS.

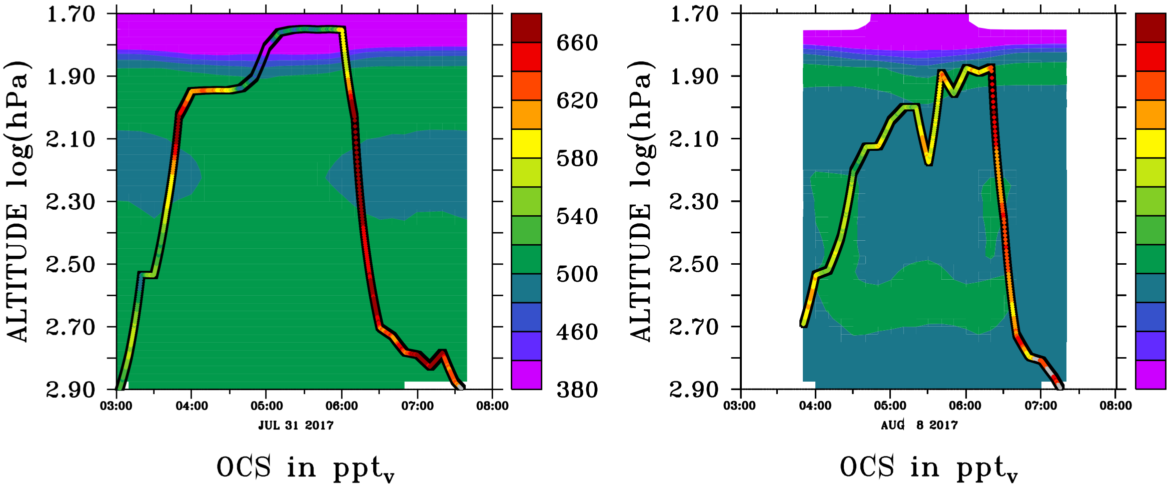

Figure 7.4: Comparison of the OCS mixing ratios in ppt$_v$ of the in-situ measurements from the AMICA instrument on the StratoClim campaign (colored ribbons) with the **Old** Sulfur Chemistry Mechanism and **without** CS_2 emissions (same color bar) on the 31 July 2017 (left) and 8 August 2017 (right). Grey: no data.

A comparison between the different model setups (section 6.3), without (Figure 7.4) and including (Figure 7.5) the New Sulfur Chemistry Mechanism and additional sulfur emissions, with the StratoClim campaign data from the AMICA instrument (colored ribbons) shows that the new model setup is improving the sulfur cycle in the model and is much closer to the measurements than before.

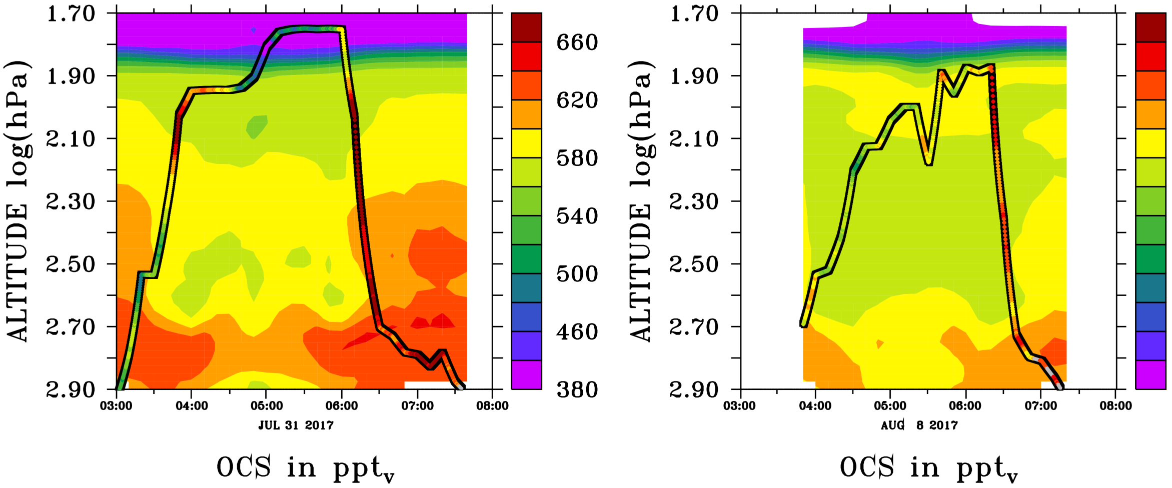

Figure 7.5: Comparison of the OCS mixing ratios in ppt$_v$ of the in-situ measurements from the AMICA instrument on the StratoClim campaign (colored ribbons) with the **New** Sulfur Chemistry Mechanism and **including** CS_2 emissions (same color bar) on the 31 July 2017 (left) and 8 August 2017 (right). Grey: no data.

Without the additional source of CS_2 from the textile industries in India and Bangladesh, which is converted into OCS by the New Sulfur Chemistry Mechanism, the OCS mixing ratios in the Asian monsoon region are significantly too low in all vertical levels up to the UTLS layer (Figure 7.4). Especially above an altitude about 150 hPa the OCS simulations are too low and the vertical gradients are too strong.

On 31 July 2017 (left) the in-situ measurements show maximum OCS mixing ratios of more than 660 ppt_v around altitudes of 100 hPa, which are not reproduced by the model (Figure 7.4), even for the improved chemistry simulations (Figure 7.5). In combination with enhanced CO mixing ratios at the same time in Figure 7.3 it indicates some missing emissions in the model.

The model has also to consider the daily cycle of OCS mixing ratios. During the take off in the morning 8:45 local time (3:00 UTC 31 July 2017 on left side) the measured OCS mixing ratios are lower than during the landing at the same airport in the afternoon (local time) below altitudes of 400 hPa.

On 8 August 2017 (right) the new model simulations (Figure 7.5) fit quite well in the morning hours, while it underestimates OCS mixing ratios at all altitudes above 630 hPa in the afternoon (local time) on the way back to the landing airport. Another explanation for this could be a too weak convection of the monsoon circulation in the model simulations during the afternoon. But a comparison with the CO mixing ratios (Figure 7.3) at the same time indicates no enhanced vertical transport of surface emissions to higher altitudes.

7.1.4 Comparison of Sulfate Measurements

With the ERC funded aircraft particle mass spectrometer ERICA (section 3.3.2) the chemical composition of aerosol particles can be identified. Figure 7.6 - Figure 7.7 show the sulfate concentration in the different model setups compared with the measurements from the ERICA instrument.

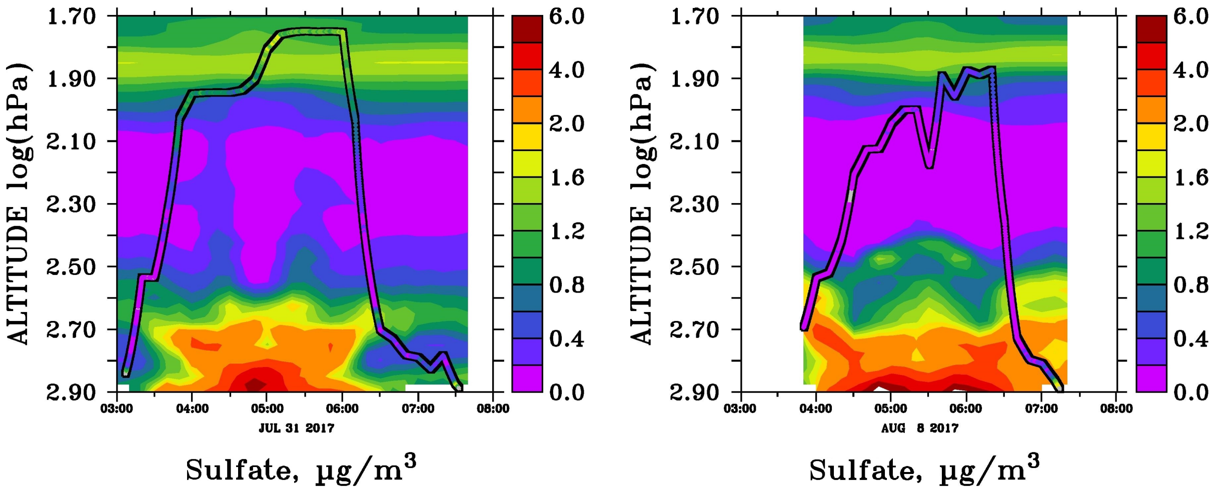

Figure 7.6: Comparison of the particulate sulfate concentration in µg/m^3 (NTP) of the in-situ measurements from the ERICA instrument on the StratoClim campaign (colored ribbons) with the **Old** Sulfur Chemistry Mechanism and **without** CS_2 emissions (same color bar) on the 31 July 2017 (left) and 8 August 2017 (right). Grey: no data.

On 31 July 2017 (left) the Geophysica enters the stratospheric aerosol layer above 100 hPa altitude, which is indicated by a strong gradient in the sulfate concentration. The measurements show increased sulfate values in this aerosol layer, which can be explained by the volcanic emissions of the Sinabung volcano at the end of July and beginning of August (Figure 4.4). This is also reproduced by the model very well, as without these volcanic emissions, the model cannot achieve the required values. However an uncertainty in the measurement can not fully be excluded.

As can be seen in subsection 6.3.4, the comparison between the two model setups shows that the sulfur concentration in the UTLS region is dominated by volcanic emissions and does not respond strongly to changes in the Sulfur Chemistry Mechanism. Here the temporal resolution of the emissions from the satellite data matters, as explosive volcanoes like Sinabung has been active over a several months period.

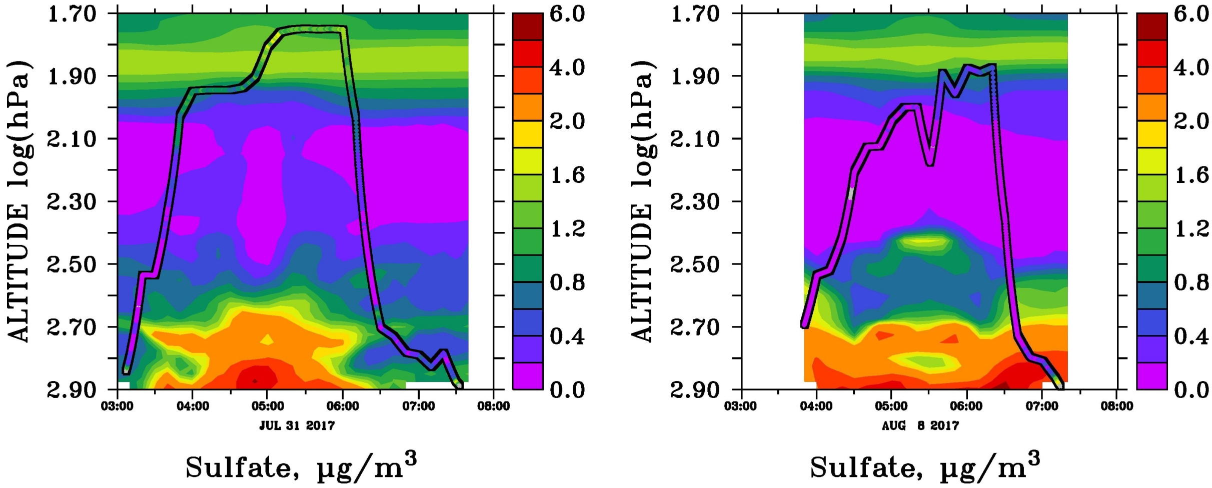

Figure 7.7: Comparison of the particulate sulfate concentration in µg/m^3 (NTP) of the in-situ measurements from the ERICA instrument on the StratoClim campaign (colored ribbons) with the **New** Sulfur Chemistry Mechanism and **including** CS_2 emissions (same color bar) on the 31 July 2017 (left) and 8 August 2017 (right). Grey: no data.

On 8 August 2017 (right) the Geophysica does not reach stratospheric altitudes and remains below the stratospheric sulfur layer. In the troposphere below altitudes of 500 hPa, the model overestimates the local sulfate concentrations compared to the measurements. Here there is a stronger dependence of the sulfur concentration on the local emissions and the chemistry setup.

Minor variations between the model and the measurements can result from uncertainties in the calibration of the instrument and when converting the model values to normal temperature (20°C) and pressure (1013 hPa) (NTP) conditions.

7.1.5 Comparison of Nucleation- and Aitken Particle Measurements

In Figure 7.8 the number concentration of nucleation and Aitken mode particles are compared between the COPAS instrument (section 3.3.2) and the EMAC model simulations.

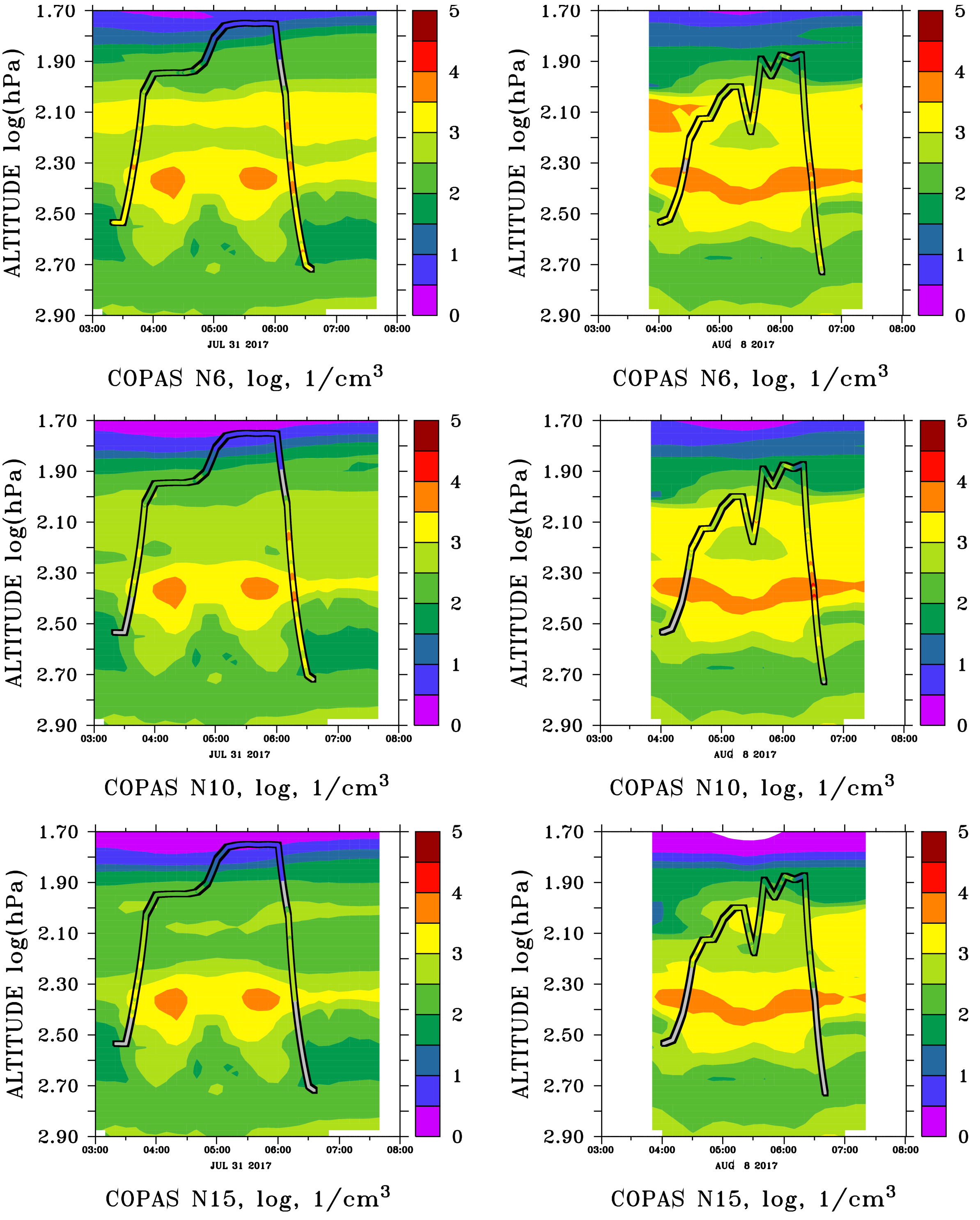

COPAS N6, log, $1/cm^3$

COPAS N6, log, $1/cm^3$

COPAS N10, log, $1/cm^3$

COPAS N10, log, $1/cm^3$

COPAS N15, log, $1/cm^3$

COPAS N15, log, $1/cm^3$

Figure 7.8: Comparison of the in-situ measurements from the COPAS instrument of particle number concentrations (colored ribbons) N6 (top), N10 (middle) and N15 (bottom) in $1/cm^3$ (log scale) with the EMAC model simulations of nucleation and Aitken mode particles (same color bar) on the 31 July 2017 (left) and 8 August 2017 (right). Grey: no data.

Figure 7.8 shows the particle number concentrations for three size bins with diameters of ≥6 nm (N6 top), ≥10 nm (N10 middle) and ≥15 nm (N15 bottom). The number concentration of the single size bins can be determined by subtracting the measurements of the different COPAS size bins. As the measurement range of the COPAS instrument differs from the aerosol modes in the model, the Aitken mode is combined with 0.002% of the nucleation mode for the calculation of N6 (top), and with 0.001% of the nucleation mode for N10 (middle). The calculation for N15 (bottom) only consists of the Aitken mode.

An enhanced number concentration of nucleation mode particles near the tropopause is detected. In the morning hours before 5:00 UTC the number concentration is dominated by fresh nucleated particles N6 (top). Later in the afternoon (local time) after 6:00 UTC the particles has been growing to N10 (middle). At high altitudes above 100 hPa in the stratospheric aerosol layer particle sizes of N15 (bottom) are dominating.

On the 31 July 2017 the number concentration of fresh nucleated particles in the UTLS region is lower than one week later, on the 8 August 2017, when the number concentration of fresh nucleated particles in altitudes between 100 hPa and 300 hPa has increased. Compared to Figure 7.7 the sulfate burden has decreased in the same time, so here we can see the nucleation of new particles from the gas phase near the tropopause. To explain the high number of these fresh nucleated particles the emissions of volcanic SO_2 from Sinabung is needed.

7.1.6 Comparison of larger Particle Measurements

The UHSAS instrument (section 3.3.2) measures the number concentration of particles with diameters in the size range from 65 nm up to 1 µm (N65), and does not completely fit with the aerosol mode boundaries in the model simulations (see Table 3.3). For this reason 20% of the Aitken mode (12 nm to 140 nm) and 80% of the accumulation mode (140 nm to 3.2 µm) of the model are combined for the calculations in Figure 7.9 (percentages are estimated from Equation 2.1).

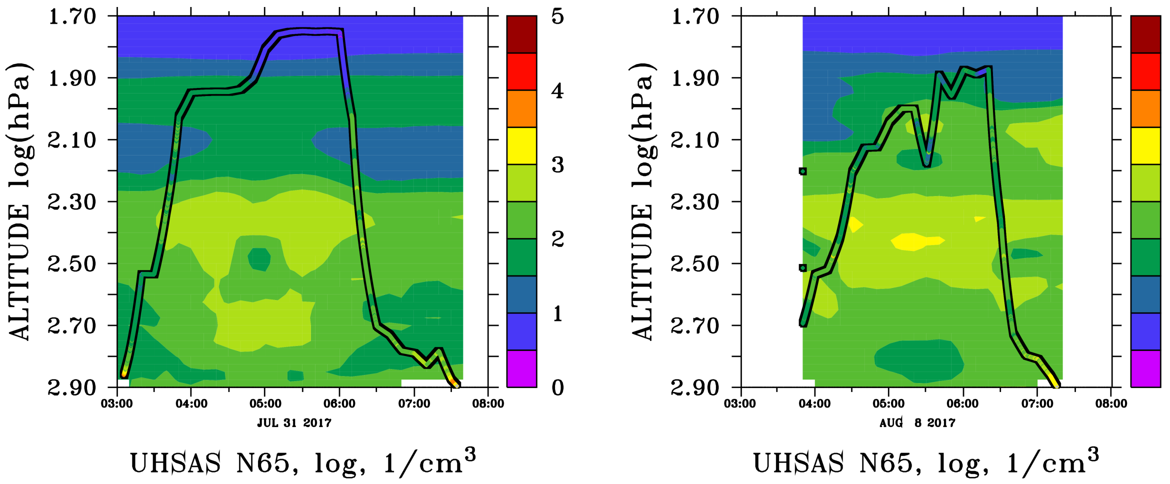

UHSAS N65, log, 1/cm^3 UHSAS N65, log, 1/cm^3

Figure 7.9: Comparison of the particle number concentration with particle diameter ≥65 nm (N65) in 1/cm^3 (log scale) of the in-situ measurements from the UHSAS instrument on the StratoClim campaign (colored ribbons) with the EMAC model simulations (same color bar) on the 31st July 2017 (left) and 8 August 2017 (right). Grey: no data.

Subsequently the greatest uncertainty when comparing between the measurements and the model simulations lies in the division of the two modes. For better comparisons the same logarithmic scale like in Figure 7.8 is also chosen for Figure 7.9.

Below altitudes of 80 hPa the particle number concentration of larger particles with particle diameter ≥65 nm in Figure 7.9 is less than the particle number concentration of the Aitken and nucleation mode particles in Figure 7.8, while above in the stratospheric aerosol layer the accumulation mode particles are dominating. The growing of particles below altitudes of 100 hPa between the 31^{st} July 2017 (left) and 8 August 2017 (right) like in Figure 7.8 can also be seen for larger N65 particles in Figure 7.9.

7.2 Discussion of the Model Validation with Aircraft Measurements

The comparison of ozone between the model simulation and the in-situ measurements of the Geophysica aircraft confirms, that the vertical resolution of the UTLS region in the model is respectable, which is necessary for all subsequent comparisons.

The Asian Summer Monsoon anti-cyclone is indicated by enhanced CO in the UTLS in the model simulations as well as the in-situ measurements of the Geophysica. Concerning CO, the simulations of anthropogenic emissions are quite suitable for middle and higher altitudes and on the surface, while it seems to be a bit overestimated in the lower troposphere.

The validation of the different model setups with the in-situ measurements of OCS verify the improvement of the New Sulfur Chemistry Mechanism in chapter 6. For the standard setup OCS is clearly underestimated at all altitudes. The measurements indicate a daily cycle with rising OCS concentrations in the afternoon (Nepal local time) below altitudes of 80 hPa on the way back to the airport in Kathmandu. Here the model still underestimates the local and time dependent emissions or is missing a temperature or sunlight dependent chemical reaction generating OCS.

The sulfur concentrations differ only slightly between the two model setups. On 31 July 2017 the simulations fit well with the measurements and are in the uncertainty range of the most recent version of the ERICA data. This also verifies the increased values, caused by volcanic emissions from Sinabung in the stratospheric aerosol layer. The volcanic SO_2 emissions are needed to explain the high SO_2 mixing ratios at about 80 hPa and the enhanced number concentration of nucleation mode particles near the tropopause. Hence the simulations show, that volcanic sulfate is often more important than pollution in the lower stratosphere.

When comparing the particle number concentration between the model simulations and the measurements, the different sizes of mode boundaries in the model and the technical detection limits of the instruments have to be considered. Between the 31 July 2017 and 8 August 2017, the results show the formation and growing of particles for all size bins from N6 to N65, that are subsidized by the Sinabung emissions.

All things considered this chapter shows how important is the cooperation between field campaign in-situ measurements and model simulations. The New Sulfur Chemistry Mechanism is validated by the aircraft measurements and the missing source of OCS in form of CS_2 and DMS oxidation is identified. Furthermore the enhanced number concentration of measured aerosol particles is confirmed by the model simulations and the volcanic emissions of the Sinabung could be identified as the origin.

The remaining differences between the model simulation and the in-situ measurements can have different reasons. On the one hand there can be problems with the instruments during the measurements or the calibration of the data. On the other hand the resolution of a global model can not resolve local emission sources or small scale structures, although the time resolution in the model is bigger. Another point are missing or underestimated emissions in the model. That shows how important are high resolutions for models and emission inventories, instead of monthly and zonal means, as often used as input data from satellites.

All these still remaining differences between the measurements and the new model setup show again how important are detailed local sulfur emissions and the New Sulfur Chemistry Mechanism in the model. Also measurements of more sulfur species like DMS and MSA would be helpful for a detailed analysis of intermediate states in the sulfur chemistry cycle.

Chapter 8

Summary and Conclusions

The goal of this thesis is to improve the EMAC model simulations of the global stratospheric aerosol and sulfate burden via validation with satellite and field campaign data.

The evaluation by the satellite data sets shows that GOMOS is important for detecting volcanic eruptions in MIPAS data gaps and for a better attribution of individual eruptions. Here, 3 dimensional plumes and 5-day time intervals are used instead of monthly data and point sources, which are more suitable for the identification and calculation of volcanic emissions. Consequently, the combination of MIPAS and GOMOS data leads to better SO_2 input for the Chemistry Climate Model to calculate the radiative forcing. Moreover, the resolution in the model simulations has been upgraded from T42L90 to T63L90 with a horizontal grid of $1.87° \times 1.87°$ and 90 vertical layers and fits better to the observations now.

The new model simulations are extended from 1991 to 2017 by additional satellite data sets of SAGE II and OSIRIS and now include almost 500 explosive volcanic eruptions instead of 230. An overview of these eruptions is given in the improved Volcanic Sulfur Emission Inventory in Table 4.1, including the estimated stratospheric SO_2 emissions as well as the plume altitudes. To avoid double counting, tropospheric sulfur emissions are treated separately.

On the basis of the improved volcanic sulfur emission inventory, the EMAC model simulates the development of the stratospheric aerosol concentration and calculates the corresponding radiative forcing. The simulations, supported by the MIPAS data, show that even small and medium-sized volcanic eruptions reaching the tropical tropopause region are significant due to the accumulation of sulfate and had to be included in the model. The global negative radiative forcing of volcanoes like Rabaul and Nabro with up to $0.13\,\mathrm{Wm^{-2}}$ could have contributed to the observed slowdown of global warming in the early 2000s. This improves the new model simulations, especially in 2007 when several eruptions were not represented in previous studies. The results of the new model simulations now conform better with the values derived from satellite observations by Solomon et al. (2011).

The aerosol particles absorb the solar near-infrared and terrestrial infrared radiation and cause a radiative heating in the stratospheric aerosol layer. The aerosol radiative heating after large volcanic eruptions like Pinatubo induces an enhanced tropical upwelling, which causes a lofting of the injected SO_2 and the aerosol as well as other chemical tracers. Here, the radiative feedback on dynamics is required to achieve the aerosol extinction in the upper part of the volcanic aerosol plume in order to correspond with the observations.

The EMAC simulations show an additional seasonal signal of enhanced radiative heating in the northern hemisphere, induced by the convective transport of mineral dust to the UTLS in the Asian monsoon region.

Concerning the sulfate background conditions in volcanically quiescent periods, there was still a missing source in the literature. So the second part of this study was to search for a potential missing or underestimated source of OCS. Moreover, the global chemistry model EMAC had a significantly outdated sulfur compound chemistry reaction pathway scheme (Karu, 2019). This has been improved by the New Sulfur Chemistry Mechanism in this study and a newly implemented source of CS_2 and DMDS. Finally the model now includes the production of OCS via oxidation of DMS and CS_2. This leads to an increase in the OCS concentration in the tropics, with a maximum in the Asian monsoon region. As a result, the concentration of DMS is significantly reduced by these newly implemented oxidation reactions in the troposphere, subsequently less MSA is produced.

In order to validate this New Sulfur Chemistry Mechanism in the EMAC model simulations, comparisons with in-situ measurements of the aircraft campaign StratoClim have been carried out. The StratoClim campaign with the Russian high-flying research aircraft M55-Geophysica, reaching the lowermost stratosphere, took place during the Asian Summer Monsoon in 2017.

The results of this validation show that the New Sulfur Chemistry Mechanism, including additional sulfur emission sources of different sulfur containing species, improves the budget of OCS in the atmosphere and is important for sulfur background conditions. The in-situ measurements also indicate a daily cycle of OCS mixing ratios, which is not represented in the model simulations thus far.

Furthermore an enhanced number concentration of freshly nucleated aerosol particles was measured during the campaign, which is confirmed by the model simulations. Considering the OSIRIS satellite data and the model simulations, it was possible to identify the sulfur emissions of the volcano Sinabung as the source of increased SO_2 emissions, which were transformed into freshly nucleated particles. This demonstrates again that after an eruption the volcanic emissions dominate all other sulfur sources in the UTLS.

The aircraft measurements also detected meteoric dust in the UTLS (Schneider et al., 2020). This suggests that meteoric dust has to be implemented in the model to reproduce observations of higher aerosol concentrations in the upper stratosphere.

Different aspects discussed in this thesis show how important the cooperation between model simulations and field campaign in-situ measurements as well as satellite observations is to improve the understanding of the stratospheric aerosol.

Chapter 9

Outlook

Scientific work is never done. For every question that is answered another one will always be found and lead to further studies.

- For the calculations of the background aerosol, correct emission databases are a key factor. As long as emissions are wrong all following calculations are wrong. Subsequently more measurements instead of interpolated emission time series are required. For instance a greater variety of sulfur species like CS_2, H_2S, DMS and MSA should be measured to get more detailed information about intermediate steps in the sulfur reaction cycle.

- Furthermore, the improvement of a detailed sulfur chemistry is required by lab based kinetic studies of DMS, CS_2 and other sulfur species. As the remaining uncertainties are still high, it is important to find out more accurate reaction pathways and conversion efficiencies into OCS, including all reaction products and precisely measured rate constants and parameters.

- The Asian Summer Monsoon induces a seasonal signal in the northern hemisphere stratospheric aerosol optical depth and the radiative forcing. Accordingly, measurements of the seasonal cycle are required. For some species such as OCS a diurnal cycle is observed that is not taken into account in the model emissions.

- Meteoric dust particles have also been detected on the StratoClim campaign (Schneider et al., 2020). They can act as additional nucleation particles for sulfate aerosol in the upper and middle stratosphere, which is not implemented in the EMAC model. Further studies on this subject would improve the model for high stratospheric altitudes as well, which is neglected in all EMAC studies so far.

- A fully understood stratospheric aerosol cycle with climate coupling to radiative effects of the stratospheric aerosol layer is important for future climate predictions like in the IPCC. For this reason the time line of the volcanic emission inventory Table 4.1 has to be continued, as it is impossible to predict future volcanic eruptions. For this purpose, complete monitoring of the atmosphere with satellite measurements is essential. As seen in chapter 4, it is important to use multi instrument data to minimize data gaps and to reduce the uncertainty of calculated volcanic emissions.

- A perfectly running Chemistry Climate Model including a detailed sulfur chemistry for stratospheric aerosol would also be able to calculate short term forecasts after big volcanic eruptions. This would be important, especially for the case of a supervolcanic eruption like Tambora in 1815 with huge impact on the global climate and dropping temperatures for the following year, known as the year without summer, which also caused catastrophic effects on the global economy. The greatest known hazard potential of a volcanic winter is currently the Yellowstone super volcano in the USA and the Phlegraean fields in Italy. Therefore, it is important to monitor volcanic activities, as a previously inactive volcano can suddenly erupt with little warning even after a long period of inactivity, like Chaiten (Chile) in 2008.

- Volcanoes do not only emit SO_2, the individual composition of volcanic emissions also includes other gases such as water vapor, CO_2, H_2S and halogens, as well as volcanic ash, which still have to be implemented in the model. Volcanic ash is also relevant for the heterogeneous chemistry of SO_2 and sulfate.

- Another topic which is connected to climate change is to use the model to study the effects of stratospheric climate engineering by simulating artificial stratospheric aerosol (Crutzen, 2006). The optimum particle size for stratospheric climate engineering, depending on considerations of scattering properties as well as sedimentation and transport losses, is for diameters of ≈500 nm (Benduhn et al., 2016), similar to natural aerosols from volcanic eruptions.

Appendix A

Reaction Tables for the New Sulfur Chemistry Mechanism of MECCA

This appendix lists the tables for the chemical reactions, automatically generated by the EMAC submodel CAABA/MECCA in MESSy version 2.52, including the New Sulfur Chemistry Mechanism in section 6.2.

- The first table shows the chemistry reactions in the gas phase, implemented in CAABA/MECCA. Here the newly implemented sulfur containing reactions are marked with G9***JS.
- The second table shows the photolysis reactions, likewise marked with J900*JS.
- The next table contains the stratospheric heterogeneous reactions imported from the MSBM submodel.
- The last part contains the newly implemented recommended absorption cross sections, used in the JVAL submodel for the photolysis reactions of CS_2 and H_2S copied from Burkholder et al. (2015).

The Chemical Mechanism of MECCA

KPP version: `2.2.1_rs5`

MECCA version: `3.7f2`

Date: May 29, 2020.

Selected reactions:
“`((St && !Hg) || (Tr && S && !Cl && !Br && !I))`”

Number of aerosol phases: 0

Number of species in selected mechanism:

Gas phase:	109
Aqueous phase:	0
All species:	109

Number of reactions in selected mechanism:

Gas phase (Gnnn):	224
Aqueous phase (Annn):	0
Henry (Hnnn):	0
Photolysis (Jnnn):	45
Aqueous phase photolysis (PHnnn):	0
Heterogeneous (HETnnn):	11
Equilibria (EQnn):	0
Isotope exchange (IEX*):	0
Tagging (TAG*):	0
Dummy (Dnn):	0
All equations:	280

This document is part of the electronic supplement to our article
“The atmospheric chemistry box model CAABA/MECCA-3.0”
in Geosci. Model Dev. (2011), available at:
`http://www.geosci-model-dev.net`

Table 1: Gas phase reactions

#	labels	reaction	rate coefficient	reference
`G1000`	UpStTrG	$O_2 + O(^1D) \rightarrow O(^3P) + O_2$	`3.3E-11*EXP(55./temp)`	Sander et al. (2011)
`G1001`	UpStTrG	$O_2 + O(^3P) \rightarrow O_3$	`6.E-34*((temp/300.)**(-2.4))*cair`	Sander et al. (2011)
`G1002a`	UpStG	$O_3 + O(^1D) \rightarrow 2\ O_2$	`1.2E-10`	Sander et al. (2011)*
`G1003`	UpStG	$O_3 + O(^3P) \rightarrow 2\ O_2$	`8.E-12*EXP(-2060./temp)`	Sander et al. (2011)
`G2100`	UpStTrG	$H + O_2 \rightarrow HO_2$	`k_3rd(temp,cair,4.4E-32,1.3,7.5E-11,-0.2,0.6)`	Sander et al. (2011)
`G2101`	UpStG	$H + O_3 \rightarrow OH + O_2$	`1.4E-10*EXP(-470./temp)`	Sander et al. (2011)
`G2102`	UpStG	$H_2 + O(^1D) \rightarrow H + OH$	`1.2E-10`	Sander et al. (2011)
`G2103`	UpStG	$OH + O(^3P) \rightarrow H + O_2$	`1.8E-11*EXP(180./temp)`	Sander et al. (2011)
`G2104`	UpStTrG	$OH + O_3 \rightarrow HO_2 + O_2$	`1.7E-12*EXP(-940./temp)`	Sander et al. (2011)
`G2105`	UpStTrG	$OH + H_2 \rightarrow H_2O + H$	`2.8E-12*EXP(-1800./temp)`	Sander et al. (2011)
`G2106`	UpStG	$HO_2 + O(^3P) \rightarrow OH + O_2$	`3.E-11*EXP(200./temp)`	Sander et al. (2011)
`G2107`	UpStTrG	$HO_2 + O_3 \rightarrow OH + 2\ O_2$	`1.E-14*EXP(-490./temp)`	Sander et al. (2011)
`G2108a`	UpStG	$HO_2 + H \rightarrow 2\ OH$	`7.2E-11`	Sander et al. (2011)
`G2108b`	UpStG	$HO_2 + H \rightarrow H_2 + O_2$	`6.9E-12`	Sander et al. (2011)
`G2108c`	UpStG	$HO_2 + H \rightarrow O(^3P) + H_2O$	`1.6E-12`	Sander et al. (2011)
`G2109`	UpStTrG	$HO_2 + OH \rightarrow H_2O + O_2$	`4.8E-11*EXP(250./temp)`	Sander et al. (2011)
`G2110`	UpStTrG	$HO_2 + HO_2 \rightarrow H_2O_2 + O_2$	`k_HO2_HO2`	**?**, **?***
`G2111`	UpStTrG	$H_2O + O(^1D) \rightarrow 2\ OH$	`1.63E-10*EXP(60./temp)`	Sander et al. (2011)
`G2112`	UpStTrG	$H_2O_2 + OH \rightarrow H_2O + HO_2$	`1.8E-12`	Sander et al. (2011)
`G3100`	UpStGN	$N + O_2 \rightarrow NO + O(^3P)$	`1.5E-11*EXP(-3600./temp)`	Sander et al. (2011)
`G3101`	UpStTrGN	$N_2 + O(^1D) \rightarrow O(^3P) + N_2$	`2.15E-11*EXP(110./temp)`	Sander et al. (2011)
`G3102a`	UpStGN	$N_2O + O(^1D) \rightarrow 2\ NO$	`7.25E-11*EXP(20./temp)`	Sander et al. (2011)
`G3102b`	StGN	$N_2O + O(^1D) \rightarrow N_2 + O_2$	`4.63E-11*EXP(20./temp)`	Sander et al. (2011)
`G3103`	UpStTrGN	$NO + O_3 \rightarrow NO_2 + O_2$	`3.E-12*EXP(-1500./temp)`	Sander et al. (2011)
`G3104`	UpStGN	$NO + N \rightarrow O(^3P) + N_2$	`2.1E-11*EXP(100./temp)`	Sander et al. (2011)
`G3105`	UpStGN	$NO_2 + O(^3P) \rightarrow NO + O_2$	`5.1E-12*EXP(210./temp)`	Sander et al. (2011)
`G3106`	StTrGN	$NO_2 + O_3 \rightarrow NO_3 + O_2$	`1.2E-13*EXP(-2450./temp)`	Sander et al. (2011)
`G3107`	UpStGN	$NO_2 + N \rightarrow N_2O + O(^3P)$	`5.8E-12*EXP(220./temp)`	Sander et al. (2011)
`G3108`	StTrGN	$NO_3 + NO \rightarrow 2\ NO_2$	`1.5E-11*EXP(170./temp)`	Sander et al. (2011)
`G3109`	UpStTrGN	$NO_3 + NO_2 \rightarrow N_2O_5$	`k_NO3_NO2`	Sander et al. (2011)*
`G3110`	StTrGN	$N_2O_5 \rightarrow NO_2 + NO_3$	`k_NO3_NO2/(2.7E-27*EXP(11000./temp))`	Sander et al. (2011)*
`G3201`	UpStTrGN	$NO + HO_2 \rightarrow NO_2 + OH$	`3.3E-12*EXP(270./temp)`	Sander et al. (2011)

Table 1: Gas phase reactions (... continued)

#	labels	reaction	rate coefficient	reference
`G3202`	UpStTrGN	$NO_2 + OH \rightarrow HNO_3$	`k_3rd(temp,cair,1.8E-30,3.0,2.8E-11,0., 0.6)`	Sander et al. (2011)
`G3203`	StTrGN	$NO_2 + HO_2 \rightarrow HNO_4$	`k_NO2_HO2`	Sander et al. (2011)*
`G3206`	StTrGN	$HNO_3 + OH \rightarrow H_2O + NO_3$	`k_HNO3_OH`	Sander et al. (2011)*
`G3207`	StTrGN	$HNO_4 \rightarrow NO_2 + HO_2$	`k_NO2_HO2/(2.1E-27*EXP(10900./temp))`	Sander et al. (2011)*
`G3208`	StTrGN	$HNO_4 + OH \rightarrow NO_2 + H_2O$	`1.3E-12*EXP(380./temp)`	Sander et al. (2011)
`G4100`	UpStG	$CH_4 + O(^1D) \rightarrow .75\ CH_3O_2 + .75\ OH + .25\ HCHO + .4\ H + .05\ H_2$	`1.75E-10`	Sander et al. (2011)
`G4101`	StTrG	$CH_4 + OH \rightarrow CH_3O_2 + H_2O$	`1.85E-20*EXP(2.82*LOG(temp)-987./temp)`	Atkinson (2003)
`G4103`	StTrG	$CH_3O_2 + HO_2 \rightarrow CH_3OOH + O_2$	`4.1E-13*EXP(750./temp)`	Sander et al. (2011)*
`G4104`	UpStTrGN	$CH_3O_2 + NO \rightarrow HCHO + NO_2 + HO_2$	`2.8E-12*EXP(300./temp)`	Sander et al. (2011)
`G4106a`	StTrG	$CH_3O_2 + CH_3O_2 \rightarrow 2\ HCHO + 2\ HO_2$	`9.5E-14*EXP(390./temp)/(1.+1./ 26.2*EXP(1130./temp))`	Sander et al. (2011)
`G4106b`	StTrG	$CH_3O_2 + CH_3O_2 \rightarrow HCHO + CH_3OH + O_2$	`9.5E-14*EXP(390./temp)/(1.+ 26.2*EXP(-1130./temp))`	Sander et al. (2011)
`G4107`	StTrG	$CH_3OOH + OH \rightarrow .7\ CH_3O_2 + .3\ HCHO + .3\ OH + H_2O$	`k_CH3OOH_OH`	**?**
`G4108`	StTrG	$HCHO + OH \rightarrow CO + H_2O + HO_2$	`9.52E-18*EXP(2.03*LOG(temp)+636./temp)`	Sivakumaran et al. (2003)
`G4110`	UpStTrG	$CO + OH \rightarrow H + CO_2$	`(1.57E-13+cair*3.54E-33)`	McCabe et al. (2001)
`G6100`	UpStTrGCl	$Cl + O_3 \rightarrow ClO + O_2$	`2.8E-11*EXP(-250./temp)`	Atkinson et al. (2007)
`G6101`	UpStGCl	$ClO + O(^3P) \rightarrow Cl + O_2$	`2.5E-11*EXP(110./temp)`	Atkinson et al. (2007)
`G6102a`	StTrGCl	$ClO + ClO \rightarrow Cl_2 + O_2$	`1.0E-12*EXP(-1590./temp)`	Atkinson et al. (2007)
`G6102b`	StTrGCl	$ClO + ClO \rightarrow 2\ Cl + O_2$	`3.0E-11*EXP(-2450./temp)`	Atkinson et al. (2007)
`G6102c`	StTrGCl	$ClO + ClO \rightarrow Cl + OClO$	`3.5E-13*EXP(-1370./temp)`	Atkinson et al. (2007)
`G6102d`	StTrGCl	$ClO + ClO \rightarrow Cl_2O_2$	`k_ClO_ClO`	Atkinson et al. (2007)
`G6103`	StTrGCl	$Cl_2O_2 \rightarrow ClO + ClO$	`k_ClO_ClO/(1.72E-27*EXP(8649./temp))`	Atkinson et al. (2007), Sander et al. (2011)*
`G6200`	StGCl	$Cl + H_2 \rightarrow HCl + H$	`3.9E-11*EXP(-2310./temp)`	Atkinson et al. (2007)
`G6201a`	StGCl	$Cl + HO_2 \rightarrow HCl + O_2$	`4.4E-11-7.5E-11*EXP(-620./temp)`	Atkinson et al. (2007)
`G6201b`	StGCl	$Cl + HO_2 \rightarrow ClO + OH$	`7.5E-11*EXP(-620./temp)`	Atkinson et al. (2007)
`G6202`	StTrGCl	$Cl + H_2O_2 \rightarrow HCl + HO_2$	`1.1E-11*EXP(-980./temp)`	Atkinson et al. (2007)
`G6203`	StGCl	$ClO + OH \rightarrow .94\ Cl + .94\ HO_2 + .06\ HCl + .06\ O_2$	`7.3E-12*EXP(300./temp)`	Atkinson et al. (2007)
`G6204`	StTrGCl	$ClO + HO_2 \rightarrow HOCl + O_2$	`2.2E-12*EXP(340./temp)`	Atkinson et al. (2007)*
`G6205`	StTrGCl	$HCl + OH \rightarrow Cl + H_2O$	`1.7E-12*EXP(-230./temp)`	Atkinson et al. (2007)
`G6206`	StGCl	$HOCl + OH \rightarrow ClO + H_2O$	`3.0E-12*EXP(-500./temp)`	Sander et al. (2011)
`G6300`	UpStTrGNCl	$ClO + NO \rightarrow NO_2 + Cl$	`6.2E-12*EXP(295./temp)`	Atkinson et al. (2007)

Table 1: Gas phase reactions (... continued)

#	labels	reaction	rate coefficient	reference
`G6301`	StTrGNCl	$ClO + NO_2 \rightarrow ClNO_3$	`k_3rd_iupac(temp,cair,1.6E-31,3.4, 7.E-11,0.,0.4)`	Atkinson et al. (2007)
`G6303`	StGNCl	$ClNO_3 + O(^3P) \rightarrow ClO + NO_3$	`4.5E-12*EXP(-900./temp)`	Atkinson et al. (2007)
`G6304`	StTrGNCl	$ClNO_3 + Cl \rightarrow Cl_2 + NO_3$	`6.2E-12*EXP(145./temp)`	Atkinson et al. (2007)
`G6400`	StTrGCl	$Cl + CH_4 \rightarrow HCl + CH_3O_2$	`6.6E-12*EXP(-1240./temp)`	Atkinson et al. (2006)
`G6401`	StTrGCl	$Cl + HCHO \rightarrow HCl + CO + HO_2$	`8.1E-11*EXP(-34./temp)`	Atkinson et al. (2006)
`G6402`	StTrGCl	$Cl + CH_3OOH \rightarrow HCHO + HCl + OH$	`5.9E-11`	Atkinson et al. (2006)*
`G6403`	StTrGCl	$ClO + CH_3O_2 \rightarrow HO_2 + Cl + HCHO$	`3.3E-12*EXP(-115./temp)`	Sander et al. (2011)
`G6404`	StGCl	$CCl_4 + O(^1D) \rightarrow ClO + 3\ Cl$	`3.3E-10`	Sander et al. (2011)
`G6405`	StGCl	$CH_3Cl + O(^1D) \rightarrow OH + Cl$	`1.65E-10`	see note*
`G6406`	StGCl	$CH_3Cl + OH \rightarrow H_2O + Cl$	`2.4E-12*EXP(-1250./temp)`	Sander et al. (2011)
`G6407`	StGCCl	$CH_3CCl_3 + O(^1D) \rightarrow OH + 3\ Cl$	`3.E-10`	see note*
`G6408`	StTrGCCl	$CH_3CCl_3 + OH \rightarrow H_2O + 3\ Cl$	`1.64E-12*EXP(-1520./temp)`	Sander et al. (2011)
`G6500`	StGFCl	$CF_2Cl_2 + O(^1D) \rightarrow ClO + Cl$	`1.4E-10`	Sander et al. (2011)
`G6501`	StGFCl	$CFCl_3 + O(^1D) \rightarrow ClO + 2\ Cl$	`2.3E-10`	Sander et al. (2011)
`G7100`	StTrGBr	$Br + O_3 \rightarrow BrO + O_2$	`1.7E-11*EXP(-800./temp)`	Atkinson et al. (2007)
`G7101`	StGBr	$BrO + O(^3P) \rightarrow Br + O_2$	`1.9E-11*EXP(230./temp)`	Atkinson et al. (2007)
`G7102a`	StTrGBr	$BrO + BrO \rightarrow 2\ Br + O_2$	`2.7E-12`	Atkinson et al. (2007)
`G7102b`	StTrGBr	$BrO + BrO \rightarrow Br_2 + O_2$	`2.9E-14*EXP(840./temp)`	Atkinson et al. (2007)
`G7200`	StTrGBr	$Br + HO_2 \rightarrow HBr + O_2$	`7.7E-12*EXP(-450./temp)`	Atkinson et al. (2007)
`G7201`	StTrGBr	$BrO + HO_2 \rightarrow HOBr + O_2$	`4.5E-12*EXP(500./temp)`	Atkinson et al. (2007)
`G7202`	StTrGBr	$HBr + OH \rightarrow Br + H_2O$	`6.7E-12*EXP(155./temp)`	Atkinson et al. (2007)
`G7203`	StGBr	$HOBr + O(^3P) \rightarrow OH + BrO$	`1.2E-10*EXP(-430./temp)`	Atkinson et al. (2007)
`G7204`	StTrGBr	$Br_2 + OH \rightarrow HOBr + Br$	`2.0E-11*EXP(240./temp)`	Atkinson et al. (2007)
`G7301`	StTrGNBr	$BrO + NO \rightarrow Br + NO_2$	`8.7E-12*EXP(260./temp)`	Atkinson et al. (2007)
`G7302`	StTrGNBr	$BrO + NO_2 \rightarrow BrNO_3$	`k_BrO_NO2`	Atkinson et al. (2007)*
`G7400`	StTrGBr	$Br + HCHO \rightarrow HBr + CO + HO_2$	`7.7E-12*EXP(-580./temp)`	Atkinson et al. (2006)
`G7403`	StTrGBr	$CH_3Br + OH \rightarrow H_2O + Br$	`2.35E-12*EXP(-1300./temp)`	Sander et al. (2011)
`G7603a`	StTrGClBr	$BrO + ClO \rightarrow Br + OClO$	`1.6E-12*EXP(430./temp)`	Atkinson et al. (2007)
`G7603b`	StTrGClBr	$BrO + ClO \rightarrow Br + Cl + O_2$	`2.9E-12*EXP(220./temp)`	Atkinson et al. (2007)
`G7603c`	StTrGClBr	$BrO + ClO \rightarrow BrCl + O_2$	`5.8E-13*EXP(170./temp)`	Atkinson et al. (2007)
`G9101JS`	StTrGS	$S + OH \rightarrow SO + H$	`6.6E-11`	Burkholder et al. (2015)
`G9102`	StGS	$S + O_2 \rightarrow SO + O(^3P)$	`1.6E-12*EXP(100./temp)`	Burkholder et al. (2015)
`G9103JS`	StTrGS	$S + O_3 \rightarrow SO + O_2$	`1.2E-11`	Burkholder et al. (2015)
`G9104JS`	StTrGS	$SH + O(^3P) \rightarrow SO + H$	`1.6E-10`	Burkholder et al. (2015)

Table 1: Gas phase reactions (... continued)

#	labels	reaction	rate coefficient	reference
G9105	StGS	$SH + O_2 \rightarrow SO + OH$	4.E-19	Sander et al. (2006)
G9106JS	StTrGS	$SH + O_3 \rightarrow HSO + O_2$	9.0E-12*EXP(-280./temp)	Burkholder et al. (2015)
G9107aJS	StTrGS	$SH + H_2O_2 \rightarrow H_2S + HO_2$	5.0E-15	Burkholder et al. (2015)*
G9107bJS	StTrGS	$SH + H_2O_2 \rightarrow HSOH + OH$	5.0E-15	Burkholder et al. (2015)*
G9107cJS	StTrGS	$SH + H_2O_2 \rightarrow HSO + H_2O$	5.0E-15	Burkholder et al. (2015)*
G9108JS	StTrGS	$SH + NO \rightarrow HSNO$	k_3rd(temp,cair,2.4E-31,2.5,2.7E-11,0.,0.6)	Burkholder et al. (2015)
G9109JS	StTrGS	$SH + NO_2 \rightarrow HSO + NO$	2.9E-11*EXP(250./temp)	Burkholder et al. (2015)
G9110JS	StTrGS	$SH + N_2O \rightarrow HSO + N_2$	5.0E-16	Burkholder et al. (2015), Manion et al. (2015)
G9111JS	StTrGS	$SH + Cl_2 \rightarrow HSCl + Cl$	1.4E-11*EXP(-690./temp)	Burkholder et al. (2015)
G9112JS	StTrGS	$SH + BrCl \rightarrow HSCl + Br$	2.3E-11*EXP(350./temp)	Burkholder et al. (2015)
G9113JS	StTrGS	$SH + Br_2 \rightarrow HSBr + Br$	6.0E-11*EXP(160./temp)	Burkholder et al. (2015)
G9115JS	StTrGS	$H_2S + O(^3P) \rightarrow SH + OH$	9.2E-12*EXP(-1800./temp)	Burkholder et al. (2015)
G9116JS	StTrGS	$H_2S + OH \rightarrow SH + H_2O$	6.1E-12*EXP(-75./temp)	Burkholder et al. (2015)
G9117JS	StTrGS	$H_2S + O_3 \rightarrow SO_2 + H_2O$	2.6E-12*EXP(-21.8/(8.31*temp))	Burkholder et al. (2015), Manion et al. (2015)
G9118JS	StTrGS	$H_2S + HO_2 \rightarrow HSO + H_2O$	5.0E-12	Manion et al. (2015)
G9120JS	StTrGS	$H_2S + Cl \rightarrow SH + HCl$	3.7E-11*EXP(210./temp)	Burkholder et al. (2015)
G9121JS	StTrGS	$H_2S + Br \rightarrow SH + HBr$	1.4E-11*EXP(-2750./temp)	Burkholder et al. (2015)
G9122aJS	StTrGS	$HSO + O_2 \rightarrow SO + HO_2$	2.0E-17	Lovejoy et al. (1987)*
G9122bJS	StTrGS	$HSO + O_2 \rightarrow SO_2 + OH$	1.7E-15	Manion et al. (2015)
G9123aJS	StTrGS	$HSO + O_3 \rightarrow SH + 2O_2$	2.7E-13*EXP(-400./temp)	Wallington et al. (2017), Burkholder et al. (2015)
G9123bJS	StTrGS	$HSO + O_3 \rightarrow SO + OH + O_2$	1.0E-13	Wallington et al. (2017)*
G9123cJS	StTrGS	$HSO + O_3 \rightarrow HSO_2 + O_2$	1.0E-12*EXP(-1000./temp)	Wallington et al. (2017), Burkholder et al. (2015)
G9125JS	StTrGS	$HSO + NO_2 \rightarrow HSO_2 + NO$	9.6E-12	Burkholder et al. (2015)
G9126JS	StTrGS	$HSO_2 + O_2 \rightarrow SO_2 + HO_2$	3.0E-13	Burkholder et al. (2015)
G9201JS	StTrGS	$SO + OH \rightarrow SO_2 + H$	2.7E-11*EXP(335./temp)	Burkholder et al. (2015)
G9202	StGS	$SO + O_2 \rightarrow SO_2 + O(^3P)$	1.6E-13*EXP(-2280./temp)	Burkholder et al. (2015)
G9203	StGS	$SO + O_3 \rightarrow SO_2 + O_2$	3.4E-12*EXP(-1100./temp)	Sander et al. (2006)
G9204JS	StTrGS	$SO + NO_2 \rightarrow SO_2 + NO$	1.4E-11	Burkholder et al. (2015)
G9205JS	StTrGS	$SO + ClO \rightarrow SO_2 + Cl$	2.8E-11	Burkholder et al. (2015)
G9206JS	StTrGS	$SO + OClO \rightarrow SO_2 + ClO$	1.9E-12	Burkholder et al. (2015)

Table 1: Gas phase reactions (... continued)

#	labels	reaction	rate coefficient	reference
G9207JS	StTrGS	$SO + BrO \rightarrow SO_2 + Br$	5.7E-11	Burkholder et al. (2015)
G9208JS	StTrGS	$SO_2 + O(^3P) \rightarrow SO_3$	k_3rd(temp,cair,1.8E-33,-2.,4.2E-14, -1.8,0.6)	Burkholder et al. (2015)
G9209JS	StTrGS	$SO_2 + OH \rightarrow HOSO_2$	k_3rd(temp,cair,3.3E-31,4.3,1.6E-12,0., 0.6)	Burkholder et al. (2015)
G9210JS	StTrGS	$HOSO_2 + O_2 \rightarrow SO_3 + HO_2$	1.3E-12*EXP(-330./temp)	Burkholder et al. (2015)
G9211JS	StTrGS	$SO_2 + O_3 \rightarrow SO_3 + O_2$	3.0E-12*EXP(-7000./temp)	Burkholder et al. (2015)*
G9212JS	StTrGS	$SO_2 + HO_2 \rightarrow SO_3 + OH$	1.0E-18	Burkholder et al. (2015)*
G9213JS	StTrGS	$SO_2 + NO_2 \rightarrow SO_3 + NO$	2.0E-26	Burkholder et al. (2015)*
G9214JS	StTrGS	$SO_2 + NO_3 \rightarrow SO_3 + NO_2$	7.0E-21	Wallington et al. (2017)*
G9215JS	StTrGS	$SO_2 + ClO \rightarrow SO_3 + Cl$	4.0E-18	Burkholder et al. (2015)*
G9221JS	StTrGS	$SO_2 + CH_3O_2 \rightarrow CH_3O_2SO_2$	5.0E-17	Burkholder et al. (2015)*
G9223	StTrGS	$SO_3 + H_2O \rightarrow H_2SO_4$	8.5E-41*exp(6540./temp)*C(ind_H2O)	Sander et al. (2003)
G9224JS	StTrGS	$SO_3 + NH_3 \rightarrow H_3NSO_3$	k_3rd(temp,cair,3.6E-30,6.1,4.3E-11,0., 0.6)	Burkholder et al. (2015)
G9301aJS	StTrGS	$OCS + O(^3P) \rightarrow SO + CO$	2.1E-11*EXP(-2200./temp)	Burkholder et al. (2015)
G9301bJS	StTrGS	$OCS + O(^3P) \rightarrow S + CO_2$	1.6E-11*EXP(-2150./temp)	Wallington et al. (2017)
G9302	TrStGS	$OCS + OH \rightarrow SH + CO_2$	1.1E-13*EXP(-1200./temp)	Sander et al. (2006)
G9305JS	StTrGS	$OCS + Cl \rightarrow SCl + CO$	1.0E-16	Burkholder et al. (2015)*
G9401JS	StTrGS	$CS + O(^3P) \rightarrow S + CO$	2.7E-10*EXP(-760./temp)	Burkholder et al. (2015)
G9402JS	StTrGS	$CS + O_2 \rightarrow .84\ OCS + .16\ SO + .84\ O(^3P) + .16\ CO$	2.9E-19	Burkholder et al. (2015)
G9403JS	StTrGS	$CS + O_3 \rightarrow OCS + O_2$	3.0E-16	Burkholder et al. (2015)
G9404JS	StTrGS	$CS + NO_2 \rightarrow OCS + NO$	7.6E-17	Burkholder et al. (2015)
G9405JS	StTrGS	$CS_2 + O(^3P) \rightarrow SO + CS$	3.2E-11*EXP(-650./temp)	Burkholder et al. (2015)
G9406aJS	StTrGS	$CS_2 + OH \rightarrow OCS + SH$	4.3E-13	Burkholder et al. (2015), Wallington et al. (2017), Manion et al. (2015)
G9406bJS	StTrGS	$CS_2 + OH \rightarrow CS_2OH$	((1.25E-16*EXP(4550./temp)) /(1.81E-3*EXP(3400./temp)+temp))	Burkholder et al. (2015), Wallington et al. (2017)
G9407aJS	StTrGS	$CS_2OH \rightarrow CS_2 + OH$	1.6E-13*EXP(-5160./temp)	Wallington et al. (2017)
G9407bJS	StTrGS	$CS_2OH + O_2 \rightarrow OCS + HOSO$	2.8E-14*EXP(-0./temp)	Burkholder et al. (2015), Wallington et al. (2017)
G9408JS	StTrGS	$HOSO + O_2 \rightarrow SO_2 + HO_2$	4.6E-11	Burkholder et al. (2015), Wallington et al. (2017), Manion et al. (2015)

Table 1: Gas phase reactions (... continued)

#	labels	reaction	rate coefficient	reference
`G9410JS`	StTrGS	$CS_2 + Cl \rightarrow CS_2Cl$	`2.5E-16`	Burkholder et al. (2015)
`G9501aJS`	StTrGS	$CH_3S + O_2 \rightarrow CH_3 + SO_2$	`6.2E-8*(temp/298.)**(-3.8)*EXP(-51.5/(8.314E-3*temp))`	Manion et al. (2015)
`G9501bJS`	StTrGS	$CH_3S + O_2 \rightarrow CH_3SOO$	`1.2E-16*EXP(1580./temp)`	Wallington et al. (2017)
`G9501cJS`	StTrGS	$CH_3S + O_2 \rightarrow CH_2S + HO_2$	`1.85E-11*(temp/298.)**(-4.7) *EXP(-34.73/(temp*8.314E-3))`	**?**, Manion et al. (2015)
`G9501dJS`	StTrGS	$CH_2S + OH \rightarrow HCS + H_2O$	`1.0E-16`	Barnes et al. (1996)*
`G9501eJS`	StTrGS	$HCS + O_2 \rightarrow OCS + OH$	`1.0E-16`	Barnes et al. (1996)*
`G9502JS`	StTrGS	$CH_3S + O_3 \rightarrow CH_3SO + O_2$	`1.5E-12*EXP(360./temp)`	Burkholder et al. (2015)
`G9503bJS`	StTrGS	$CH_3S + NO \rightarrow CH_3SNO$	`k_3rd(temp,cair,3.2E-29,4.,3.5E-11,1.8,0.6)`	Burkholder et al. (2015)
`G9504JS`	StTrGS	$CH_3S + NO_2 \rightarrow CH_3SO + NO$	`3.0E-11*EXP(240./temp)`	Burkholder et al. (2015)
`G9505JS`	StTrGS	$CH_3S + CO \rightarrow OCS + CH_3$	`8.4E-13*(temp/298)**1.57*EXP(-27.9/(8.314E-3*temp))`	Manion et al. (2015)
`G9506JS`	StTrGS	$CH_3S + Br_2 \rightarrow BrSCH_3 + Br$	`1.7E-10`	Burkholder et al. (2015)
`G9507JS`	StTrGS	$CH_3SH + OH \rightarrow CH_3S + H_2O$	`9.9E-12*EXP(360./temp)`	Burkholder et al. (2015)
`G9509JS`	StTrGS	$CH_3SH + NO_3 \rightarrow CH_3S + HNO_3$	`4.4E-13*EXP(210./temp)`	Burkholder et al. (2015), Wallington et al. (2017)
`G9510JS`	StTrGS	$CH_3SH + Cl \rightarrow .98\ CH_3S + .02\ CH_2SH + HCl$	`1.2E-10*EXP(150./temp)`	Burkholder et al. (2015), Wallington et al. (2017)
`G9511JS`	StTrGS	$CH_3SH + Br \rightarrow CH_3S + HBr$	`9.2E-12*EXP(-390./temp)`	Burkholder et al. (2015)
`G9512JS`	StTrGS	$CH_3SH + BrO \rightarrow CH_3S + HOBr$	`3.5E-14`	Burkholder et al. (2015), Manion et al. (2015)
`G9517aJS`	StTrGS	$CH_3SO + O_3 \rightarrow CH_2SO + OH + O_2$	`4.0E-13`	Burkholder et al. (2015)
`G9517bJS`	StTrGS	$CH_3SO + O_3 \rightarrow CH_3S + 2O_2$	`4.0E-13`	Burkholder et al. (2015)
`G9518JS`	StTrGS	$CH_3SO + NO_2 \rightarrow CH_3SOO + NO$	`1.2E-11`	Burkholder et al. (2015)
`G9519JS`	StTrGS	$CH_3SOO \rightarrow CH_3S + O_2$	`3.5E10*exp(-3560./temp)`	Wallington et al. (2017)
`G9521JS`	StTrGS	$CH_3SOO + NO \rightarrow CH_3S + NO + O_2$	`1.1E-11`	Burkholder et al. (2015)
`G9522JS`	StTrGS	$CH_3SOO + NO_2 \rightarrow CH_3S + NO_2 + O_2$	`2.2E-11`	Burkholder et al. (2015), Wallington et al. (2017)
`G9523`	TrGS	$CH_3SOO \rightarrow SO_2 + CH_3O_2$	`1.8E13*EXP(-8661./temp)`	Barone et al. (1995)
`G9524`	TrGS	$CH_3SOO + O_3 \rightarrow CH_3SO_3$	`3.E-13`	Barone et al. (1995)
`G9525JS`	StTrGS	$CH_3SOO + NO_2 \rightarrow CH_3SO_3 + NO$	`2.2E-12`	Burkholder et al. (2015), Wallington et al. (2017)
`G9526`	TrGS	$CH_3SO_3 + HO_2 \rightarrow CH_3SO_3H + O_2$	`5.E-11`	Barone et al. (1995)

Table 1: Gas phase reactions (... continued)

#	labels	reaction	rate coefficient	reference
`G9527`	StTrGS	$CH_3SO_3H + OH \rightarrow CH_3SO_3 + H_2O$	`8.3E-15`	Burkholder et al. (2015)
`G9601JS`	StTrGS	$DMS + O(^3P) \rightarrow CH_3SO + CH_3$	`1.3E-11*EXP(410./temp)`	Burkholder et al. (2015)
`G9602b`	TrGS	$DMS + OH \rightarrow DMSO + HO_2$	`k_DMS_OH`	Atkinson et al. (2004)*
`G9602aJS`	StTrGS	$DMS + OH \rightarrow CH_3SCH_2 + H_2O$	`1.2E-11*EXP(-280./temp)`	Burkholder et al. (2015), Wallington et al. (2017)
`G9602bJS`	StTrGS	$DMS + OH \rightarrow CH_3S + CH_3OH$	`1.2E-11*EXP(-280./temp)`	Wallington et al. (2017)
`G9602cJS`	StTrGS	$DMS + OH \rightarrow CH_3SOH + CH_3$	`1.2E-11*EXP(-280./temp)`	Wallington et al. (2017)
`G9602dJS`	StTrGS	$DMS + OH \rightarrow (CH_3)_2SOH$	`1.2E-11*EXP(-280./temp)`	Burkholder et al. (2015), Wallington et al. (2017)
`G9604JS`	StTrGS	$DMS + O_3 \rightarrow DMSO + O_2$	`2.8E-22`	Burkholder et al. (2015), Manion et al. (2015)*
`G9605`	TrGS	$DMS + NO_3 \rightarrow CH_3SOO + HNO_3 + HCHO$	`1.9E-13*EXP(520./temp)`	Atkinson et al. (2004)
`G9605aJS`	StTrGS	$DMS + NO_3 \rightarrow CH_3SCH_2 + HNO_3$	`1.9E-13*EXP(530./temp)`	Burkholder et al. (2015)
`G9607`	TrGS	$DMS + Cl \rightarrow CH_3SOO + HCl + HCHO$	`3.3E-10`	Atkinson et al. (2004)
`G9607aJS`	StTrGS	$DMS + Cl \rightarrow CH_3SCH_2 + HCl$	`9.4E-11*EXP(190./temp)`	Burkholder et al. (2015)*
`G9607bJS`	StTrGS	$DMS + Cl \rightarrow ClSCH_3 + CH_3$	`3.5E-10`	Wallington et al. (2017)*
`G9607cJS`	StTrGS	$DMS + Cl \rightarrow CH_3S + CH_3Cl$	`9.4E-11*EXP(190./temp)`	Wallington et al. (2017)
`G9607dJS`	StTrGS	$DMS + Cl \rightarrow ClS(CH_3)_2$	`1.9E-10`	Wallington et al. (2017)
`G9608JS`	StTrGS	$DMS + ClO \rightarrow .73\ DMSO + .73\ Cl + .27\ CH_3SCH_2 + .27\ HOCl$	`2.1E-15*EXP(340./temp)`	Wallington et al. (2017), Burkholder et al. (2015)
`G9609JS`	StTrGS	$DMS + Cl_2 \rightarrow CH_3SCH_2Cl + HCl$	`5.0E-14`	Burkholder et al. (2015)*
`G9610`	TrGS	$DMS + Br \rightarrow CH_3SOO + HBr + HCHO$	`9.E-11*EXP(-2386./temp)`	Jefferson et al. (1994)
`G9610aJS`	StTrGS	$DMS + Br \rightarrow CH_3SCH_2 + HBr$	`9.0E-11*EXP(-2390./temp)`	Burkholder et al. (2015)
`G9611`	TrGS	$DMS + BrO \rightarrow DMSO + Br$	`4.4E-13`	Ingham et al. (1999)
`G9614JS`	StTrGS	$DMSO + O(^3P) \rightarrow SO_2 + 2CH_3$	`2.0E-12*EXP(440./temp)`	Burkholder et al. (2015)
`G9615JS`	StTrGS	$DMSO + NO_3 \rightarrow CH_3(O)S(O)CH_3 + NO_2$	`2.9E-13`	Burkholder et al. (2015)
`G9616aJS`	StTrGS	$DMSO + Cl \rightarrow CH_3S(O)CH_2 + HCl$	`1.4E-11`	Burkholder et al. (2015)
`G9616bJS`	StTrGS	$DMSO + Cl \rightarrow CH_3(Cl)S(O)CH_3$	`1.2E-10`	Burkholder et al. (2015)
`G9618JS`	StTrGS	$DMSO + Br \rightarrow CH_3SCH_2O + HBr$	`1.1E-14`	Burkholder et al. (2015), Manion et al. (2015)
`G9620`	TrGS	$DMSO + OH \rightarrow .6\ SO_2 + .4\ CH_3SO_3H + HCHO + .6\ CH_3O_2 + .4\ HO_2$	`1.E-10`	Hynes and Wine (1996)
`G9620aJS`	StTrGS	$DMSO + OH \rightarrow CH_3S(O)OH + CH_3$	`6.1E-12*EXP(800./temp)`	Burkholder et al. (2015)
`G9621JS`	StTrGS	$CH_3S(O)OH + OH \rightarrow .9\ SO_2 + .9\ CH_3 + .9\ H_2O$	`9.0E-11`	Burkholder et al. (2015)
`G9621aJS`	StTrGS	$CH_3S(O)OH + OH \rightarrow .1\ CH_3SO_3H + .1\ H$	`9.0E-11`	Chen et al. (2018)*

Table 1: Gas phase reactions (... continued)

#	labels	reaction	rate coefficient	reference
`G9622JS`	StTrGS	$CH_3S(O)OH + O_3 \rightarrow CH_3SO_3H + O_2$	`2.0E-18`	Chen et al. (2018)
`G9623JS`	StTrGS	$DMDS + O(^3P) \rightarrow CH_3SO + CH_3S$	`3.9E-11*EXP(290./temp)`	Burkholder et al. (2015)
`G9624aJS`	StTrGS	$DMDS + OH \rightarrow CH_3SH + CH_3SO$	`6.0E-11*EXP(400./temp)`	Wallington et al. (2017)
`G9624bJS`	StTrGS	$DMDS + OH \rightarrow CH_3S + CH_3SOH$	`6.0E-11*EXP(400./temp)`	Wallington et al. (2017)
`G9624cJS`	StTrGS	$DMDS + OH \rightarrow CH_3SS(OH)CH_3$	`6.0E-11*EXP(400./temp)`	Burkholder et al. (2015)
`G9625JS`	StTrGS	$DMDS + NO_3 \rightarrow CH_3S + CH_3SO + NO_2$	`5.0E-13*EXP(60./temp)`	Burkholder et al. (2015)
`G9701JS`	StTrGS	$CH_3SCH_2 + O_2 \rightarrow CH_3SCH_2O_2$	`5.7E-12`	Burkholder et al. (2015), **?**
`G9703aJS`	StTrGS	$CH_3SCH_2O_2 + NO \rightarrow CH_3S + HCHO + NO_2$	`4.9E-12*EXP(260./temp)`	Burkholder et al. (2015)
`G9703bJS`	StTrGS	$CH_3SCH_2O_2 + NO \rightarrow CH_3SCH_2O + NO_2$	`4.9E-12*EXP(260./temp)`	Wallington et al. (2017)
`G9704JS`	StTrGS	$CH_3SCH_2O_2 + NO_2 \rightarrow CH_3SCH_2O_2NO_2$	`9E-12`	Wallington et al. (2017)
`G9705aJS`	StTrGS	$CH_3SCH_2O_2 + CH_3SCH_2O_2 \rightarrow CH_3SCHO + CH_3SCH_2OH + O_2$	`1.0E-11`	Wallington et al. (2017)
`G9705bJS`	StTrGS	$CH_3SCH_2O_2 + CH_3SCH_2O_2 \rightarrow CH_3SCH_2O + CH_3SCH_2O + O_2$	`1.0E-11`	Burkholder et al. (2015)
`G9706JS`	StTrGS	$CH_3SCH_2O + O_2 \rightarrow CH_3SCHO + HO_2$	`5.0E-15`	Barnes et al. (1985), **?**
`G9707JS`	StTrGS	$CH_3SCH_2O \rightarrow CH_3S + HCHO$	`1.0E-16`	Burkholder et al. (2015), Wallington et al. (2017)*
`G9708JS`	StTrGS	$CH_3SCHO + OH \rightarrow OCS + CH_3 + H_2O$	`1.1E-11`	Barnes et al. (1985)*
`G9709JS`	StTrGS	$CH_2SH + O_2 \rightarrow CH_2S + HO_2$	`6.5E-12`	Burkholder et al. (2015)
`G01Diag`	StTrG	$O_3(s) \rightarrow LO_3(s)$	`k_O3s`	Roelofs and Lelieveld (1997)

Table 2: Photolysis reactions

#	labels	reaction	rate coefficient	reference
`J9000JS`	TrStJSG	$OCS + h\nu \rightarrow S + CO$	`JX(ip_OCS)`	Sander et al. (2014)
`J9001JS`	TrStJSG	$SO_2 + h\nu \rightarrow SO + O(^3P)$	`JX(ip_SO2)`	Sander et al. (2014)*
`J9002aJS`	TrStJSG	$SO_3 + h\nu \rightarrow SO_2 + O(^3P)$	`JX(ip_SO3)`	see note*
`J9003JS`	TrStJSG	$H_2SO_4 + h\nu \rightarrow SO_3 + H_2O$	`JX(ip_H2SO4)`	Vaida et al. (2003)
`J9004aJS`	TrStJSG	$H_2S + h\nu \rightarrow S + H_2$	`JX(ip_H2S)`	Burkholder et al. (2015)*
`J9005JS`	TrStJSG	$CS_2 + h\nu \rightarrow SO_2 + CS$	`JX(ip_CS2)`	Burkholder et al. (2015)
`J1000a`	UpStTrGJ	$O_2 + h\nu \rightarrow O(^3P) + O(^3P)$	`jx(ip_O2)`	Sander et al. (2014)
`J1001a`	UpStTrGJ	$O_3 + h\nu \rightarrow O(^1D) + O_2$	`jx(ip_O1D)`	Sander et al. (2014)
`J1001b`	UpStTrGJ	$O_3 + h\nu \rightarrow O(^3P) + O_2$	`jx(ip_O3P)`	Sander et al. (2014)
`J2100a`	UpStGJ	$H_2O + h\nu \rightarrow H + OH$	`jx(ip_H2O)`	Sander et al. (2014)
`J2101`	UpStTrGJ	$H_2O_2 + h\nu \rightarrow 2\ OH$	`jx(ip_H2O2)`	Sander et al. (2014)
`J3100`	UpStGNJ	$N_2O + h\nu \rightarrow O(^1D) + N_2$	`jx(ip_N2O)`	Sander et al. (2014)
`J3101`	UpStTrGNJ	$NO_2 + h\nu \rightarrow NO + O(^3P)$	`jx(ip_NO2)`	Sander et al. (2014)
`J3102a`	UpStGNJ	$NO + h\nu \rightarrow N + O(^3P)$	`jx(ip_NO)`	Sander et al. (2014)
`J3103a`	UpStTrGNJ	$NO_3 + h\nu \rightarrow NO_2 + O(^3P)$	`jx(ip_NO2O)`	Sander et al. (2014)
`J3103b`	UpStTrGNJ	$NO_3 + h\nu \rightarrow NO + O_2$	`jx(ip_NOO2)`	Sander et al. (2014)
`J3104`	StTrGNJ	$N_2O_5 + h\nu \rightarrow NO_2 + NO_3$	`jx(ip_N2O5)`	Sander et al. (2014)
`J3201`	StTrGNJ	$HNO_3 + h\nu \rightarrow NO_2 + OH$	`jx(ip_HNO3)`	Sander et al. (2014)
`J3202`	StTrGNJ	$HNO_4 + h\nu \rightarrow .667\ NO_2 + .667\ HO_2 + .333\ NO_3 + .333\ OH$	`jx(ip_HNO4)`	Sander et al. (2014)
`J4100`	StTrGJ	$CH_3OOH + h\nu \rightarrow HCHO + OH + HO_2$	`jx(ip_CH3OOH)`	Sander et al. (2014)
`J4101a`	StTrGJ	$HCHO + h\nu \rightarrow H_2 + CO$	`jx(ip_COH2)`	Sander et al. (2014)
`J4101b`	StTrGJ	$HCHO + h\nu \rightarrow H + CO + HO_2$	`jx(ip_CHOH)`	Sander et al. (2014)
`J4102`	StGJ	$CO_2 + h\nu \rightarrow CO + O(^3P)$	`jx(ip_CO2)`	Sander et al. (2014)
`J4103`	StGJ	$CH_4 + h\nu \rightarrow CO + 0.31\ H + 0.69\ H_2 + 1.155\ H_2O$	`jx(ip_CH4)`	Sander et al. (2014)
`J6000`	StTrGClJ	$Cl_2 + h\nu \rightarrow Cl + Cl$	`jx(ip_Cl2)`	Sander et al. (2014)
`J6100`	StTrGClJ	$Cl_2O_2 + h\nu \rightarrow 2\ Cl$	`jx(ip_Cl2O2)`	Sander et al. (2014)
`J6101`	StTrGClJ	$OClO + h\nu \rightarrow ClO + O(^3P)$	`jx(ip_OClO)`	Sander et al. (2014)
`J6200`	StGClJ	$HCl + h\nu \rightarrow Cl + H$	`jx(ip_HCl)`	Sander et al. (2014)
`J6201`	StTrGClJ	$HOCl + h\nu \rightarrow OH + Cl$	`jx(ip_HOCl)`	Sander et al. (2014)
`J6301a`	StTrGNClJ	$ClNO_3 + h\nu \rightarrow Cl + NO_3$	`jx(ip_ClNO3)`	Sander et al. (2014)
`J6301b`	StTrGNClJ	$ClNO_3 + h\nu \rightarrow ClO + NO_2$	`jx(ip_ClONO2)`	Sander et al. (2014)
`J6400`	StGClJ	$CH_3Cl + h\nu \rightarrow Cl + CH_3O_2$	`jx(ip_CH3Cl)`	Sander et al. (2014)
`J6401`	StGClJ	$CCl_4 + h\nu \rightarrow 4\ Cl$	`jx(ip_CCl4)`	Sander et al. (2014)
`J6402`	StGCClJ	$CH_3CCl_3 + h\nu \rightarrow 3\ Cl$	`jx(ip_CH3CCl3)`	Sander et al. (2014)

Table 2: Photolysis reactions (... continued)

#	labels	reaction	rate coefficient	reference
`J6500`	StGFClJ	$CFCl_3 + h\nu \rightarrow 3\ Cl$	`jx(ip_CFCl3)`	Sander et al. (2014)
`J6501`	StGFClJ	$CF_2Cl_2 + h\nu \rightarrow 2\ Cl$	`jx(ip_CF2Cl2)`	Sander et al. (2014)
`J7000`	StTrGBrJ	$Br_2 + h\nu \rightarrow Br + Br$	`jx(ip_Br2)`	Sander et al. (2014)
`J7100`	StTrGBrJ	$BrO + h\nu \rightarrow Br + O(^3P)$	`jx(ip_BrO)`	Sander et al. (2014)
`J7200`	StTrGBrJ	$HOBr + h\nu \rightarrow Br + OH$	`jx(ip_HOBr)`	Sander et al. (2014)
`J7301`	StTrGNBrJ	$BrNO_3 + h\nu \rightarrow 0.85\ Br + 0.85\ NO_3 + 0.15\ BrO + 0.15\ NO_2$	`jx(ip_BrNO3)`	Sander et al. (2014)*
`J7400`	StGBrJ	$CH_3Br + h\nu \rightarrow Br + CH_3O_2$	`jx(ip_CH3Br)`	Sander et al. (2014)
`J7500`	StGFBrJ	$CF_3Br + h\nu \rightarrow Br$	`jx(ip_CF3Br)`	Sander et al. (2014)
`J7600`	StTrGClBrJ	$BrCl + h\nu \rightarrow Br + Cl$	`jx(ip_BrCl)`	Sander et al. (2014)
`J7601`	StGFBrJ	$CF_2ClBr + h\nu \rightarrow Br + Cl$	`jx(ip_CF2ClBr)`	Sander et al. (2014)
`J9004`	StGS	$H_2SO_4 \rightarrow$ meteor	`k_meteor`	Bruehl et al. (2015)

General notes

J-values are calculated with an external module (e.g., JVAL) and then supplied to the MECCA chemistry.

Values that originate from the Master Chemical Mechanism (MCM) by Rickard and Pascoe (2009) are translated according in the following way:
J(11) → `jx(ip_COH2)`
J(12) → `jx(ip_CHOH)`
J(15) → `jx(ip_HOCH2CHO)`
J(18) → `jx(ip_MACR)`
J(22) → `jx(ip_ACETOL)`
J(23)+J(24) → `jx(ip_MVK)`
J(31)+J(32)+J(33) → `jx(ip_GLYOX)`
J(34) → `jx(ip_MGLYOX)`
J(41) → `jx(ip_CH3OOH)`
J(53) → $J(iC_3H_7ONO_2)$
J(54) → $J(iC_3H_7ONO_2)$
J(55) → $J(iC_3H_7ONO_2)$
J(56)+J(57) → `jx(ip_NOA)`

Specific notes

`J9001JS`: 552.3 kJ mol-1 217 nm (1)

`J9002aJS`: 348.1 kJ mol-1 343 nm (1)

`J9004aJS`: 297.5 kJ mol-1 401.7 nm (1)

`J7301`: The quantum yields are recommended by Sander et al. (2011) for $\lambda > 300$nm and used here for the entire spectrum.

Table 6: Heterogeneous reactions

#	labels	reaction	rate coefficient	reference
`HET200`	StHetN	$N_2O_5 + H_2O \rightarrow 2\ HNO_3$	`khet_St(ihs_N2O5_H2O)`	see general notes*
`HET410`	StHetCl	$HOCl + HCl \rightarrow Cl_2 + H_2O$	`khet_St(ihs_HOCl_HCl)`	see general notes*
`HET420`	StHetNCl	$ClNO_3 + HCl \rightarrow Cl_2 + HNO_3$	`khet_St(ihs_ClNO3_HCl)`	see general notes*
`HET421`	StHetNCl	$ClNO_3 + H_2O \rightarrow HOCl + HNO_3$	`khet_St(ihs_ClNO3_H2O)`	see general notes*
`HET422`	StHetNCl	$N_2O_5 + HCl \rightarrow ClNO_2 + HNO_3$	`khet_St(ihs_N2O5_HCl)`	see general notes*
`HET510`	StHetBr	$HOBr + HBr \rightarrow Br_2 + H_2O$	`khet_St(ihs_HOBr_HBr)`	see general notes*
`HET520`	StHetNBr	$BrNO_3 + H_2O \rightarrow HOBr + HNO_3$	`khet_St(ihs_BrNO3_H2O)`	see general notes*
`HET540`	StHetNClBr	$ClNO_3 + HBr \rightarrow BrCl + HNO_3$	`khet_St(ihs_ClNO3_HBr)`	see general notes*
`HET541`	StHetNClBr	$BrNO_3 + HCl \rightarrow BrCl + HNO_3$	`khet_St(ihs_BrNO3_HCl)`	see general notes*
`HET542`	StHetClBr	$HOCl + HBr \rightarrow BrCl + H_2O$	`khet_St(ihs_HOCl_HBr)`	see general notes*
`HET543`	StHetClBr	$HOBr + HCl \rightarrow BrCl + H_2O$	`khet_St(ihs_HOBr_HCl)`	see general notes*

General notes

Heterogeneous reaction rates are calculated with an external module (e.g., MECCA_KHET) and then supplied to the MECCA chemistry (see `www.messy-interface.org` for details)

I3. H_2S (hydrogen sulfide)

Back to Index

$H_2S + h\nu$	$\rightarrow H_2 + S(^3P)$	297.5 kJ mol^{-1}	401.7 nm	(1)
	$\rightarrow HS + H$	381.6 kJ mol^{-1}	313 nm	(2)

(Recommendation: 02-25, Note: 10-6, Evaluated: 10-6)

Absorption Cross Sections: The UV absorption spectrum of hydrogen sulfide, H_2S, is weak at wavelengths >250 nm. H_2S has a strong absorption band with diffuse structure centered near 200 nm and a broad VUV spectrum. The H_2S absorption cross section at 184.9 nm has been measured by Wine et al.[3] to be 3.82×10^{-18} cm^2 molecule^{-1} and at 121.6 nm by Watanabe and Jursa[2] and Vatsa and Volpp[1] to be 2.65×10^{-17} cm^2 molecule^{-1} (average value). The recommended absorption cross sections in Table 4I-2 are taken from Wu and Chen.[4] Note that the values given here do not reproduce the full detail of the diffuse band structure.

Photolysis Quantum Yield and Product Studies: Photolysis is a minor atmospheric loss process for H_2S throughout the troposphere and stratosphere.

Table 4I-2. Recommended Absorption Cross Sections of H_2S at 298 K

λ (nm)	$10^{20}\ \sigma$ (cm^2)	λ (nm)	$10^{20}\ \sigma$ (cm^2)
180	189	216	187
182	242	218	155
184	302	220	129
186	382	222	106
188	452	224	86.4
190	534	226	69.6
192	616	228	55.3
194	636	230	43.2
196	724	232	33.3
198	667	234	25.5
200	670	236	19.3
202	623	238	14.3
204	512	240	10.4
206	423	242	7.55
208	359	244	5.38
210	307	246	3.75
212	260	248	2.55
214	223	250	1.69

Note:
Wu and Chen[4]

(1) Vatsa, R. K.; Volpp, H.-R. Absorption cross-sections for some atmospherically important molecules at the H atom Lyman-α wavelength (121.567 nm). *Chem. Phys. Lett.* **2001**, *340*, 289-295.

(2) Watanabe, K.; Jursa, A. S. Absorption and photoionization cross sections of H_2O and H_2S. *J. Chem. Phys.* **1964**, *41*, 1650-1653.

(3) Wine, P. H.; Kreutter, N. M.; Gump, C. A.; Ravishankara, A. R. Kinetics of OH reactions with the atmospheric sulfur compounds H_2S, CH_3SH, CH_3SCH_3, and CH_3SSCH_3. *J. Phys. Chem.* **1981**, *85*, 2660-2665, doi:10.1021/j150618a019.

(4) Wu, C. Y. R.; Chen, F. Z. Temperature-dependent photoabsorption cross sections of H_2S in the 1600-2600 Å region. *J. Quant. Spectrosc. Radiat. Transfer* **1998**, *60*, 17-23.

I4. H_2SO_4 (sulfuric acid)

Back to Index

$H_2SO_4 + h\nu$	$\rightarrow OH + HSO_3$	397.1 kJ mol^{-1}	301 nm	(1)
	$\rightarrow 2OH + SO_2$	510.6 kJ mol^{-1}	234 nm	(2)

(Recommendation: 10-6, Note: 10-6, Evaluated: 10-6)

Absorption Cross Sections: The gas–phase absorption spectrum of sulfuric acid, H_2SO_4, was reported by Burkholder et al.[1] (195–330 nm) at 473 K, using diode array spectroscopy, to have cross sections $<1 \times 10^{-21}$ cm^2 molecule^{-1}. Hintze et al.[2] studied the spectrum of H_2SO_4 vapor at 403–423 K and reported an upper limit of 1 × 10^{-18} cm^2 $molecule^{-1}$ for the absorption cross sections between 140 and 170 nm and an upper limit of 1 × 10^{-19} cm^2 $molecule^{-1}$ in the wavelength range 170-195 nm.

Photolysis Quantum Yield and Product Studies: No recommendation.

(1) Burkholder, J. B.; Mills, M.; McKeen, S. Upper limit for the UV absorption cross sections of H_2SO_4. *Geophys. Res. Lett.* **2000**, *27*, 2493-2496.

(2) Hintze, P. E.; Kjaergaard, H. G.; Vaida, V.; Burkholder, J. B. Vibrational and electronic spectroscopy of sulfuric acid vapor. *J. Phys. Chem. A* **2003**, *107*, 1112-1118, doi:10.1021/jp0263626.

I5. CS_2 (carbon disulfide)

Back to Index

CS_2 + hν → CS + S(^{3}P) 440.2 kJ mol^{-1} 272 nm (1)
→ CS + S(^{1}D) 550.6 kJ mol^{-1} 217 nm (2)

(Recommendation: 10-6, Note: 15-10, Evaluated: 10-6)

Absorption Cross Sections: The UV absorption spectrum of carbon disulfide, CS_2, has two distinct highly structured bands with a strong absorption extending from 185 to 230 nm and a weaker band in the 290–380 nm range. The absorption cross sections have been measured in a number of studies (Cook and Ogawa[4] (60–96.5 nm, 298 K), Carnovale et al.[2] (31–248 nm, 298 K), Leroy et al.[8] (314–330 nm, 294 K), Leroy et al.[9] (314–330 nm, 197–288 K), Wine et al.[12] (280–360 nm, 298 K), Wu and Judge[13] (319–330 nm, 294 K), Dove et al.[5] (190–500 nm, 300–4000 K), Hearn and Joens[7] (296–334 nm, 300 K), Ahmed and Kumar[1] (188–340 nm, 300 K), Xu and Joens[14] (187–220 nm, 300 K), Chen and Wu[3] (180–228 nm, 295 K), Grosch et al.[6] (195–370 nm, 295–773 K), and Sunanda et al.[11] (105–226 nm, 298 K)), which are in reasonable agreement. Due to the high degree of structure in the absorption spectrum, absorption cross sections at specific wavelengths should be obtained from the original literature. The absorption cross sections in Table 4I-3 were obtained by averaging the data from Hearn and Joens[7] over 1 nm intervals.

Photolysis Quantum Yield and Product Studies: The photochemistry of CS_2 has been reviewed by Okabe[10] and discussed by Wine et al.[12] Wine et al. report that electronically excited CS_2 may react with O_2 to yield OCS.

Table 4I-3. Recommended Absorption Cross Sections of CS_2 at 298 K

λ (nm)	10^{20} σ (cm^2)	λ (nm)	10^{20} σ (cm^2)	λ (nm)	10^{20} σ (cm^2)	λ (nm)	10^{20} σ (cm^2)
275	0.017	299	2.017	323	5.180	347	0.328
276	0.020	300	1.879	324	3.517	348	0.109
277	0.027	301	3.269	325	8.628	349	0.368
278	0.043	302	3.166	326	5.023	350	0.239
279	0.050	303	3.131	327	3.481	351	0.127
280	0.053	304	4.438	328	2.849	352	0.255
281	0.062	305	4.461	329	2.848	353	0.066
282	0.080	306	3.658	330	3.802	354	0.172
283	0.103	307	5.122	331	1.301	355	0.247
284	0.122	308	7.101	332	3.057	356	0.052
285	0.158	309	4.930	333	1.552	357	0.133
286	0.209	310	8.838	334	1.506	358	0.055
287	0.254	311	5.611	335	1.375	359	0.059
288	0.309	312	6.692	336	0.861	360	0.119
289	0.445	313	8.148	337	1.377	361	0.042
290	0.438	314	7.842	338	0.591	362	0.048
291	0.635	315	9.440	339	1.121	363	0.021
292	0.640	316	7.039	340	0.489	364	0.037
293	0.878	317	9.462	341	0.386	365	0.012
294	0.801	318	7.159	342	0.573	366	0.036
295	1.137	319	9.803	343	0.387	367	0.023
296	1.134	320	4.518	344	0.556	368	0.020
297	1.861	321	6.122	345	0.353	369	0.011
298	2.287	322	4.221	346	0.350	370	0.018

Note: Hearn and Joens[7] average values

Appendix B

Glossaries

Acronyms

AIRS	Atmospheric Infrared Sounder
AMICA	Airborne Mid-Infrared CAvity enhanced spectrometer
AMS	Aerosol Mass Spectrometer
AOD	Aerosol Optical Depth
ASM	Asian Summer Monsoon
ATAL	Asian Tropopause Aerosol Layer
ATSR	Along Track Scanning Radiometer
ATTL	Asian Tropopause Transition Layer
BMIL	Base Model Interface Layer
BML	Base Model Layer
CAABA/MECCA	Chemistry As A Boxmodel Application/Module Efficiently Calculating the Chemistry of the Atmosphere
CALIOP	Cloud-Aerosol Lidar with Orthogonal Polarization
CALIPSO	Cloud-Aerosol Lidar and Infrared Pathfinder Satellite Observations
CARIBIC	Civil Aircraft for the Regular Investigation of the atmosphere Based on an Instrument Container
CCI	Climate Change Initiative
CCM	Chemistry Climate Model
CCMI	Chemistry Climate Model Initiative
CLS	Confined Lower Stratosphere
COLD	Carbon Oxide Laser Detector
COPAS	COndensation PArticle counting System
CPC	Condensation Particle Counter
DKRZ	Deutsches Klimarechenzentrum
DLR	Deutsches Zentrum für Luft- und Raumfahrt

ECHAM5	5^{th} generation of European Centre Hamburg general circulation model
ECMWF	European Centre for Medium-Range Weather Forecasts
EMAC	ECHAM5/MESSy Atmospheric Chemistry
ENSO	El Niño-Southern Oscillation
ENVISAT	European Environmental Satellite
EOSDIS	Earth Observing System Data and Information System of NASA
EQSAM3	3rd EQuilibrium Simplified Aerosol Model
ERBE	Earth Radiation Budget Experiment
ERBS	Earth Radiation Budget Satellite
ERICA	ERc Instrument for Chemical composition of Aerosols
ESA	European Space Agency
FOZAN	Fast OZone ANalizer
GMXe	Global Modal-aerosol eXtension
GOME-2	Global Ozone Monitoring Experiment–2
GOMOS	Global Ozone Monitoring by Occultation of Stars
GPC	gas-to-particle-conversion
IASI	Infrared Atmospheric Sounding Interferometer
IPCC	Intergovernmental Panel on Climate Change
IR	Infra Red
IUPAC	International Union of Pure and Applied Chemistry
JPL	Jet Propulsion Laboratory
KPP	Kinetic PreProcessor
LAMS	Laser Ablation Mass Spectrometer
MESSy	Modular Earth Submodel System
MIPAS	Michelson Interferometer for Passive Atmospheric Sounding
MSBM	Multiphase Stratospheric Box Model
NASA	National Aeronautics and Space Administration
NIST	National Institute of Standards and Technology
NTP	normal temperature (20°C) and pressure (1013 hPa)
OMI	Ozone Monitoring Instrument
OSIRIS	Optical Spectrograph and InfraRed Imaging System

ppb_v	parts per billion by volume (10^{-9})
ppm_v	parts per million by volume (10^{-6})
ppq_v	parts per quadrillion by volume (10^{-15})
ppt_v	parts per trillion by volume (10^{-12})
PSC	Polar Stratospheric Cloud
QBO	quasi-biennial oscillation
RAD	RADiation
SAGE	Stratospheric Aerosol and Gas Experiment
SMCL	SubModel Core Layer
SMIL	SubModel Interface Layer
StratoClim	Stratospheric and upper tropospheric processes for better climate predictions
TOMS	Total Ozone Mapping Spectrometer
UHSAS	Ultra High Sensitivity Aerosol Spectrometer
UTC	Universal Time Coordinated
UTLS	upper troposphere/lower stratosphere
UV	Ultra Violet
VEI	Volcanic Explosivity Index
WMO	World Meteorological Organization

Chemistry

Al	aluminum
Ca	calcium
CH_3SH	methyl mercaptan
CH_4	methane
CO	carbon monoxide
CO_2	carbon dioxide
CS_2	carbon disulfide
DMDS	dimethyl disulfide (CH_3SSCH_3)
DMS	dimethyl sulfide (CH_3SCH_3)
DMSO	dimethyl sulfoxide (CH_3SOCH_3)
Fe	iron
$FeMgSiO_4$	olivine
H_2O	water
H_2O	water vapor
H_2S	hydrogen sulfide
H_2SO_4	sulfuric acid
HCN	hydrogen cyanide
HNO_3	nitric acid
K	potassium
Mg	magnesium
MSA	methyl sulfonic acid (CH_3SO_3H)
N_2O	nitrous oxide
Na	sodium
Ni	nickel
NO_2	nitrogen dioxide
NO_3	nitrogen trioxide
NO_x	nitrogen oxide
O	elemental oxygen
O_2	oxygen
O_3	ozone
OCS	carbonyl sulfide
OH	hydroxyl radical

SH	hydrosulfide
Si	silicon
SO_2	sulfur dioxide
SO_3	sulfur trioxide

Symbols

Symbol	**Value/[Unit]**	**Description**
D	[-]	divergence
D_p	[nm]	particle diameter
$\overline{D_p}$	[nm]	mean particle diameter
f_{Csf}	[-]	Cunningham-slip-flow correction
f_{Slinn}	[-]	Slinn factor
g	$9.81\,\mathrm{m/s^2}$	gravitational acceleration
I	[W/sr]	intensity of the radiation
dI	[W/sr]	variation of the radiation intensity
M_A	28.97 g/mol	molar mass of dry air
N	[-]	number of aerosol particles
n	[$\mathrm{cm^{-3}}$]	number concentration
N_A	$6.022{\cdot}10^{23}\,\mathrm{mol^{-1}}$	Avogadro constant
n_N	[$\mathrm{\mu m^{-1}cm^{-3}}$]	particle size distribution
p	[hPa]	air pressure
p_s	[hPa]	surface pressure
Q_{abs}	[-]	absorption efficiency
Q_{sca}	[-]	scattering efficiency
Q_{ext}	[-]	extinction efficiency
q	[ppb ppm or ppt]	mixing ratio
r	[nm]	particle radius
T	[K or °C]	temperature (0 °C $\widehat{=}$ 273.15 K)
t	[s]	time
v_S	[m/s]	Stokes velocity
v_t	[m/s]	terminal sedimentation velocity
z	[m]	altitude coordinates
η_a	[$\mathrm{kg\ m^{-2}\ s^{-1}}$]	dynamic viscosity of air
λ_a	[m]	mean free path of air molecules

χ	[-]	number mixing ratio of the particles and the air molecules
π	3.14159... [-]	mathematical constant Pi
ρ_a	[kg/m^3]	air density
ρ_p	[kg/m^3]	aerosol particle density
σ_{abs}	[m^{-1}]	absorption coefficient
σ_{ext}	[m^{-1}]	extinction coefficient
σ_{sca}	[m^{-1}]	scattering coefficient
σ	[-]	standard deviation of the aerosol size distribution
τ	[-]	optical depth
ξ	[s^{-1}]	vorticity

List of Tables

List of Figures

References

Abdelkader, M., S. Metzger, R. E. Mamouri, M. Astitha, L. Barrie, Z. Levin, and J. Lelieveld
2015. Dust-air pollution dynamics over the eastern Mediterranean. *Atmospheric Chemistry and Physics*, 15(16):9173–9189.

Andersson, S. M., B. G. Martinsson, J. Friberg, C. A. M. Brenninkmeijer, A. Rauthe-Schöch, M. Hermann, P. F. J. van Velthoven, and A. Zahn
2013. Composition and evolution of volcanic aerosol from eruptions of Kasatochi, Sarychev and Eyjafjallajökull in 2008–2010 based on CARIBIC observations. *Atmospheric Chemistry and Physics*, 13(4):1781–1796.

Astitha, M., J. Lelieveld, M. Abdel Kader, A. Pozzer, and A. De Meij
2012. Parameterization of dust emissions in the global atmospheric chemistry-climate model EMAC: Impact of nudging and soil properties. *Atmospheric Chemistry and Physics*, 12(22):11057–11083.

Atkinson, R., D. L. Baulch, R. A. Cox, J. N. Crowley, R. F. Hampson, R. G. Hynes, M. E. Jenkin, M. J. Rossi, J. Troe, and T. J. Wallington
2007. Evaluated kinetic and photochemical data for atmospheric chemistry: Volume IV – gas phase reactions of organic halogen species. *Atmospheric Chemistry and Physics*, 7(6):16349–17067.

Barnes, I., K. H. Becker, and I. V. Patroescu
1994. The tropospheric oxidation of dimethyl sulfide: A new source of carbonyl sulfide. *Geophysical Research Letters*, 21(22):2389–2392.

Barnes, I., J. Hjorth, and N. Mihalopoulos
2006. Dimethyl sulfide and dimethyl sulfoxide and their oxidation in the atmosphere. *Chemical reviews*, 106(3):940–75.

Benduhn, F. and M. G. Lawrence
2013. An investigation of the role of sedimentation for stratospheric solar radiation management. *Journal of Geophysical Research: Atmospheres*, 118(14):7905–7921.

Benduhn, F., J. Schallock, and M. G. Lawrence
2016. Early growth dynamical implications for the steerability of stratospheric solar radiation management via sulfur aerosol particles. *Geophysical Research Letters*, 43(18):9956–9963.

Bertaux, J. L., E. Kyrölä, D. Fussen, A. Hauchecorne, F. Dalaudier, V. Sofieva, J. Tamminen, F. Vanhellemont, O. Fanton d'Andon, G. Barrot, A. Mangin, L. Blanot, J. C. Lebrun, K. Pérot,

T. Fehr, L. Saavedra, G. W. Leppelmeier, and R. Fraisse
2010. Global ozone monitoring by occultation of stars: an overview of GOMOS measurements on ENVISAT. *Atmospheric Chemistry and Physics*, 10(24):12091–12148.

Bingen, C., C. E. Robert, K. Stebel, C. Brühl, J. Schallock, F. Vanhellemont, N. Mateshvili, M. Höpfner, T. Trickl, J. E. Barnes, J. Jumelet, J.-P. Vernier, T. Popp, G. de Leeuw, and S. Pinnock
2017. Stratospheric aerosol data records for the climate change initiative: Development, validation and application to chemistry-climate modelling. *Remote Sensing of Environment*, 203:296–321.

Bingen, C., F. Vanhellemont, and D. Fussen
2003. A new regularized inversion method for the retrieval of stratospheric aerosol size distributions applied to 16 years of SAGE II data (1984-2000): Method, results and validation. *Annales Geophysicae*, 21(3):797–804.

Blake, N. J., D. G. Streets, J. H. Woo, I. J. Simpson, J. Green, S. Meinardi, K. Kita, E. Atlas, H. E. Fuelberg, G. Sachse, M. A. Avery, S. A. Vay, R. W. Talbot, J. E. Dibb, A. R. Bandy, D. C. Thornton, F. S. Rowland, and D. R. Blake
2004. Carbonyl sulfide and carbon disulfide: Large-scale distributions over the western Pacific and emissions from Asia during TRACE-P. *Journal of Geophysical Research D: Atmospheres*, 109(15):1–15.

Bluth, G. J., S. D. Doiron, C. C. Schnetzler, A. J. Krueger, and L. S. Walte
1992. Global Tracking of the SO2 Clouds from the June, 1991 Mount Pinatubo Eruptions. *Geophysical Research Letters*, 19(2):151–154.

Bönisch, H., A. Engel, T. Birner, P. Hoor, D. W. Tarasick, and E. A. Ray
2011. On the structural changes in the Brewer-Dobson circulation after 2000. *Atmospheric Chemistry and Physics*, 11(8):3937–3948.

Boucher, O.
2015. *Atmospheric Aerosols*. Dordrecht: Springer Netherlands.

Bourassa, A. E., L. A. Rieger, N. D. Lloyd, and D. A. Degenstein
2012a. Odin-OSIRIS stratospheric aerosol data product and SAGE III intercomparison. *Atmospheric Chemistry and Physics*, 12(1):605–614.

Bourassa, A. E., A. Robock, W. J. Randel, T. Deshler, L. A. Rieger, N. D. Lloyd, E. J. Llewellyn, and D. A. Degenstein
2012b. Large volcanic aerosol load in the stratosphere linked to Asian monsoon transport. *Science*, 336(6090):78–81.

Bourassa, A. E., C. Z. Roth, D. J. Zawada, L. A. Rieger, C. A. McLinden, and D. A. Degenstein
2018. Drift-corrected Odin-OSIRIS ozone product: Algorithm and updated stratospheric ozone trends. *Atmospheric Measurement Techniques*, 11(1):489–498.

Brewer, A. W.
1949. Evidence for a world circulation provided by the measurements of helium and water vapour distribution in the stratosphere. *Royal Meteorological Society*, 75:351–363.

Brühl, C., J. Lelieveld, P. J. Crutzen, and H. Tost
2012. The role of carbonyl sulphide as a source of stratospheric sulphate aerosol and its impact on climate. *Atmospheric Chemistry and Physics*, 12(3):1239–1253.

Brühl, C., J. Lelieveld, H. Tost, M. Höpfner, and N. Glatthor
2015. Stratospheric sulfur and its implications for radiative forcing simulated by the chemistry climate model EMAC. *Journal of Geophysical Research*, 120(5):2103–2118.

Brühl, C., J. Schallock, K. Klingmüller, C. Robert, C. Bingen, L. Clarisse, A. Heckel, and P. North
2018. Stratospheric aerosol radiative forcing simulated by the chemistry climate model EMAC using aerosol CCI satellite data. *Atmospheric Chemistry and Physics*, 18(April):1–15.

Brunamonti, S., T. Jorge, P. Oelsner, S. Hanumanthu, B. B. Singh, K. R. Kumar, S. Sonbawne, S. Meier, D. Singh, F. G. Wienhold, B. P. Luo, M. Boettcher, Y. Poltera, H. Jauhiainen, R. Kayastha, J. Karmacharya, R. Dirksen, M. Naja, M. Rex, S. Fadnavis, and T. Peter
2018. Balloon-borne measurements of temperature, water vapor, ozone and aerosol backscatter on the southern slopes of the Himalayas during StratoClim 2016–2017. *Atmospheric Chemistry and Physics*, 18(21):15937–15957.

Burkholder, J. B., S. P. Sander, J. Abbatt, J. R. Barker, R. E. Huie, C. E. Kolb, M. J. Kurylo, V. L. Orkin, D. M. Wilmouth, and P. H. Wine
2015. Chemical Kinetics and Photochemical Data for Use in Atmospheric Studies. Evaluation number 18. *JPL Publication 15-10.*

Cai, Y., D. C. Montague, W. Mooiweer-Bryan, and T. Deshler
2008. Performance characteristics of the ultra high sensitivity aerosol spectrometer for particles between 55 and 800 nm: Laboratory and field studies. *Journal of Aerosol Science*, 39(9):759–769.

Carn, S. A., L. Clarisse, and A. J. Prata
2016. Multi-decadal satellite measurements of global volcanic degassing. *Journal of Volcanology and Geothermal Research*, 311:99–134.

Chin, M. and D. D. Davis
1993. Global sources and sinks of OCS and CS2 and their distributions. *Global Biogeochemical Cycles*, 7(2):321–337.

Crutzen, P. J.
1976. The possible importance of CSO for the sulfate layer of the stratosphere. *Geophysical Research Letters*, 3(2):73–76.

Crutzen, P. J.
2006. Albedo Enhancement by Stratospheric Sulfur Injections: A Contribution to Resolve a Policy Dilemma? *Climatic Change*, 77(3-4):211–220.

Curtius, J.
2006. Nucleation of atmospheric aerosol particles. *Comptes Rendus Physique*, 7(9-10):1027–1045.

Diehl, T., A. Heil, M. Chin, X. Pan, D. Streets, M. Schultz, and S. Kinne
2012. Anthropogenic, biomass burning, and volcanic emissions of black carbon, organic carbon, and SO2 from 1980 to 2010 for hindcast model experiments. *Atmospheric Chemistry and Physics Discussions*, 12(9):24895–24954.

Dietmüller, S., P. Jöckel, H. Tost, M. Kunze, C. Gellhorn, S. Brinkop, C. Frömming, M. Ponater, B. Steil, A. Lauer, and J. Hendricks
2016. A new radiation infrastructure for the Modular Earth Submodel System (MESSy, based on version 2.51). *Geoscientific Model Development*, 9(6):2209–2222.

Eichinger, R., H. Garny, P. Šácha, J. Danker, S. Dietmüller, and S. Oberländer-Hayn
2020. Effects of missing gravity waves on stratospheric dynamics; part 1: climatology. *Climate Dynamics*, 54(5-6):3165–3183.

Fairlie, T. D., J. P. Vernier, M. Natarajan, and K. M. Bedka
2014. Dispersion of the Nabro volcanic plume and its relation to the Asian summer monsoon. *Atmospheric Chemistry and Physics*, 14(13):7045–7057.

Finlayson-Pitts, B. J. and J. N. J. Pitts
1986. *Atmospheric chemistry. Fundamentals and experimental techniques.* United States: John Wiley & Sons.

Fischer, H., M. Birk, C. Blom, B. Carli, M. Carlotti, T. von Clarmann, L. Delbouille, A. Dudhia, D. Ehhalt, M. Endemann, J. M. Flaud, R. Gessner, A. Kleinert, R. Koopman, J. Langen, M. López-Puertas, P. Mosner, H. Nett, H. Oelhaf, G. Perron, J. Remedios, M. Ridolfi, G. Stiller, and R. Zander
2008. MIPAS: an instrument for atmospheric and climate research. *Atmospheric Chemistry and Physics*, 8(8):2151–2188.

Ganzeveld, L. and J. Lelieveld
1995. Dry deposition parameterization in a chemistry general circulation model and its influence on the distribution of reactive trace gases. *Journal of Geophysical Research*, 100(D10):20999.

Gao, C., A. Robock, and C. Ammann
2008. Volcanic forcing of climate over the past 1500 years: An improved ice core-based index for climate models. *Journal of Geophysical Research Atmospheres*, 113(23):1–15.

Giorgetta, M. A., E. Manzini, and E. Roeckner
2002. Forcing of the quasi-biennial oscillation from a broad spectrum of atmospheric waves. *Geophysical Research Letters*, 29(8):86–1–86–4.

Giorgetta, M. A., E. Manzini, E. Roeckner, M. Esch, and L. Bengtsson
2006. Climatology and forcing of the quasi-biennial oscillation in the MAECHAM5 model. *Journal of Climate*, 19(16):3882–3901.

Glantz, P., A. Bourassa, A. Herber, T. Iversen, J. Karlsson, and A. Kirkevåg
2014. Remote sensing of aerosols in the Arctic for an evaluation of global climate model simulations. *Journal of Geophysical Research: Atmospheres*, 119:8169–8188.

Glatthor, N., M. Höpfner, I. T. Baker, J. Berry, J. E. Campbell, S. R. Kawa, G. Krysztofiak, A. Leyser, B.-M. Sinnhuber, G. P. Stiller, J. Stinecipher, and T. Von Clarmann
2015. Tropical sources and sinks of carbonyl sulfide observed from space. *Geophysical Research Letters*, 42(22):10,082–10,090.

Grainger, R. G., A. Lambert, C. D. Rodgers, F. W. Taylor, and T. Deshler
1995. Stratospheric aerosol effective radius, surface area and volume estimated from infrared measurements. *Journal of Geophysical Research*, 100(D8):16507–16518.

Grewe, V., D. Brunner, M. Dameris, J. Grenfell, R. Hein, D. Shindell, and J. Staehelin
2001. Origin and variability of upper tropospheric nitrogen oxides and ozone at northern mid-latitudes. *Atmospheric Environment*, 35(20):3421–3433.

Guo, S., G. J. Bluth, W. I. Rose, I. M. Watson, and A. J. Prata
2004. Re-evaluation of SO2 release of the 15 June 1991 Pinatubo eruption using ultraviolet and infrared satellite sensors. *Geochemistry, Geophysics, Geosystems*, 5(4):1–31.

Halmer, M. M., H.-U. Schmincke, and H.-F. Graf
2002. The annual volcanic gas input into the atmosphere, in particular into the stratosphere: a global data set for the past 100 years. *Journal of Volcanology and Geothermal Research*, 115(3-4):511–528.

Hartmann Hansen, M., K. Ingvorsen, and B. B. Jorgensen
1978. Meohanisms of hydrogen sulfide release from coastal marine sediments to the atmosphere. *Limnology and Oceanography*, 23(1):68–76.

Haynes, P. H., C. J. Marks, M. E. McIntyre, T. G. Shepherd, and K. P. Shine
1991. On the "downward control' of extratropical diabatic circulations by eddy-induced mean zonal forces.

Hervig, M. E., L. L. Gordley, L. E. Deaver, D. E. Siskind, M. H. Stevens, J. M. Russell, S. M. Bailey, L. Megner, and C. G. Bardeen
2009. First Satellite Observations of Meteoric Smoke in the Middle Atmosphere. *Geophysical Research Letters*, 36(18):L18805.

Hines, C. O.
1997. Doppler-spread parameterization of gravity-wave momentum deposition in the middle atmosphere. Part 1: Basic formulation. *Journal of Atmospheric and Solar-Terrestrial Physics*, 59(4):371–386.

Hodshire, A. L., P. Campuzano-Jost, J. K. Kodros, B. Croft, B. A. Nault, J. C. Schroder, J. L. Jimenez, and J. R. Pierce
2019. The potential role of methanesulfonic acid (MSA) in aerosol formation and growth and the associated radiative forcings. *Atmospheric Chemistry and Physics*, 19(5):3137–3160.

Holton, J. R.
1992. *An Introduction to Dynamic Meteorology*, 3 rd edition. Academic Press.

Holton, J. R., P. H. Haynes, M. E. McIntyre, A. R. Douglass, R. B. Rood, and L. Pfister
1995. Stratosphere-troposphere exchange. *Reviews of Geophysics*, 33(4):403.

Höpfner, M., C. D. Boone, B. Funke, N. Glatthor, U. Grabowski, A. Günther, S. Kellmann, M. Kiefer, A. Linden, S. Lossow, H. C. Pumphrey, W. G. Read, A. Roiger, G. P. Stiller, H. Schlager, T. Von Clarmann, and K. Wissmüller
2015. Sulfur dioxide (SO2) from MIPAS in the upper troposphere and lower stratosphere 2002–2012. *Atmospheric Chemistry and Physics*, 15(12):7017–7037.

Höpfner, M., N. Glatthor, U. Grabowski, S. Kellmann, M. Kiefer, A. Linden, J. Orphal, G. P. Stiller, T. von Clarmann, B. Funke, and C. D. Boone
2013. Sulfur dioxide (SO2) as observed by MIPAS/Envisat: temporal development and spatial distribution at 15–45km altitude. *Atmospheric Chemistry and Physics*, 13(20):10405–10423.

Höpfner, M., J. Ungermann, S. Borrmann, R. Wagner, R. Spang, M. Riese, G. Stiller, O. Appel, A. M. Batenburg, S. Bucci, F. Cairo, A. Dragoneas, F. Friedl-Vallon, A. Hünig, S. Johansson, L. Krasauskas, B. Legras, T. Leisner, C. Mahnke, O. Möhler, S. Molleker, R. Müller, T. Neubert, J. Orphal, P. Preusse, M. Rex, H. Saathoff, F. Stroh, R. Weigel, and I. Wohltmann
2019. Ammonium nitrate particles formed in upper troposphere from ground ammonia sources during Asian monsoons. *Nature Geoscience*.

Hünig, A.
2020. *Development , characterization and first field deployments of a novel aerosol mass spectrometer combining laser ablation and flash vaporization techniques for aircraft application at high altitudes*. PhD thesis, Johannes Gutenberg-Universität Mainz.

IPCC
2013. *2013: Climate Change 2013: The Physical Science Basis. Contribution of Working Group I to the Fifth Assessment Report of the Intergovernmental Panel on Climate Change*. Cambridge, United Kingdom and New York, NY, USA: Cambridge University Press.

Jöckel, P.
2006. Technical note: Recursive rediscretisation of geo-scientific data in the Modular Earth Submodel System (MESSy). *Atmospheric Chemistry and Physics*, 6(11):3557–3562.

Jöckel, P., A. Kerkweg, A. Pozzer, R. Sander, H. Tost, H. Riede, A. Baumgaertner, S. Gromov, and B. Kern
2010. Development cycle 2 of the Modular Earth Submodel System (MESSy2). *Geoscientific Model Development*, 3(2):717–752.

Jöckel, P., R. Sander, A. Kerkweg, H. Tost, and J. Lelieveld
2005. Technical Note: The Modular Earth Submodel System (MESSy) – a new approach towards Earth System Modeling. *Atmospheric Chemistry and Physics*, 4(6):7139–7166.

Jöckel, P., H. Tost, A. Pozzer, C. Brühl, J. Buchholz, L. Ganzeveld, P. Hoor, A. Kerkweg, M. G. Lawrence, R. Sander, B. Steil, G. Stiller, M. Tanarhte, D. Taraborrelli, J. van Aardenne, and J. Lelieveld
2006. The atmospheric chemistry general circulation model ECHAM5/MESSy1: consistent simulation of ozone from the surface to the mesosphere. *Atmospheric Chemistry and Physics*, 6(4):6957–7050.

Jöckel, P., H. Tost, A. Pozzer, M. Kunze, O. Kirner, C. A. M. Brenninkmeijer, S. Brinkop, D. S. Cai, C. Dyroff, J. Eckstein, F. Frank, H. Garny, K.-D. Gottschaldt, P. Graf, V. Grewe, A. Kerkweg, B. Kern, S. Matthes, M. Mertens, S. Meul, M. Neumaier, M. Nützel, S. Oberländer-Hayn, R. Ruhnke, T. Runde, R. Sander, D. Scharffe, and A. Zahn
2016. Earth System Chemistry integrated Modelling (ESCiMo) with the Modular Earth Submodel System (MESSy) version 2.51. *Geoscientific Model Development*, 9(3):1153–1200.

Johnson, J. E., A. R. Bandy, D. C. Thornton, and T. S. Bates
1993. Measurements of atmospheric carbonyl sulfide during the NASA Chemical Instrumentation Test and Evaluation project: Implications for the global COS budget. *Journal of Geophysical Research: Atmospheres*, 98(D12):23443–23448.

Johnson, J. E. and T. S. Bates
1993. Atmospheric Measurements of Carbonyl Sulfide, Dimethyl Sulfide, and Carbon-Disulfide Using the Electron-Capture Sulfur Detector. *Journal of Geophysical Research-Atmospheres*, 98(D12):23411–23421.

Junge, C. E., C. W. Chagnon, and J. E. Manson
1961. Stratospheric aerosols. *Journal of Meteorology*, 18(1):81–108.

Karu, E.
2019. *Atmospheric Sulfur Compounds in the Troposphere and Stratosphere Measured with an Atomic Emission Detector*. PhD thesis, Johannes Gutenberg-Universität in Mainz.

Kerkweg, A.
2005. *Global Modelling of Atmospheric Halogen Chemistry in the Marine Boundary Layer*. PhD thesis, Friedrich-Wilhelms-Universität Bonn.

Kerkweg, A., J. Buchholz, L. Ganzeveld, A. Pozzer, H. Tost, and P. Jöckel
2006a. Technical Note: An implementation of the dry removal processes DRY DEPosition and SEDImentation in the Modular Earth Submodel System (MESSy). *Atmospheric Chemistry and Physics*, 6(4):6853–6901.

Kerkweg, A., R. Sander, H. Tost, and P. Jöckel
2006b. Technical Note: Implementation of prescribed (OFFLEM), calculated (ONLEM), and pseudo-emissions (TNUDGE) of chemical species in the Modular Earth Submodel System (MESSy). *Atmospheric Chemistry and Physics*, 6(3):5485–5504.

Kettle, A. J. and M. O. Andreae
2000. Flux of dimethylsulfide from the oceans: A comparison of updated data sets and flux models. *Journal of Geophysical Research*, 105(D22):26793–26808.

Kettle, A. J., U. Kuhn, M. Von Hobe, J. Kesselmeier, and M. O. Andreae
2002. Global budget of atmospheric carbonyl sulfide: Temporal and spatial variations of the dominant sources and sinks. *Journal of Geophysical Research: Atmospheres*, 107:1–16.

Klingmüller, K., S. Metzger, M. Abdelkader, V. A. Karydis, G. L. Stenchikov, A. Pozzer, and J. Lelieveld
2018. Revised mineral dust emissions in the atmospheric chemistry–climate model EMAC (MESSy 2.52 DU_Astitha1 KKDU2017 patch). *Geoscientific Model Development*, 11(3):989–1008.

Klingmüller, K., B. Steil, C. Brühl, H. Tost, and J. Lelieveld
2014. Sensitivity of aerosol radiative effects to different mixing assumptions in the AEROPT 1.0 submodel of the EMAC atmospheric-chemistry–climate model. *Geoscientific Model Development*, 7(5):2503–2516.

Kloss, C.
2017. *Carbonyl Sulfide in the Stratosphere: airborne instrument development and satellite based data analysis*. PhD thesis, Bergischen Universität Wuppertal.

Kremser, S., L. W. Thomason, M. von Hobe, M. Hermann, T. Deshler, C. Timmreck, M. Toohey, A. Stenke, J. P. Schwarz, R. Weigel, S. Fueglistaler, F. J. Prata, J.-P. Vernier, H. Schlager, J. E. Barnes, J.-C. Antuña-Marrero, D. Fairlie, M. Palm, E. Mahieu, J. Notholt, M. Rex, C. Bingen, F. Vanhellemont, A. Bourassa, J. M. C. Plane, D. Klocke, S. A. Carn, L. Clarisse, T. Trickl, R. Neely, A. D. James, L. Rieger, J. C. Wilson, and B. Meland
2016. Stratocpsheric aerosol - Observations, processes and impact on climate. *Reviews of Geophysics*, 54:1–58.

Kyrölä, E., J. Tamminen, V. Sofieva, J. L. Bertaux, A. Hauchecorne, F. Dalaudier, D. Fussen, F. Vanhellemont, O. Fanton D'Andon, G. Barrot, M. Guirlet, T. Fehr, and L. Saavedra De Miguel
2010. GOMOS O3, NO2, and NO3 observations in 2002-2008. *Atmospheric Chemistry and Physics*, 10(16):7723–7738.

Lana, A., T. G. Bell, R. Simó, S. M. Vallina, J. Ballabrera-Poy, a. J. Kettle, J. Dachs, L. Bopp, E. S. Saltzman, J. Stefels, J. E. Johnson, and P. S. Liss
2011. An updated climatology of surface dimethlysulfide concentrations and emission fluxes in the global ocean. *Global Biogeochemical Cycles*, 25(1).

Landgraf, J. and P. J. Crutzen
1998. An Efficient Method for Online Calculations of Photolysis and Heating Rates. *Journal of the Atmospheric Sciences*, 55(5):863–878.

Lee, C., R. V. Martin, A. Van Donkelaar, H. Lee, R. R. Dickerson, J. C. Hains, N. Krotkov, A. Richter, K. Vinnikov, and J. J. Schwab
2011. SO2 emissions and lifetimes: Estimates from inverse modeling using in situ and global, space-based (SCIAMACHY and OMI) observations. *Journal of Geophysical Research Atmospheres*, 116(6):1–13.

Lelieveld, J., E. Bourtsoukidis, C. Brühl, H. Fischer, H. Fuchs, H. Harder, A. Hofzumahaus, F. Holland, D. Marno, M. Neumaier, A. Pozzer, H. Schlager, J. Williams, A. Zahn, and H. Ziereis 2018. The South Asian monsoon—pollution pump and purifier. *Science*, 361(6399):270–273.

Lelieveld, J., C. Brühl, P. Jöckel, B. Steil, P. J. Crutzen, H. Fischer, M. A. Giorgetta, P. Hoor, M. G. Lawrence, R. Sausen, and H. Tost
2007. Stratospheric dryness: Model simulations and satellite observations. *Atmospheric Chemistry and Physics*, 7(5):1313–1332.

Lennartz, S. T., G. Krysztofiak, C. A. Marandino, B.-M. Sinnhuber, S. Tegtmeier, F. Ziska, R. Hossaini, K. Krüger, S. A. Montzka, E. Atlas, D. E. Oram, T. Keber, H. Bönisch, and B. Quack
2015. Modelling marine emissions and atmospheric distributions of halocarbons and dimethyl sulfide: the influence of prescribed water concentration vs. prescribed emissions. *Atmospheric Chemistry and Physics*, 15(20):11753–11772.

Lennartz, S. T., C. A. Marandino, M. Von Hobe, P. Cortes, B. Quack, R. Simo, D. Booge, A. Pozzer, T. Steinhoff, D. L. Arevalo-Martinez, C. Kloss, A. Bracher, E. Atlas, and K. Krüger
2017. Direct oceanic emissions unlikely to account for the missing source of atmospheric carbonyl sulfide. *Atmospheric Chemistry and Physics*, 17(1):385–402.

Love, S. G. and D. E. Brownlee
1993. A direct measurement of the terrestrial mass accretion rate of cosmic dust. *Science (New York, N.Y.)*, 262(5133):550–553.

Mallik, C., N. Chandra, S. Venkataramani, and S. Lal
2016. Variability of atmospheric carbonyl sulfide at a semi-arid urban site in western India. *Science of the Total Environment*, 551-552:725–737.

Manzini, E., N. A. McFarlane, and C. McLandress
1997. Impact of the Doppler spread parameterization on the simulation of the middle atmosphere circulation using the MA/ECHAM4 general circulation model. *Journal of Geophysical Research: Atmospheres*, 102(D22):25751–25762.

Martinsson, B. G., J. Friberg, O. S. Sandvik, M. Hermann, P. F. Van Velthoven, and A. Zahn
2017. Particulate sulfur in the upper troposphere and lowermost stratosphere - Sources and climate forcing. *Atmospheric Chemistry and Physics*, 17(18):10937–10953.

McCormick, M. P. and R. E. Veiga
1992. SAGE II measurements of early Pinatubo aerosols. *Geophysical Research Letters*, 19(2):155–158.

Meinardi, S., I. J. Simpson, N. J. Blake, D. R. Blake, and F. S. Rowland
2003. Dimethyl disulfide (DMDS) and dimethyl sulfide (DMS) emissions from biomass burning in Australia. *Geophysical Research Letters*, 30(9).

Metzger, S. and J. Lelieveld
2007. Reformulating atmospheric aerosol thermodynamics and hygroscopic growth into haze and clouds. *Atmospheric Chemistry and Physics*, 7(1):849–910.

Mills, M. J., A. Schmidt, R. Easter, S. Solomon, D. E. Kinnison, S. J. Ghan, R. R. Neely, D. R. Marsh, A. Conley, C. G. Bardeen, and A. Gettelman
2016. Global volcanic aerosol properties derived from emissions, 1990-2014, using CESM1(WACCM). *Journal of Geophysical Research*, 121(5):2332–2348.

Minnis, P., E. F. Harrison, L. L. Stowe, G. G. Gibson, F. M. Denn, D. R. Doelling, and W. L. Smith
1993. Radiative climate forcing by the Mount Pinatubo eruption. *Science*, 259(5100):1411–1415.

Montzka, S. A., P. Calvert, B. D. Hall, J. W. Elkins, T. J. Conway, P. P. Tans, and C. S. Sweeney
2007. On the global distribution, seasonality, and budget of atmospheric carbonyl sulfide (COS) and some similarities to CO2. *Journal of Geophysical Research Atmospheres*, 112(9):1–15.

Mote, P. W., K. H. Rosenlof, E. Mcintyre, E. S. Carr, J. C. Gille, R. Holton, S. Kinnersley, H. C. Pumphrey, M. Russell, and J. W. Wal
1996. An atmospheric tape recorder: The imprint of tropical tropopause temperatures on stratospheric water vapor. *Journal of Geophysical Research*, 101(95):3989–4006.

Neely, R. R., J. M. English, O. B. Toon, S. Solomon, M. Mills, and J. P. Thayer
2011. Implications of extinction due to meteoritic smoke in the upper stratosphere. *Geophysical Research Letters*, 38(24):n/a–n/a.

Newhall, C. G. and S. Self
1982. The volcanic explosivity index (VEI): An estimate of explosive magnitude for historical volcanism. *Journal of Geophysical Research: Atmospheres*, 87(1):1231–1238.

Nordeng, T. E.
1994. Extended version of the convective parametrization scheme at ECMWF and their impact on the mean and transient activity of the model in the tropics. Technical report, ECMWF.

Plane, J. M. C.
2012. Cosmic dust in the earth's atmosphere. *Chemical Society Reviews*, 41(19):6507.

Plane, J. M. C., W. Feng, and E. C. M. Dawkins
2015. The Mesosphere and Metals: Chemistry and Changes. *Chemical Reviews*, 115(10):4497–4541.

Pozzer, A., A. de Meij, K. J. Pringle, H. Tost, U. M. Doering, J. van Aardenne, and J. Lelieveld
2012. Distributions and regional budgets of aerosols and their precursors simulated with the EMAC chemistry-climate model. *Atmospheric Chemistry and Physics*, 12(2):961–987.

Pozzer, A., P. Jöckel, R. Sander, J. Williams, L. Ganzeveld, and J. Lelieveld
2006. Technical Note: The MESSy-submodel AIRSEA calculating the air-sea exchange of chemical species. *Atmospheric Chemistry and Physics*, 6(12):5435–5444.

Predybaylo, E., G. L. Stenchikov, A. T. Wittenberg, and F. Zeng
2017. Impacts of a pinatubo-size volcanic eruption on ENSO. *Journal of Geophysical Research*, 122(2):925–947.

Pringle, K., H. Tost, and S. Metzger
2010a. GMXe – Users Manual. Technical report, Air Chemistry Department Max-Planck Institute of Chemistry, Mainz.

Pringle, K. J., H. Tost, S. Metzger, B. Steil, D. Giannadaki, A. Nenes, C. Fountoukis, P. Stier, E. Vignati, and J. Lelieveld
2010b. Description and evaluation of GMXe: a new aerosol submodel for global simulations (v1). *Geoscientific Model Development*, 3(2):391–412.

Pruppacher, H. R. and J. D. Klett
2010. *Microphysics of Clouds and Precipitation*, volume 18 of *Atmospheric and Oceanographic Sciences Library*, second rev edition. Dordrecht: Springer Netherlands.

Rasch, P. J., P. J. Crutzen, and D. B. Coleman
2008. Exploring the geoengineering of climate using stratospheric sulfate aerosols: The role of particle size. *Geophysical Research Letters*, 35(2):L02809.

Ravegnani, F., T. Georgiadis, L. Stefanutti, V. Yushkov, and A. Oulanovsky
1999. In-situ stratospheric ozone measurements by means of a fast ozone sensor (FOZAN) onboard the M55-Geophysica aircraft. *Optical Spectroscopic Techniques and Instrumentation for Atmospheric and Space Research III*, 3756(October 1999):502.

Rieger, L. A., A. E. Bourassa, and D. A. Degenstein
2015. Merging the OSIRIS and SAGE II stratospheric aerosol records. *Journal of Geophysical Research*, 120(17):8890–8904.

Rieger, L. A., E. P. Malinina, A. V. Rozanov, J. P. Burrows, A. E. Bourassa, and D. A. Degenstein
2018. A study of the approaches used to retrieve aerosol extinction, as applied to limb observations made by OSIRIS and SCIAMACHY. *Atmospheric Measurement Techniques*, 11(6):3433–3445.

Robert, C. É., C. Bingen, F. Vanhellemont, N. Mateshvili, E. Dekemper, C. Tétard, D. Fussen, A. Bourassa, and C. Zehner
2016. AerGOM, an improved algorithm for stratospheric aerosol retrieval from GOMOS observations. Part 2: Intercomparisons. *Atmospheric Measurement Techniques*, 9:4701–4718.

Roeckner, E., G. Bäuml, L. Bonaventura, R. Brokopf, M. Esch, M. Giorgetta, S. Hagemann, I. Kirchner, L. Kornblueh, A. Rhodin, U. Schlese, U. Schulzweida, A. Tompkins, E. Manzini, A. Rhodin, U. Schlese, U. Schulzweida, and A. Tompkins
2003. The atmospheric general circulation model ECHAM5. Part I: Model description. Technical Report 349, Max-Planck-Institute für Meteorologie, Hamburg.

Roeckner, E., R. Brokopf, M. Esch, M. A. Giorgetta, S. Hagemann, L. Kornblueh, E. Manzini,

U. Schlese, and U. Schulzweida
2006. Sensitivity of simulated climate to horizontal and vertical resolution in the ECHAM5 atmosphere model. *Journal of Climate*, 19(16):3771–3791.

Roedel, W. and T. Wagner
2011. *Physik unserer Umwelt: Die Atmosphäre*, 4 edition. Berlin, Heidelberg: Springer Berlin Heidelberg.

Rosenfeld, D.
2007. Aerosol-Cloud Interactions Control of Earth Radiation and Latent Heat Release Budgets. In *Solar Variability and Planetary Climates*, Y. Calisesi, R. M. Bonnet, L. Gray, J. Langen, and M. Lockwood, eds., Pp. 149–157. New York, NY: Springer New York.

Sander, R., A. Baumgaertner, S. Gromov, H. Harder, P. Jöckel, A. Kerkweg, D. Kubistin, E. Regelin, H. Riede, A. Sandu, D. Taraborrelli, H. Tost, and Z.-Q. Q. Xie
2011. The atmospheric chemistry box model CAABA/MECCA-3.0. *Geoscientific Model Development*, 4(2):373–380.

Sander, R., P. Jöckel, O. Kirner, A. T. Kunert, J. Landgraf, and A. Pozzer
2014. The photolysis module JVAL-14, compatible with the MESSy standard, and the JVal PreProcessor (JVPP). *Geoscientific Model Development*, 7(6):2653–2662.

Santer, B. D., C. Bonfils, J. F. Painter, M. D. Zelinka, C. Mears, S. Solomon, G. A. Schmidt, J. C. Fyfe, J. N. Cole, L. Nazarenko, K. E. Taylor, and F. J. Wentz
2014. Volcanic contribution to decadal changes in tropospheric temperature. *Nature Geoscience*, 7(3):185–189.

Schneider, J., R. Weigel, T. Klimach, A. Dragoneas, O. Appel, A. Hünig, S. Molleker, F. Köllner, H.-C. Clemen, O. Eppers, P. Hoppe, P. Hoor, C. Mahnke, M. Krämer, C. Rolf, J.-U. Grooß, A. Zahn, F. Obersteiner, F. Ravegnani, A. Ulanovsky, H. Schlager, M. Scheibe, G. S. Diskin, J. P. DiGangi, J. B. Nowak, M. Zöger, and S. Borrmann
2020. Aircraft - based observation of meteoric material in lower stratospheric aerosol particles between 15 and 68 ° N. *Atmospheric Chemistry and Physics Discussions*, Pp. 1–26.

Seinfeld, J. H. and S. N. Pandis
1998. *Atmospheric chemistry and physics: From Air Pollution to Climate Change*. New York: John Wiley & Sons, Inc.

Sheng, J. X., D. K. Weisenstein, B. P. Luo, E. Rozanov, A. Stenke, J. Anet, H. Bingemer, and T. Peter
2015. Global atmospheric sulfur budget under volcanically quiescent conditions: Aerosol-chemistry-climate model predictions and validation. *Journal of Geophysical Research*, 120(1):256–276.

Solomon, S.
1999. Stratospheric ozone depletion: A review of concepts and history. *Reviews of Geophysics*, 37(3):275–316.

Solomon, S., J. S. Daniel, R. R. Neely, J.-P. Vernier, E. G. Dutton, and L. W. Thomason
2011. The persistently variable ”background” stratospheric aerosol layer and global climate change. *Science*, 333(6044):866–870.

Solomon, S., D. Kinnison, R. R. Garcia, J. Bandoro, M. Mills, C. Wilka, R. R. Neely, A. Schmidt, J. E. Barnes, J.-P. Vernier, and M. Höpfner
2016. Monsoon circulations and tropical heterogeneous chlorine chemistry in the stratosphere. *Geophysical Research Letters*, 43(24):12,624–12,633.

Spang, R., L. Hoffmann, R. Müller, J. U. Grooß, I. Tritscher, M. Höpfner, M. Pitts, A. Orr, and M. Riese
2018. A climatology of polar stratospheric cloud composition between 2002 and 2012 based on MIPAS/Envisat observations. *Atmospheric Chemistry and Physics*, 18(7):5089–5113.

Stefanutti, L., L. Sokolov, S. Balestri, A. R. MacKenzie, and V. Khattatov
1999. The M-55 Geophysica as a platform for the Airborne Polar Experiment. *Journal of Atmospheric and Oceanic Technology*, 16(10):1303–1312.

Stier, P., J. Feichter, S. Kinne, S. Kloster, E. Vignati, J. Wilson, L. Ganzeveld, I. Tegen, and M. Werner
2005. The aerosol-climate model ECHAM5-HAM. *Atmospheric Chemistry and Physics*, 5:1125–1156.

Thomas, M. A.
2008. *Simulation of the climate impact of Mt. Pinatubo eruption using ECHAM5*. PhD thesis, Universität Hamburg.

Thomason, L. W., S. P. Burton, B. P. Luo, and T. Peter
2008. SAGE II measurements of stratospheric aerosol properties at non-volcanic levels. *Atmospheric Chemistry and Physics*, 8:983–995.

Thomason, L. W. and T. Peter
2006. Assessment of stratospheric aerosol properties (ASAP). Technical Report 1295, SPARC.

Tiedtke, M.
1989. A Comprehensive Mass Flux Scheme for Cumulus Parameterization in Large-Scale Models. *Monthly Weather Review*, 117(8):1779–1800.

Timmreck, C., H. F. Graf, and J. Feichter
1999. Simulation of Mt. Pinatubo volcanic aerosol with the Hamburg climate model ECHAM4. *Theoretical and Applied Climatology*, 62(3-4):85–108.

Tompkins, A. M.
2002. A Prognostic Parameterization for the Subgrid-Scale Variability of Water Vapor and Clouds in Large-Scale Models and Its Use to Diagnose Cloud Cover. *Journal of the Atmospheric Sciences*, 59(12):1917–1942.

Tost, H.
2006. *Global Modelling of Cloud, Convection and Precipitation Influences on Trace Gases and Aerosols*. PhD thesis, Bonn.

Tost, H., P. Jöckel, A. Kerkweg, R. Sander, and J. Lelieveld
2006a. Technical note: A new comprehensive SCAVenging submodel for global atmospheric chemistry modelling. *Atmospheric Chemistry and Physics*, 5:11157–11181.

Tost, H., P. Jöckel, and J. Lelieveld
2006b. Influence of different convection parameterisations in a GCM. *Atmospheric Chemistry and Physics*, 6(12):5475–5493.

Tost, H., P. Jöckel, and J. Lelieveld
2007. Lightning and convection parameterisations - uncertainties in global modelling. *Atmospheric Chemistry and Physics*, 7(3):4553–4568.

Tost, H., M. G. Lawrence, C. Brühl, and P. Jöckel
2010. Uncertainties in atmospheric chemistry modelling due to convection parameterisations and subsequent scavenging. *Atmospheric Chemistry and Physics*, 10(4):1931–1951.

Twomey, S.
1977. The Influence of Pollution on the Shortwave Albedo of Clouds. *Journal of the Atmospheric Sciences*, 34(7):1149–1152.

Uin, J.
2016. Ultra-High-Sensitivity Aerosol Spectrometer (UHSAS) Instrument Handbook. Technical Report April, ARM Climate Research Facility.

Ulanovsky, A. E., V. A. Yushkov, N. M. Sitnikov, and F. Ravegnani
2001. The FOZAN-II Fast-Response Chemiluminescent Airborne Ozone Analyzer. *Instruments and Experimental Techniques*, 44(2):249–256.

Vanhellemont, F., D. Fussen, N. Mateshvili, C. Tétard, C. Bingen, E. Dekemper, N. Loodts, E. Kyrölä, V. Sofieva, J. Tamminen, A. Hauchecorne, J. L. Bertaux, F. Dalaudier, L. Blanot, O. Fanton D'Andon, G. Barrot, M. Guirlet, T. Fehr, and L. Saavedra
2010. Optical extinction by upper tropospheric/stratospheric aerosols and clouds: GOMOS observations for the period 2002-2008. *Atmospheric Chemistry and Physics*, 10(16):7997–8009.

Vanhellemont, F., N. Mateshvili, L. Blanot, C. É. Robert, C. Bingen, V. Sofieva, F. Dalaudier, C. Tétard, D. Fussen, E. Dekemper, E. Kyrölä, M. Laine, J. Tamminen, and C. Zehner
2016. AerGOM, an improved algorithm for stratospheric aerosol retrieval from GOMOS observations. Part 1: Algorithm description. *Atmospheric Measurement Techniques*, 2016:1–24.

Vehkamäki, H., M. Kulmala, I. Napari, K. E. J. Lehtinen, C. Timmreck, M. Noppel, and A. Laaksonen
2002. An improved parameterization for sulfuric acid – water nucleation rates for tropospheric and stratospheric conditions. *Journal of Geophysical Research*, 107:1–10.

Vernier, J.-P., T. D. Fairlie, T. Deshler, M. Natarajan, T. Knepp, K. Foster, F. G. Wienhold, K. M. Bedka, L. Thomason, and C. Trepte
2016. In situ and space-based observations of the Kelud volcanic plume: The persistence of ash in the lower stratosphere. *Journal of Geophysical Research : Atmospheres*, Pp. 104–118.

Vernier, J.-P., L. W. Thomason, and J. Kar
2011a. CALIPSO detection of an Asian tropopause aerosol layer. *Geophysical Research Letters*, 38(7):1–6.

Vernier, J.-P., L. W. Thomason, J.-P. P. Pommereau, A. E. Bourassa, J. Pelon, A. Garnier, A. Hauchecorne, L. Blanot, C. Trepte, D. A. Degenstein, and F. Vargas
2011b. Major influence of tropical volcanic eruptions on the stratospheric aerosol layer during the last decade. *Geophysical Research Letters*, 38(12):n/a–n/a.

Vignati, E., J. Wilson, and P. Stier
2004. M7: An efficient size-resolved aerosol microphysics module for large-scale aerosol transport models. *Journal of Geophysical Research: Atmospheres*, 109(D22).

von Glasow, R., N. Bobrowski, and C. Kern
2009. The effects of volcanic eruptions on atmospheric chemistry. *Chemical Geology*, 263(1-4):131–142.

Walcek, C. J.
2000. Minor flux adjustment near mixing ratio extremes for simplified yet highly accurate monotonic calculation of tracer advection. *Journal of Geophysical Research Atmospheres*, 105(D7):9335–9348.

Watts, S. F.
2000. The mass budgets of carbonyl sulfide, dimethyl sulfide, carbon disulfide and hydrogen sulfide. *Atmospheric Environment*, 34(5):761–779.

Weigel, R., S. Borrmann, J. Kazil, A. Minikin, A. Stohl, J. C. Wilson, J. M. Reeves, D. Kunkel, M. De Reus, W. Frey, E. R. Lovejoy, C. M. Volk, S. Viciani, F. D'Amato, C. Schiller, T. Peter, H. Schlager, F. Cairo, K. S. Law, G. N. Shur, G. V. Belyaev, and J. Curtius
2011. In situ observations of new particle formation in the tropical upper troposphere: The role of clouds and the nucleation mechanism. *Atmospheric Chemistry and Physics*, 11(18):9983–10010.

Weigel, R., M. Hermann, J. Curtius, C. Voigt, S. Walter, T. Böttger, B. Lepukhov, G. V. Belyaev, and S. Borrmann
2009. Experimental characterization of the COndensation PArticle counting System for high altitude aircraft-borne application. *Atmospheric Measurement Techniques*, 1(1):321–374.

Weisenstein, D. K.
1997. A two-dimensional model of sulfur species and aerosols. *Journal of Geophysical Research Atmospheres*, 102(D11):13019–13035.

Wine, P. H., W. L. Chameides, and A. R. Ravishankara
1981. Potential role of CS2 photooxidation in tropospheric sulfur chemistry. *Geophysical Research Letters*, 8(5):543–546.

Wong, T., B. A. Wielicki, R. B. Lee, G. L. Smith, K. A. Bush, and J. K. Willis
2006. Reexamination of the observed decadal variability of the earth radiation budget using altitude-corrected ERBE/ERBS nonscanner WFOV data. *Journal of Climate*, 19(16):4028–4048.

Acknowledgements

Scientific work is never the work of a single person alone, so now is the time to thank all the people who made it possible for me to write my dissertation.

The research leading to these results has received funding from the European Research Council under the European Union's Seventh Framework Programme (FP7/2007–2013)/ERC grant agreement 226144 as part of StratoClim project and funding from ESA Aerosol CCI. There is a close collaboration with the SPARC/SSIRC (Stratospheric Sulphur and its Role in Climate) stratospheric aerosol model intercomparison project (http://www.sparc-ssirc.org 18 December 2020) and the ESA Aerosol CCI concerning SO_2 injections derived from satellite data and model intercomparisons.

The computations have been performed at the mistral supercomputer at DKRZ, Hamburg, Germany. Thanks to our IT group for reanimations of my computer, saving my data and technical support.

I want to thank the GOMOS, MIPAS, OSIRIS, SAGE and EOSDIS (NASA) teams for productive cooperation and providing their satellite data sets. Without this data running model simulations would not be possible. Many thanks to the ERICA, COPAS, UHSAS and AMICA teams for providing the data from the StratoClim project, which was essential for the validation of the modeling results. Also thanks to the colleagues from GEOMAR Helmholtz-Center for Ocean Research Kiel for the discussions on the missing sources of sulfur precursor gases from the ocean.

I am grateful to my colleges from the MPIC modelers group, the StratoClim campaign, the CARIBIC project and my supervisors for their support and giving me the opportunity for writing my thesis and working at the Max-Planck-Institute. I am also grateful to my colleagues from the EMAC community helping me to implement the New Sulfur Chemistry Mechanism into "MESSy" and all other MESSy developers and users for their support. I would always remember my fellow office mates too for the fun-time we spent together and for stimulating discussions. Many, many thanks to my "English experts" for proofreading my text and helpful comments, all mistakes are my fail. I want to thank all of you for the warm welcome and the nice discussions at so many conferences and meetings.

At last but not least I want to thank my family and friends for all their passion and love. I consider myself nothing without them. They gave me enough moral support, encouragement and motivation to accomplish my goals.

Erklärung zur Doktorarbeit

Hiermit versichere ich, die vorliegende Dissertation selbstständig und nur mit Verwendung der angegebenen Literatur und Hilfsmittel erstellt zu haben. Sowie noch keinen Promotionsversuch unternommen zu haben. Die Arbeit wurde bisher in gleicher oder ähnlicher Form keiner anderen Prüfungsbehörde vorgelegt und auch nicht veröffentlicht.

Mainz,

Jennifer Schallock